ÇUKUROVA UNIVERSITY
INSTITUTE OF NATURAL AND APPLIED SCIENCES

PhD THESIS

Mohammad BARGHI LATRAN

OPTIMAL DESIGN AND RESEARCH ON MULTI OBJECTIVE CONTROL STRATEGY FOR MULTILEVEL MULTIFUNCTIONAL INVERTER IN LARGE SCALE GRID CONNECTED PHOTOVOLTAIC SYSTEM

DEPARTMENT OF ELECTRICAL AND ELECTRONICS ENGINEERING

ADANA-2017

ÇUKUROVA UNIVERSITY
INSTITUTE OF NATURAL AND APPLIED SCIENCES

OPTIMAL DESIGN AND RESEARCH ON MULTI OBJECTIVE CONTROL STRATEGY FOR MULTILEVEL MULTIFUNCTIONAL INVERTER IN LARGE SCALE GRID CONNECTED PHOTOVOLTAIC SYSTEM

Mohammad BARGHI LATRAN
PhD THESIS

DEPARTMENT OF ELECTRICAL AND ELECTRONICS ENGINEERING

We certify that the thesis titled above was reviewed and approved for the award of degree of the Doctor of Philosophy by the board of jury on 05/12/2016.

…….....	…….....	…….....
Assoc. Prof. Dr. Ahmet TEKE	Prof. Dr. Mustafa GÖK	Asst. Prof. Dr. Lütfü SARIBULUT
SUPERVISOR	MEMBER	MEMBER

…….....	…….....
Asst. Prof. Dr. Murat FURAT	Asst. Prof. Dr. Adnan TAN
MEMBER	MEMBER

This PhD Thesis is written at the Department of Electrical and Electronics Engineering of Institute of Natural and Applied Sciences of Çukurova University.

Registration Number:

Prof. Dr. Mustafa GÖK
Director
Institute of Natural and Applied Sciences

This thesis was supported by the Scientific Research Project Unit of Çukurova University for my thesis (Project Number: FDK-2016-6392)

ABSTRACT

PhD THESIS

OPTIMAL DESIGN AND RESEARCH ON MULTI OBJECTIVE CONTROL STRATEGY FOR MULTILEVEL MULTIFUNCTIONAL INVERTER IN LARGE SCALE GRID CONNECTED PHOTOVOLTAIC SYSTEM

Mohammad BARGHI LATRAN

ÇUKUROVA UNIVERSITY
INSTITUTE OF NATURAL AND APPLIED SCIENCES
DEPARTMENT OF ELECTRICAL AND ELECTRONICS ENGINEERING

Supervisor : Assoc. Prof. Dr. Ahmet TEKE
Year: 2017, Pages: 283
Jury : Assoc. Prof. Dr. Ahmet TEKE
: Prof. Dr. Mustafa GÖK
: Asst. Prof. Dr. Lütfü SARIBULUT
: Asst. Prof. Dr. Murat FURAT
: Asst. Prof. Dr. Adnan TAN

This thesis focuses on the multilevel multifunctional grid connected inverter architecture, taking into account how to interconnect photovoltaic (PV) systems into the future smart microgrid with maximizes efficiency, power quality (PQ) and reliability of the power system. The desirable approach should be capable to sustain high quality energy transfer between PV power plants and utility grid and to enhance the PQ at the both consumers and source side. This thesis presents investigations into issues of PQ and reliability of grid connected inverters and offers advanced topological and sophisticated control solutions to significantly improve performance of these systems. In this context, a PV based multilevel inverter proposed to simultaneously maintain high-quality power exchange between PV systems and the utility grid in disturbed grids and perform simultaneous mitigation of PQ problems using novel control algorithm. Furthermore, to produce optimum power and operate at the maximum proficiency a maximum power point tracking method proposed to extract maximum power of the PV system when the PV system receives uniform and non-uniform irradiance or subjected to partial shading. Additionally a wavelet transform based voltage sag/swell detectıon algorithm is proposed to detect voltage sag/swell disturbances.

Key Words: Multilevel Multifunctional Grid Connected Inverter, Power Quality, Photovoltaic System, Maximum Power Point Tracking.

ÖZ

DOKTORA TEZİ

BÜYÜK ÖLÇEKLİ ŞEBEKE BAĞLANTILI FOTOVOLTAIK SISTEMLERDE ÇOK SEVIYELI ÇOK FONKSIYONLU EVIRGEÇ İÇIN ÇOK AMAÇLI KONTROL STRATEJISININ OPTIMUM TASARIMI VE ARAŞTIRILMASI

Mohammad BARGHI LATRAN

ÇUKUROVA ÜNİVERSİTESİ
FEN BİLİMLERİ ENSTİTÜSÜ
ELEKTRİK ELEKTRONİK MÜHENDİSLİĞİ ANABİLİM DALI

Danışman : Doç. Dr. Ahmet TEKE
Yıl: 2017, Pages: 283
Jüri : Doç. Dr. Ahmet TEKE
: Prof. Dr. Mustafa GÖK
: Yrd. Doç. Dr. Lütfü SARIBULUT
: Yrd. Doç. Dr. Murat FURAT
: Yrd. Doç. Dr. Adnan TAN

Bu çalışma şebekenin güç kalitesini iyileştirmek için fotovoltaik sistemlerin şebekeye nasıl bağlanacağını dikkate alarak, şebeke bağlantılı çok-seviyeli çok-fonksiyonlu eviricinin (ÇSÇFE) yapısına odaklanmaktadır. Bu çalışma, şebeke bağlantılı eviricilerin güç kalitesi ve güvenirliliği konularında araştırmaları sunmakta olup, bu sistemlerin verimliliğini arttırmak için ileri seviye topolojik ve kontrol yöntemi çözümlerini önermektedir. Bu kapsamda geliştirilen ÇSÇFE, şebeke bağlantılı evirici fotovoltaik sistem ve şebeke arasında yüksek kaliteli aktif güç transferini, ortak bağlantı noktasında (OBN) güç kalitesi problemlerinin giderilmesini ve şebekede etkin bir kontrolünün gerçekleştirilmesini sağlamıştır. Önerilen ÇSÇFE yüksek kaliteli aktif gücü şebekeye enjekte etmesinin yanı sıra OBN'deki farklı güç kalitesi problemleri ve reaktif gücü eşzamanlı olarak yeni kontrol yöntemleriyle kompanze edebilmektedir. Bunların yanısıra, fotovoltaik sistemlerinin verimliliğini arttırmak için normal ve kısmi gölgelenme şartları altında fotovoltaik sistemlerden maksimum gücü elde etmek için yeni bir maksimum güç noktası takibi yöntemi geliştirilmiştir. Ayrıca gerilim çukuru ve tepelerinin tespiti için dalgacık tabanlı yeni bir metot geliştirilmiştir.

Anahtar Kelimeler: Çok Seviyeli Çok Fonksiyonlu Evirici, Güç Kalitesi, Fotovoltaik, Maksimum Güç Noktası Takibi.

EXTENDED ABSTRACT

Electric power networks have vital role to construct infrastructures in modern society. Furthermore, preventing power outage, reducing carbon dioxide emission while minimizing environmental effects and increasing energy efficiency have becomes more important subjects in the world. Due to this priority, the annual installations and capacity of renewable energy based distributed energy systems are increasing rapidly. Solar and wind energy are two of the most valid types of renewable energy sources. Solar energy is more advantageous than wind energy, as it can be installed every place with proper placement of PV arrays.

Solar PVs are on a fast track of technological development. Innovations in material science research have led to newer generations of PV cells that promise much higher efficiency and lower cost in the future. Advances in PV technology and incentive policies for deployment of RESs have significantly increased the capacity of installed PV systems. During the last decade, grid connected PV systems in the range of megawatt have been installed and currently are operational all over the world.

In recent times, construction of PV plants becomes increasingly affordable owing to consistent decline in the PV equipment costs and advance in auxiliary technology. PV equipment has a limited lifespan of around 20–25 years. Therefore, the optimal utilization of the PV equipment becomes very important issue. Unfortunately, due to complex relationship between temperature, solar radiation, and total resistance of PV panels the extraction of maximum power from PV system is a challenging task. In addition, PV systems exhibit a nonlinear output efficiency characteristic which is known as the Power-Voltage (P–V) curve where there is a unique point referred as maximum power point (MPP). At this point, the PV system produces optimum power and operates at the maximum proficiency. However, the position of the MPP on *P-V* curve is not known, so a suitable maximum power point tracking (MPPT) technique is required to track the

operating point of PV system at its MPP. The case will be more complicated when the PV system receives non-uniform irradiance and PV system is subjected to partial shading (PS). In this situation, P–V curve will be characterized by multiple peaks which one of them is the global maximum power point (GMPP). The tracking of the GMPP seems to be an optimization problem.

The capacities of PV plants are continuously growing with the increasing popularity of PV systems. In this context, the installed capacity and application of photovoltaic energy systems is increasing. Additionally, by increasing the number of utilized photovoltaic systems, new control methods must be developed for the proper operation and management of new power grid embedded with PV units to improve or maintain the system reliability, stability and quality. Since the connection of photovoltaic systems to the power system network is a very important issue, power electronics and intelligent technologies play an important role in the operation of PV systems.

In practice, due to non-controllable and stochastic nature of the solar energy the output power from PV systems is intrinsically unstable. Therefore, from the network-wise point of view it can lead to many problems due to increasing the number of installed PV systems in the distribution system. This situation can pose a threat to PQ, voltage regulation and balance issues in the power system network. Hence, the provision of PQ standards, electromagnetic compatibility, acoustic noise limits, safety and protection requirements are important issues for PV systems. Hence, in the interlinking of the PV plants with the power system network, it is necessary to comply with various standards given by the utility companies. These standards deal with topics such as interconnection issues, operation principles and issues related to PQ, stability, reliability, safety, etc. In addition, some of these standards define the structure and properties of existing and future PV panels.

Utility grid control strategy manages capacitor groups, voltage regulators and tap changer transformers to perform power flow control and mitigate

disturbances. However, due to operation range limitations of these devices, inefficient control of system reliability, stability and efficiency can be ensured. The unbalances in the system can cause the improper power flow analysis and the selection of wrong control strategy by utility grid to achieve system control. Besides, the harmonics in the system can cause loss of information on communication devices and misoperation of smart metering devices, relays and circuit breakers. High technology active power quality conditioners (APQC) are used to achieve power flow control, apt to bring the voltage back within statutory limits, to compensate reactive power and to eliminate PQ problems in the system caused by renewable energy based distributed energy systems. APQC and renewable energy based distributed energy systems are new trends to meet increasing power demand and increasing power system. However, the connection of APQC and renewable energy based distributed energy systems on the same point of common coupling (PCC) can cause the coordination and correct placement problems. APQCs have the same power converter stage of renewable energy based grid connected inverters. Thus these stages can be multiplexed. Power converter stage of a grid connected inverters can be utilized to realize the functionalities of the grid connected inverter and the APQCs, as well as, Volt-VAr control compared with multiple devices with different individually in dependent functionalities. Therefore, there just a little modification in control algorithm is needed to change the conventional grid connected inverters into multifunctional grid connected inverters by providing multifunctional operation. This will provide an increase in system stability, a decrease in the investment and maintenance costs and an ease in the system operation.

Thus, PV systems can be effectively controlled to improve the PQ, reliability, stability and efficiency of existed system by application of advanced power electronics, enforcement of MPPT methods and utilization of intelligent control techniques. Although the main goal of PV systems is to obtain active power; static synchronous compensator and active power filter functionality can be

realized. PV systems can be interfaced with the power system network either in series or parallel position. However, the target compensated quantities, such as harmonics, unbalance, and reactive power, are directly related to the currents. As such, the parallel type architecture is widely utilized because it effectively injects compensating currents at PCC.

The application of new technologies in renewable energy based distributed energy systems is important step of new generation energy production technologies. As the number of voltage levels on the DC side increases, the synthesized output waveform adds more steps, producing a staircase wave which approaches the sinusoidal wave with minimum harmonic distortion and low EMI. The proposed ML-MFGCI will provide high quality active power transfer between PV systems and the utility grid, elimination of PQ problems on PCC and inefficient control of system reliability, stability and efficiency in the utility grid.

This thesis focuses on the ML-MFGCI architecture, taking into account how to interconnect PV systems into the future smart microgrid with maximizes efficiency, PQ, and reliability of the power system. The desirable approach should be capable to sustain high quality energy transfer between PV power plants and utility grid and be capable to enhance the PQ at the both consumers and source side. This thesis presents investigations into issues of PQ and reliability of grid connected inverters and offers advanced topological and sophisticated control solutions to significantly improve performance and cost effectiveness of these systems.

In this context, a PV based ML-MFGCI proposed to simultaneously maintain high-quality power transfer exchange between PV systems and the utility grid in disturbed grids and perform simultaneous mitigation of PQ problems using novel control algorithm. To achieve the best results various ML-MFGCI structures are examined, strengths and weaknesses aspects of each topology are highlighted. Furthermore, to produces optimum power and operates at the maximum proficiency a MPPT method proposed to extract maximum power of the PV system

when the PV system receives non-uniform irradiance or subjected to PS. Additionally a wavelet transform based voltage sag/swell detectıon algorithm is proposed to detect voltage sag/swell disturbances.

GENİŞLETİLMİŞ ÖZET

Elektrik güç şebekeleri, modern toplumlarda altyapı sistemlerinin oluşturulmasında önemli bir röle sahiptir. Bu gelişmelerin yanı sıra, yaşanan elektrik kesintilerini önlemek, karbondioksit salınımını azaltarak çevresel etkileri en aza indirmek ve enerji verimliliğini artırmak tüm dünyada öncelikli bir konu haline gelmiştir. Belirtilen önceliklerin yanı sıra yenilenebilir enerji tabanlı dağınık üretim sistemlerindeki (YETDÜS) gelişmelerle birlikte, bu sistemlerin kurulu gücü ve sayısı hızlı bir şekilde artmaktadır. Güneş ve rüzgâr enerjisi en geçerli iki çeşit yenilenebilir enerji kaynaklarıdır. Güneş enerjisi fotovoltaik dizilerin uygun olarak yerleştirilmesiyle birçok yere kurulabilecekleri için, rüzgâr enerjisine göre daha avantajlıdır. Bugünlerde, fotovoltaik sistemlerin şebeke bağlantılı olarak kullanımı şebeke bağlantısız olarak kullanımına göre daha fazla uygulama alanına sahiptir.

Fotovoltaik teknolojik gelişimleri hızlı bir şekilde takip etmektedir. Malzeme bilimi araştırmalarındaki yenilikler, verimliliği daha yüksek ve maliyeti daha düşük olan yeni nesil fotovoltaik hücrelerinin üretilmesine yol açmıştır. Ayrıca, fotovoltaik teknolojisindeki ilerlemeler ve yenilenebilir enerji tabanlı güç sistemlerinin kurulmasına yönelik teşvik politikaları, fotovoltaik sistemlerinin kurulu kapasitesini önemli ölçüde artırmıştır. Son on yılda, megavat seviyelerindeki şebekeye bağlantılı fotovoltaik sistemleri kurulmuş olup ve faaliyetlerine devam etmektedirler.

Son zamanlarda, fotovoltaik ekipmanlarının maliyetindeki düşüşü ve yardımcı teknolojideki kaydedilen ilerlemeler fotovoltaik tesislerinin yapımını giderek daha uygun hale getirmiştir. Bu bağlamda, fotovoltaik ekipmanlarının ömrü yaklaşık 20-25 yıl arasında değişmektedir. Bu nedenle, fotovoltaik ekipmanlarının optimum kullanımı çok önemli bir konudur. Sıcaklık, güneş radyasyonu ve fotovoltaik panellerinin toplam direnci arasındaki karmaşık ilişki nedeniyle, fotovoltaik sisteminden maksimum güç elde edilmesini zorlaştırmıştır.

Buna ek olarak, fotovoltaik sistemleri, Güç-Gerilim eğrisi olarak bilinen doğrusal olmayan bir çıkış karakteristiği sergilemektedir. Bu eğrinin üzerinde tek bir maksimum güç noktası (MGN) bulunmaktadır. Bu noktada, fotovoltaik sistemi optimum gücü üretir ve maksimum verimlilikle çalışır. Bununla birlikte, MGN'nin Güç-Gerilim eğrisi üzerindeki konumu bilinmemektedir, bu nedenle, PV sisteminin MGN'deki çalışma noktasının bulunması için uygun bir maksimum güç noktası takipçisi (MGNT) tekniği gerekmektedir. Bunların yanı sıra fotovoltaik sistemi düzensiz ışınım alırsa veya kısmi gölgelenmeye maruz kaldığında durum daha da karmaşık hale gelmektedir. Bu durumda, Güç-Gerilim eğrisi üzerinde birden çok bölgesel MGN noktası ortaya çıkmaktadır. Bu bölgesel MGN noktalarından birisi noktası olarak öne çıkmaktadır. Dolayısıyla bu global MGN noktasının takibi için kullanılan MGNT tekniğinin optimize edilmesi gerekmektedir.

Fotovoltaik tabanlı enerji üretimi dünyadaki yeni enerji üretim teknikleri içinde en bilindik olanıdır. Fotovoltaik sistemlerin öneminin artmasıyla fotovoltaik tabanlı enerji santrallerinin kapasitesi de sürekli olarak büyümektedir. Bu kapsamda, fotovoltaik enerji sistemlerinin kurulu gücü ve uygulaması artmaktadır. Fotovoltaik sistemlerin sayısının artmasıyla, şebeke bağlantılı yeni fotovoltaik sistemlerin doğru çalışması, yönetimi, sistem kalitesinin ve güvenirliliğinin iyileştirilmesi ve devam ettirilmesi için yeni kontrol metotlarının geliştirilmesi gereklidir. Fotovoltaik sistemlerin şebekeye bağlanması çok önemli bir konu olduğundan, fotovoltaik sistemlerin çalışmasında güç elektroniği ve akıllı teknolojiler önemli bir rol oynamaktadır.

Pratikte güneş enerjisinin kontrol edilemeyen ve stokastiksel doğası nedeniyle fotovoltaik dizilerin aktif güç çıkışı dengeli değildir. Bu nedenle, şebeke açısından dağıtım sisteminde dağınık fotovoltaik sistemlerin sayısının artması birçok problem yol açabilmektedir. Bu durum şebekede güç kalitesi, gerilim regülasyonu ve denge konularında tehlike oluşturabilmektedir. Bu nedenle, güç kalitesi standartlarının, elektromanyetik uyumluluğun, akustik gürültü sınırlarının, güvenlik ve koruma ihtiyaçlarının sağlanması fotovoltaik sistemlerin önemli

gereksinimleridir. Fotovoltaik modülleri şebekeye bağlarken, üretici şirketler tarafından yayınlanan çeşitli standartlara uyulması gerekmektedir. Bu standartlar, şebekeye bağlı güç kalitesi, kararlılık, güvenilirlik ve güvenlik konularıyla ilgilidir. Ayrıca, bu standartlar mevcut ve gelecekteki fotovoltaik modüllerin yapısı ve özelliklerini tanımlar.

Şebeke yönetim sistemi güç akışının güvenilir bir biçimde sağlanması ve ortaya çıkan sorunların giderilmesi için genellikle kondansatör gruplarını, gerilim düzenleyicileri ve kademe değiştirici trafoları kontrol etmektedir. Ancak bu cihazların çalışma sınırlarından dolayı, şebeke kararlılığı, verimliliği ve güvenirliliğinin etkin bir şekilde kontrol edilmesinde yetersiz kalmaktadır. Bunların yanı sıra, şebekedeki dengesizlikler şebekede güç akışı analizlerinin hatalı yapılmasına ve akıllı şebeke yönetimi tarafından yanlış stratejilerin seçilmesine neden olmaktadır. Ayrıca, şebekede var olan harmonikler, iletişim için kullanılan cihazlarda veri kaybına ve akıllı ölçüm cihazlarının, rölelerin ve kesicilerin yanlış çalışmasına neden olmaktadır. Şebekede hem güç akışının kontrollü, şebeke geriliminin profilinin korunması ve reaktif güç kompanzasyonu için hem de YETDÜS'ler tarafından kaynaklanan ve sistemde var olan güç kalitesi sorunlarının etkin bir şekilde giderilmesi için ileri teknoloji aktif güç kalitesi koşullandırıcılar (AGKK) kullanılmaktadır. Ancak AGKK'ların YETDÜS'ler ile aynı şebekeye bağlanması, uygulamada bu iki cihazın koordinasyonunun sağlanması ve optimum yerleşim yerinin belirlenmesi gibi zorluklara yol açmaktadır. AGKK'ların evirici bölümüyle YETDÜS'lerin evirici bölümü benzer güç elektroniği topolojisindedir. Bu yapısal benzerlik kullanılarak tek bir eviriciyle YETDÜS tarafından üretilen enerjinin şebekeye enjekte edilmesi ve oluşan güç kalitesi problemlerinin giderilmesini aynı anda sağlanabilir. Bu özelliği kullanmak için eviricinin geleneksel kontrol yönteminin geliştirilmesi ve çok-fonksiyonlu olarak (aktif güç enjeksiyonu ve güç kalitesi kompanzasyonu) çalıştırılmasının sağlanması gerekmektedir. Böylece, şebekedeki kararlılığın artması, ek yatırımların ve bakım maliyetlerinin azalması ve şebeke kontrolünün kolaylaştırılması sağlanacaktır.

Dolayısıyla fotovoltaik sistemler güç elektroniği, MGNT yöntemleri ve sayısal kontrol tekniklerindeki gelişmelerle, ortak bağlantı noktasındaki güç kalitesini iyileştirmek için etkili bir şekilde kontrol edilebilirler. Her ne kadar fotovoltaik sistemler aktif güç üretse de, bu sistemlere reaktif gücü kompanze etme ve aktif filtreleme özellikleri eklenebilir. Fotovoltaik sistemler şebekeye seri veya paralel olarak bağlanabilir. Fakat harmonikler, dengesizlik ve reaktif güç enjekte edilen akımla ilgili olduğundan pratikte paralel bağlı topolojiler daha fazla tercih edilmektedir. Bu topolojiler ortak bağlantı noktasına gerekli olan akımı etkili bir şekilde enjekte edebilirler.

Çok seviyeli eviricilerin YETDÜS'lerde kullanılması yeni nesil enerji üretim teknolojilerindeki önemli adımlar olarak görülmektedir. YETDÜS'lerde çok seviyeli eviricilerin kullanılması anahtarlama elemanlarında daha az güç tüketimi sağladığından, düşük harmonik bileşen içerdiğinden ve düşük elektromanyetik girişim oluşturduğundan, şebeke bağlantılı eviricilerin verimliliğinin artmasını ve enjekte edilen gücün kalitesinin iyileşmesini sağlamaktadır.

Bu çalışma şebekenin güç kalitesini iyileştirmek için fotovoltaik sistemlerin şebekeye nasıl bağlanacağını dikkate alarak, şebeke bağlantılı çok-seviyeli ve çok-fonksiyonlu eviricinin yapısına odaklanmaktadır. İstenen özellik fotovoltaik ve şebeke arasında yüksek kaliteli güç transferinin gerçekleştirilmesi ve kullanıcı ve şebeke tarafındaki bağlantı noktalarında güç kalitesinin iyileştirilmesidir. Bu çalışma, şebeke bağlantılı eviricilerin güç kalitesi ve güvenirliliği konularında araştırmaları sunmakta olup ve bu sistemlerin verimliliğini arttırmak ve en ekonomik çözümü sunmak için ileri seviye topolojik ve kontrol yöntemi çözümlerini önermektedir.

Bu kapsamda çok-seviyeli çok-fonksiyonlu şebeke bağlantılı evirici (ÇS-ÇFŞBE) geliştirilerek fotovoltaik sistem ve şebeke arasında yüksek kaliteli aktif güç transferini, ortak bağlantı noktasında güç kalitesi problemlerinin giderilmesini ve şebekede etkin bir kontrolünün gerçekleştirilmesini sağlamıştır. Önerilen ÇS-

ÇFŞBE yüksek kaliteli aktif gücü şebekeye enjekte etmesinin yanı sıra OBN'deki farklı güç kalitesi problemleri ve reaktif gücü eşzamanlı olarak yeni kontrol yöntemleriyle kompanze edebilmektedir. Ayrıca en iyi sonucu elde etmek için farklı ÇS-ÇFŞBE yapısı denenerek, bu yapıların güçlü ve zayıf yönleri açıklanmıştır. Bunların yanı sıra, fotovoltaik sistemlerinin verimliliğini arttırmak için normal ve kısmi gölgelenme şartlar altında fotovoltaik sistemlerinden maksimum gücü elde etmek için yeni bir MGNT yöntemi geliştirilmiştir. Ayrıca gerilim çukuru ve tepelerinin tespiti için dalgacık tabanlı yeni bir metot geliştirilmiştir.

ACKNOWLEDMENTS

I would like to thank to my supervisor Assoc. Prof. Dr. Ahmet TEKE who made this thesis possible for his wisdom, time, patience, guidance and valued positive criticisms throughout this work.

CONTENTS **PAGE**

LIST OF TABLES **PAGE**

LIST OF FIGURES **PAGE**

LIST OF SYMBOLS

a_0	:	Fixed Dilation Step Parameter in Wavelet Transform
a_1	:	First Diode Ideality Factor in Dual-Diode Model of PV Module
a_2	:	Second Diode Ideality Factor in Dual-Diode Model PV Module
b_0	:	Location Parameter in Wavelet Transform
cA	:	The Output Signal From Low Pass Filter
cD	:	The Output Signal From High Pass Filter
C_{DC}	:	DC Link Capacitor
C_f	:	Filter Capacitor
cd	:	Clamping Diodes Number
CUN	:	Current Unbalance Ratio
d	:	Duty Cycle
D	:	Diode
f	:	Nominal Frequency
f_{res}	:	Resonance Frequency
f_{sw}	:	Switching Frequency
fd	:	Number of Freewheling Diodes
F(n)	:	Decomposed Original Signal
G		Radiance on PV Module Surface
G_{STC}		Radiance at Standard Test Condition
H	:	Input signal of Hysteresis Band
I_C	:	Current of Filter Capacitor
I_d	:	Active Power Component of Current in Synchronously Rotating Frame
I_{d1}	:	First Diode Reverse Saturation Current in Dual-Diode Model of PV module
I_{d2}	:	Second Diode Reverse Saturation Current in Dual-Diode Model of

		PV module
I_f	:	Flowing Current Through Inverter Side Filter Inductance
I_g	:	Flowing Current Through Grid Side Filter Inductance
I_l	:	Rated RMS Value of Maximum Demand Load Current
I_m	:	Maximum Power Point Current's in PV system
I_P	:	Current Flowing Through Parallel Resistance in PV Module
I_{PV}	:	Photocurrent in PV module
$I_{PV\text{-}STC}$	:	PV module's Current at Standard Test Condition
I_{SC}	:	Maximum Short Circuit Current at PCC
Is	:	Source Current
I_{String}	:	String Current in PV system
I_q	:	Reactive Power Component of Current in synchronously rotating frame
I_α	:	Active Power Component of Current in Stationary Frame
I_β	:	Reactive Power Component of Current in Stationary Frame
K	:	Boltzmann Constant
K_d	:	Resonance Damping Gain
k_i	:	Short Circuit Current Coefficient
k_v	:	Open Circuit Voltage Coefficient
L_a	:	Line Inductance
L_{DC}	:	DC Link Inductance
L_f	:	Inverter Side Filter Inductance
L_g	:	Grid Side Filter Inductance
m	:	Modulation Index
n	:	Level Number of Multilevel Inverter
N	:	Neutral Point
N_p	:	Paralel Cell/Modules Number in PV System
N_p	:	Series Cell/Modules Number in PV System

N_{String}	:	String Number in PV System
N_{SW}	:	Converter Switching Position Number
P	:	Active Power
P_{MAX}	:	Maximume Power in PV System
P_{Measur}	:	Measured Power
P_{MPP-n}	:	Nominal maximum Power of PV System
q	:	Elementary Charge Module
Q	:	Reactive Power
R_a	:	Line Resistance
R_P	:	Paralel Resistance in PV Module
R_S	:	Series Resistance in PV Module
S	:	Apparent Power
T	:	Temperature in Kelvin
$T_{m,n}$	:	Wavelet Coefficient
T_W	:	Scale-Location Grid of Signal in Time-Frequency Domain
T_{STC}	:	Standard Test Condition Temperature in Kelvin
s	:	Switching Number
V_{cf}	:	Voltage of Output Filter Capacitor
V_d	:	Active Power Component of Voltage in Synchronously Rotating Frame
V_{dc}	:	DC Link Voltage
V_{dc-1}	:	DC Voltage in Upper Capacitor in Three Level Natural Point Camped Inverter
V_{dc-2}	:	DC Voltage in Lower Capacitor in Three Level Natural Point Camped Inverter
V_m	:	Maximum power point's voltage in PV System
V_{MPP-n}	:	Voltage at Nominal Maximum Power Point
$V_{nominal}$	:	Nominal Voltage of Grid

$V_{dc\text{-}ref}$	:	Reference DC Voltage
V_{PCC}	:	Voltage in Point of Common Coupling
V_{PV}	:	PV System Voltage
V_{OC}	:	Open Circuit Voltage
$V_{OC,STC}$	:	Open Circuit Voltage of PV at Standard Test Condition
V_{RMS}	:	Root Mean Square of Voltage
V_q	:	Reactive Power Component of Voltage in Synchronously Rotating Frame
V_T	:	Thermal Voltage in PV Module
x	:	Average Equivalent Model
$\hat{x}$	:	Small-Signal Terms of Averaged x Variable
X	:	DC Set Point
Z_a	:	Line Impedance
$Z_{Virtual}$	:	Virtual Impedance
τ	:	Translation in Wavelet Transform
ω	:	Grid Angular Frequency (rad/s)
$\varphi_{m,n}$	:	Orthonormal Wavelet

1. INTRODUCTION

1.1. Motivation for the Thesis

Traditionally, electric power systems worldwide have been designed with a vertically connected arrangement, characterized by a centralized generation that supplies a large number of consumers by centralized generators. With restructuring in the electrical power systems, the arrangement of electrical power systems are changing from now day's centralized bulk systems to small power generators which directly connected to distribution power system or on the consumers side. This type of generating units is known as dispersed generation or distributed generation (DG). The incremental demand for electrical energy and recent technological advances are leading a growth in the prevalence of DG systems. In addition to enhance the general performance of electrical power systems the installation of new DG systems aims to obtaining a profit. In other words, installing new DG systems, besides being economically profitable, can improve the stability, security, reliability and quality of the given power system and reduce power loss owing to energy transport and distribution. However, potential benefits of installing new DG systems depend on making perfect decisions about how many DG systems should be installed on power system, which types of DG systems are the most suitable, where they should be connected to electric power system and which generation capacity is the most suitable (Caamaño-Martín et al., 2008), (Habibi et al., 2013), (Torrent-Fontbona et al., 2016).

Spread of automation in the control and management of electrical networks, technological development and liberalization of energy markets will also support the wide install of DG systems. However, increasing the penetration of DG units on power system and wide spread use of renewable energy sources (RESs) challenge the entire structure of traditional electrical network. So, to undertake increasingly complex operations the entire structure of future electrical network must be redesigned. Three possible architectures for future electrical network are

envisioned: (i) Microgrids, (ii) Active Networks supported by information and communication technology and (iii) the Internet model.

Microgrid (MG), characterizing higher reliability and flexibility, becomes an increasingly attractive technology for the arrangement of future electrical network (Calderaro et al., 2012; Wang et al., 2010). MGs paradigm is becoming an attractive technology for the active distribution network. MGs provide the opportunity of integrating RESs in distributed manners. This miniature version of the legacy system is considered to be the building blocks of the futuristic smart grid vision (Wang et al., 2010), (Shamiur Rahman et al., 2016).

A MG can be strategically sited at any place of the distribution system, most especially at the electrical power system for power system reinforcement, thereby deferring or eliminating the need for power system upgrades and enhance power system integrity, reliability, and efficiency. From an electrical power system wise point of view, existed MGs should increase the entire efficiency of electrical power system by integrating large number and size of DG systems, including RESs, reducing greenhouse gas emissions and power system losses, as well as improve system quality and reliability. In addition to economic considerations, the potential to increase the capacity of the system to host DG is of great interest (Petinrin and Shaaban, 2016), (Appen et al., 2013).

In despite of the potential benefits that the wide spread use of DG systems may bring, their penetration challenges a proper control strategy to provide reliable and stable operation of MGs in both islanded and grid connected modes and ensure smooth transition between them. The main challenges arise from differences existing between physical characteristics of traditional electrical power generators and inverter based MGs (Sadabadi et al., 2017).

Moreover, the PQ problems of MG is much more serious than that of the conventional electric power system because of the randomness and intermittency of DG systems, the high penetration between traditional electric power system and MG, the diversity of DG systems, load, energy conversion unit, energy storage

system (ESS), and operating state (Li and Zhu, 2015). This situation can bring important challenges in the operation of the MG especially at high-level penetration of DG systems (Khalid et al., 2016). Therefore, taking into account the output power uncertainties of DG systems and randomness of demand, the planners need a proper strategy to evaluate maximum capacity of DG systems that can be installed in a distribution system without technical constraint violations (Wang et al., 2016).

As well as, the existing of the nonlinear and unbalance loads in distribution systems can cause various PQ problems for MGs. Nevertheless, a MG should be able to operate under this situation without any performance degradations (Paridari et al., 2013). However, hosting capacity of the grid may significantly reduce compared to free PQ problems and balanced system (Meyer et al., 2011).

Therefore, the existing distribution networks have been constructed without consideration for DG connection (Toma et al., 2008). However, current local controls such as voltage regulators, load tap changers and capacitor banks will not be enough once the penetration level of DG systems exceeds the hosting capacity of the utility grid as well as due to mechanical limitations cannot provide timely responses to the rapid fluctuation and these devices are unable to adapt to the dynamic nature of DGs and load profiles (Zafar and Ravishankar, 2016). The inability of managing PQ has caused RES spillage in industrial practice, which inevitably delays the development of a flexible sustainable power system (Cheng et al., 2016). The drive towards to overcome this problems may result in simultaneous installation of DGs and active APQCs in power systems. The APQC devices can be used to performance criterion improvement of power systems such as minimize the active and reactive power losses, reduce overall cost of the system, provide flexible control and operation, enhance overall efficiency and reliability of the system, increase hosting capacity of the system, improve PQ of the system, increase the loadability of the systems, relieved transmission and distribution congestion, reduction of power system oscillations, increase power transfer capability of the

system, reducing greenhouse gas emissions, provide reactive power supporting in emergency situation such as under fault condition, sudden change in field excitation of alternators or load increase in power systems. These DG systems and APQCs have the potential to interact with each other. This situation may either improve or deteriorate power system stability and reliability depending upon the chosen control strategies, size and installed location of DG systems and APQCs. The various interactions can potentially arise between the DG systems and APQCs, as well as, between multiple APQCs in power system. These likely interactions can be classified into different frequency ranges and various interaction problems between DG systems and APQCs or between multiple APQCs. However due to circulating current between DGs and APQCs in local power system network, the individual performance of DG systems as well as APQCs can be distorted. So that the entire power systems performances with DG systems and APQCs are also distorted. It is known as interaction problem that occur between DG systems and APQCs in power systems. This situation is disadvantages of simultaneous operation of DG systems incorporated with APQCs in power systems. Thereby, the effect of these interaction problems needs to minimize in the power systems (Singh et al., 2015).

On the other hands, interest in direct current microgrids (DCMGs) might grow soon though owing to the proliferation of DG, fuel cells and EESs, which are direct current (DC) by nature. Furthermore, modern electronic circuit based high-tech loads needs mostly DC rather than alternative current (AC) supply, hence raising the attractiveness of DCMGs, which generally needs lesser power conversion processes and stages. By means of DCMGs architectures the overall reliability, PQ, local system cost can be improved. However, one of the most significant considerations in the planning and design of both DC and AC distribution system networks is that of PQ. The two primary effects of the PQ issues on a distribution system are the adversely effected of equipment operation by PQ problems and the diminution in power factor caused by certain frequency

range and magnitude of harmonics. Moreover, the DC system has advantage of not needing phase synchronization and frequency control procedures in the integration of multiple DC sources. Despite that, AC power systems need sources to be synchronized with each other, which adding another complexity process of control procedure. However, DC architectures can present reliability, stability and quality challenges because of the inherently nonlinear characters of the power electronic converters, which are used to create the DC voltage. Moreover, existing PQ problems on the AC system can induce cause damaging resonance currents, unacceptable level of electromagnetic interference (EMI) and problematic voltage oscillations on the DC bus (Chiang Loh et al., 2013), (Whaite et al., 2015).

1.2. Subject and Scope of the Thesis

The world's natural resources are constantly diminishing, the demand for energy is rapidly increasing and the impacts of climate change require re-thinking of our habits. There is no question that we need to find sustainable alternatives that lead us into a new energy age. To ensure sustainable growth in the future, renewable energy needs to play an increasingly significant role in the global energy mix. Wind, sun, and water are three infinite resources of pure energy that are ready to be harvested to meet the demand for clean power. Renewable Energy Sources (RES) have a widespread deployment and an intense activity is conducted in research level for their optimal integration and coexistence with the traditional energy systems. Additionally, various regulations and standards have been introduced by international organizations and energy markets (Siemens AG, 2011), (Perpinias et al., 2015).

Solar PVs are on a fast track of technological development. Innovations in material science research have led to newer generations of PV cells that promise much higher efficiency and lower cost in the future. Advances in PV technology and incentive policies for deployment of RESs have significantly increased the capacity of installed PV systems. During the last decade, grid connected PV

systems in the range of megawatt have been installed and currently are operational all over the world (Wu et al., 2015), (Moradi-Shahrbabak et al., 2014).

In recent times, construction of PV plants becomes increasingly affordable owing to consistent decline in the PV equipment costs and advance in auxiliary technology. PV equipment has a limited lifespan of around 20–25 years. Therefore, the optimal utilization of the PV equipment becomes very important issue. Unfortunately, due to complex relationship between temperature, solar radiation, and total resistance of PV panels the extraction of maximum power from PV system is a challenging task. In addition, PV systems exhibit a nonlinear output efficiency characteristic which is known as the Power-Voltage (P–V) curve where there is a unique point referred as maximum power point (MPP). At this point, the PV system produces optimum power and operates at the maximum proficiency. However, the position of the MPP on *P-V* curve is not known, so a suitable MPPT technique is required to track the operating point of PV system at its MPP. The case will be more complicated when the PV system receives non-uniform irradiance and PV system is subjected to PS. In this situation, P–V curve will be characterized by multiple peaks which one of them is the GMPP. The tracking of the GMPP seems to be an optimization problem (Sharma and Agarwal, 2014), (Chen et al., 2014), (Joshia and Arora, 2017), (Kermadi and Berkouk, 2017).

There is a wide spread of potential applications for multifunctional inverters based PV system to given high PQ, e.g. for industry, and effectively integrate into electrical power system operation and energy supply (Braun and Stetz, 2008). The RES based DG units are typically interfaced into grid over a power electronics converter, with the exception of traditional rotating machines. In this situation, it is possible to have both directly connected, as well as power electronic interfaced units. In some MG design philosophies, to improve droop response, support in emergency case such as current fault control and etc., regardless of the kind of DG system, all units are connected over power electronics unit (Bollen et al., 2017). So, DG units can efficiently be used to enhance the

system operation with improved PQ at the point of common coupling (PCC) by using advanced power electronics and sophisticated digital control technologies. The multifunctional grid connected inverter (MFGCI) is special kind of the grid connected inverter that has elicited much attention in recent years. MFGCIs inject active power from DG systems to grid as well as provide increased functionality through improve system PQ and support the voltage profile and reactive power; thus, the capability of the ancillary service for the grid can be improve (Teke and Barghi-Latran, 2014).

The utilization of DG systems based MFGCI in flexible MGs helps to reduce the overall cost of the system and increased functionality provided by MFGCI in the flexible operation mode. However, the complexity of controller is increased and extra stresses on the power electronics components are expected. In resilient MGs operation of MFGCI, the situation is more severe owing to stochastic behavior of DG systems and consumers (Aly et al., 2017).

Conventional six-pulse is widely used in grid connected PV systems, regardless of the disadvantages such as low-quality output voltage waveforms and high switching losses. These conventional inverters have normally to meet grid codes and stringent standards owing to the use of a high switching frequency. However, this situation cause increased voltage stresses and high switching losses, *dv/dt*, etc. However, this may not always be possible to meet grid codes and strict standards such as at the light load conditions whereas current THD is high (Azmi et al., 2013). Otherwise, large scale grid-connected PV systems need higher power inverters (Balamurugan et al., 2017). As an alternative to two level inverters, multilevel inverters are considered as efficient alternatives to high-power applications, presenting a high-quality output voltage, while increasing the efficiency, robustness, and lowering the electromagnetic interference (Mortezaei et al., 2017). These advantages come at the cost of an intelligent control scheme which is allows to independently control of active and reactive power, regulation and balancing of capacitor voltage, control of DC bus voltage, along with

circulating currents that are set according to the balancing targets (Steurer et al., 2016).

In medium and high power applications, multilevel inverter technology is a very efficient alternative as the heart of interfacing systems for integration of PV systems into utility grid. The superior harmonic spectrum, decreased voltage rating for the switches, decreased common mode voltages and lesser voltage changes (*dv/dt*) are important advantages of multilevel inverters. However, the complexity of control method rises compared to the traditional two-level inverter. Multilevel multifunctional grid connected inverters (ML-MFGCIs) are new breed of power converter used in large scale PV applications and have superior advantages such as lower switching power dissipation, lower harmonic distortion and lower electromagnetic interference (EMI) outputs. ML-MFGCIs perform the high quality power from PV systems and provide flexible functionality with improved power PQ, voltage and reactive power support and increased capability of the auxiliary service for the utility grid (Barghi-Latran and Teke, 2015).

On the other hands, the simplest approach is to treat each MG as an independent power network with either AC sources feed only AC loads or DC sources feed the DC loads. That definitely defeats the goal of connecting the two MGs and would need much higher generator ratings in order to always meet supply and demand within each MG. By the existing power electronics in the DGs structure, it is hence possible to have AC and DC sub-grids interconnected to form hybrid MGs with lesser power conversion stages, and thus higher efficiency. The sub-grids can subsequently connected with each other by interlinking power electronics devices to build hybrid AC and DC MG. The mission of interlinking power electronics devices is to ensure bidirectional power exchange between the sub-grids, depended to their prevailing internal demand and supply conditions. So, the main challenge would then be the enforcement of appropriate power flow between the sub-grids before mutual support and retention of high efficiency can be provided without fast communication link. In this sense, it seems reasonable that

the DCMG area can be connected to ESS such as batteries, supercapacitors, or hydrogen-based fuel cells (Chiang Loh et al., 2012), (Chiang Loh et al., 2013), (Guerrero et al., 2013).

Given the non-controllable and stochastic nature of the RESs, the use of an ESS is a potential solution to overcome reliability and stability problems leading by instantaneous variations of RES generation. In such case, when the production power from RES is higher than the plant power commitment the surplus produced energy accumulate and delivers it back in the opposite condition. The coordination of the RES system with ESS, a feature of the smart MG, were tend to bring the voltage back within statutory limits. Thus improves the voltage quality and offers adjusted active power capacity to the distribution system. Distributed ESS in the utility grid is a key enabler for a MG with high penetration of RES as well as provides high quality and reliable power supply. Also, it makes procedure being more effectively and improves system performance. The combined ESSs and bidirectional MFGCI can product controllable output power to simplify the dispatched energy generation and demand matching (Justo et al., 2013), (Khalid et al., 2016), (Petinrin and Shaaban, 2016).

Thus combined ESSs and bidirectional ML-MFGCI can provide very sophisticated hybrid MG operation which is offer additional functionality such as energy management and peak shaving and maximizes efficiency, PQ, and reliability of power system (Braun and Stetz, 2008).

1.3. Objective and Structure of the Thesis

In the previous sections, the necessity and alternative technical solutions to traditional grid connected inverter and conventional PQ compensators is argued against the background of steadily increasing power system quality, stability and reliability problems by increasing the number and size of PV system installation. Out of this general need the overall goal of this thesis is derived.

"This thesis focuses on the ML-MFGCI architecture, taking into account how to interconnect PV systems into the future smart microgrid with maximizes efficiency, PQ, and reliability of the power system. The desirable approach should be capable to sustain high quality energy transfer between PV power plants and utility grid and be capable to enhance the PQ at the both consumers and source side. This thesis presents investigations into issues of PQ and reliability of grid connected inverters and offers advanced topological and sophisticated control solutions to significantly improve performance and cost effectiveness of these systems."

ML-MFI is one of the most important technologies in PV based electrical power generation. ML-MFI technology is based on the synthesis of the AC voltage from several different voltage levels on the DC bus. When the number of voltage levels on the DC side increases, the produced output waveform includes more steps, generating a staircase wave and low harmonic distortion which closes the sinusoidal waveform. ML-MFI topologies are increasingly used in large scale PV system applications due to their many advantages such as low power dissipation on power switches, low harmonic contents and low EMI outputs. The selected switching method to control the inverter will also have an effective role on functionality of inverter such as transferring the active power from PV generator to utility grid as well as reactive power compensation, grid current harmonic and unbalance mitigation and control the voltage profile at PCC.

In recent research studies, novel control algorithms and topologies for ML-MFGCIs interfaced with large scale PV system are developed to optimize the energy conversion, to control the PQ of the utility grid, to perform low cost operation with high efficiency over a wide power range, and to have a high reliability. The higher power rates together with the enhanced PQ have been the major drive for large scale installations and leading for research and development of ML-MFGCI in PV systems.

The objectives of this thesis are as follows:

- To describe high power, advanced power electronics devices in large scale PV systems.
- To describe the multifunctional power electronics devices in large scale PV systems.
- To describe the modeling of neutral point clamped multilevel multifunctional grid connected inverter in large scale PV system.
- To evaluate the performance of the modeled multilevel multifunctional grid connected inverter with case studies.
- To describe the maximum power point tracker for multilevel multifunctional grid connected inverter with case studies.
- To develop a new control method for multilevel multifunctional grid connected inverter with case studies.
- To develop a new signal extraction method for multilevel multifunctional grid connected inverter with case studies.
- To describe more functionality for multilevel multifunctional grid connected inverter with case studies.
- To develop a fast voltage sag/swell detection method with and without phase jumps under unbalanced and distorted source voltages with flicker and harmonics.

The thesis is divided into 6 chapters. An overview about the structure gives in Figure 1.1

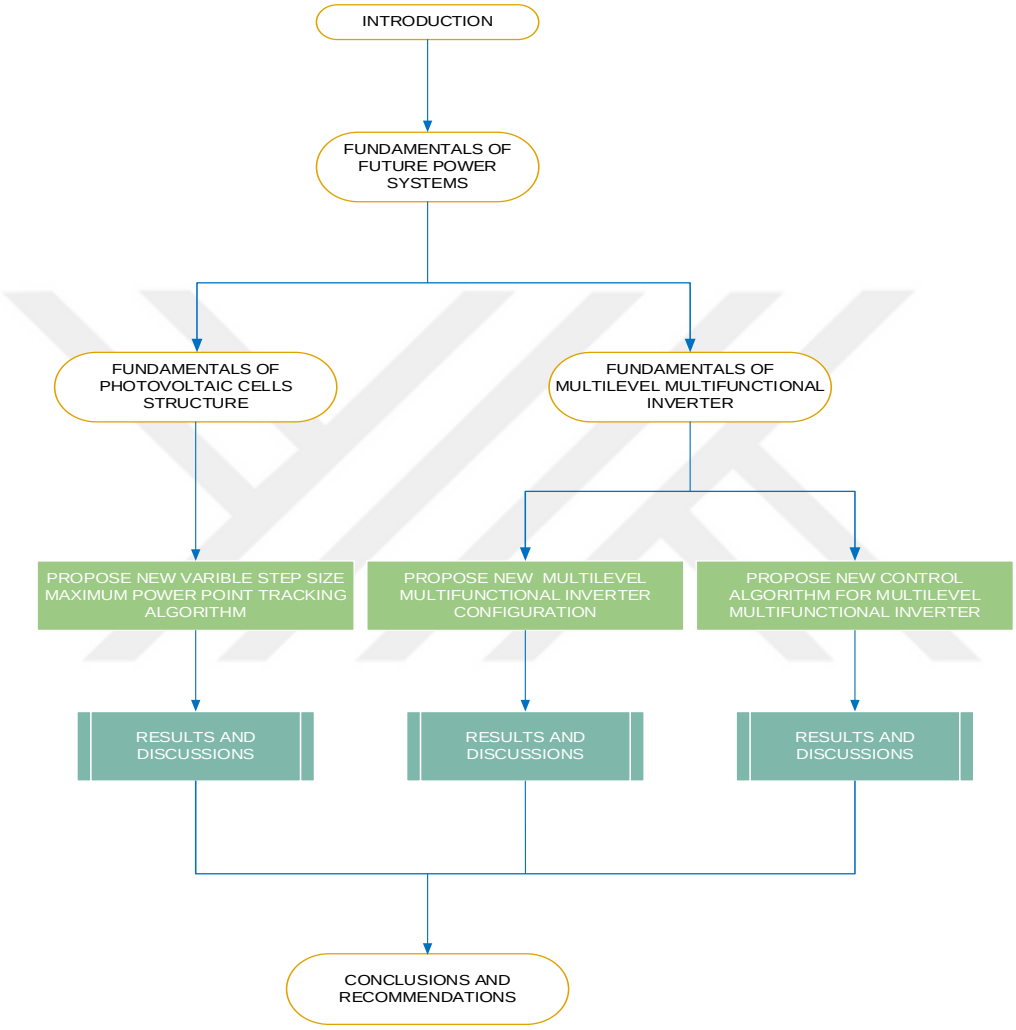

Figure 1.1. Flowchart of thesis structure

Chapter 1: This chapter presents an overview of future renewable energy resources based electrical power system and gives general information about the topic and organization, subject, object and contribution of this thesis.

Chapter 2: In this chapter, a comprehensive review on the topologies and control strategies of ML-MFGCIs are performed. The development of new control strategies and execution of multifunctional compensation capabilities in large scale PV systems are the main research trends related to both active power flow control and mitigation of various PQ disturbances using ML-MFGCIs. The different aspects of ML-MFGCIs, the novel developments and practical applications in this field of research were discussed in detail. The detailed classification, challenges and future trends on ML-MFGCIs are presented.

Chapter 3: This chapter presents a detailed analysis of the physical structure of solar cells and their *I-V* and *P-V* characteristics. Due to changing of output power from PV arrays with atmospheric condition changing the implementation of the MPPT control strategy becomes indispensable condition to extract maximum power from the PV arrays have been represented. Moreover, the necessities of the GMPPT algorithm to track maximum power during PS conditions have been outlined. Thus, the proposed algorithm and details the techniques used to improve its efficiency especially under unstable atmospheric conditions presented in this chapter. It starts by introducing a new rule for modifying the step size in IncCond MPPT algorithm. Then, it describes the methods used to overcome the problems of rapidly as well as slowly changing atmospheric conditions and PS. This chapter is concluded by the flow chart of the proposed algorithm. Finally it presents the simulation results which are illustrates the significantly improvements in the MPPT process in comparison to conventional algorithm under different atmospheric conditions.

Chapter 4: This chapter presents a detailed analysis and discussion on the PQ problems mitigation in new power systems which are supported by renewable energy resources based distributed generation systems. Due to installing of non-controllable and stochastic nature of renewable energy sources on power systems and closed to consumers as well as existing of severely PQ problems in week power systems the utilization of the compensators becomes indispensable condition

to maintain quality, reliability and stability of the power system have been represented. The benefits of the multilevel inverters in high power rating application have been remarked. Moreover, the capability of the interlinked inverters to use as multifunctional inverter with modifying the control strategy of the interlinked inverters has been outlined. Thus, proposed control algorithm for a PV based multifunctional neutral point clamped multilevel inverter to simultaneously maintain high-quality power transfer exchange between PV systems and the utility grid in disturbed grids and perform simultaneous mitigation of PQ problems in steady-state and transient conditions are presented in this chapter. It starts by introducing a new rule for modifying the PV based interlinked neutral point clamped multilevel inverter's control algorithm. Then, it describes the methods used to transfer high quality power from PV systems into power networks and overcome the PQ problems. This chapter is concluded by proposed control algorithm formulation and scheme. Finally it presents the simulation results which are illustrates the significantly improvements in the quality of power system in steady-state and transient conditions and transfer high quality power from PV system into system with maximum power tracking capability.

Chapter 5: This chapter presents a novel sag/swell detection algorithm based on wavelet transform under distorted source voltages including flicker and harmonics. Due to increasing usage of devices which are more sensitive to voltage sag/swell the implementation of fast voltage sag/swell detection method becomes indispensable condition to protect end users from exposed to the unexpected mis-operation and outage have been represented. The difficulties of voltage sag/swell detection in the existing of harmonics and flicker have been outlined. The complexity of the situation when a voltage sag/swell with phase jumps occurs in unbalanced system has been remarked. Thus, the proposed algorithm and details the techniques used to improve the efficiency of fast voltage sag/swell detection especially under distorted system with harmonics and flicker presented in this chapter. It starts by introducing a new rule for modifying the wavelet transform in

fast voltage sag/swell detection method. Then, it describes the methods used to overcome the problems of existing of harmonics and flicker in unbalanced system when the voltage sag/swell with and without phase jumps occur. This chapter is concluded by the flow chart of the proposed algorithm. Finally it presents the simulation results which are illustrates the significantly improvements in the voltage sag/swell detection process in comparison to conventional algorithm under different conditions.

Chapter 6: In this chapter general conclusions of this thesis work are given. A summary of the obtained results in this thesis work is presented. The key contributions are highlighted. In addition, proposals of future work based on this thesis work are mentioned.

1.4. Contribution of the Thesis

The contributions of this thesis to the existing literature can be summarized as follows:

- A detailed description and analysis of various multilevel multifunctional inverter configurations, control strategies, switching methods and their functionalities are introduced in this thesis. Main and recent research studies on multilevel multifunctional inverter based PV system are summarized by reviewing near 100 papers.
- A new variable step size maximum power point tracking (VSS-MPPT) algorithm based incremental conductance (IncCond) strategy investigated to track the maximum power voltages in steady state and variant atmospherics conditions.
- A new partial shading condition detection algorithm proposed to increase the efficiency of the PV system under partial shading condition with complex radiation combination.

- A GMPPT algorithm according to proposed partial shading detection algorithm and variable step size IncCond MPPT method is proposed.
- The performance comparison between proposed MPPT algorithm and conventional fixed step size IncCond method based MPPT under various atmospherics condition is presented.
- A multiobjective control strategy investigated for multifunctional neutral point clamped inverter (MF-NPCI) to exchange active power with power system network as well as compensate various PQ problems existed in power system. According to proposed control algorithm PV based MF-NPCI can be used in three modes. The first mode is the normal inverter which is injects active power from PV arrays into power system as well as compensates reactive power. The second mode is the APQC which is only compensate the existing PQ problems according theirs control algorithms and the third mode is the multifunctional mode which is injects active power from PV system into power system and compensates PQ problems. Reference signal extraction, overall control, active power control and DC link voltage balance methods investigated to fulfill these functions. The proposed MF-NPCI can acts as bidirectional inverter hence it can exchange active power between AC and DC subgrid and compensate voltage/current harmonics, load unbalance, neutral line current and reactive power as well as regulate PCC voltage. Furthermore proposed MF-NPCI can compensate three, two and single phase voltage sag and swells.
- A novel sag/swell detection algorithm based on wavelet transform under distorted source voltages including flicker and harmonics proposed. The developed detection algorithm consists of the combination of a second level of Daubechies filters and an eighth level of Daubechies filters to detect voltage sag/swell with and without positive/negative phase jumps.

2. LITERATURE REVIEW OF MULTILEVEL MULTIFUNCTIONAL GRID CONNECTED INVERTERS

The application of PV as a source of electrical energy in the DG systems is gaining more attention with the advances in power electronics technology. The one of the key technologies in the PV based DG systems is grid connected inverter that is utilized to interface PV power systems into the utility grid. ML-MFGCIs are new breed of power converter used in large scale PV applications and have superior advantages such as lower switching power dissipation, lower harmonic distortion and lower EMI outputs. ML-MFGCIs perform the high quality power from PV systems and provide flexible functionality with improved PQ, voltage and reactive power support and increased capability of the auxiliary service for the utility grid. This chapter presents a detailed analysis of various ML-MFGCI configurations for 1-phase and 3-phase systems and control strategies to compensate the different PQ problems.

2.1. Impact of inverter configurations on reliability, efficiency and cost of grid connected PV systems

Grid connected PV systems typically have four possible inverter scenarios: (a) module inverter, (b) string inverter, (c) multi-string inverter and (d) central inverter as shown in Figure 2.1. The central inverter can be used in PV power plant larger than tens kWp with lower cost and higher efficiency. Major disadvantages of central inverter configuration are the use of high voltage DC cables; common MPPT and module mismatch. Compared to central inverter, string inverter configuration can achieve MPPT separately, leading to maximum total energy yield. Whereas, there are mismatches in the PV panels connected in series. For this reason, the module inverter configuration is developed that acts on a single PV panel with a single MPPT. The main drawback of a module inverter configuration is the lower overall efficiency. Multi-string inverter configuration is an intermediate configuration between the string inverter and the module inverter

configurations. In this configuration, each PV string can be controlled independently, so flexible with a high overall efficiency (Blaabjerg et al., 2013).

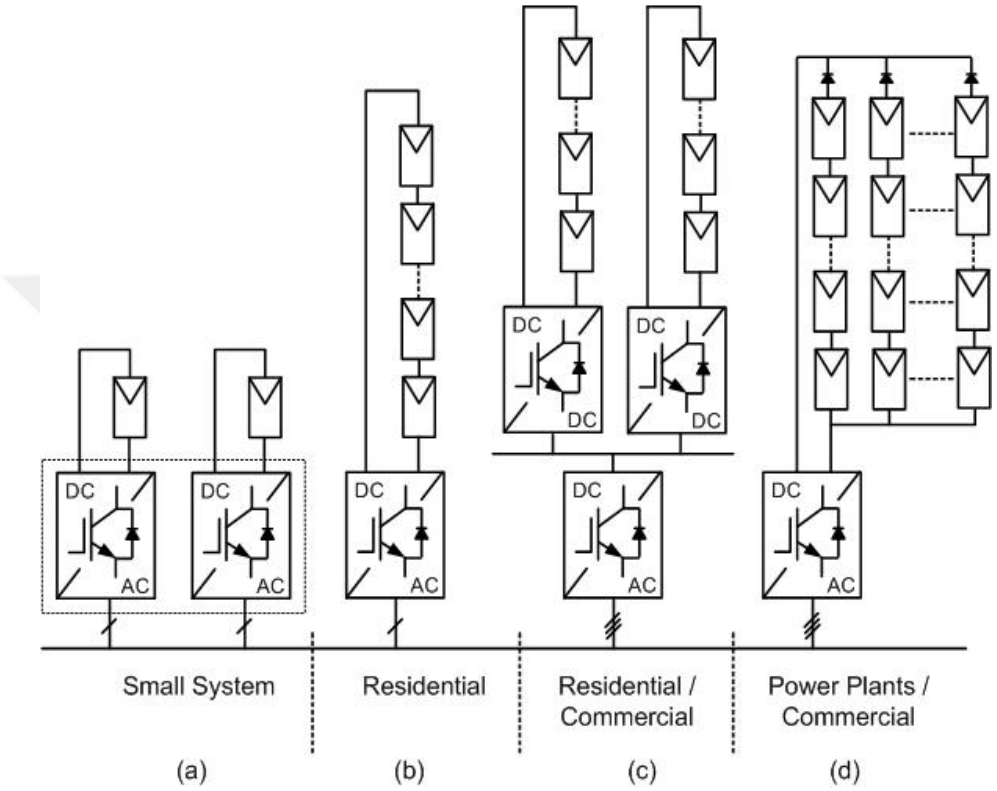

Figure 2.1. Grid connected PV systems: (a) module inverter, (b) string inverter, (c) multi-string inverter, (d) central inverter.

The cost reduction of PV energy systems is one of the most important considerations, which affects the installation capacity of overall PV power plant. Generally, a Levelized Cost of Energy (LCOE) index is adopted to quantify and compare the cost for different PV systems (Campbell et al., 2009), (U.S. Energy Information Administration, 2013). Campbell et al,. (2009) prepared an overview of LCOE indicators in PV power plants and impact of the plant's capacity factor on LCOE. He et al., (2012) developed a method to optimize and evaluate inverter

configurations for grid connected PV systems to show that how the inverter configurations and their operating strategy would impact on lifetime energy yield, LCOE considering the PV array scale, system cost, environmental conditions and inverter reliability and efficiency.

Pregeij et al., (2002) shows the effects of inverter failures in PV system's lifetime and investigates the suitability of several inverter configurations based on criteria of life cycle costs and total lifetime energy output. Kornelakis and Koutroulis (2009) proposed a method to suggest, among a list of commercially available system devices, the type and optimal numbers of system devices, PV module and installation details of inverters. Hung et al., (2010) focused on the impact of a more efficient inverter of PV system on LCOE and balance of system cost, analyzing real grid connected PV system, transformerless inverter applications, bipolar and unipolar PV array configurations.

The optimal solution to reduce LCOE index in large scale PV system is the use of multilevel inverters instead of classical inverters. Beser et al., (2010) proposed new multilevel inverter configurations with less power switches for reduction LCOE in PV systems. In order to improve the efficiency and reduce the cost of a PV system, the use of transformerless PV multilevel inverters is an alternative of increasing interest as stated by Patrao et al., (2011). However, this topology has some problems related to the galvanic connection between the grid and the PV generator (e.g. efficiency degradation and safety problems). In some studies, such as the findings of González et al., (2008), the authors focused on to eliminate the injection of DC current to utility grid by transformerless multilevel inverters in PV systems. Blaabjerg and Koutroulis (2011) proposed a technique for the optimal design of the power section and output filter of grid-connected PV inverter. In most PV systems, DC–DC converter is used for boosting the low voltage output of PV panels as well as MPPT. In some studies, such as Alonso-Martı´nez et al., (2011) paper's, authors suggested the multilevel inverter for boosting the output voltage with self MPPT capability to eliminate DC–DC

converter (extra cost for LCOE in PV system). Additionally, ML-MFGCIs provide ancillary services, such as low voltage ride through, reactive power control, frequency control and mitigate PQ problems in order to ensure a reliable, stable and efficient power conversion from PV systems. Because the grid connected inverters (GCIs) are usual current controlled voltage source inverters (VSI), the auxiliary services of ML-MFGCIs to enhance PQ on current issues can easily be embedded in. However, the functionalities for voltage issues are hardly achieved using the current controlled-VSIs GCIs. ML-MFGCIs inject the active power from PV systems to utility grid as well as can act as (i) active power filter (APF), (ii) power factor corrector (PFC), (iii) current unbalance compensator (CUC), (iv) voltage sag/swell/interruption/unbalance compensator (SSIUC) and so on (Zeng et al., 2013).

2.2. Multilevel multifunctional grid connected inverter topologies

In medium and high power applications, ML-MFGCI technology is a very efficient alternative as the heart of interfacing systems for integration of PV systems into utility grid. The superior harmonic spectrum, decreased voltage rating for the switches, decreased common mode voltages and lesser voltage changes (*dv/dt*) are important advantages of ML-MFGCIs. However, the complexity of control method rises compared to the traditional two-level inverter. As illustrated in Figure 2.2, ML-MFGCIs can be classified based on the power circuit structure to mitigate PQ problems: (1) voltage source ML-MFGCIs; (2) current source ML-MFGCIs.

The current source inverter (CSI) based topology has the advantages of its inherent boost characteristics, longer lifetime of the storage unit, inherent fault protection capability and direct control of the output current (Bai et al., 2007), (Xiangwu et al., 2007). The reason of the CSI not being as popular as VSI is that inductors employed in CSI as energy storage devices have higher conduction losses

and therefore compared to DC link capacitors of VSI have lower energy storage efficiency (Melin et al., 2008), (Zhang and Ooi, 1992). However, with the development of superconducting magnetic energy storage (SMES) technologies the problem related to conventional inductors are going to be solved and hence CSIs can be considered appropriate for high power application. Moreover, the recently-introduced reverse blocking IGBT has eliminated the need for series diode and thus making CSI a good alternative. Recently, the interest of researchers for multilevel inverters based on CSI for various applications has noticeably increased (Dash and Kazerani, 2011).

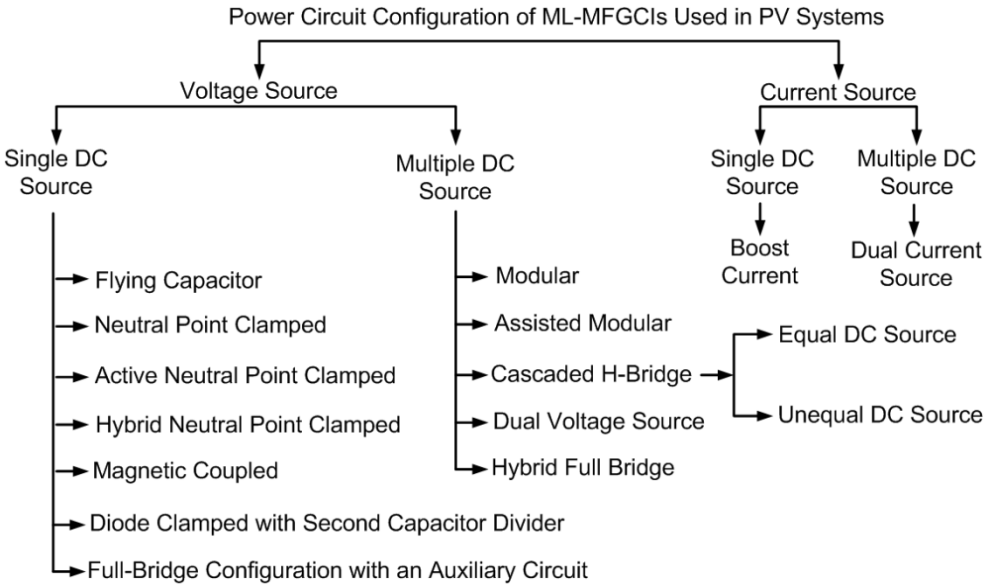

Figure 2.2. Classification of ML-MFGCI based on power circuit structure.

2.3. Modulation techniques used in ML-MFGCI

The modulation techniques of ML-MFGCIs can be classified as four categories as (i) Sinusoidal pulse width modulation (SPWM), (ii) Hysteresis, (iii) Selective harmonic elimination (SHE) and (iv) Space vector pulse width modulation (SVPWM) as shown in Figure 2.3. In SPWM, multi-carrier SPWM control methods can be used to increase the performance of multilevel inverters and have been classified according to vertical or horizontal arrangements of carrier signal. The vertical carrier distribution techniques are defined as level shifted (LS-PWM), which includes phase disposition (PD-PWM), phase opposition disposition (PODPWM) and alternative phase opposition disposition (APOD-PWM), while horizontal arrangement is known as phase shifted (PS) control technique. In fact PS-PWM is only useful for cascaded H-bridges and flying capacitors, while PD-PWM is more useful for NPC (Barghi-Latran and Teke, 2015).

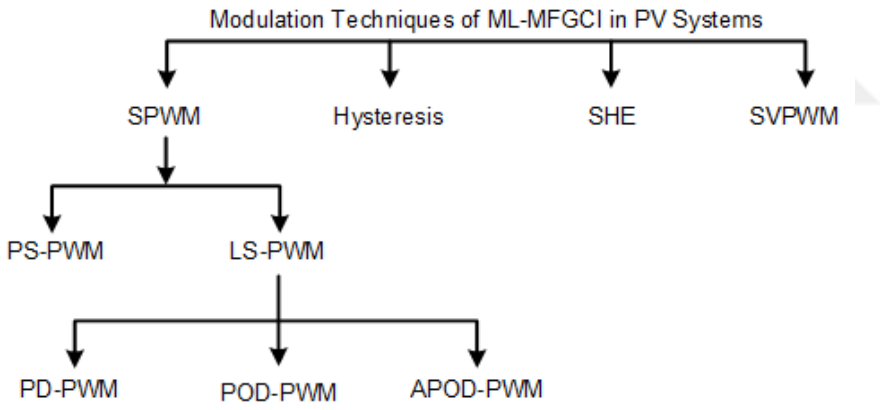

Figure 2.3. Classification of ML-MFGCIs based on modulation techniques.

2.4. Classification of ML-MFGCIs based on control techniques

An advanced control technique is very critical for the efficient operation of ML-MFGCI system. ML-MFGCI control technique calculates the current and voltage reference signals and determines the switching sequence of inverter

switches. There are various control techniques and algorithms in the literature applied to ML-MFGCI systems. Frequency domain techniques, i.e. Fast Fourier Transform, are not widely used due to large computation time and delay in calculating the reference signals (Khadkikar, 2012). Time domain techniques use instantaneous derivation of compensating current or voltage signals. There has been a huge number of control techniques successfully applied to ML-MFGCIs in the time domain. Most common time domain control methods used in MLMFGCI are the instantaneous active and reactive power (also called as 3-phase pq theory) (Akagi et al., 1984) and synchronous reference frame method (also called as 3-phase dq theory) (Bhattacharya and Divan, 1995). These methods convert the current and voltage signals in ABC frame to stationary reference frame (pq theory) or synchronously rotating frame (dq theory) to extract the fundamental and harmonic quantities (Khadkikar, 2012). In pq theory, instantaneous active and reactive powers are calculated, while, dq theory concerns with the current free of the source voltage. The active and reactive power concern with fundamental components (pq theory) and the fundamental component in distorted voltage or current (dq theory) are DC quantities in these theories. ML-MFGCI controller based on instantaneous active and reactive power theory were studied by Patrao et al., (2011), Zeng et al.,(2013), Shafiyi et al., (2012), Flores at al., (2009), Zhou et al., (2009), pq theory has limitations when the source voltages are unbalanced and/or distorted. The pqr theory is modified and referred as “pq0 theory” to eliminate these limitations that were studied by Cavalcanti et al., (2012), Oliveira (2010), while synchronously rotating frame (SRF) theory based controller were studied by Mei et al., (2013), Dash and Kazerani (2011), Liu et al., (2013). Besides these methods numerous control methods such as instantaneous symmetrical component, unity power factor, neural network, wavelet transform and etc. are used to control ML-MFGCI.

2.5. Analysis and discussions

A traditional grid connected PV plant contains a large number of PV modules connected in series and parallel to constitute strings and sub-arrays. The inverters are then connected to the medium voltage (*MV*) electric grid through a power transformer. The large scale PV plants can be further classified as centralized and multi-string types. In centralized type, the central inverter performs a unique MPPT algorithm for all the strings and interfaces to the *MV* grid. In multi-string architecture, the strings are connected to DC/DC converters that convert the PV string output voltage into a common DC bus which feeds a central inverter that interfaces to the *MV* grid. Two-stage converters allow the PV panels to operate over a wider voltage range than is possible with a centralized architecture and reduce losses due to panel mismatch and PS. On the other hand, DC/DC converter increases the costs and decreases the conversion efficiency. Although both architectures use central inverters, grid connected centralized architectures currently represent the state-of-the-art for megawatt-scale PV plants due to their low cost-per-watt, easy maintenance and high conversion efficiency (Villegas-Nunez, 2013).

As shown in Figure 2.4, standard central inverters will continue to be the most widely used inverter type in 2016 due to the growing demand for large commercial and grid connected projects, also the demand for turnkey substations is forecast to grow quickly in emerging markets, since these products help speed up installation times or simplify designs for large projects (Holz, 2013).

Medium and high power multilevel inverters are optimal solution for large scale grid connected PV systems. The multilevel inverter not only achieves power generation tracking, but also can complete the reactive, unbalance, and harmonic current compensation and named as multilevel multifunctional inverter. In the central type PV plants without any DC–DC converter for MPPT, the new generation multilevel inverters act as maximum power tracer to achieve high conversion efficiency.

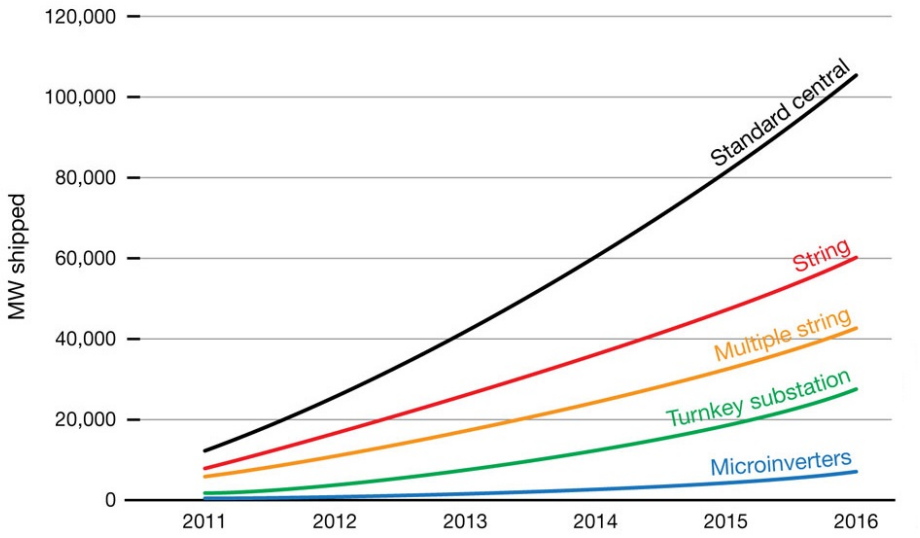

Figure 2.4. Standard central inverters are currently the most widely used inverter type in the world (Villegas-Nunez, 2013).

The evolution of ML-MFGCI in PV systems over the last years has resulted in several research, proven topologies and control methods. There have many topologies and control strategies of ML-MFGCIs for PV systems been well documented for different capacities and auxiliary functionalities. Several abbreviations of ML-MFGCIs based on the topology or application were described in Section 3 are presented in Table 2.2. These abbreviations can be used to emphasize the main features of MFGCIs more concisely (Khadkikar, 2012).

Table 2.1. Abbreviations of ML-MFGCI configurations

Abbreviation	**Description**
VSML-MFCGI	Voltage Source ML-MFGCI
CSML-MFGCI	Current Source ML-MFGCI
NPC-MFGCI	Neutral Point Clamped MFGCI
ANPC-MFGCI	Active Neutral Point Clamped
DC-MFGCI	Diode Clamped MFGCI
FC-MFGCI	Flying Capacitor MFGCI
CHB-MFGCI	Cascaded H-Bridge MFGCI
ACHB-MFGCI	Asymmetric Cascaded H-Bridge MFGCI
DVS-MFGCI	Dual Voltage Source MFGCI
MC-MFGCI	Magnetic Coupled MFGCI
M-MFGCI	Modular MFGCI
AM-MFGCI	Assisted Modular MFGCI
DCS-MFGCI	Dual Current Source MFGCI
HFB-MFGCI	Hybrid Full-Bridge MFGCI
HNPC-MFGCI	Hybrid Neutral Point Clamped MFGCI
BC-MFGCI	Boost Current MFGCI

The future ML-MFGCIs must evolve to meet the technological advances of PV cells, semiconductor parts, magnetic components and smart grid integration. ML-MFGCIs are expected to meet the following requirements, future trends and challenges:

1) The available ML-MFGCIs are mainly experimental prototypes and their capacities are low. The trend in the industry is toward higher power ratings for ML-MFGCIs, because the MLMFGCIs cost per watt decreases as ML-MFGCIs power increases. Therefore, ML-MFGCIs with power ratings up to a few megawatts may be offered to the commercial market.
2) The functionalities of ML-MFGCIs still need exploit. ML-MFGCI controls must be able to enhance grid reliability and PQ, and support grid voltage and frequency stability. With the increase in PV penetration, future ML-MFGCIs for large solar plants will need to incorporate several grid-control functionalities.

3) Another trend, for the DC side of the ML-MFGCI, is the use of higher system voltages to reduce wire costs and power losses. On the DC side, most large PV systems have been operating with a DC voltage limit of 1000 V. In order to increase cost savings and efficiency, and accommodate technological advances in PV cells that allow for operation at 1500 V. Also researches may be able to improve their production modeling results by accounting for the relationship between inverter efficiency and DC input voltage. While this relationship varies by topology, it is also product specific.
4) The elimination of the output transformer from ML-MFGCIs systems not only reduces the cost, size, and weight of the conversion stage but also increases the system overall efficiency. However, if the transformer is removed, the galvanic isolation between the PV generator and the grid is lost. This may cause safety hazards in the event of ground faults. Furthermore, when no transformer is used, the ML-MFGCI could inject direct current (DC) to the grid, causing the saturation of the transformers along the distribution network.

However, the additional functionalities of available ML-MFGCIs are still not perfect. Besides, it is hard to say which topology is better than the others, and a further study on the topology theory of ML-MFGCIs is essential necessary (Zeng et al., 2013). Table 2.2 summarizes a detailed comparison of different ML-MFGCIs topologies.

Table 2.2. Technical aspects of different multilevel multifunctional grid connected inverters in PV systems

Utility	Functionality	Topology	Levels number	Control method	Modulation strategy	Reference
1-Phase	APF, PFC	CHB-MFGCI	7	-	Adaptive SHE	(Zeng et al., 2012)
	APF, PFC	CHB- MFGCI	11	pq with PI and repetitive controller	PS-SPWM	(Xiao et al., 2012)
	APF	CHB-MFGCI	7	*	LS-PWM and PS-PWM	(Chavarria et al., 2013)
	PFC	Full-bridge with auxiliary circuit	5	Digital PI current control algorithm	SPWM	(Rahim et al., 2010)
	PFC	CHB-MFGCI	13	-	***	(Bandara et al., 2012)
	PFC	AM-MFGCI	31	pq	Calculation of witching angles	(Patrao et al., 2011)
	PFC	DC-MFGCI	3	-	-	(Blaabjerg and Koutroulis, 2011)
	PFC	DC-MFGCI	5	Digital PI current control algorithm	Carrier PWM	(Selvaraj and Rahim, 2009)
	PFC	CHB-MFGCI	5	PI current control algorithm	PS-PWM	(Alepuz et al., 2006)

Table 2.2. Continuous

1-Phase	PFC	Full-bridge with auxiliary circuit	5	Digital PI current control algorithm	Carrier PWM	(Rahim and Selvaraj, 2010)
	PFC	CHB-MFGCI	5	PI and PR current control algorithm	-	(Busquets et al., 2008)
	PFC	ACHB-MFGCI	19	Average power control	-	(Pimentel et al., 2009)
	PFC	CHB-MFGCI	3	Dual-loop current controller	Carrier PWM	(Oliveira et al., 2010)
	PFC	CHB-MFGCI	9	pq based a fully FLC without any PWM and PI controller	FLC base	(Cecati et al., 2010)
	PFC	M-MFGCI	5	dq current control	SVLM based on PD-PWM	(Mei et al., 2013)
	PFC	CHB-MFGCI	7	pq	PS-PWM	(Rezaei et al., 2011)
	PFC	NPC-MFGCI	3	pq- DPC	-	(Rivera et al., 2012)
	PFC	BC-MFGCI	5	open-loop	SPWM	(Hatziadoniu et al. 1999)
3-Phase	APF, PFC, CUC	NPC-MFGCI	3	Combination of VOC and SVPWM	SVPWM	(Tsengenes et al., 2011)

Table 2.2. Continuous

3-Phase	APF, PFC, SSIUC	CHB-MFGCI	21	pq	Introduce new PWM method	(Flores et al., 2009)
	SSIUC-PFC	NPC-MFGCI	3	FL based current control	-	(Altin and Ozdemir, 2013)
	APF, PFC, CUC	CHB-MFGCI	5	pq (real power theory)	Carrier PWM	(Villanueva et al., 2009)
	APF, PFC	DVS-MFGCI	3	PI base current control	SVPWM	(Grandi and Ostojic, 2009), (Grandi et al., 2009)
	APF, PFC	NPC-MFGCI	3	the pq theory (pq0-current control)	SVPWM	(Lee et al., 2009), (Rajasekar and Gupta, 2011)
	APF, PFC	HFB-MFGCI	9	pq- current control method	SVPWM	(Zhou et al., 2009)
	APF	HNPC-MFGCI	-	Direct Current Control	SHE-Hysteresis band strategy	(Miñambres et al., 2010), (Miñambres et al., 2013)
	PFC	NPC-MFGCI	5	Digital PI current control algorithm	SPWM	(Ravi et al., 2011)

Table 2.2. Continuous

3-Phase	PFC	DVS-MFGCI		Sliding mode control	-	(Pires et al., 2012)
	PFC	CHB-MFGCI	5	dq current control by two PI controllers	SVPWM	(Rajkumar and Manoharan, 2013)
	PFC	NPC-MFGCI	3	pq with PR	SVPWM	(Tsengenes et al., 2012)
	PFC	NPC-MFGCI	3	pq-an extended DPC	SVPWM	(Hamzaouia et al., 2011)
	PFC	NPC-MFGCI	3	dq current control	Carrier PWM	(Dash and Kazerani, 2012)
	PFC	HFB-MFGCI		dq current control	PS-PWM	(Dash and Kazerani, 2011)
	PFC	CHB-MFGCI	7	dq- VOC	PS-PWM	(Cavalcanti et al., 2012)

2.6. Summary

ML-MFGCIs play an important role in distributed generation to integrate PV systems into the utility grid. In recent research studies, novel control algorithms and topologies for ML-MFGCIs interfaced with large scale PV system are developed to optimize the energy conversion, to control the PQ of the utility grid, to perform low cost operation with high efficiency over a wide power range, and to have a high reliability. The higher power rates together with the enhanced PQ have been the major drive for large scale installations and leading for research and development of ML-MFGCI in PV systems.

In this chapter, a comprehensive review on the topologies and control strategies of ML-MFGCIs are performed. The development of new control strategies and execution of multifunctional compensation capabilities in large scale PV systems are the main research trends related to both active power flow control and mitigation of various PQ disturbances using ML-MFGCIs. The different aspects of ML-MFGCIs, the novel developments and practical applications in this field of research were discussed in detail. The detailed classification, challenges and future trends on ML-MFGCIs will help researchers, users, and suppliers of electrical power to acquire an overview for future research and studies on this subject.

3. MAXIMUM POWER POINT TRACKING

3.1. Physical Structure of a Solar Cell

Solar cells consist of a semiconducting device that absorbs light and converts it into electricity. In dark conditions, a solar cell, such as a diode, has an exponential characteristic in the Current-Voltage (*I-V*) output characteristic. When it absorbs light, photons with energy rather than semiconductor's band gap energy are absorbed and generate an electron-hole pair. This is known as photovoltaic effect. These charge carriers that have been created in the depletion area are then separated through an available electric field. This condition brings a p-n junction in forward-bias and hence performs a voltage. When a load is connected, current flows through the load also called the photo-current. However, when p-n junction happens in forward-bias a leakage current flows in the inverse direction of the photo-current. As shown in Figures 3.1, the PV cell can be operates on wide range of voltages and currents. To identify the MPP of the PV cell, the greatness of load resistance from zero (a short circuit) to infinity (an open circuit) must be changed. On the *I–V* curve, the MPP obtains when the produced current and voltage are in their maximum value. Zero power products at open-circuit voltage condition with zero current, or at short-circuit current condition with zero voltage. Therefore, MPP is somewhere between these two points. Maximum power is generated at about the "knee" of the curve. This point represents the maximum efficiency of the solar device in converting sunlight into electricity (Knopf, 1999), (Walker, 2001), (Khaligh and Onar, 2009), (Fennich, 2013).

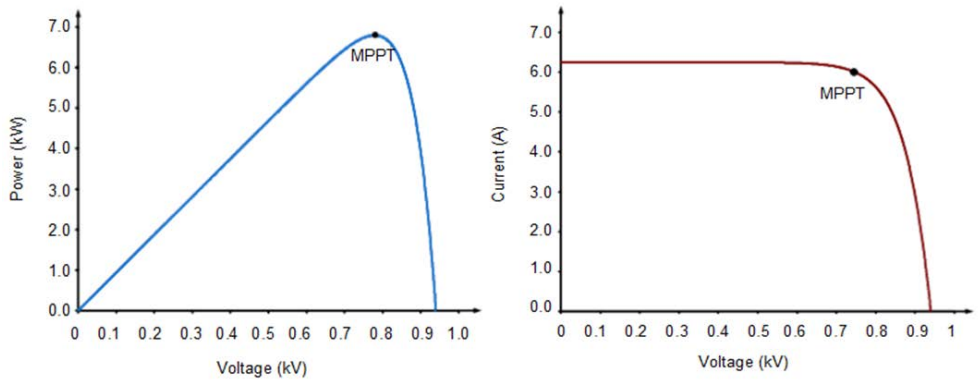

Figure 3.1. The characteristics of a PV cell (a) *P-V* curve (b) *I-V* curve

According to the description of the solar cell, a PV model can be illustrated by the equivalent circuit shown in Figure 3.2 and called as dual-diode model. In the dual-diode model, series resistance is a combination of resistive losses such as metal grid, semiconductor material, contacts and current collecting bus that are caused in a current path. The PV module contains numerous solar cells connected in parallel and series, hence the effectiveness of resistor becomes more visible and clear, and its rate is multiplied by cells quantity. In this mode parallel resistance specifies the leakage current in PV module. Its effect is far less noticeable unless there is a large system that consists of a number of PV modules connected in parallel (Malki, 2011), (Fennich, 2013).

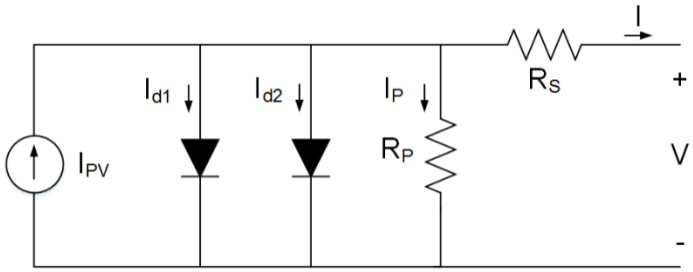

Figure 3.2. Dual-diode model of the PV module

The output current of the dual-diode model of the PV module can be expressed as Eq. (3.1) (Ishaque et al, 2011), (Fennich, 2013).

$$I = I_{PV} - I_{01}\left[\exp(\frac{V + IR_S}{\alpha_1 \times V_{T1}}) - 1\right] - I_{02}\left[\exp(\frac{V + IR_S}{\alpha_2 \times V_{T2}}) - 1\right] - \left(\frac{V + IR_S}{R_P}\right) \quad (3.1)$$

where I and V are the PV module's current and voltage, respectively, I_{PV} is photocurrent, I_{o1} and I_{o2} are the diodes reverse saturation currents of the first and second diode, respectively, $V_{T1,2} = N_s kT/q$ is the thermal voltage of the PV module having N_s cells in series and N_p cells in parallel where q *=1.602 e-19 C* is the elementary charge and K*= 1.380 e-23 j/k* is the Boltzmann's constant., a_1 and a_2 are the diode ideality factors, T is the temperature in Kelvin, R_s is series resistance, and R_p is parallel resistance. In order to calculate the current generated by the incident light *Ipv*, temperature and irradiance are big factors to the equation. The output current of the double-diode model of the PV module can be illustrated by Eq. (3.2).

$$I_{PV} = (I_{PV-STC} + K_i.\Delta T)\left(\frac{G}{G_{STC}}\right) \quad (3.2)$$

where $\Delta T = T - T_{STC}$, (in Kelvin T_{STC} *= 25 C*), I_{PV_STC} is the PV module's current at standard testing conditions (STC) (in Ampere), G is the radiance on the PV module surface, G_{STC} (*1000 W/m^2*) is their radiance at STC, and K_i is the short circuit current coefficient. The reverse saturation current that considers the temperature variation can be expressed by Eq. (3.3).

$$I_0 = \frac{(I_{PV-STC} + K_i.\Delta T)}{\exp\left[(V_{OC-STC} + K_V.\Delta T)/\alpha.\Delta T\right] - 1} \quad (3.3)$$

where K_V and $V_{OC.STC}$ are is the open circuit voltage coefficient and PV open circuit voltage at standard testing conditions (STC), respectively. Thus, the entire saturation current in double-diode model of PV module can be calculated as Eq. (3.4).

$$I_0 = \frac{(I_{PV-STC} + K_i.\Delta T)}{\exp\left[(V_{OC-STC+} + K_V.\Delta T)/((\alpha_1 + \alpha_2)/\gamma).V_T\right] - 1} \tag{3.4}$$

According to Shockley diffusion theory, the diffusion current α_1 is commonly a unity. However, the value of α_2 is flexible. If $\alpha_2 \geq 1.2$, $(\alpha_1 + \alpha_2)/\gamma = 1$ and $\alpha_1 = 1$, then γ can be chosen to be ≥ 2.2. By selecting the values of α_1 and α_2, Eq. 3.1 can be simplified in terms of γ as Eq. (3.5).

$$I = I_{PV} - I_0\left[\exp(\frac{V + IR_S}{V_T}) + \exp(\frac{V + IR_S}{(\gamma - 1)\times V_T}) - 2\right] - \left(\frac{V + IR_S}{R_P}\right) \tag{3.5}$$

In the dual-diode model of the PV module, for more accuracy high degrees of freedom are provided. However, the single-diode model wide spread used for PV module modeling since it is sufficient to represent characteristics and dynamics of PV module. Although due to its complexity of the dual-diode model is not widely used (Khaligh and Onar, 2009). The single-diode model for PV module shows in Figure 3.3.

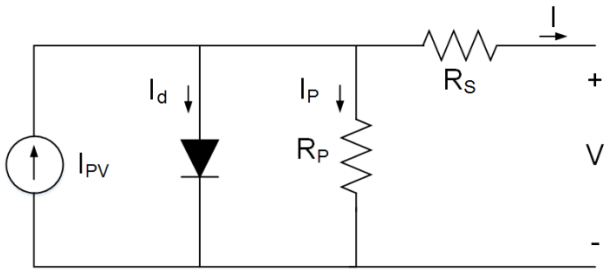

Figure 3.3. Single-diode model of the PV module

The output current of the dual-diode model of the PV module can be expressed as Eq. (3.6) (Koizumi and Kurokawa, 2005), (Khaligh and Onar, 2009).

$$I = I_{PV} - I_0\left[\exp(\frac{V + IR_S}{\alpha \times V_T}) - 1\right] - \left(\frac{V + IR_S}{R_P}\right) \tag{3.6}$$

Generally, in the single-diode model the parallel resistance is high enough and behaves such open circuit condition. Therefore neglecting of the parallel resistance in PV model will not loss the accuracy of the model significantly. So, the single-diode of PV equivalent model can be represented as Figure 3.4. The output current of the single-diode model of the PV module without parallel resistance can be expressed as Eq. (3.7) (Hansen, 2000), (Khaligh and Onar, 2009).

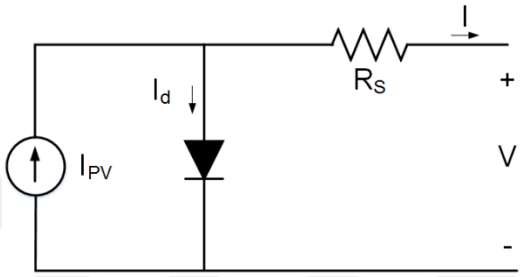

Figure 3.4. Single-diode model of the PV module without parallel resistance.

$$I = I_{PV} - I_0 \left[\exp\left(\frac{V + IR_S}{\alpha \times V_T}\right) - 1 \right] \tag{3.7}$$

For more simplification, the series resistance is very small and behaves such as short circuit condition. In this way, a simplified equivalent model of single-diode model of PV module without series and parallel resistance can be illustrated as Figure 3.5. The output current of the single-diode model of the PV module without resistances resistance can be expressed as Eq. (3.8) (Hansen, 2000), (Khaligh and Onar, 2009).

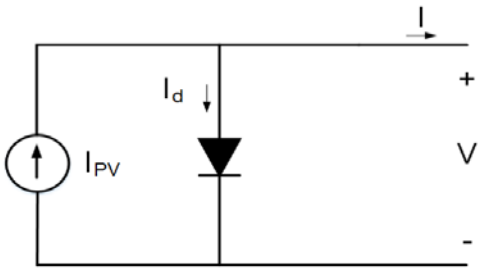

Figure 3.5. Single-diode model of the PV module without resistances.

$$I = I_{PV} - I_0 \left[\exp(\frac{V}{\alpha \times V_T}) - 1 \right] \quad (3.8)$$

3.2. Maximum Power Point Tracking Technology

As emphasized in the previous sections, the output power of PV arrays is changing with weather conditions such as solar radiance and atmospheric temperature. Therefore, in PV generation systems utilization of the MPPT control strategy becomes indispensable condition to extract maximum power from the PV arrays.

In recent years, numerous MPPT strategies such as fractional open-circuit voltage, fractional short-circuit current, hill climbing, perturb and observe (P&O), IncCond, incremental resistance, ripple correlation control, fuzzy logic, neural network, particle swarm optimization, and sliding mode have been brings to extract maximum power point in the PV systems. Fractional open-circuit voltage and short-circuit current techniques ensure a straightforward and efficient way to achieve maximum power. However, they have more power loss due to requiring of periodical disconnection or short-circuit of the PV arrays to measure the open-circuit voltage or short-circuit current. P&O and hill climbing methods are widely utilized to extract maximum power due to their easily and simple implementation. The hill climbing technique perturb in the duty ratio of the power converter, while P&O strategy perturb in the operating voltage of the PV arrays. Nevertheless, due to the perturbation the oscillations in steady state conditions can be occur in both methods. IncCond strategy, which is based on the slope of the PV array power versus voltage curve, brings to enhance the accuracy of tracking and improve dynamic performance of tracking under rapidly varying conditions. In IncCond method the slope of power versus voltage curve at the MPP is zero. Other existing such as neural network, fuzzy logic, optimized algorithms, and sliding mode control strategies show enhanced performance. However, they are not wide spread

used owing to their complexity and need of expensive digital processor (Liu et al., 2008), (Killi and Samanta, 2015).

The conventional MPPT techniques are generally utilized with a fixed perturbation step size identified by the tradeoff between tracking speed and efficiency necessities. The extracted power from PV arrays with a lager step size perturbation tends faster dynamics behavior but excessive oscillations in steady state conditions and results a low efficiency. This situation will be reversed with smaller step size MPPT strategy. However, to overcome to tradeoff between tracking speed and efficiency dilemma problem the variable step size iteration can be utilized. In next section, a modified VSS-MPPT algorithm is proposed for the IncCond based MPPT technique and is dedicated to prepare a straightforward and significant strategy to enhance tracking accuracy as well as tracking dynamics. The proposed modified IncCond MPPT algorithm improves the efficiency of the entire system through increasing the tracking speed and reducing the power loss in steady state (Killi and Samanta, 2015), (Belkaid et al., 2017).

3.3. Partial Shading Conditions

In the grid connected PV system, the PV system is interfaced with power system network an inverter which may have mainly two different topologies as central and string. For many years, the central inverter has been the preferable choice for large as well as small PV system installations. In the central configuration, to form a string numerous of PV modules connect in series. To form an array, several of these strings arrange in parallel which is then connect to a central inverter. This is called as series-parallel connection of PV modules and is a typical setup for the PV power plant. Simple installation, less maintenance, and high reliability are merits of such arrangement. However, it does expose several disadvantages, one of which is the severe reduction in the output power when one or a number of modules are subjected to PS (Ishaque et al., 2011), (Ishaque, and Salam, 2013), (Ramli, and Salam, 2014). When one of the PV modules in the

series-parallel connected PV system is shaded or does not obtain enough solar radiation, as shown in Figure 3.6(a), it dissipates the power generated by the other PV modules. *I–V* curve of each PV module is shown in Figure 3.6(b). If the PV string operates at current I_a, the shaded PV module will be forced to operate at the reverse direction and behavior as a load (Shimizu et al., 2003). This situation brings to highly power dissipation, and the leading local heat will raise damage to the shaded PV module. Generally to prevent this situation PV strings equipping with bypass diodes (Olalla et al., 2013). As shown in Figure 3.6(a), to avoid PV cells self-heating and protect PV modules under PS conditions bypass diodes are added into PV system configuration (Poshtkouhi et al., 2012), (Pilawa-Podgurski, and Perreault, 2013). Under uniform solar radiation, the bypass diodes are reverse-biased and don't have any impacts on the PV system operation. However, during PS conditions the bypass diode is forward-biased and the current flows through the diode instead of the PV module (Tey, and Mekhilef, 2014). Figure 3.7 shows the model of a generalized series-parallel arrangement of a PV system. The output current of this configuration using double-diode model can be represented by Eq. (3.9) (Ishaque et al., 2011).

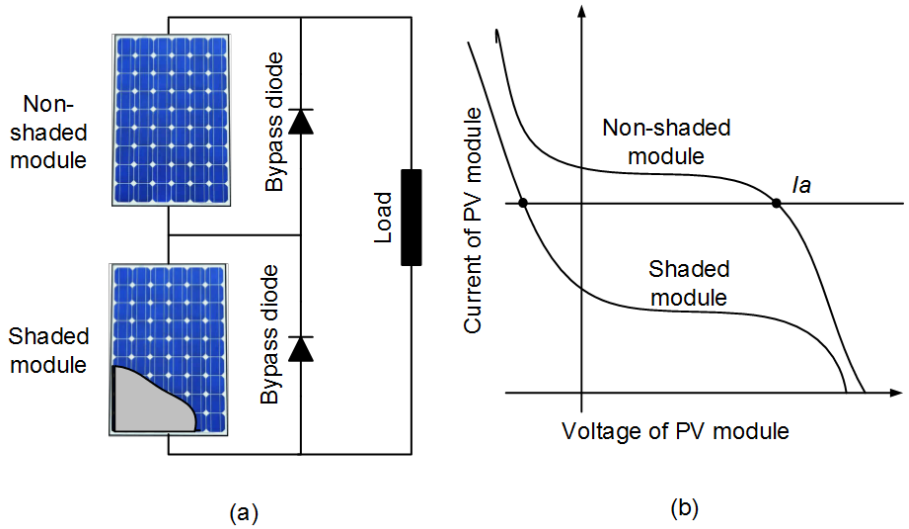

Figure 3.6. (a) PV string subjected to PS conditions. (b) *P–V* curve of PV modules.

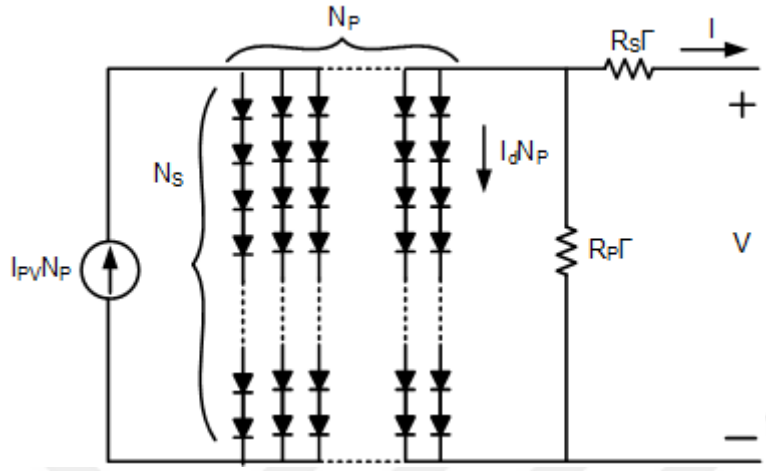

Figure 3.7. Series parallel combination of PV system.

$$I = N_P\left[I_{PV} - I_0\left(I_{d1} + I_{d2} - 2\right)\right] - \left(\frac{V + IR_S\Gamma}{R_P\Gamma}\right) \tag{3.9}$$

where $I_{d1} = \exp\left(V + IR_S\Gamma / V_T N_S\right)$ and $I_{d2} = \exp\left(V + IR_S\Gamma / (\gamma - 1)V_T N_S\right)$

$$\gamma = 1 + \alpha_2 \geq 2.2 \tag{3.10}$$

$$\Gamma = \frac{N_S}{N_P} \tag{3.11}$$

where N_S and N_P are the series and parallel PV module numbers, respectively (Ishaque, and Salam, 2013). Figure 3.8 shows a more practical configuration of a PV system, where two additional diodes are connected. One of these diodes used to protect modules from hotspot and paralleled with each PV module which is known as bypass diode. Another diode used to protect the PV systems arrays from being affected by the current unbalance between the PV system strings which is connected at the end of each PV string and known as blocking diode (Ahmed and Salam, 2015). However, the connection of bypass diodes will change the output characteristics of the module and results multiple

peaks on the *P–V* curve (Tey and Mekhilef, 2014). The position of the MPP on the *P–V* curve depends on the radiation and environment temperature operating conditions (Konstantopoulos and Koutroulis, 2014). This effect can be visualized by a series-parallel arrangement comprised of three strings, each having six sets of PV modules, as shown in Figure 3.7. In this configuration, each module has a nominal rating of 240 W at STC. When the PV array receives a uniform irradiance of 1000 W/m^2, the bypass diodes are reverse biased and current flows due to the series connection PV modules.

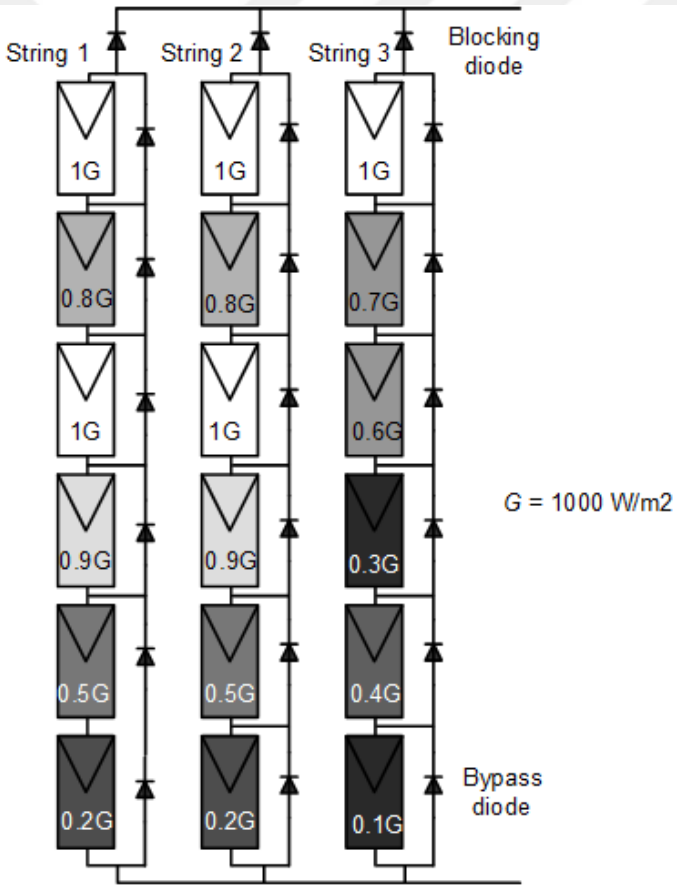

Figure 3.8. The practical arrangement of a PV array under PS.

Figure 3.9 shows *P–V* and *I–V* curves for the existed PV system where exhibits a single MPP under a uniform solar irradiance of 1000 W/m^2 on all the PV modules. However, when PV array is subjected to PS, the shaded modules receive a reduced solar insolation as illustrated in Figure 3.8. However, when PV array is subjected to PS, the shaded modules receive a reduced solar radiation as illustrated in Figure 3.8. The voltage difference between unequally insolated modules activates the bypass diode of the lower insolated string. As a result, the resulting *P–V* and *I-V* curve for each shaded string is characterized by multi peaks. Figures 3.10, 3.11, 3.12 and 3.13 illustrates typical *I–V* and *P–V* curves under a non-uniform solar irradiance for the strings 1, 2, 3 and whole PV system respectively.

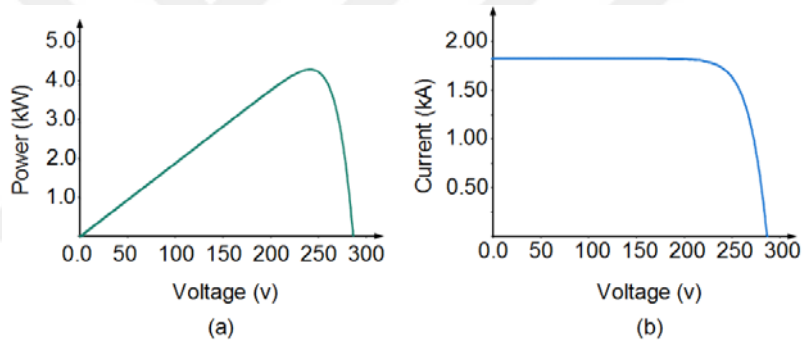

Figure 3.9. Operation of PV under G = 1000 W/m2uniform insolation (a) *P–V* curve (b) *I–V* curves.

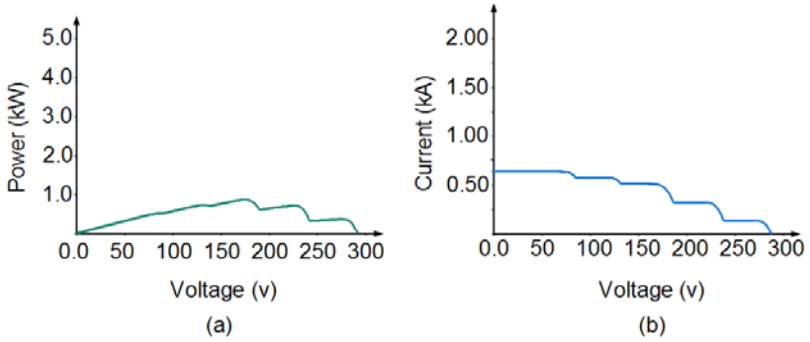

Figure 3.10. Operation of string_1 in PV system under PS: (a) *P–V* curve,. (b) *I–V* curve.

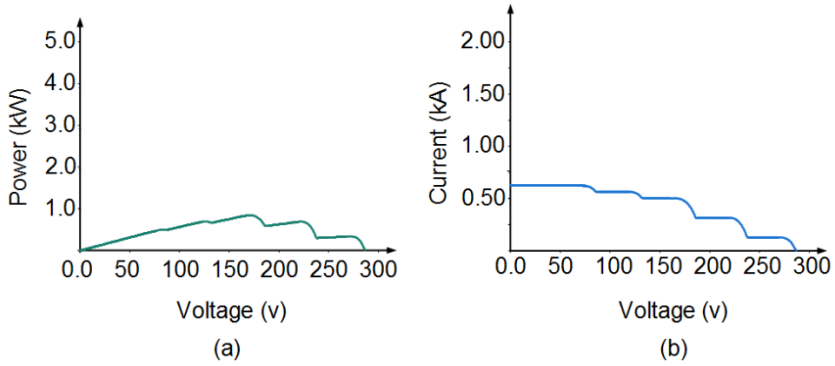

Figure 3.11. Operation of string 2 in PV system under PS: (a) *P–V* curve, (b) *I–V* curve.

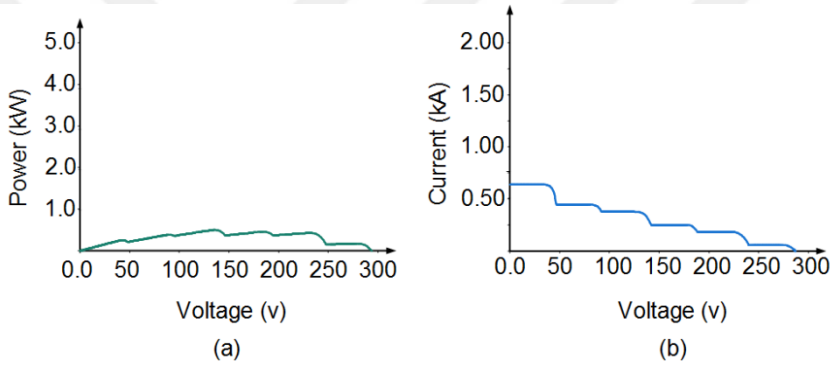

Figure 3.12. Operation of string 3 in PV system under PS: (a) *P–V* curve, (b) *I–V* curve.

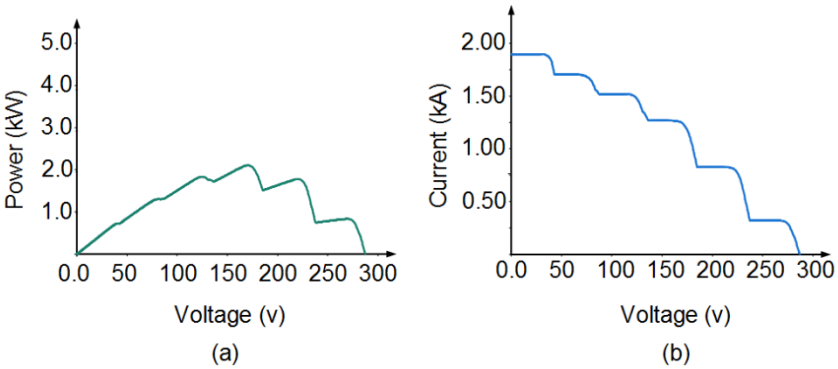

Figure 3.13. Operation of PV system under PS: (a) *P–V* curves for PV system. (b) *I–V* curves for PV system.

To maximize the efficiency of the PV system, a GMPP tracking algorithm should be applied to track maximum power during PS conditions. During PS conditions conventional MPPT algorithms are likely to be trapped at one of the local peak, simply because its algorithm could not differentiate the local with the global peak. Therefore, it oscillates around the vicinity of the local peak and remains there indefinitely—a significant reduction in the PV power yield will be experienced (Ishaque et al., 2012), (Ahmed and Salam, 2015).

3.4. Proposed Maximum Power Point Tracking Method

To appreciate the behavior of the PV system, the single-diode model of the PV systems are used to characterize the voltage and current relationship of the PV system. As emphasized earlier, the internal parasitic parallel and series resistance is usually neglected, as series resistance is very small and parallel resistance is usually very large. Thus, the voltage and current relationship of the PV system can be rewritten as Eq. (3.12) (Ahmed and Salam, 2015).

$$I = I_{PV} - I_0\left[e^{(AV)} - 1\right] \cong I_{PV} - I_0\left[e^{(AV)}\right] \tag{3.13}$$

where

$$A = \frac{1}{V_T} \tag{3.13}$$

The A depend on the atmospheric temperature and continuously change according to changing of atmospheric temperature throughout day. Thus, a direct calculation of A is not possible; some numerical solution is required. The short-circuit current (I_{SC}) and the open-circuit voltage (V_{OC}) can be derived as:

$$I = I_{PV} = I_{SC} \quad [\text{when } V = 0 \text{ and } I = I_{SC}\,] \tag{3.14}$$

and

$$0 = I_{PV} - I_0\left(A.V_m\right) \quad \text{[when } V = V_{OC} \text{ and } I = 0\text{]} \tag{3.15}$$

$$I_0 = I_{PV}\left(A.V_{OC}\right) \tag{3.16}$$

Thus, if the MPP is considered (V_m, I_m), the following expression can be derived from Eq. (3.17):

$$I_m = I_{PV} - I_0\left[e^{(A.V_m)}\right] \tag{3.17}$$

$$I_m = I_{SC} - I_{SC}e^{(-A.V_{OC})}\left[e^{(A.V_m)}\right] \tag{3.18}$$

$$I_m = I_{SC}\left(1-\left[e^{A(V_m-V_{OC})}\right]\right) \tag{3.19}$$

Thus according Eq. (3.16) numerical value for *A* can be determined by Eq. (3.20).

$$A = \frac{1}{(V_m - V_{OC})}\ln\left(1-\frac{I_m}{I_{SC}}\right) \tag{3.20}$$

Eq. 3.17 converts *m* in to a measurable quantity using the parameters provided by the manufacture. Hence, the expression for the voltage can be illustrated as Eq. (3.21).

$$V = V_{OC} + \left[\frac{1}{A}\ln\left(1-\frac{I}{I_{SC}}\right)\right] \tag{3.21}$$

The Eq. 3.19 represents the exponential relationship of the maximum power point voltage and open circuit voltage of the PV system. As show in Figure 3.14 critical observations shows that the line power of the PV system under uniform irradiance is the same with inverse filliped of the line which is represent

the relationship of the maximum power point voltage and open circuit voltage. So the maximum power point voltage in any point can be calculated with Eq. (3.22). The accuracy of the Eq. (3.22) examined and represented in Figure 3.15.

$$V_{MPP} = V_{MPP-nominal} + \left[\frac{1}{A}\ln\left(1-\frac{P_{Measur}}{P_{MPP-n}}\right)\right].N_S \tag{3.22}$$

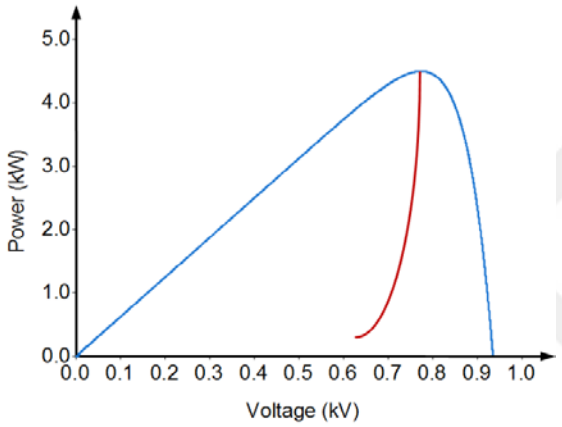

Figure 3.14. The relationship of the power and voltage in the PV system according to solar irradiance changing.

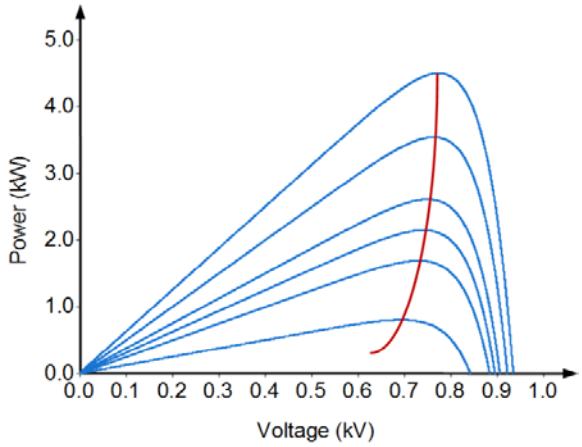

Figure 3.15. The power line of the PV system.

While the Eq. (3.22) explains the relationship of the maximum power point voltage and power, so we can use this relationship to adjust the step size for tracking the maximum power point of the PV system. Therefore in this progress according to this relationship a VSS-MPPT method proposed. Proposed method flowchart shown in Figure 4.16.

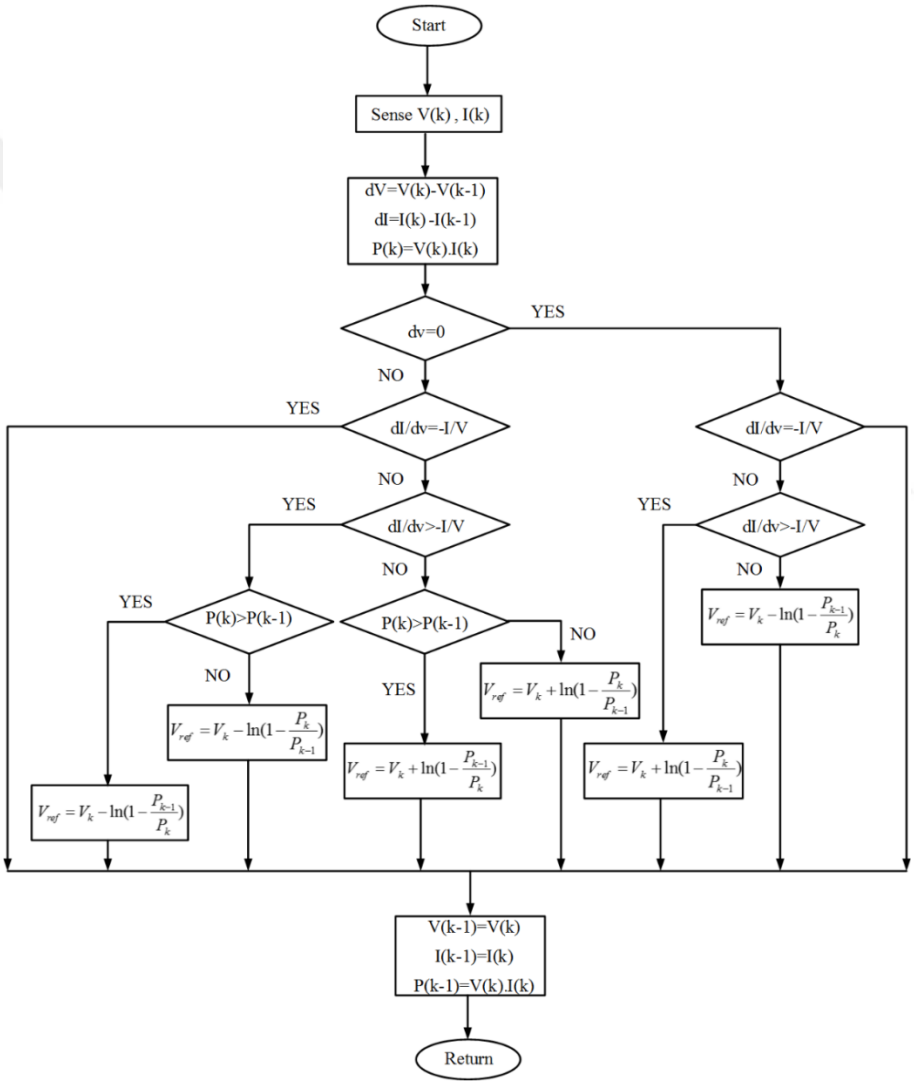

Figure 3.16. The flowchart of the proposed VSS-MPPT method.

Moreover under PS condition the unbalanced currents injects from PV strings into system at same voltage. However this unbalance current maintains the maximum power point voltage. So the strings current unbalance rate can be calculated with Eq. (3.23). If the strings current unbalance rate is larger than the desired value and the currents of more than half of strings are lower than the average current, a PS condition has been occurred and MPPT algorithm tracks the local MPP. So, to track the global MPP the string voltage should be decrease. Proposed GMPPT method flowchart shown in Figure 3.17.

$$I_{Avr} = \frac{\sum_{i=1}^{N_{String}} I_{String}}{N_{String}} \tag{3.23}$$

where N_{String} is number of strings on PV system.

CUN%= (Max current deviation from avr current / Avr current)×100 (3.24)

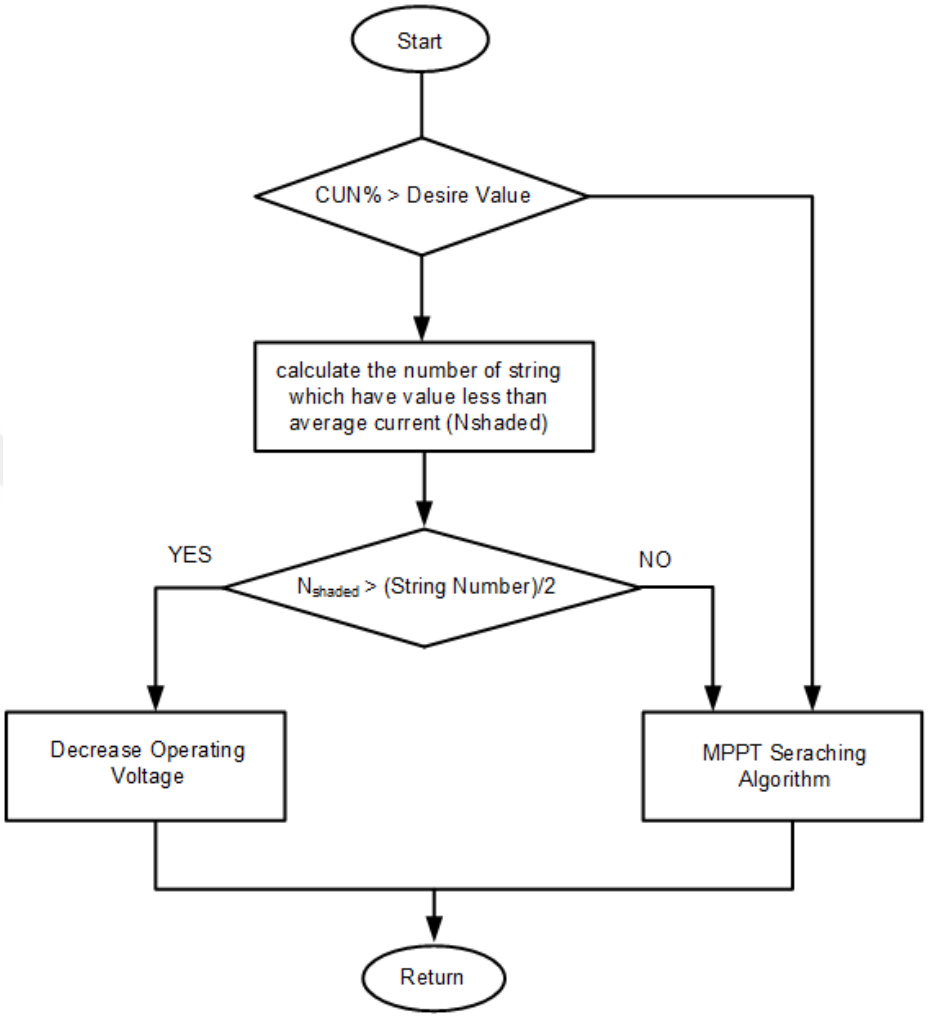

Figure 3.17. The flowchart of the proposed MPPT method.

3.5. Results

The simulations are configured to validate the performance of the proposed variable-step size IncCond MPPT algorithm and performance comparing of the proposed algorithm versus conventional fixed-step size IncCond MPPT strategy under same conditions. To carry out simulation study, as shown in Figure 3.18, 19 PV modules are connected in series and three strings connected in parallel arrangement to form the PV system. Bypass diodes are incorporated to avoid self-

heating of the PV modules which protects PV modules from hot spots. The specifications of a PV module used in this study are given in Table 3.1. In Figure 3.18, *N* expresses the number of series connected PV panels. The simulation results are carried out using PSCAD/EMTDC to performance verification process.

Table 3.1. Electrical characteristics of SunPower E19 PV module

Electrical Performance in Standard Test Conditions (*STC)	
Max power (P_{max}) (W_p)	240 W
Voltage at Pmax (V_m) (V)	40.5 V
Current at Pmax (I_m) (A)	5.93 A
Short circuit current (I_{sc}) (A)	6.30 A
Open Circuit Voltage (V_{oc}) (V)	48.6 V
Temperature Coefficient of V_{oc}	-132.5 mV/K
Temperature Coefficient of I_{sc}	3.5 mA/K
*STC: : Irradiance of 1000W/m², AM 1.5, and cell temperature 25° C	
Number of series cells in one panel	72

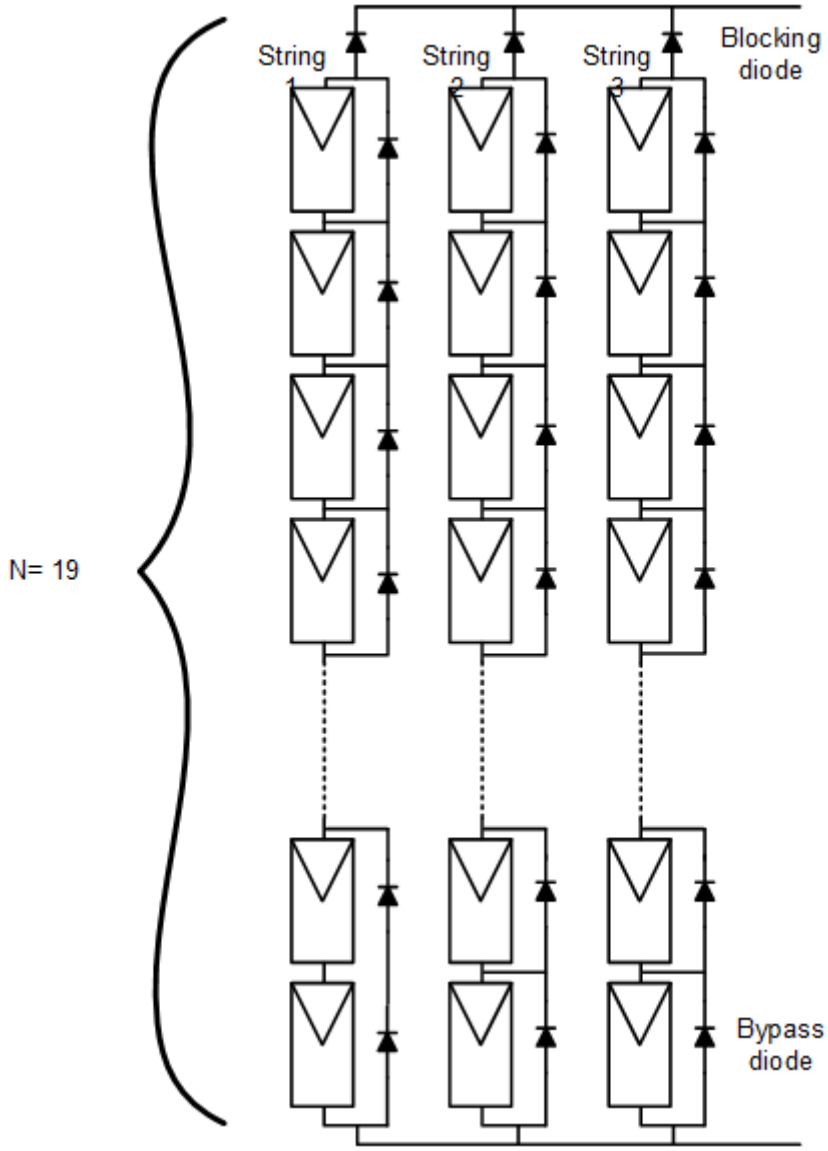

Figure 3.18. Series-parallel arrangement of the under study PV system.

The scheme of the overall PV system is shown in Figure 3.19. The single stage inverter has been designed to interface between PV system and utility grid and injects power from PV system to utility grid. Its main switch is the insulated-gate bipolar transistor (IGBT) controllable by the gate signal with a switching

frequency of f = 10 kHz. Input and output capacitors and inductors are used as filters: $L_f = 0.01\ mH$, $C_f = 10\ \mu F$, $C_{dc} = 500\ \mu F$.

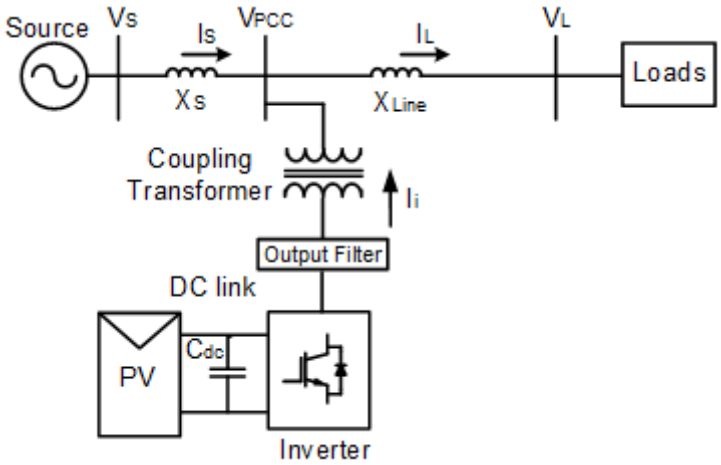

Figure 3.19. The scheme of the overall PV system.

***Case 1*:** In this case, the performance of the proposed variable-step size IncCond MPPT algorithm and conventional fixed-step size IncCond MPPT strategy with 2 *V* and 5 *V* step sizes are compared. In this case, modules insulated with 10000 W/m^2 and inverter work at 580 V_{DC} (voltage in the output of PV system) without MPPT control. To compare the performance of the proposed variable-step size IncCond MPPT algorithm and conventional fixed-step size IncCond MPPT strategy at steady state without any changes in the insolation level, MPPT controls switch in 1.5 *s*. Figures 3.20 represents the tracked MPP voltage by proposed and conventional MPPT algorithms. As shown in Figure 3.20, the conventional IncCond MPPT algorithm with 5 *V* step size and proposed algorithm tracks the MPP voltage faster than conventional IncCond MPPT algorithm with 2 *V* step size. However as seen from Figure 20, the proposed algorithm tracks the exact voltage of MPP. Also Figure 3.21 shows the extracted power by proposed and conventional MPPT algorithms. Compared with the conventional IncCond MPPT

method, the proposed algorithm exhibits a good dynamic performance with small steady state oscillations. It should be noted that the black lines in the Figures 3.20 and 3.21 are the lines that should be followed by tracking algorithms.

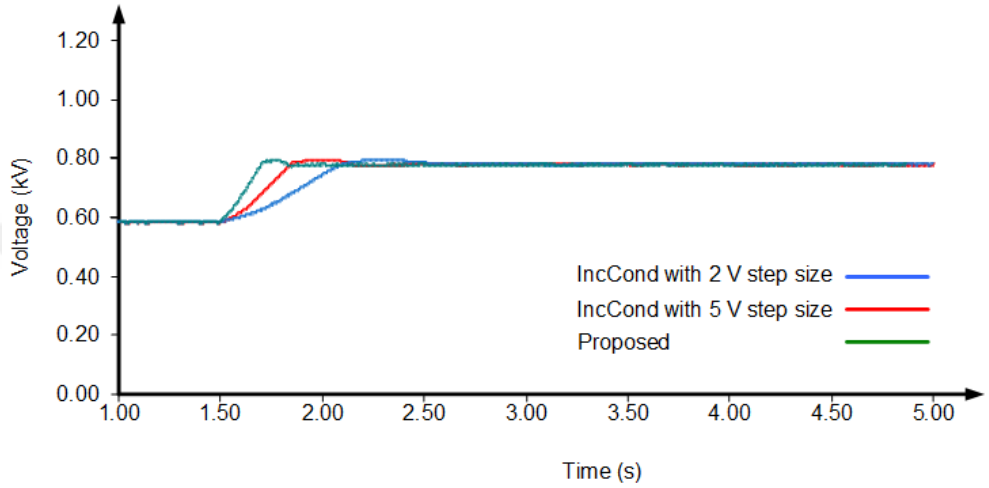

Figure 3.20. Tracked voltage by proposed and conventional fixed-step size IncCond method in case 1.

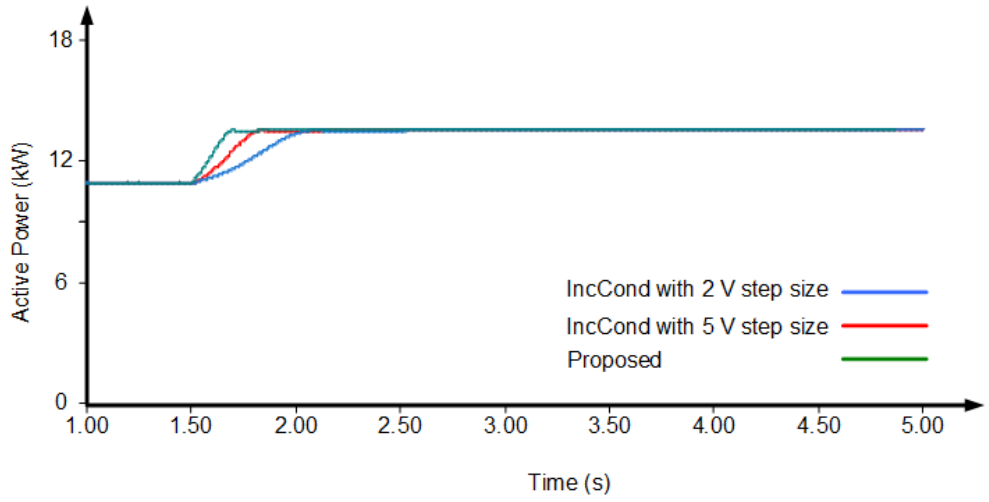

Figure 3.21. Extracted power from PV system by proposed and conventional fixed-step size IncCond method in case 1.

***Case 2*:** In this case, the performance of the proposed variable-step size IncCond MPPT algorithm and conventional fixed-step size IncCond MPPT strategy with 2 *V* and 5 *V* step sizes are compared in the slow radiation changing condition. As shown in Figure 3.22 the solar radiation slowly changed (without step change) in 1.5 *s* from 500 to 10000 W/m^2 at 7.45 *s*. Figures 3.23 represents the tracked MPP voltage by proposed and conventional MPPT algorithms. As shown in Figures 3.23 the proposed algorithm rapidly follows the MPP voltage. Also Figure 3.24 shows the extracted power by proposed and conventional MPPT algorithms. As seen from Figure 3.24, due to rapidly follows the MPP voltage, the proposed algorithm has better performance than conventional method in terms of MPPT. Compared with the conventional IncCond MPPT method, the proposed algorithm exhibits a good dynamic performance with small steady state oscillations. Moreover, the dynamic performance of the proposed algorithm is obviously faster than that of fixed step size method.

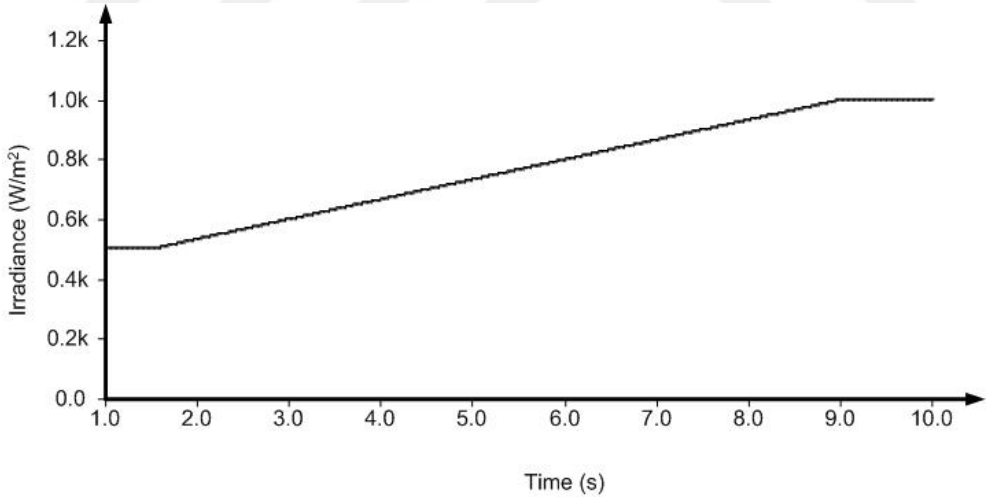

Figure 3.22. Solar radiation changing in case 2.

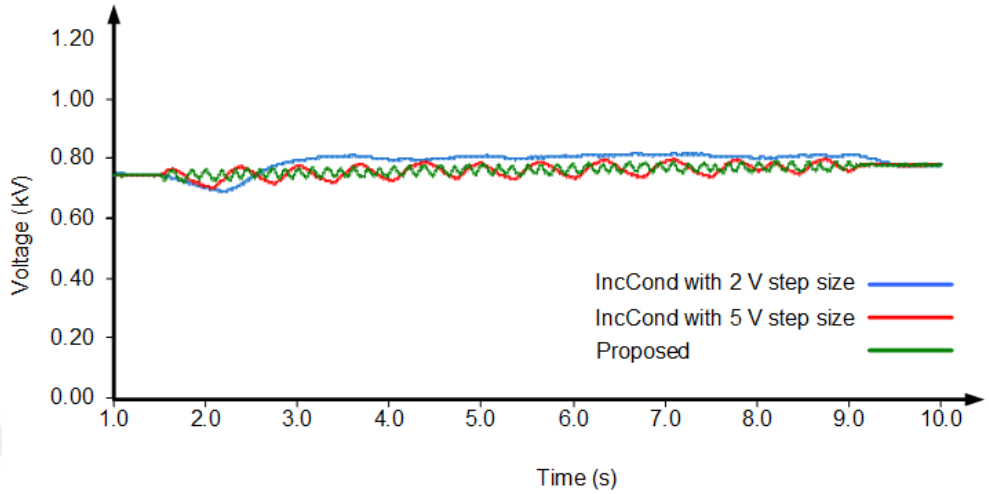

Figure 3.23. Tracked voltage by proposed and conventional fixed-step size IncCond method in case 2.

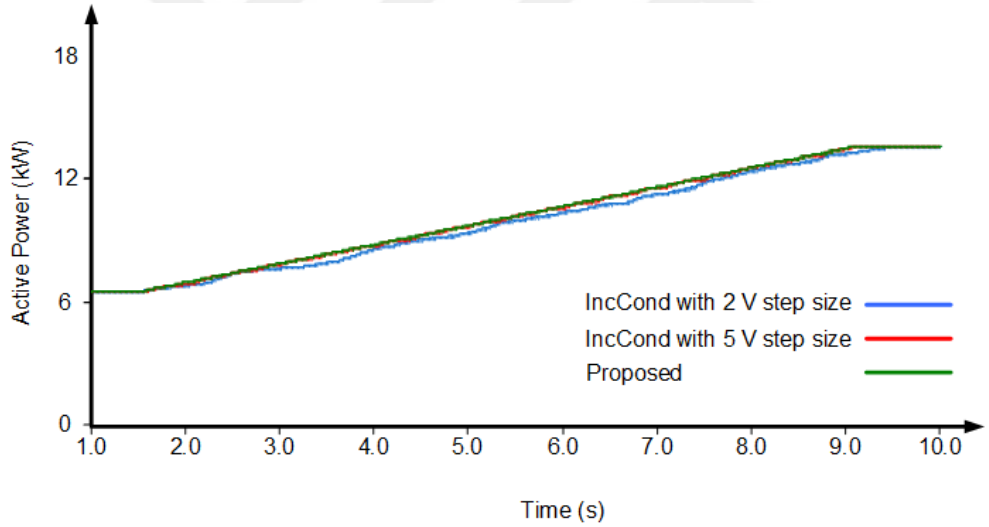

Figure 3.24. Extracted power from PV system by proposed and conventional fixed-step size IncCond method in case 2.

Case 3: In this case, the performance of the proposed variable-step size IncCond MPPT algorithm and conventional fixed-step size IncCond MPPT strategy with 2 *V* and 5 *V* step sizes are compared in the fast radiation changing condition. As shown in Figure 3.25 the solar radiation slowly changed (without

step change) in 1.5 *s* from 500 to 10000 W/m^2 at 0.163 *s*. Figures 3.26 represents the tracked MPP voltage by proposed and conventional MPPT algorithms. As shown in Figures 3.26 the proposed algorithm rapidly follows the MPP voltage. Also Figure 3.27 shows the extracted power by proposed and conventional MPPT algorithms. As seen from Figure 3.27 due to rapidly follows the MPP voltage, the proposed algorithm has better performance than conventional method in terms of MPPT. Compared with the conventional IncCond MPPT method, the proposed algorithm exhibits a good dynamic performance with small steady state oscillations. Moreover, the dynamic performance of the proposed algorithm is obviously faster than that of fixed step size method.

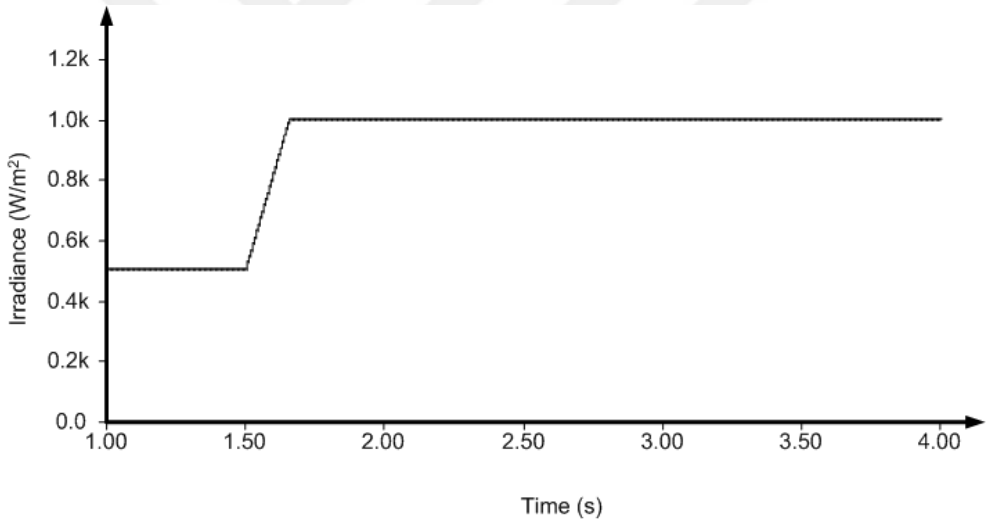

Figure 3.25. Solar radiation changing in case 3.

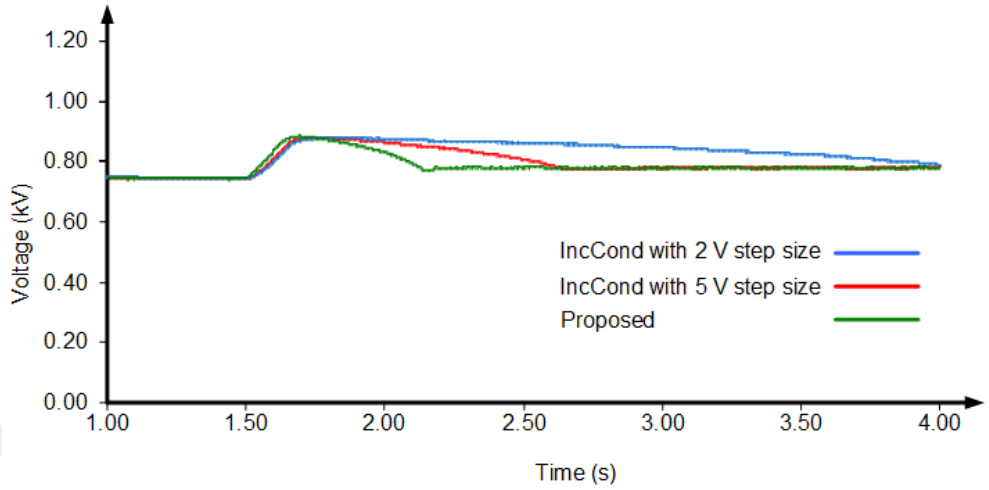

Figure 3.26. Tracked voltage by proposed and conventional fixed-step size IncCond method in case 3.

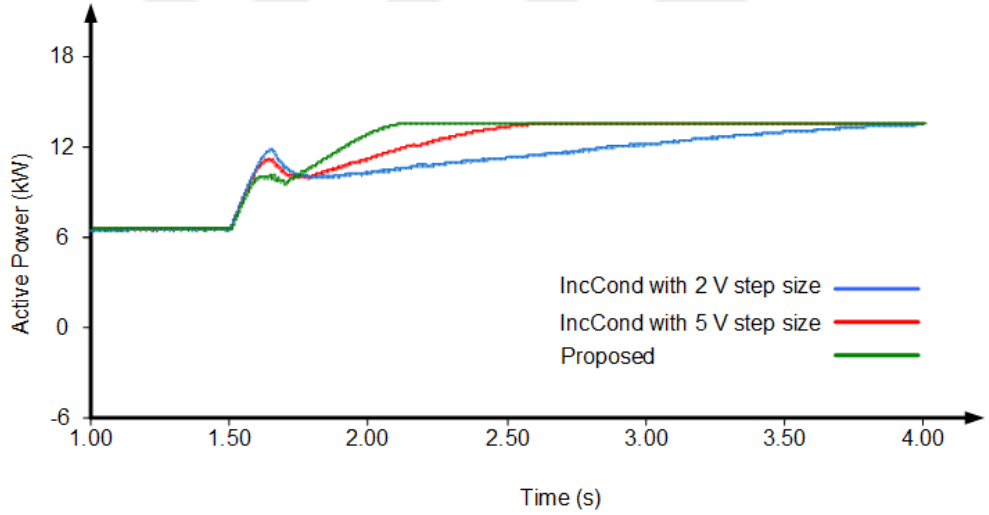

Figure 3.27. Extracted power from PV system by proposed and conventional fixed-step size IncCond method in case 3.

***Case 4*:** In this case, the performance of the proposed variable-step size IncCond MPPT algorithm and conventional fixed-step size IncCond MPPT strategy with 2 and 5 step sizes are compared when the solar radiation is changed as a sinusoidal function. As shown in Figure 3.28, the solar radiation change as a sinusoidal function between 500 and 10000 W/m^2. Figures 3.29 represent the

tracked MPP voltage by proposed and conventional MPPT algorithms. As shown in Figures 3.29 the proposed algorithm rapidly follows the MPP voltage. Also Figure 3.30 shows the extracted power by proposed and conventional MPPT algorithms. As seen from Figure 3.30 due to rapidly follows the MPP voltage, the proposed algorithm has better performance than conventional method in terms of MPPT. Compared with the conventional IncCond MPPT method, the proposed algorithm exhibits a good dynamic performance with small steady state oscillations. Moreover, the dynamic performance of the proposed algorithm is obviously faster than that of fixed step size method. It should be noted that the black lines in the Figures 3.29 and 3.30 are the lines that should be followed by tracking algorithms.

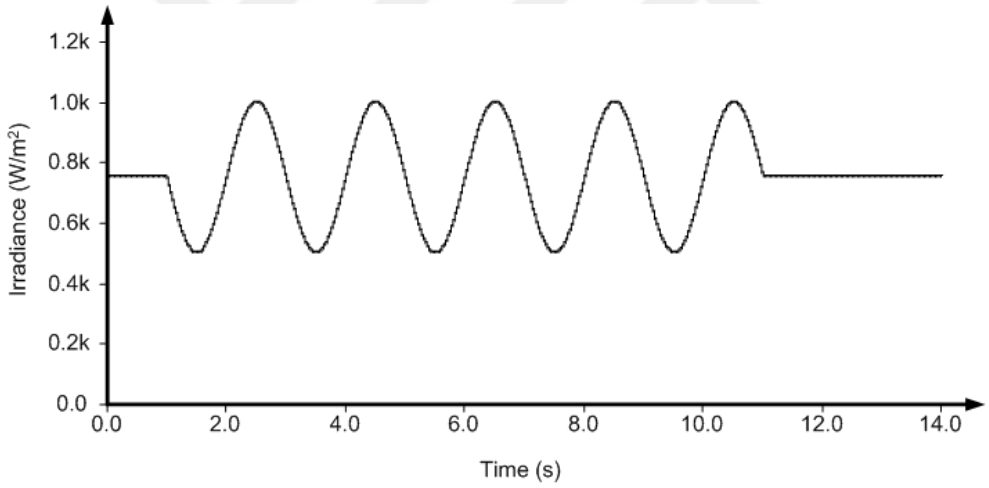

Figure 3.28. Solar radiation changing in case 4.

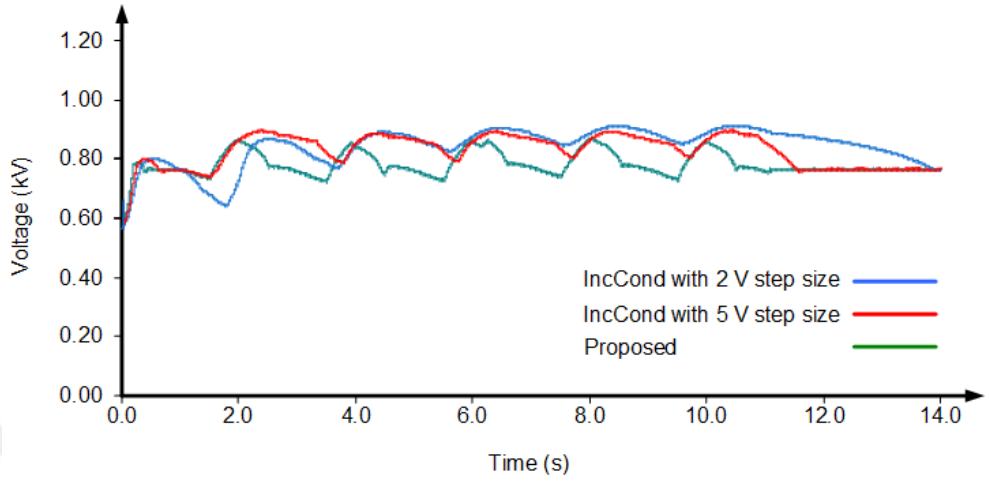

Figure 3.29. Tracked voltage by proposed and conventional fixed-step size IncCond method in case 4.

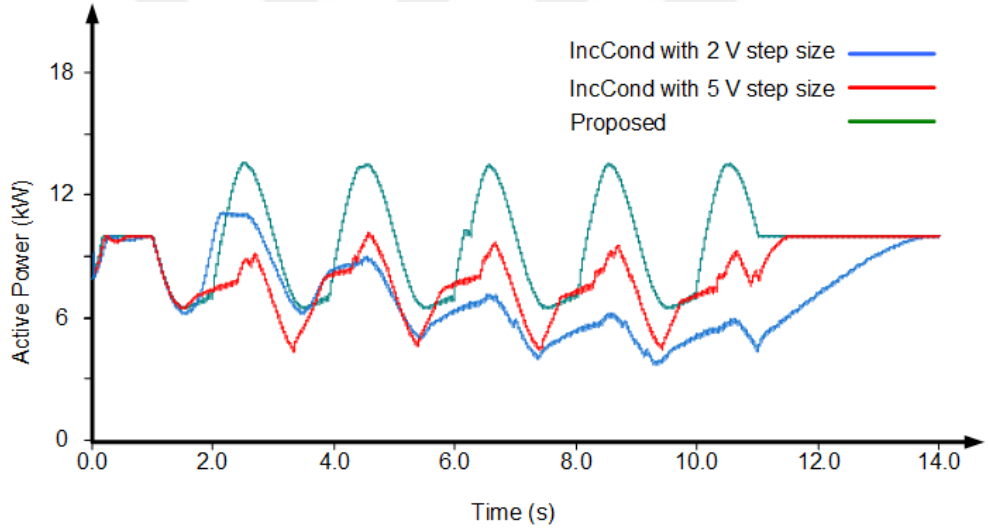

Figure 3.30. Extracted power from PV system by proposed and conventional fixed-step size IncCond method in case 4.

***Case 5*:** In this case, the performance of the proposed variable-step size IncCond MPPT algorithm examined in the PS condition and compared with conventional fixed-step size IncCond MPPT strategy with 2 *V* and 5 *V* step sizes. To carry out PS condition in the analyzed PV system, the modules insolation levels

shaped according to Figure 3.31. To execute a PS condition the modules insolation levels changed as Figure 3.32.

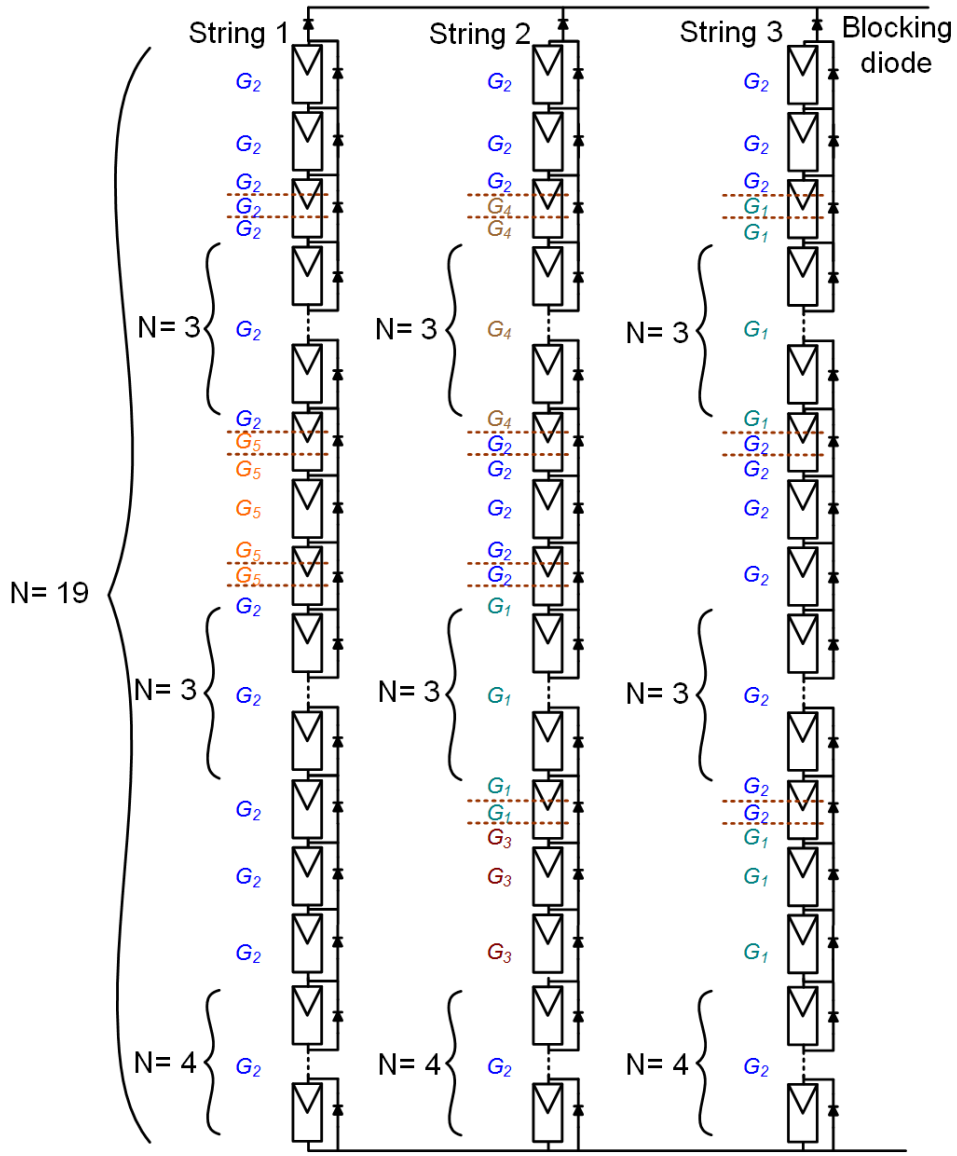

Figure 3.31. The arrangement of PV modules with various insolation levels to carry out PS condition in the analyzed PV system.

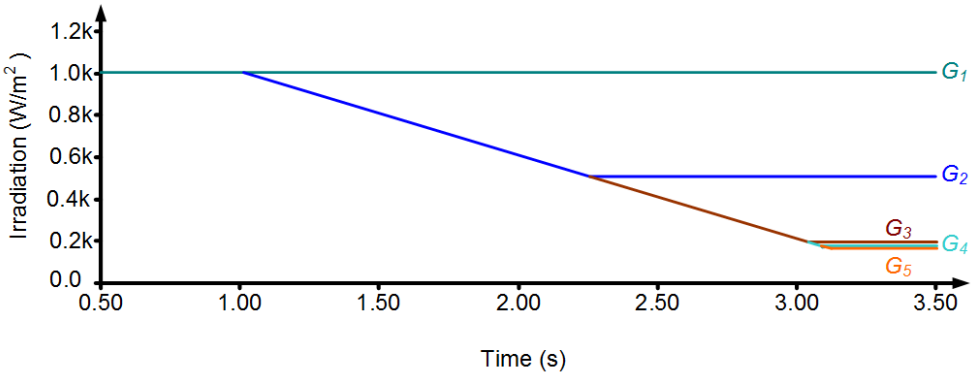

Figure 3.32. The changes of the radiation levels on the PV modules to execute PS condition in the analyzed PV system.

The *P-V* and *I-V* curves of under study PV system under PS condition according to PV modules arrangement and radiation levels, which are expressed in Table 3.2 and Figures 3.31 and 3.32, are clarified in Figures 3.33 and 3.34, respectively.

Table 3.2. Time dependence solar radiation levels on the PV modules

Time (*s*)	**Solar Radiation (W/m^2)**				
	G_1	G_2	G_3	G_4	G_5
t=1.00 s	1000	1000	1000	1000	1000
t=1.75 s	1000	750	750	750	750
t=2.26 s	1000	500	500	500	500
t=2.90 s	1000	500	250	250	250
t=3.20 s	1000	500	189	173	158

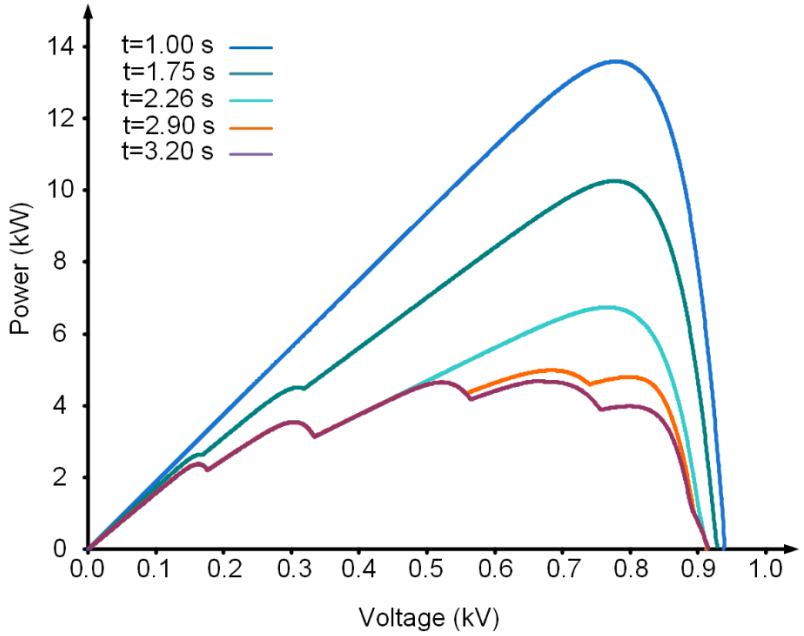

Figure 3.33. Under study PV system *P-V* curve's during PS condition.

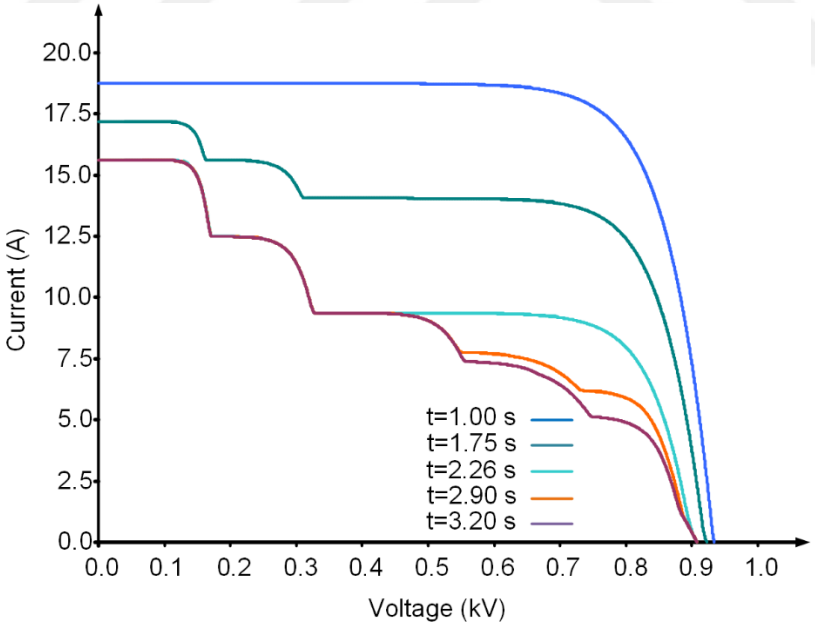

Figure 3.34. Under study PV system *I-V* curve's during PS condition.

As shown in Figures 3.35 the proposed algorithm exactly tracks the GMPP. However, conventional method cannot tracks the GMPP and the voltage of MPP be trapped at the local MPP. The injected current from PV system strings into system with the conventional and proposed algorithms is shown in Figures 3.36 and 3.37, respectively. As shown in Figures 3.36 and 3.37, versus to conventional method the PS detects with proposed method and operating voltage converge to GMPP voltage, hence the injected current from string 1 has increased. Also Figure 3.38 shows the extracted power by proposed and conventional MPPT algorithms during PS condition. As seen from Figure 3.38 due to rapidly tracks the exact GMPP voltage, the proposed algorithm has better performance than conventional method in terms of GMPPT.

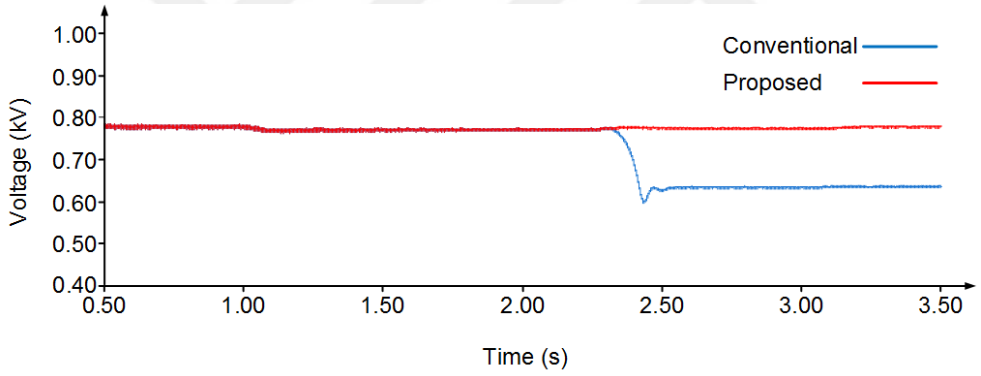

Figure 3.35. Tracked voltage by proposed and conventional fixed-step size IncCond method under PS condition.

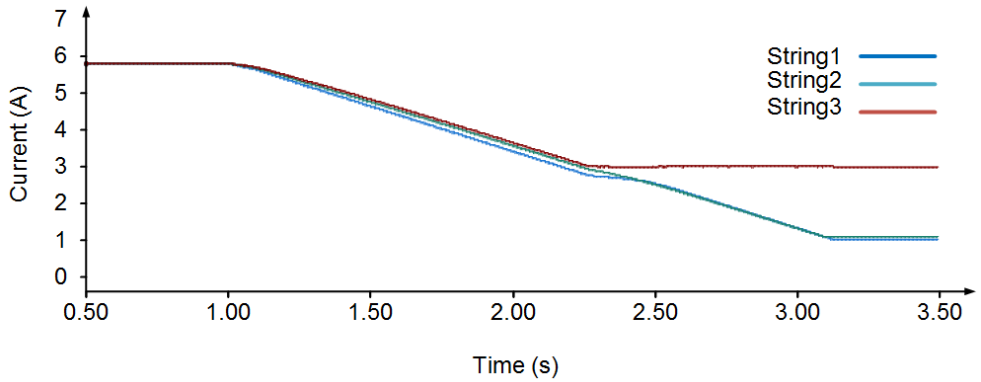

Figure 3.36. Extracted current from PV system by conventional fixed-step size IncCond method under PS condition.

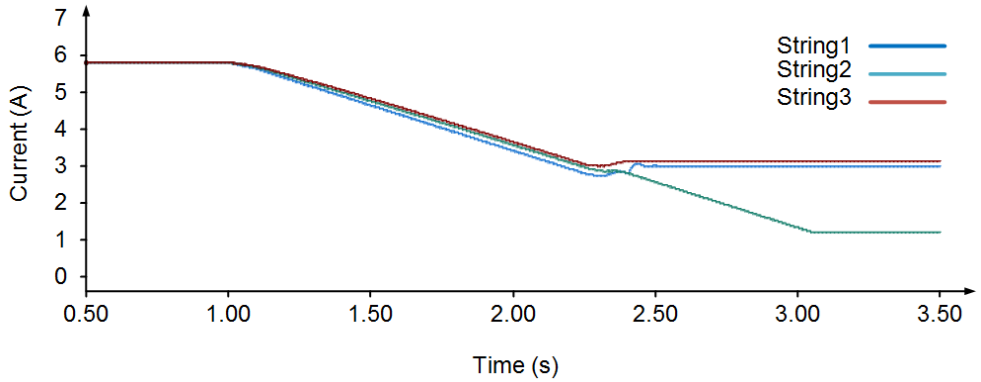

Figure 3.37. Extracted current by proposed method under PS condition.

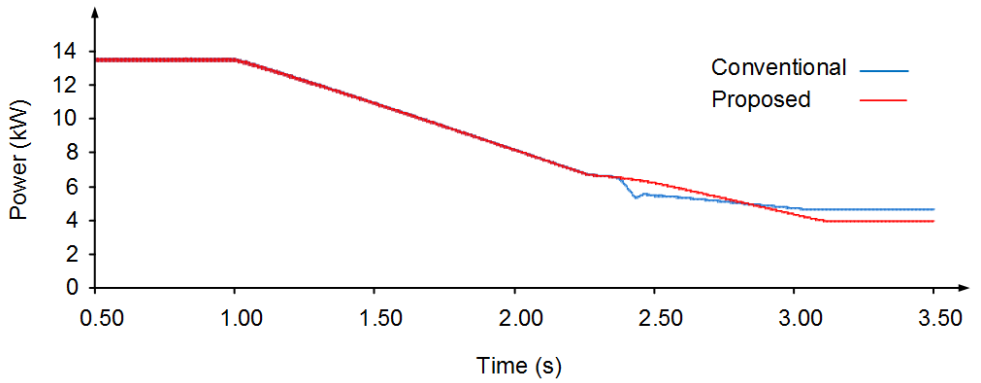

Figure 3.38. Extracted power by proposed and conventional fixed-step size IncCond method under PS condition.

3.6. Summary

In this chapter, a detailed analysis of the physical structure of solar cells and their *I-V* and *P-V* characteristics has been presented. Due to changing of output power from PV arrays with atmospheric condition changing the implementation of the MPPT control strategy becomes indispensable condition to extract maximum power from the PV arrays have been represented. Moreover, the necessities of the GMPPT algorithm to track maximum power during PS conditions have been outlined. Thus, the proposed algorithm and details the techniques used to improve its efficiency especially under unstable atmospheric conditions presented in this chapter. It starts by introducing a new rule for modifying the step size in IncCond MPPT algorithm. Then, it describes the methods used to overcome the problems of rapidly as well as slowly changing atmospheric conditions and PS. This chapter is concluded by the flow chart of the proposed algorithm.

Furthermore, simulation results of the proposed variable step size IncCond MPPT algorithm have been presented. The simulations were run in EMTDC/PSCAD environment, where the response of the proposed algorithm has been analyzed under several irradiation schemes. The results have been compared to the responses of conventional IncCond MPPT algorithm, showing the improvements in transient, dynamic, and steady-state responses. Moreover, the dynamic performance of the proposed algorithm is obviously faster than that of fixed step size method. Moreover, the proposed algorithm tested in the PS condition. Finally it presents the simulation results which are illustrates the significantly improvements in the MPPT process in comparison to conventional algorithm under different atmospheric conditions.

4. MULTILEVEL MULTIFUNCTIONAL GRID CONNECTED INVERTER

The incremental demand for electrical energy and recent technological advances are leading a growth in the prevalence of RES systems. In addition to enhance the general performance of electrical power systems the installation of new RES systems aims to obtaining a profit. In other words, installing new RES systems, besides being economically profitable, can improve the stability, security, reliability and quality of the given power system and reduce power loss owing to energy transport and distribution. However, potential benefits of installing new RES systems depend on making perfect decisions about how many RES systems should be installed on power system, which types of RES systems are the most suitable, where they should be connected to electric power system and which generation capacity is the most suitable (Caamaño-Martín et al., 2008), (Habibi et al., 2013), (Torrent-Fontbona et al., 2016).

Solar PVs are on a fast track of technological development. Innovations in material science research have led to newer generations of PV cells that promise much higher efficiency and lower cost in the future. Advances in PV technology and incentive policies for deployment of RESs have significantly increased the capacity of installed PV systems. During the last decade, grid connected PV systems in the range of megawatt have been installed and currently are operational all over the world (Moradi-Shahrbabak et al., 2014), (Wu et al., 2015).

The capacities of PV plants are continuously growing with the increasing popularity of PV systems. In this context, the installed capacity and application of photovoltaic energy systems is increasing. Additionally, by increasing the number of utilized photovoltaic systems, new control methods must be developed for the proper operation and management of new power grid embedded with PV units to improve or maintain the system reliability, stability and quality. Since the

connection of photovoltaic systems to the power system network is a very important issue, power electronics and intelligent technologies play an important role in the operation of PV systems (Alonso et al., 2003), (Bhusal et al., 2007), (Laaksonen and Mohamed, 2008), (Arai et al., 2008), (Akorede et al., 2010), (Salam et al., 2010).

In practice, due to non-controllable and stochastic nature of the solar energy the output power from PV systems is intrinsically unstable. Therefore, from the network-wise point of view it can lead to many problems due to increasing the number of installed PV systems in the distribution system. This situation can pose a threat to PQ, voltage regulation and balance issues in the power system network. Hence, the provision of PQ standards, electromagnetic compatibility, acoustic noise limits, safety and protection requirements are important issues for PV systems. Hence, in the interlinking of the PV plants with the power system network, it is necessary to comply with various standards given by the utility companies. These standards deal with topics such as interconnection issues, operation principles and issues related to PQ, stability, reliability, safety, etc. In addition, some of these standards define the structure and properties of existing and future PV panels (Carrasco et al., 2006).

As well as, the existing of the nonlinear and unbalance loads in distribution systems can cause various PQ problems for MGs. Nevertheless, a MG should be able to operate under this situation without any performance degradations (Paridari et al., 2013). However, hosting capacity of the grid may significantly reduce compared to free PQ problems and balanced system (Meyer et al., 2011).

Therefore, the existing distribution networks have been constructed without consideration for RES connection (Toma et al., 2008). However, current local controls such as voltage regulators, load tap changers and capacitor banks will not be enough once the penetration level of RES systems exceeds the hosting capacity of the utility grid as well as due to mechanical limitations cannot provide

timely responses to the rapid fluctuation and these devices are unable to adapt to the dynamic nature of RESs and load profiles (Zafar and Ravishankar, 2016). The inability of managing PQ has caused RES spillage in industrial practice, which inevitably delays the development of a flexible sustainable power system (Cheng et al., 2016). The drive towards to overcome this problems may result in simultaneous installation of DGs and APQCs in power systems. The APQC devices can be used to performance criterion improvement of power systems such as minimize the active and reactive power losses, reduce overall cost of the system, provide flexible control and operation, enhance overall efficiency and reliability of the system, increase hosting capacity of the system, improve PQ of the system, increase the loadability of the systems, relieved transmission and distribution congestion, reduction of power system oscillations, increase power transfer capability of the system, reducing greenhouse gas emissions, provide reactive power supporting in emergency situation such as under fault condition, sudden change in field excitation of alternators or load increase in power systems. These DG systems and APQCs have the potential to interact with each other. This situation may either improve or deteriorate power system stability and reliability depending upon the chosen control strategies, size and installed location of DG systems and APQCs. The various interactions can potentially arise between the DG systems and APQCs, as well as, between multiple APQCs in power system. These likely interactions can be classified into different frequency ranges and various interaction problems between DG systems and APQCs or between multiple APQCs. However due to circulating current between DGs and APQCs in local power system network, the individual performance of DG systems as well as APQCs can be distorted. So that the entire power systems performances with DG systems and APQCs are also distorted. It is known as interaction problem that occur between DG systems and APQCs in power systems. This situation is disadvantages of simultaneous operation of DG systems incorporated with APQCs in power systems. Thereby, the

effect of these interaction problems needs to minimize in the power systems (Singh et al., 2015).

APQCs have the same power converter stage of renewable energy based grid connected inverters. Thus these stages can be multiplexed. Power converter stage of a grid connected inverters can be utilized to realize the functionalities of the grid connected inverter and the PQ conditioners, as well as, Volt-VAr control compared with multiple devices with different individually in dependent functionalities. Therefore, there just a little modification in control algorithm is needed to change the conventional grid connected inverters into multifunctional grid connected inverters by providing multifunctional operation. This will provide an increase in system stability, a decrease in the investment and maintenance costs and an ease in the system operation (Sannino et al., 2003).

Thus, PV systems can be effectively controlled to improve the power quality, reliability, stability and efficiency of existed system by application of advanced power electronics, enforcement of MPPT methods and utilization of intelligent control techniques. Although the main goal of PV systems is to obtain active power; static synchronous compensator and active power filter functionality can be realized. PV systems can be interfaced with the power system network either in series or parallel position. However, the target compensated quantities, such as harmonics, unbalance, and reactive power, are directly related to the currents. As such, the parallel type architecture is widely utilized because it effectively injects compensating currents at PCC (Kumar and, Rao, 2012.).

Conventional six-pulse is widely used in grid connected PV systems, regardless of the disadvantages such as low-quality output voltage waveforms and high switching losses. These conventional inverters have normally to meet grid codes and stringent standards owing to the use of a high switching frequency. However, this situation cause increased voltage stresses and high switching losses,

dv/dt, etc. However, this may not always be possible to meet grid codes and strict standards such as at the light load conditions whereas current THD is high (Azmi et al., 2013). Otherwise, large scale grid-connected PV systems need higher power inverters (Balamurugan et al., 2017). As an alternative to two level inverters, multilevel inverters are considered as efficient alternatives to high-power applications, presenting a high-quality output voltage, while increasing the efficiency, robustness, and lowering the electromagnetic interference (Mortezaei et al., 2017). These advantages come at the cost of an intelligent control scheme which is allows to independently control of active and reactive power, regulation and balancing of capacitor voltage, control of DC bus voltage, along with circulating currents that are set according to the balancing targets (Steurer et al., 2016).

In medium and high power applications, multilevel inverter technology is a very efficient alternative as the heart of interfacing systems for integration of PV systems into utility grid. The superior harmonic spectrum, decreased voltage rating for the switches, decreased common mode voltages and lesser voltage changes (*dv/dt*) are important advantages of multilevel inverters. However, the complexity of control method rises compared to the traditional two-level inverter. ML-MFGCIs are new breed of power converter used in large scale PV applications and have superior advantages such as lower switching power dissipation, lower harmonic distortion and lower EMI outputs. ML-MFGCIs perform the high quality power from PV systems and provide flexible functionality with improved power PQ, voltage and reactive power support and increased capability of the auxiliary service for the utility grid (Barghi-Latran and Teke, 2015).

In this context, a control algorithm proposed for a PV based multifunctional neutral point clamped multilevel inverter to simultaneously maintain high-quality power transfer exchange between PV systems and the utility grid in disturbed grids and perform simultaneous mitigation of PQ problems using novel control

algorithm. Furthermore, ML-MFGCI used as single stage arrangement to produces optimum power and operates at the maximum proficiency.

4.1. Neutral point clamped Multilevel Inverter

Three level neutral point clamped multifunctional grid connected inverter (NPC-MFGCI) is principally comprised of double two-level VSIs stacked one over the other. As shown in Figure 4.1, the negative point of the upper inverter and the positive point of the lower one are assembled together to constitute the new phase output, while to make the neutral point *n*, the initial phase outputs are connected via two clamping diodes. Each power switch has to block solely half of the entire inverter voltage; hence the power rating of the inverter can be doubled. NPC-MFGCI topology can be expanded to more output voltage levels and higher power rates by adding additional power switches and clamping diodes to be able to block higher voltages (Rodrı´guez et al., 2009).

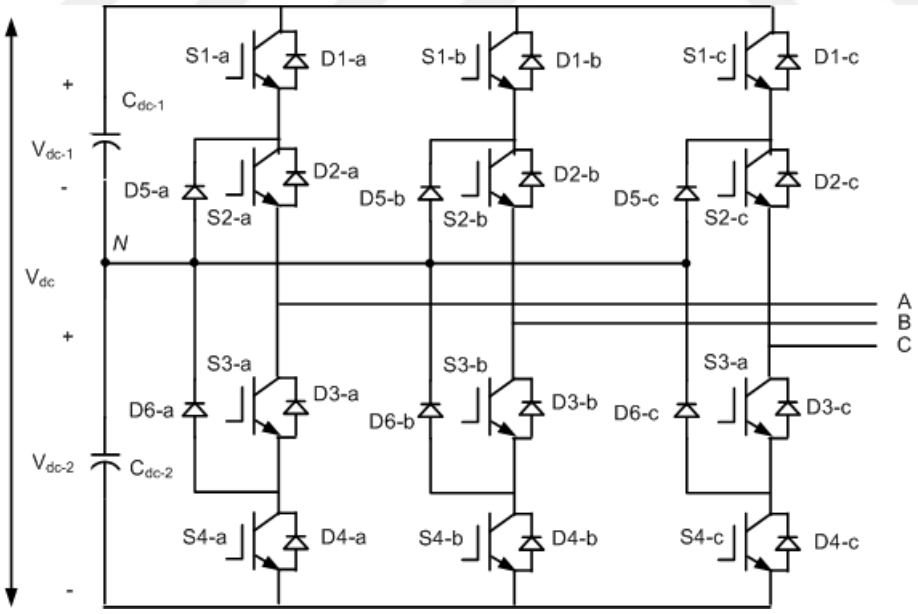

Figure 4.1. Three-phase three-level NPC inverter.

Here the name diode clamped makes more sense, since there are more voltage-level clamping nodes than only the neutral *N* (Rodrı´guez et al., 2009). The clamping diodes need completely different voltage ratings for reverse voltage blocking because each triggered switch is required to block a voltage level of $V_{dc}/(n-1)$. The number of diodes needed for each phase can be calculated as $(n-1)\times(n-2)$, where *n* represents the levels of inverter. In DC-MFGCI, if *n* is assumed as the numbers of levels, the number of capacitors (*C*) used in diode clamped side can be calculated by Eq. (4.1). The per phase number of freewheeling diodes (*fd*), and the number of clamping diodes (*cd*) can be determined by Eqs. (4.2) and (4.3).

$$C=n-1 \tag{4.1}$$

$$fd=2(n-1) \tag{4.2}$$

$$cd=(n-1)\times(n-2) \tag{4.3}$$

Diode clamped multilevel inverters are efficient in applications operating at fundamental frequency switching. However, the number of clamping diodes needed is quadratically associated with the number of output voltage levels (Colak et al., 2011).

The main circuit topology of the three levels NPC-MLI shown in Figure 4.1. Possible converter switching positions for three-phase three level inverter can be calculated as (Zhukov, 2012):

$$N_{sw}=n^m=3^3=27 \tag{4.4}$$

All these switching positions correspond to the three possible states of each inverter phase leg. Thus, independently of two other phases each phase terminal of the inverter can be connected to DC bus in the three terminal points: upper positive

'$+V_{DC}/2$' DC rail, neutral '0' point or lower negative '$-V_{DC}/2$' DC rail (Zhukov, 2012).

Figure 4.2 demonstrates when IGBTs S2 and S3 are switched on. Upper neutral point clamp diode D5 and IGBT S2 are conducting so that the phase output and the DC bus midpoint are connected with positive phase current. The output is connected to the midpoint with negative phase current when the current flows through IGBT S3 and lower neutral-point-clamp diode D6. IGBTs S3 and S4 are switched on with negative phase current in Figure 3 (c). The negative phase current goes either through IGBT switches S1 and S2 or inverse diodes D3 and D4. The phase is connected to positive or negative DC bus, respectively (Hämäläinen, 2015).

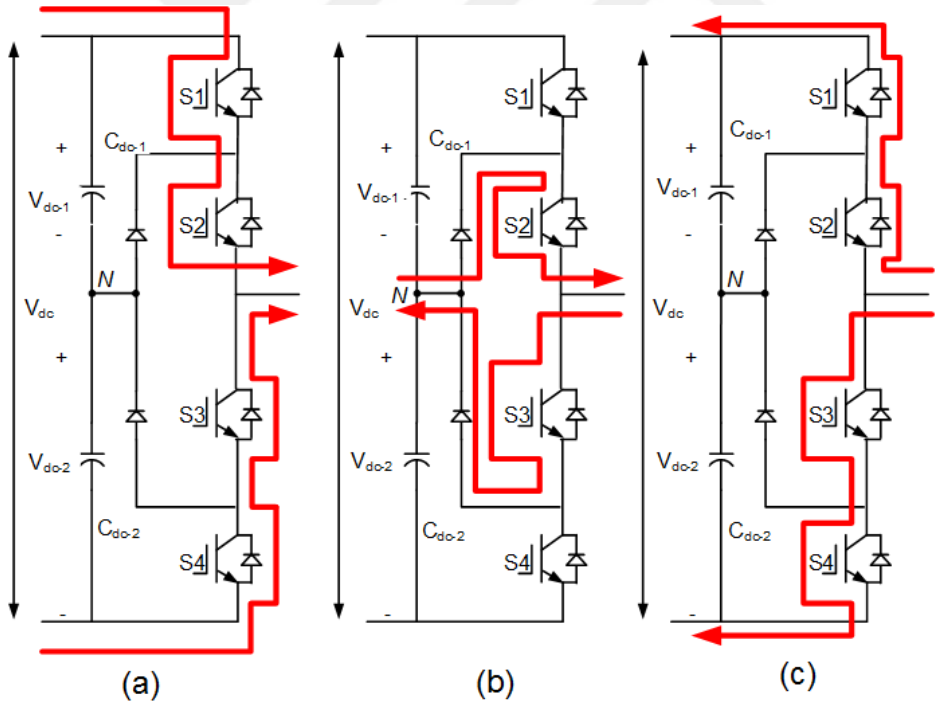

Figure 4.2. (a) IGBTs S1 and S2 are switched on with positive phase current. (b) IGBTs S2 and S3 are switched on. (c) IGBTs S3 and S4 are switched on with negative phase current.

For a three-level three-phase NPC VSI, there are twenty-seven switching states that represent the connections of the output terminals (a, b and c) to their respective DC-link points. The output voltages of NPC inverter can be determined using Eqs. (4.5) and (4.6) (Meng-Yeong, 2009).

$$\begin{aligned} V_{as} &= (2/3).V_{DC}\left[m_{a1} - m_{a3} - (1/2)\left(m_{b1} - m_{b3} + m_{c1} - m_{c3}\right)\right] \\ V_{bs} &= (2/3).V_{DC}\left[m_{b1} - m_{b3} - (1/2)\left(m_{a1} - m_{a3} + m_{c1} - m_{c3}\right)\right] \\ V_{cs} &= (2/3).V_{DC}\left[m_{c1} - m_{c3} - (1/2)\left(m_{b1} - m_{b3} + m_{a1} - m_{a3}\right)\right] \end{aligned} \tag{4.5}$$

$$\begin{aligned} V_{ab} &= V_{ao} - V_{bo} = V_{DC}\left[m_{a1} - m_{a3} - m_{b1} + m_{b3}\right] \\ V_{bc} &= V_{bo} - V_{co} = V_{DC}\left[m_{b1} - m_{b3} - m_{c1} + m_{c3}\right] \\ V_{ca} &= V_{co} - V_{ao} = V_{DC}\left[m_{c1} - m_{c3} - m_{a1} + m_{a3}\right] \end{aligned} \tag{4.6}$$

There are several benefits and drawbacks with NPC MLIs. The addition of clamping diodes in the NPC structure allows the system *kVA* rating to be increased due to an increased *DC* bus voltage, while keeping the switching device voltage stress at acceptable levels. Additionally, purely reactive power transfer can be made and controlled without affecting the balance of the capacitor voltages, however active power control, e.g. grid connected applications, is difficult using this type of inverter. There are also some negative consequences regarding the current ratings of the active switching devices. If the NPC inverter is designed for worst case scenarios, then the *2(m -2)* outer switches will be oversized because the inner switches require longer conduction periods, especially at a low switching frequency and/or modulation index. If designing for average duty, the inner switches may be undersized. The capacitors require pre-charge circuitry to limit the

capacitor current when energizing the dc bus. In contrast, all three phases of the NPC MLI utilize the same capacitor bank, which can prove detrimental to the entire system if the dc bus becomes defective. A distinct advantage of the ML-VSI is the fact that the common mode voltage step height decreases as the number of levels of the inverter increase (Somogyi, 2015).

4.2. Control of the neutral point clamped multilevel multifunctional inverter

Figure 4.3 shows the system configuration of the proposed ML-MFGCI which is based on a three-phase 3-level neutral point clamped multilevel inverter, using IGBT switches connected in parallel with the utility grid and an LCL filter to eliminate the high frequency harmonics which are injected from ML-MFGCI into utility grid.

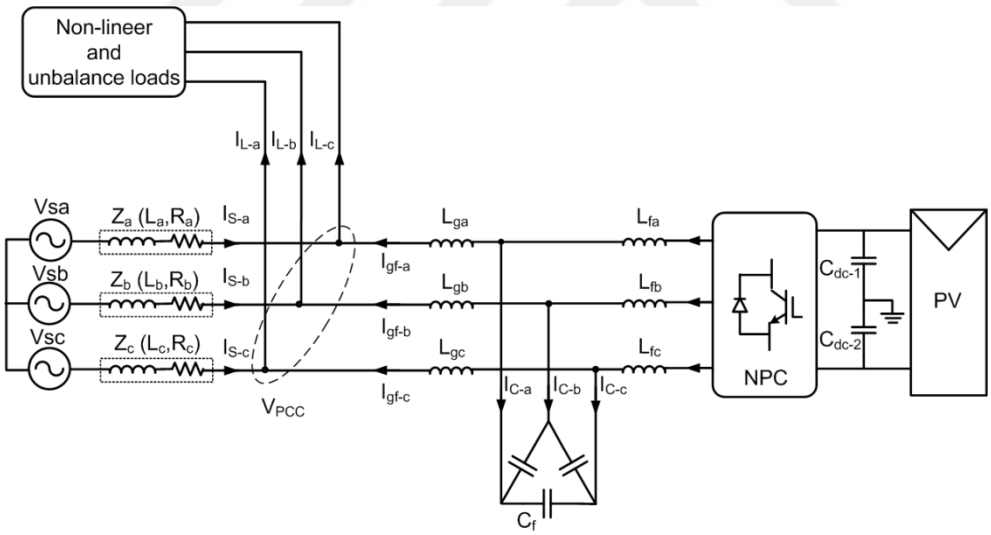

Figure 4.3. The scheme of LCL-filtered NPC base ML-MFGCI.

To explain the physical meaning of multi-objective control algorithm in the LCL-filtered ML-MFGCI with active resonance damping capability, the average and small-signal models are derived with mathematical expressions in following

subsections. It can be seen that the direct and quadrature channels of average equivalent circuit are coupled by two voltage-controlled current sources and four current-controlled voltage sources. Figure 4.4 shows the single-phase equivalent circuit of the presented *LCL*-filtered ML-MFGCI (Wang et al., 2013).

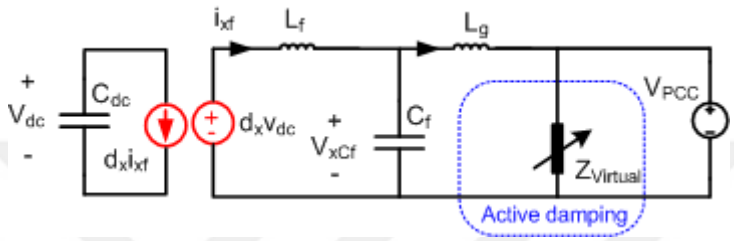

Figure 4.4. Single-phase equivalent circuit of the LCL-filtered ML-MFGCI with active resonance damping.

A. Average Model of LCL-filtered ML-MFGCI with active resonance damping

In Figure 4.4, the terminal voltages of the LCL filtered ML-MFGCI can be expressed as average duty cycles and inverter DC link voltage as Eq. (4.7).

$$\begin{bmatrix} V_a \\ V_b \\ V_c \end{bmatrix} = \begin{bmatrix} d_a \\ d_b \\ d_c \end{bmatrix} \cdot V_{dc} \tag{4.7}$$

where, V_a, V_b, and V_c are the ML-MFGCI 's output phase voltages and d_a, d_b, and d_c are the average duty cycle functions of inverter for each phase. To actively damp the resonance in the *LCL* filter, the capacitor current is sensed and subtracted from modulation signal through a damping gain K_d. According to Figure 4.4, the average equivalent circuit model of each phase can be written as (Wang et al., 2013):

$$\frac{d}{dt}\begin{bmatrix} I_{af} \\ I_{bf} \\ I_{cf} \end{bmatrix} = \frac{v_{dc}}{L_f}\begin{bmatrix} d_a \\ d_b \\ d_c \end{bmatrix} - \frac{1}{L_f} V_{C_f} \tag{4.8}$$

$$\frac{d}{dt}\begin{bmatrix} v_{acf} \\ v_{bcf} \\ v_{ccf} \end{bmatrix} = \frac{1}{C_f}\begin{bmatrix} I_{af} \\ I_{bf} \\ I_{cf} \end{bmatrix} - \frac{1}{C_f}\begin{bmatrix} I_{ag} \\ I_{bg} \\ I_{cg} \end{bmatrix} \tag{4.9}$$

$$\frac{d}{dt}\begin{bmatrix} I_{ag} \\ I_{bg} \\ I_{cg} \end{bmatrix} = \frac{1}{L_g} V_{C_f} - \frac{1}{L_g}\begin{bmatrix} v_{ag} \\ v_{bg} \\ v_{cg} \end{bmatrix} - \frac{1}{L_g}\begin{bmatrix} I_{af} - I_{ag} \\ I_{bf} - I_{bg} \\ I_{cf} - I_{cg} \end{bmatrix} \cdot K_d \tag{4.10}$$

By transforming the average equivalent model of the system from stationary *abc* frame to synchronous rotating *dq* frame using single phase park transform Eqs. (4.11), (4.12), the single phase direct and quadrature components of the average equivalent model can represented by Eqs. (4.13)-(4.16), where ω is the grid angular frequency and the subscript *x* represents the average equivalent model variables (Wang et al., 2013).

$$\begin{bmatrix} I_{a\alpha} \\ I_{a\beta} \end{bmatrix} = \begin{bmatrix} I_a(\omega t + \varphi) \\ I_a\left(\omega t + \varphi + \frac{\pi}{2}\right) \end{bmatrix} \tag{4.11}$$

$$\begin{bmatrix} I_{ad} \\ I_{aq} \end{bmatrix} = \begin{bmatrix} \sin(\omega t) & -\cos(\omega t) \\ \cos(\omega t) & \sin(\omega t) \end{bmatrix} \begin{bmatrix} I_{a\alpha} \\ I_{a\beta} \end{bmatrix} \tag{4.12}$$

$$\frac{d}{dt}\begin{bmatrix} I_{df} \\ I_{qf} \end{bmatrix} = \begin{bmatrix} \frac{1}{L_f} & 0 \\ 0 & \frac{1}{L_f} \end{bmatrix} \cdot v_{dc} \cdot \begin{bmatrix} d_d \\ d_q \end{bmatrix} - \begin{bmatrix} \frac{1}{L_f} & 0 \\ 0 & \frac{1}{L_f} \end{bmatrix} \begin{bmatrix} v_{dc_f} \\ v_{qc_f} \end{bmatrix} + \omega \begin{bmatrix} I_{qf} \\ -I_{df} \end{bmatrix} \tag{4.13}$$

$$\frac{d}{dt}\begin{bmatrix} I_{dg} \\ I_{qg} \end{bmatrix} = \begin{bmatrix} \frac{1}{L_g} & 0 \\ 0 & \frac{1}{L_g} \end{bmatrix} \cdot \begin{bmatrix} v_{dc_f} \\ v_{qc_f} \end{bmatrix} - \begin{bmatrix} \frac{1}{L_g} & 0 \\ 0 & \frac{1}{L_g} \end{bmatrix} \begin{bmatrix} v_{dPCC} \\ v_{qPCC} \end{bmatrix} + \omega \begin{bmatrix} I_{qg} \\ -I_{dg} \end{bmatrix} - \begin{bmatrix} \frac{1}{L_g} & 0 \\ 0 & \frac{1}{L_g} \end{bmatrix} \begin{bmatrix} I_{df} - I_{dg} \\ I_{qf} - I_{qg} \end{bmatrix} . K_d \tag{4.14}$$

$$\frac{d}{dt}\begin{bmatrix} V_{dc_f} \\ V_{qc_f} \end{bmatrix} = \frac{1}{C_f}\begin{bmatrix} I_{df} \\ I_{qf} \end{bmatrix} - \frac{1}{C_f}\begin{bmatrix} I_{dg} \\ I_{qg} \end{bmatrix} + \omega \begin{bmatrix} V_{qc_f} \\ -V_{dc_f} \end{bmatrix} \tag{4.15}$$

$$\frac{d}{dt} V_{dc} = -\frac{1}{C_f}\begin{bmatrix} d_d \\ d_q \end{bmatrix} \begin{bmatrix} I_{df} \\ I_{qf} \end{bmatrix} \tag{4.16}$$

Figure 4.5 shows the average equivalent model of the system with active resonance damping in synchronous reference frame (SRF). The direct and

quadrature components are coupled by four current controlled voltage sources and four voltage controlled current sources (Wang et al., 2013).

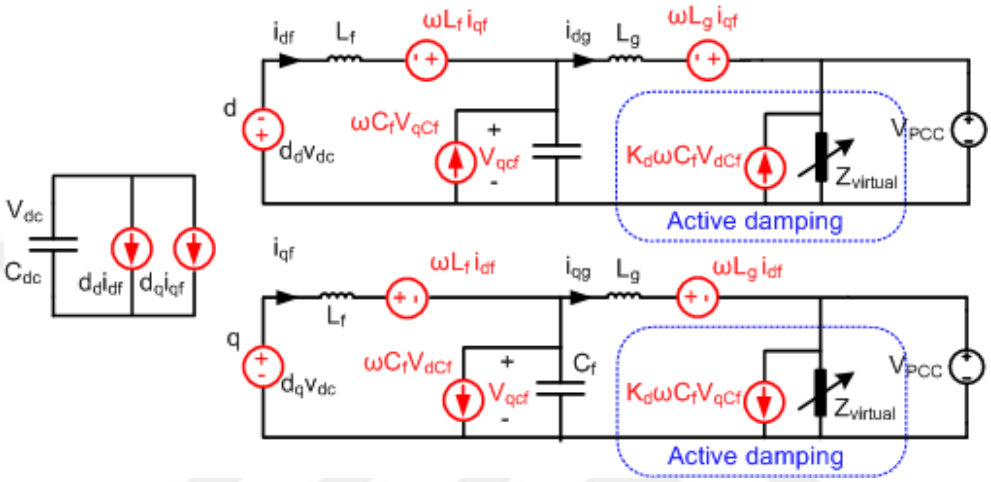

Figure 4.5. The average equivalent model of the LCL-filtered ML-MFGCI with active resonance damping in SRF.

B. Small-signal Model LCL filtered ML-MFGCI with active resonance damping

The small-signal model of the system with active resonance damping can be achieved with perturbing the average equivalent model of the system around the DC set point, as Eq. (4.17). In Eq. (4.17) X and $\hat{x}$ represents the DC set point and the small-signal terms of the averaged x variable, respectively (Wang et al., 2013).

$$\bar{x} = X + \hat{x}$$

(4.17)

The state-space model of the *LCL*-filtered inverter with active resonance damping can be expressed by Eqs. (4.18)-(4.24).

$$\frac{d}{dt}X = A \cdot X + B \cdot U \tag{4.18}$$

$$Y = C \cdot X + D \cdot U \tag{4.19}$$

$$Y = X = \left[\hat{I}_{df} \quad \hat{I}_{qf} \quad \hat{I}_{dg} \quad \hat{I}_{qg} \quad \hat{v}_{dc_f} \quad \hat{v}_{qc_f} \quad \hat{v}_{dc} \right]^T \tag{4.20}$$

$$U = \left[\hat{d}_d \quad \hat{d}_q \quad \hat{v}_{dg} \quad \hat{v}_{qg} \right]^T \tag{4.21}$$

$$A = \begin{bmatrix} 0 & \omega & 0 & 0 & \frac{-1}{L_f} & 0 & \frac{D_d}{L_f} \\ -\omega & 0 & 0 & 0 & 0 & \frac{-1}{L_f} & \frac{D_q}{L_f} \\ \frac{-K_d}{L_g} & 0 & \frac{K_d}{L_g} & \omega & \frac{1}{L_g} & 0 & 0 \\ 0 & \frac{-K_d}{L_g} & -\omega & \frac{K_d}{L_g} & 0 & \frac{1}{L_g} & 0 \\ \frac{1}{C_f} & 0 & \frac{-1}{C_f} & 0 & 0 & \omega & 0 \\ 0 & \frac{1}{C_f} & 0 & \frac{-1}{C_f} & -\omega & 0 & 0 \\ \frac{-D_d}{C_{dc}} & \frac{-D_q}{C_{dc}} & 0 & 0 & 0 & 0 & 0 \end{bmatrix} \tag{4.22}$$

$$B = \begin{bmatrix} \frac{v_{dc}}{L_f} & 0 & 0 & 0 \\ 0 & \frac{v_{dc}}{L_f} & 0 & 0 \\ 0 & 0 & \frac{-1}{L_g} & 0 \\ 0 & 0 & 0 & \frac{-1}{L_g} \\ 0 & 0 & 0 & 0 \\ 0 & 0 & 0 & 0 \\ \frac{-i_{df}}{C_{dc}} & \frac{-i_{qf}}{C_{dc}} & 0 & 0 \end{bmatrix} \quad (4.23)$$

$$C = I \quad (4.24)$$

$$D = 0 \quad (4.25)$$

According to Eqs. (4.18)-(4.25), the small-signal model of *LCL*-filtered inverter with active resonance damping can be represented by Figure 4.5 (Wang et al., 2013)..

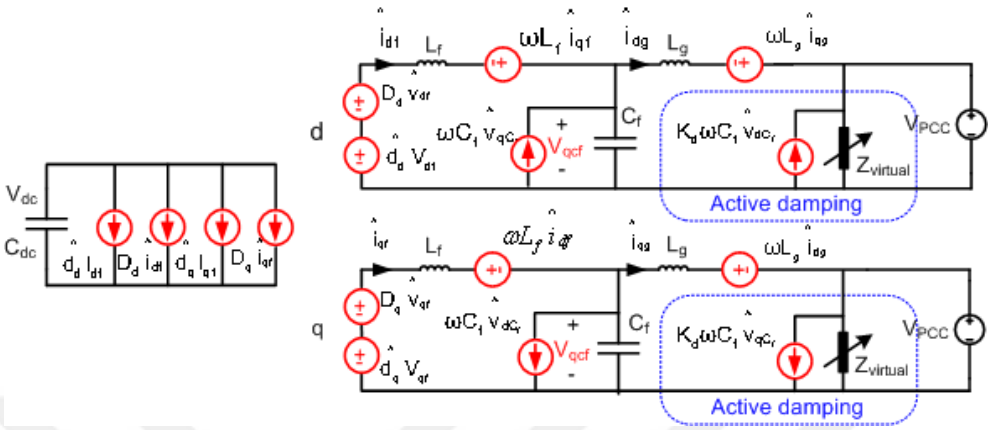

Figure 4.6. Small-signal model of the LCL-filtered ML-MFGCI with active resonance damping.

4.2.1. Extraction of the Reference Voltage and Current Signals Under Unbalance and Distorted Signals

The main objectives of the proposed control algorithm for ML-MFGCI are to achieve balanced and less harmonics source currents by compensating distorted unbalanced load currents as well as to inject the active power from PV system into utility grid. Other objectives of proposed control are compensating the reactive power, voltage sag/swells as well as voltage regulation. In general, the distribution voltage is generally unbalanced and distorted with harmonics. For reactive power compensation the balanced phase angle of phase voltages should be determined. Moreover, for voltage sag/swells compensation as well as voltage regulation the symmetric fundamental component of the phase voltages should be determined. In order to generate the balanced reference voltage and currents to control the ML-MFGCI under distorted and unbalanced conditions, a balanced and less harmonics set of voltage ad currents needs to be extracted.

In order to mitigate quality problems related to the current, it is necessary to generate reference signals for the current and to be synchronized with the power system. The synchronous reference frame (SRF) method is used to separate the

active and reactive components of the current. Thus, these components can be controlled independently of each other. The AC components of current expressed as DC components in SRF and make the control process simpler (Li et al., 2012). The block diagram of the SRF based reference signal generation (RSG) is shown in Figure 4.3. To extract the fundamental component of signals an Enhanced Phase Locked Loop Quadrature Signals Generator (EPLL-QSG) based Positive-sequence Component Detector (PCD) is utilized. As shown in Figure 4.7, the PCD is divided into three parts: The first step transforms the signals into the stationary reference frame (Iα, Iβ). The next step uses an EPLL-QSG block which contains two EPLL-QSG blocks to filter out harmonics and achieve the 90-degrees shifted signals of Iα and Iβ. The block diagram of EPLL is shown in Figure 4.8.

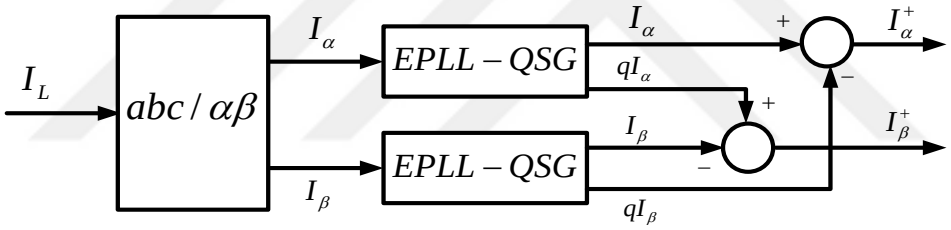

Figure 4.7. Enhanced Phase Locked Loop Quadrature Signals Generator based Positive-sequence Component Detector.

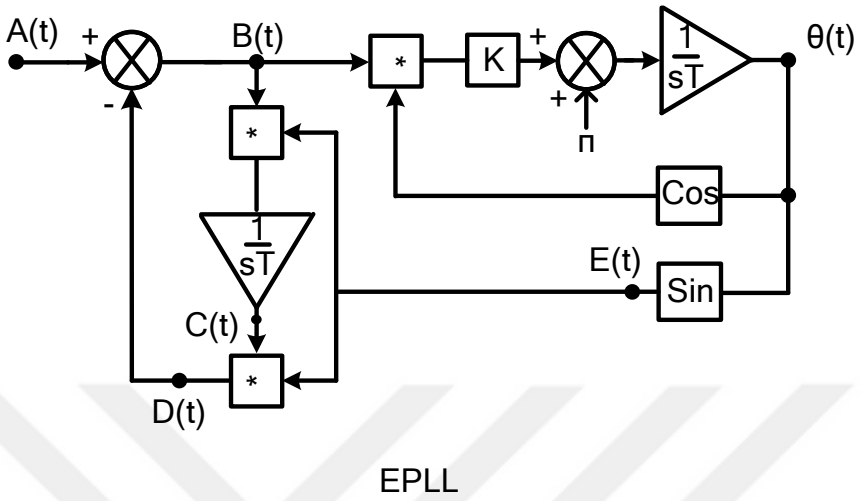

Figure 4.8. The block diagram of the enhanced phase locked loop.

As shown in Figure 4.8 the EPLL receives the input signal *A(t)* (supply voltage or load current) and provides an on-line estimate of the following signals:

(1) *B(t)*, the difference of input and the synchronized fundamental component.
(2) *C(t)*, the amplitude of D(t).
(3) *D(t)*, the synchronized fundamental component.
(4) *E(t)*, PLL signal.
(5) *θ(t)*, the phase angle of D(t).

$$B(t) = A(t) - k_2 t \tag{4.26}$$

$$\theta(t) = \cos\theta(t) - \left(-\frac{A}{\omega}\cos\omega t - \frac{k_2}{2} t \right) \tag{4.27}$$

$$E(t) = \sin\left(\cos\theta(t) - \left(-\frac{A}{\omega}\cos\omega t - \frac{k_2}{2} t \right) + \pi t \right) \tag{4.28}$$

$$C(t) = -\frac{k_3 A}{\omega}\cos\omega t - \frac{k_2 k_3}{2}t^2 \tag{4.29}$$

$$D(t) = C(t)\sin\left(-\frac{C(t)}{k_3} + \pi t\right) \tag{4.30}$$

There exists a compromise between speed and accuracy. For large K_1, K_2 and K_3, the convergence of the estimated values to actual values is faster and the steady state misadjustment is higher. This is an inherent characteristic of an adaptive algorithm. Parameters K_1, K_2 and K_3 ought to be selected appropriately according to the application. If only the total "flicker content" of a signal is to be extracted, then the filter can be set to operate in an alternative mode. In this mode, the filter is set to operate at a low speed to track only the fundamental signal and not the flicker. The result is that the smooth "averaged" fundamental is extracted on the output and the total distortion signal at the error terminal.

In the next step of PCD process to calculate the instantaneous positive-sequence of the fundamental frequency component of the I_α and I_β signals, as Eq. (4.31) the positive-sequence calculator (PSC) can be used .

$$I^{+}_{F\alpha,F\beta} = \frac{1}{2}\begin{bmatrix} 1 & -q \\ q & 1 \end{bmatrix} I_{F\alpha,F\beta} \tag{4.31}$$

where

$$q = e^{-j\frac{\pi}{2}} \tag{4.32}$$

As shown in Figure 4.9, to achieve the current control, the extracted fundamental frequency component of the positive-sequence of the I_α and I_β signals convert to synchronous reference frame by using the Eq. (4.32).

$$\begin{bmatrix} I_d \\ I_q \end{bmatrix} = \frac{2}{3}\begin{bmatrix} \cos\theta & \sin\theta \\ -\sin\theta & \cos\theta \end{bmatrix}\begin{bmatrix} I_\alpha \\ I_\beta \end{bmatrix} \tag{4.32}$$

To control the PCC voltage and as well as reactive power compensation, the positive-sequence fundamental voltage signals are transformed into the synchronous reference frame with positive-sequence fundamental voltages phase angle. The quadrature component of the transfer voltage signals gives the amplitude of positive-sequence fundamental voltage signal. The quadrature component of the positive-sequence fundamental voltage signal is compared with nominal phase voltage amplitude and the difference of this value is passed through a PI regulator. The output signal of PI regulator is compared with quadrature component of the current and the difference of these two values makes the quadrature component of the compensation signal. In the other hand, to regulate the inverter DC voltages of the multilevel inverter, to compensate the current harmonics and load unbalances and active power injection from PV system into utility grid, the DC capacitor voltage is compared with reference DC voltage and the differences is passed through PI regulators. The output signal of the PI regulators is compared with direct component of positive-sequence fundamental current signal and make the direct component of the compensation signal. In the next step, the generated direct and quadrature compensation signals are transfer into ABC frame with related positive-sequence fundamental voltage phase angle. In the final step, the ABC frame current signals are passed through a Chebyshev low pass filter.

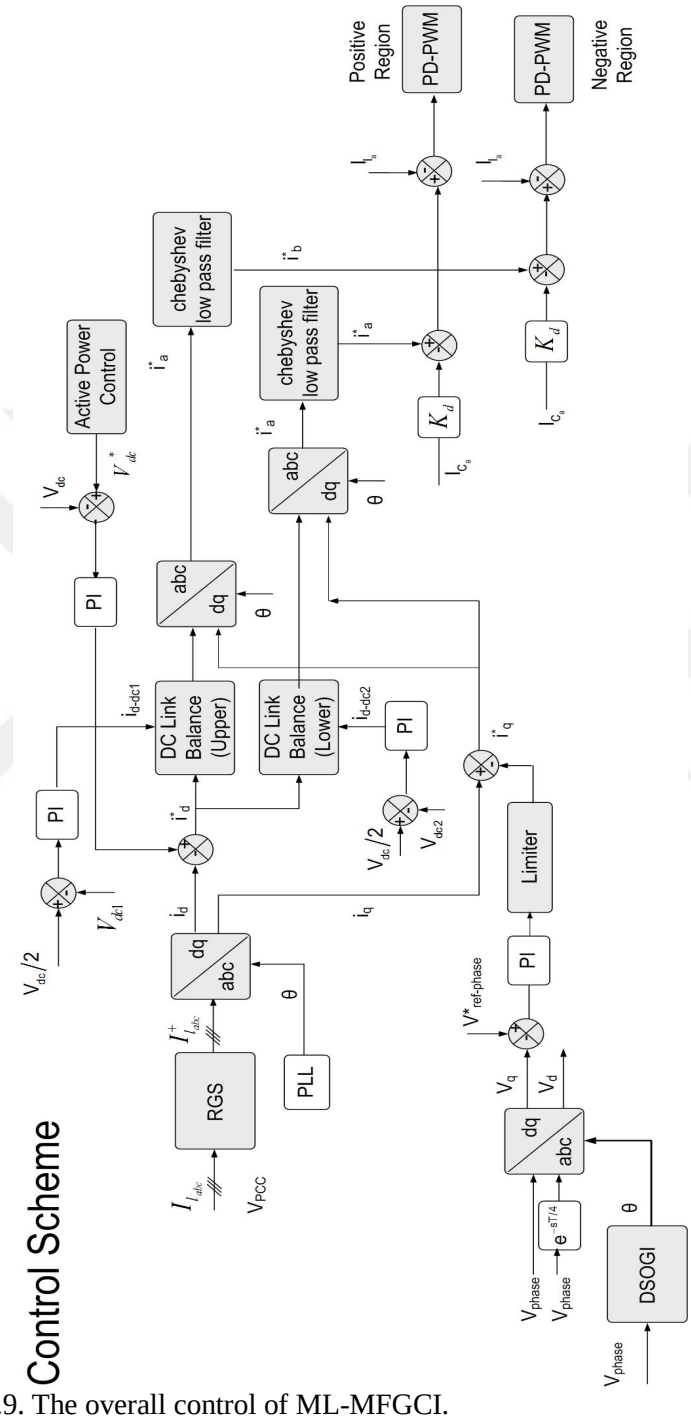

Figure 4.9. The overall control of ML-MFGCI.

As seen from Figure 4.9 the overall control strategy of the proposed ML-MFGCI is based on the generated current reference (I^{+}_{la}, I^{+}_{lb}, I^{+}_{lc}) signals and the common DC bus voltage (V_{DC}). Furthermore, in order to obtain the desired compensation performance as well as to transfer the active power from PV system to utility grid, three PI controller are used to control the DC link voltages for active power control in balance DC link capacitors voltage. This function is obtained by changing the reference voltage of the DC bus capacitors. Under normal conditions, the DC voltage set to MPPT voltage determined by the MPPT. During the voltage sag or over voltage, the ML-MFGCI should inject reactive power into power system to clear voltage swell or voltage over voltage. So during these faults, the inverter capacity needs to be adjusted to inject requirement reactive power into power system without exceeding ML-MFGCI nominal capacity. Thus to prevent active power injection into utility grid the produced energy by PV system must be reduced. Therefore, as shown in Figure 4.10, if the operating voltage of the PV system is brought closer to the open circuit voltage, the energy generated by the PV system will decrease. To balance the DC bus capacitors voltages the Eqs. (4.32) and (4.33) are developed to prevent common mode voltage and compensation of neutral current.

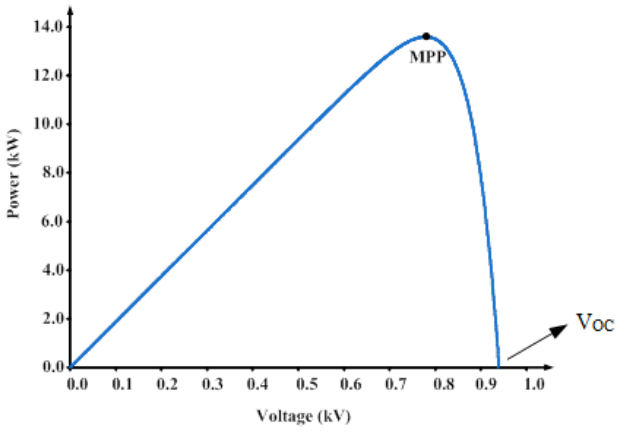

Figure 4.10. *P-V* characteristic curve of the PV system.

$$\begin{cases} i_d^* + i_{d-dc1} & for \quad i_d^* \geq 0 \\ i_d^* - i_{d-dc1} & for \quad i_d^* < 0 \end{cases} \tag{4.32}$$

$$\begin{cases} i_d^* + i_{d-dc2} & for \quad i_d^* \geq 0 \\ i_d^* - i_{d-dc2} & for \quad i_d^* < 0 \end{cases} \tag{4.33}$$

4.3. Results

The proposed ML-MFGCI can be used in three modes. The first mode is the normal inverter mode and active power from PV arrays into power system as well as compensates reactive power is injected. The second mode is the APQC mode and only the existing PQ problems according to control algorithm is compensated. The third mode is the multifunctional mode and active power from PV system into power system is injected and PQ problems are compensated. Figure 4.11 shows the scheme of power system and ML-MFGCI arrangement which used to verify the proposed control algorithm for NL-MFGCI in various load and power quality transient condition. The system test parameters are listed in Table 4.1.

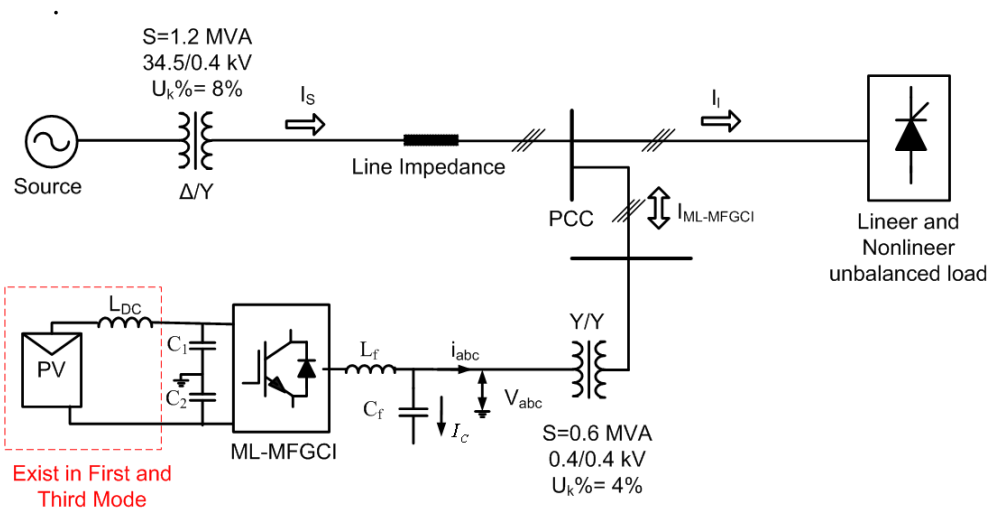

Figure 4.11. The scheme of studied power system with ML-MFGCI arrangement.

Table 4.1. System Test Parameters

System Parameters	**Value**
Power System Parameters	
Mains Voltage/Frequency	230 V_{RMS} (Phase to Neutral), 50 Hz
Feeder impedance	Z_F = 0.008 + j0.0078 Ω
ML-MFGI Parameters	
Nominal Capacity	S = 0.6 MVA
DC Link Voltage (Varies According to MPPT voltage)	V_{dc} = 680 V
DC Link Capacitors	C_{dc1} = C_{dc2}= 0.2 F
Switching Frequency	f_{sw} = 5 kHz
LCL filter	L_{ff} = 50 µH, L_{Tr} = 30 µH, C_f = 300 µF (R=10 Ω in the passive damping)
Resonance Frequency of Filter	f_{res} = 2 kHz
PV System Capacity	S_{FV} = 0.5 MW
Control System Parameters	**Value**
PI Controller to Control Overall DC Link Voltage	
Proportional Gain	30
Integral Time Constant	0.005 s
PI Controllers to Control Upper and Lower Capacitors Voltage	
Proportional Gain	1
Integral Time Constant	0.1 s
PI Controllers to Control the PCC Phase Voltages	
Proportional Gain	10
Integral Time Constant	0.0001 s
PSCAD/EMTDC Parameters	**Value**
Solution Time	15 µs
Chanel Plot Step	100 µs
Duration of Simulation Run	5 s

Case 1: To verify the efficiency of the first mode control algorithm, the performance of the ML-MFGCI is tested for the unbalanced power system which is distorted with harmonics. In the first mode major challenge is the interlinking of the inverter with worse power system in terms of power quality, stability and reliability. In most case of the existing PQ problems such as harmonic and unbalances in the current or voltage leads incorrect inverter operation. If the control algorithm of the inverter not prepared for these situations it injects unbalance current with the inclusion of harmonics. Hence the proposed control algorithm used to control of the inverter for first mode under distorted and unbalanced system. Figure 4.12 shows the PCC phase voltage waveforms of under study heavy loaded system with high level voltage/current harmonic distortion and load unbalance problems.

The RMS value of fundamental component of the phase voltages for phase *A*, *B* and *C* with 230.11 V_{RMS} positive and 4.52 V_{RMS} negative sequence components are 226.4 V_{RMS}, 234.14 V_{RMS} and 230.2 V_{RMS}, respectively.

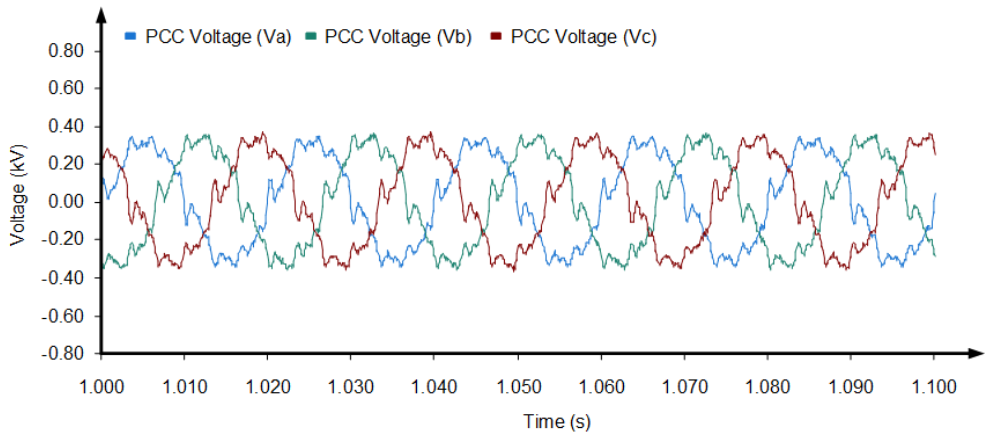

Figure 4.12. The PCC phase voltage waveforms with high harmonic distortion and load unbalance problems.

The distorted PCC phase voltages have 16.85%, 16.47% and 17.85% THD's in the phase *A*, *B* and *C*, respectively. The harmonic spectrum of the PCC phase voltages show is in the Figures 4.13, 4.14 and 415.

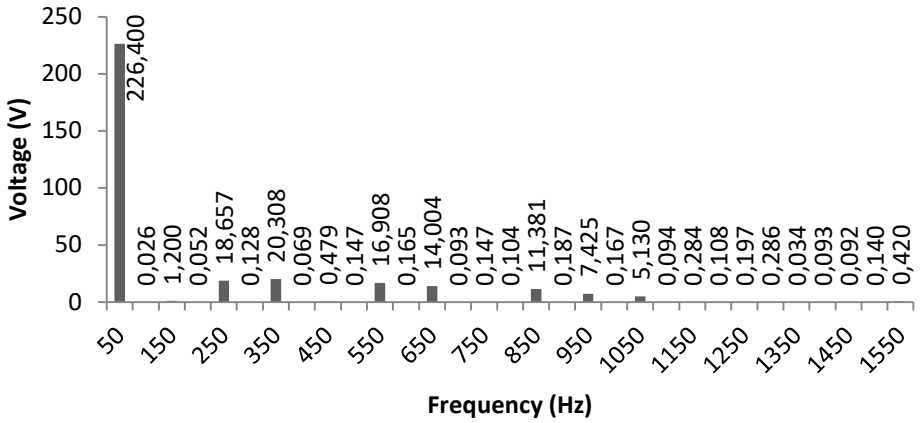

Figure 4.13. The harmonic spectrum of PCC voltage in phase *A* with high harmonic distortion and load unbalance problems.

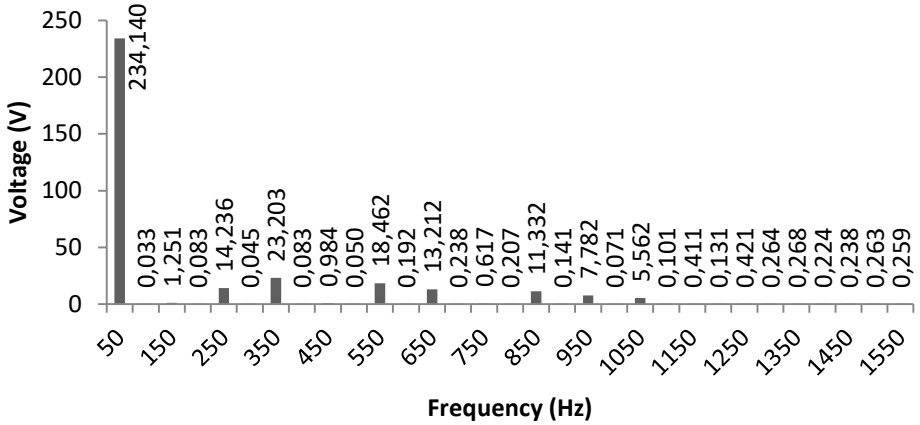

Figure 4.14. The harmonic spectrum of PCC voltage in phase *B* with high harmonic distortion and load unbalance problems.

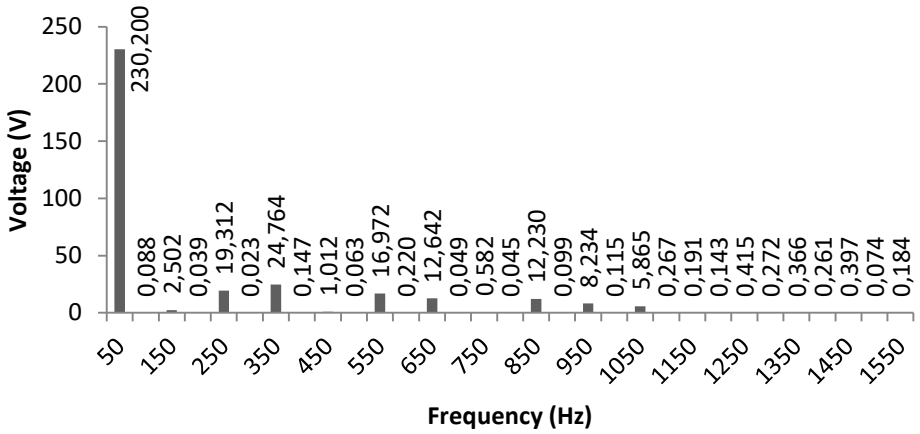

Figure 4.15. The harmonic spectrum of PCC voltage in phase *C* with high harmonic distortion and load unbalance problems.

The details of the PCC phase voltages harmonic content are illustrated in Table 4.2.

Table 4.2. Harmonic contents of PCC phase with high harmonic distortion and load unbalance problems.

	Harmonic Contents of PCC Voltage					
	Phase A		Phase B		Phase C	
Order	(%)	Value (V)	(%)	Value (V)	(%)	Value (V)
1	100.000	226.400	100.000	234.140	100.000	230.200
2	0.01140	0.02581	0.01426	0.03338	0.03828	0.08811
3	0.52986	1.19960	0.53436	1.25116	1.08702	2.50232
4	0.02314	0.05238	0.03564	0.08344	0.01711	0.03938
5	8.24094	18.6575	6.08017	14.2361	8.38918	19.3118
6	0.05651	0.12795	0.01915	0.04484	0.01008	0.02321
7	8.96989	20.3078	9.91009	23.2034	10.7576	24.7641
8	0.03028	0.06856	0.03527	0.08257	0.06394	0.14718
9	0.21163	0.47912	0.42038	0.98428	0.43974	1.01228
10	0.06512	0.14744	0.02155	0.05047	0.02756	0.06345
11	7.46825	16.9081	7.88520	18.4624	7.37291	16.9724
12	0.07306	0.16541	0.08216	0.19238	0.09565	0.22018
13	6.18545	14.0038	5.64258	13.2115	5.49169	12.6418
14	0.04128	0.09345	0.10165	0.23800	0.02149	0.04946
15	0.06482	0.14676	0.26342	0.61677	0.25297	0.58234
16	0.04581	0.10372	0.08835	0.20686	0.01934	0.04452
17	5.02684	11.3807	4.83987	11.3320	5.31292	12.2303
18	0.08246	0.18669	0.06002	0.14054	0.04292	0.09881
19	3.27961	7.42503	3.32383	7.78241	3.57678	8.23376
20	0.07369	0.16684	0.03053	0.07149	0.04999	0.11508
21	2.26575	5.12965	2.37548	5.56196	2.54762	5.86462
22	0.04157	0.09412	0.04326	0.10128	0.11583	0.26665
23	0.12563	0.28442	0.17557	0.41109	0.08299	0.19104
24	0.04789	0.10842	0.05596	0.13103	0.06193	0.14257
25	0.08679	0.19650	0.17977	0.42092	0.18024	0.41492
26	0.12629	0.28591	0.11255	0.26352	0.11803	0.27170
27	0.01510	0.03418	0.11433	0.26769	0.15881	0.36559
28	0.04128	0.09347	0.09578	0.22425	0.11344	0.26114
29	0.04081	0.09240	0.10185	0.23846	0.17261	0.39736
30	0.06195	0.14025	0.11216	0.26260	0.03205	0.07377
31	0.18567	0.42035	0.11048	0.25867	0.08012	0.18443
	THD=16.85%		THD=16.47%		THD=17.85%	

The load draws 1.498 *kA*, 1.405 *kA* and 1.618 *kA* in phase *A*, *B* and *C*, respectively. Due to unbalance loaded the load currents becomes unbalance and emerge a negative sequence current. The load current has 1.504 *kA* positive

sequence component and 0.1244 *kA* negative sequence component with 8.2% unbalance ratios in the load current. Figure 4.16 shows the load current waveforms under same condition.

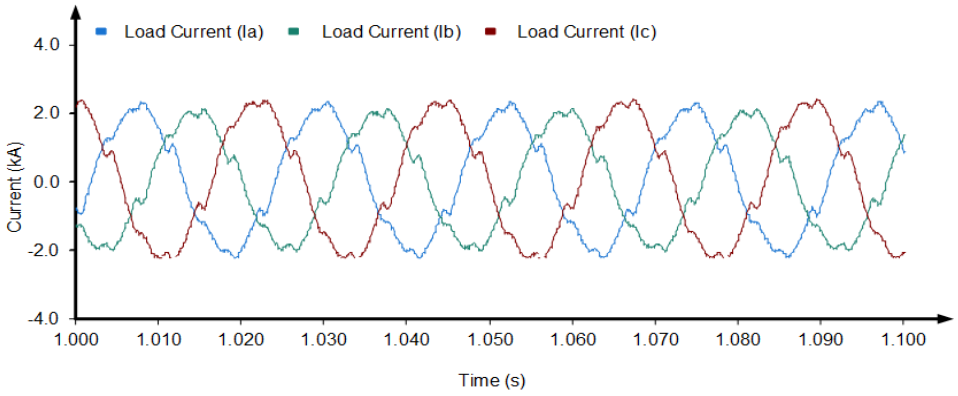

Figure 4.16. The load current waveforms with high harmonic distortion and load unbalance problems.

The load current have 9.4%, 9.5% and 9.2% THD's in the phase *A*, *B* and *C*, respectively. The harmonic spectrum of the PCC phase voltages show is in the Figures 4.17, 4.18 and 4.19.

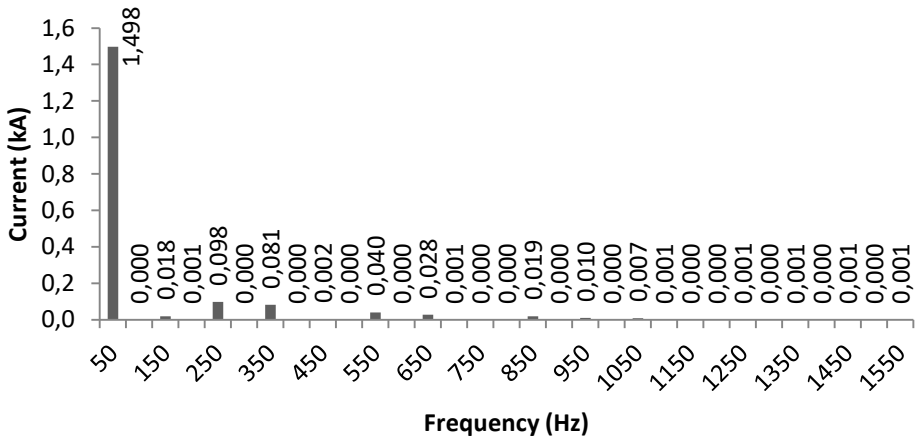

Figure 4.17. The harmonic spectrum of load current in phase *A* with high harmonic distortion and load unbalance problems.

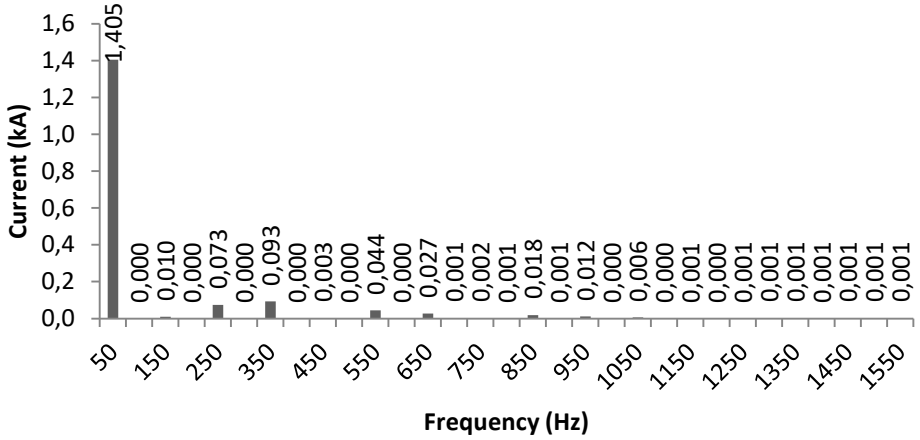

Figure 4.18. The harmonic spectrum of load current in phase *B* with high harmonic distortion and load unbalance problems.

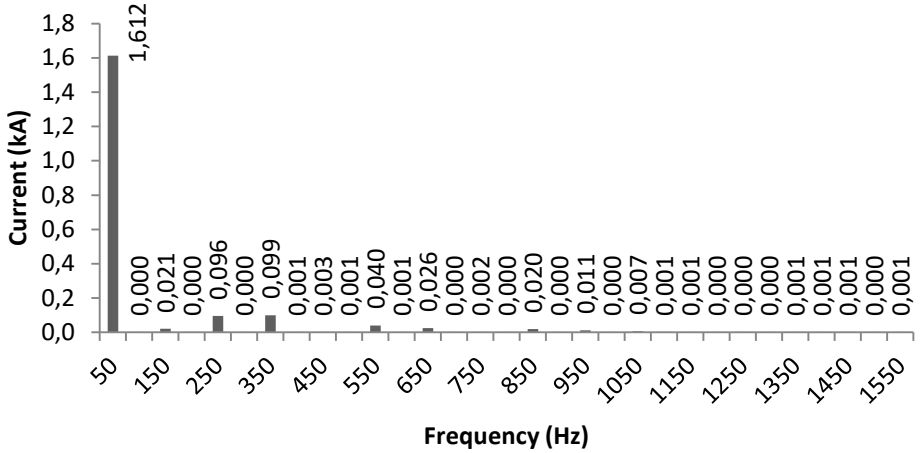

Figure 4.19. The harmonic spectrum of load current in phase *C* with high harmonic distortion and load unbalance problems.

The details of the load currents harmonic content are illustrated in Table 4.3.

Table 4.3. Harmonic contents of load current with high harmonic distortion and load unbalance problems.

	Harmonic Contents of Load Current					
	Phase A		Phase B		Phase C	
Order	(%)	Value (kA)	(%)	Value (kA)	(%)	Value (kA)
1	100.000	1.49800	100.000	1.40500	100.000	1.61180
2	0.02228	0.00033	0.00612	0.00009	0.01122	0.00018
3	1.20289	0.01802	0.69890	0.00982	1.30136	0.02106
4	0.04236	0.00063	0.02521	0.00035	0.01663	0.00027
5	6.55757	0.09823	5.21996	0.07334	5.92986	0.09595
6	0.02625	0.00039	0.01299	0.00018	0.01785	0.00029
7	5.43684	0.08144	6.61539	0.09295	6.09364	0.09860
8	0.01899	0.00028	0.01999	0.00028	0.03825	0.00062
9	0.10860	0.00163	0.22921	0.00322	0.18251	0.00295
10	0.00682	0.00010	0.00209	0.00003	0.03129	0.00051
11	2.70311	0.04049	3.14030	0.04412	2.49661	0.04040
12	0.02757	0.00041	0.03217	0.00045	0.04051	0.00066
13	1.84831	0.02769	1.89260	0.02659	1.58536	0.02565
14	0.03819	0.00057	0.07815	0.00110	0.00708	0.00011
15	0.00826	0.00012	0.13309	0.00187	0.11485	0.00186
16	0.02131	0.00032	0.04987	0.00070	0.01081	0.00017
17	1.24754	0.01869	1.27775	0.01795	1.24115	0.02008
18	0.00382	0.00006	0.06091	0.00086	0.01899	0.00031
19	0.65663	0.00984	0.84691	0.01190	0.70667	0.01143
20	0.02799	0.00042	0.02580	0.00036	0.02389	0.00039
21	0.47765	0.00716	0.45341	0.00637	0.42862	0.00694
22	0.04333	0.00065	0.01188	0.00017	0.03961	0.00064
23	0.01545	0.00023	0.03756	0.00053	0.03546	0.00057
24	0.02043	0.00031	0.02684	0.00038	0.01018	0.00016
25	0.06825	0.00102	0.04250	0.00060	0.02058	0.00033
26	0.00374	0.00006	0.05894	0.00083	0.02299	0.00037
27	0.06422	0.00096	0.07827	0.00110	0.03528	0.00057
28	0.00968	0.00014	0.03727	0.00052	0.04974	0.00080
29	0.08286	0.00124	0.08175	0.00115	0.09094	0.00147
30	0.01285	0.00019	0.06606	0.00093	0.02931	0.00047
31	0.06172	0.00092	0.07134	0.00100	0.05967	0.00097
	THD=9.4%		THD=9.5%		THD=9.2%	

Figure 4.20 shows the injected current from inverter into system. As seen from figure the injected current by inverter in distorted and unbalance system is pure sinusoidal. The RMS value of the injected current from PV linked inverter is

0.776 *kA* in phase *A*, 0.734 *kA* in phase *B* and 0.760 *kA* in phase *C*. the injected current have 0.734 *kA* positive sequence component and 0.015 *kA* negative sequence component with 2% unbalance ratio which is within in standards limits.

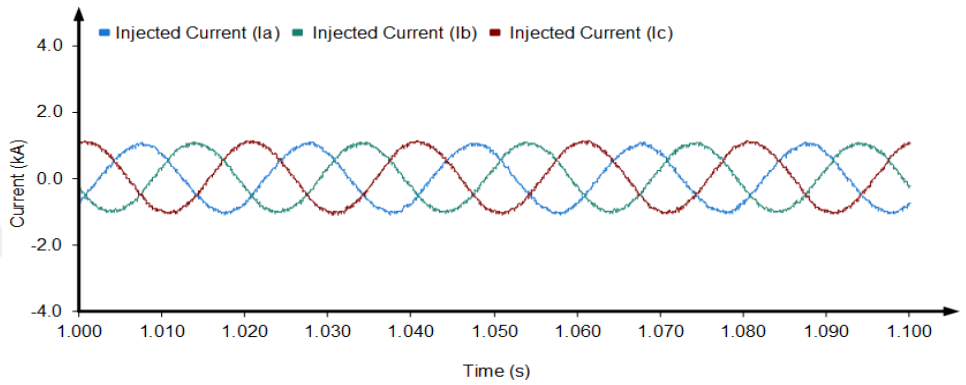

Figure 4.20. The injected current waveforms from PV linked inverter into power system in distorted and unbalance system.

The injected current have 2.3%, 2.24% and 2.1% THD's in the phase *A*, *B* and *C*, respectively. According to results the amounts of THD for injected current from PV linked inverter comply in standards limits. The harmonic spectrum of the PCC phase voltages show is in the Figures 4.21, 4.22 and 4.23.

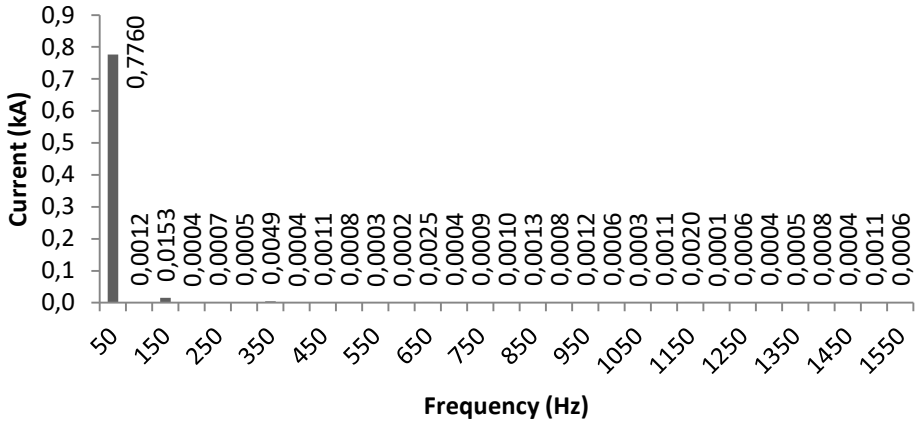

Figure 4.21. The harmonic spectrum of injected current by PV linked inverter in phase *A* with high harmonic distortion and load unbalance problems.

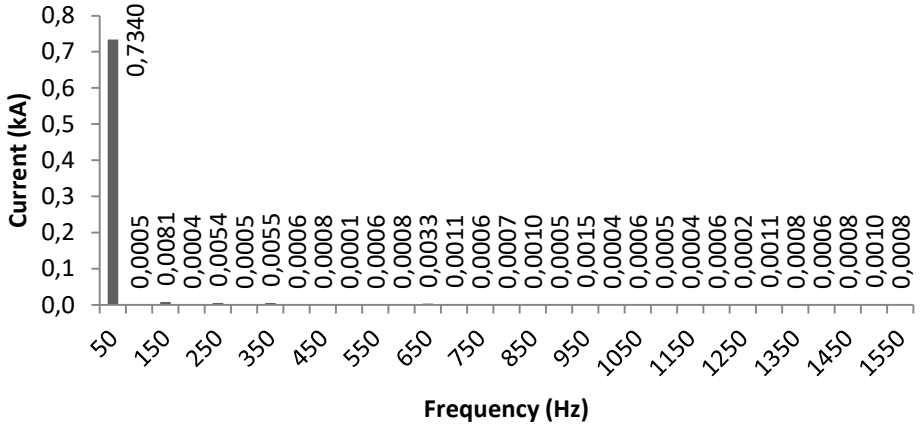

Figure 4.22. The harmonic spectrum of injected current by PV linked inverter in phase *B* with high harmonic distortion and load unbalance problems.

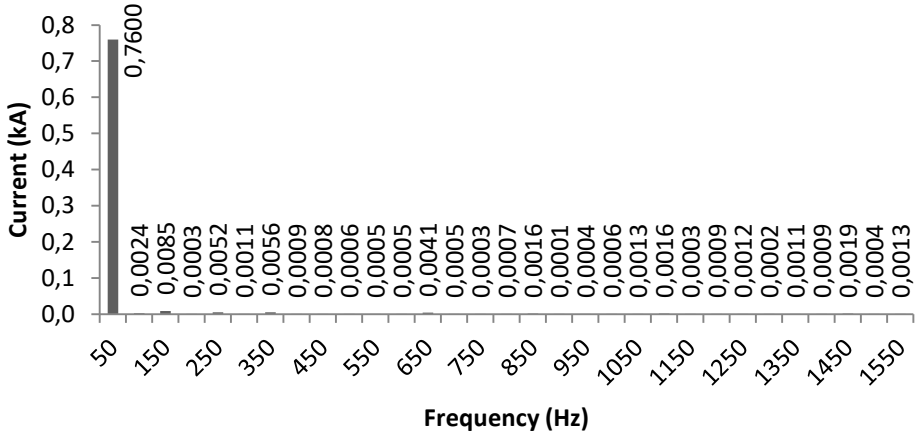

Figure 4.23. The harmonic spectrum of injected current by PV linked inverter in phase *C* with high harmonic distortion and load unbalance problems.

The details of the injected currents harmonic content are illustrated in Table 4.4.

Table 4.4. Harmonic contents of injected current with high harmonic distortion and load unbalance problems.

	Harmonic Contents of Injected Current					
	Phase A		Phase B		Phase C	
Order	(%)	Value (kA)	(%)	Value (kA)	(%)	Value (kA)
1	100.000	0.77600	100.000	0.73400	100.000	0.76000
2	0.15498	0.00120	0.07083	0.00052	0.31292	0.00238
3	1.96961	0.01528	1.09857	0.00806	1.12073	0.00852
4	0.04731	0.00037	0.05379	0.00039	0.03353	0.00025
5	0.09197	0.00071	0.74116	0.00544	0.69060	0.00525
6	0.06973	0.00054	0.06409	0.00047	0.13874	0.00105
7	0.63640	0.00494	0.75327	0.00553	0.73896	0.00562
8	0.04862	0.00038	0.08745	0.00064	0.11562	0.00088
9	0.13638	0.00106	0.10691	0.00078	0.10914	0.00083
10	0.10114	0.00078	0.00773	0.00006	0.08171	0.00062
11	0.03417	0.00027	0.08699	0.00064	0.06865	0.00052
12	0.03013	0.00023	0.10555	0.00077	0.06088	0.00046
13	0.32541	0.00253	0.44489	0.00327	0.54427	0.00414
14	0.04926	0.00038	0.14849	0.00109	0.06211	0.00047
15	0.10994	0.00085	0.07505	0.00055	0.03317	0.00025
16	0.12951	0.00100	0.09954	0.00073	0.09106	0.00069
17	0.17299	0.00134	0.13494	0.00099	0.20477	0.00156
18	0.10100	0.00078	0.06250	0.00046	0.01284	0.00010
19	0.15351	0.00119	0.20071	0.00147	0.05543	0.00042
20	0.07193	0.00056	0.04877	0.00036	0.08285	0.00063
21	0.03805	0.00030	0.08748	0.00064	0.17192	0.00131
22	0.14502	0.00113	0.06449	0.00047	0.20932	0.00159
23	0.26083	0.00202	0.05741	0.00042	0.04415	0.00034
24	0.01262	0.00010	0.07564	0.00056	0.12110	0.00092
25	0.08336	0.00065	0.03072	0.00023	0.16325	0.00124
26	0.04746	0.00037	0.15093	0.00111	0.02089	0.00016
27	0.06701	0.00052	0.10600	0.00078	0.14311	0.00109
28	0.10763	0.00084	0.07986	0.00059	0.11730	0.00089
29	0.05363	0.00042	0.10756	0.00079	0.24584	0.00187
30	0.14486	0.00112	0.13004	0.00095	0.05017	0.00038
31	0.08287	0.00064	0.10651	0.00078	0.17693	0.00134
	THD=2.31%		THD=2.24%		THD=2.1%	

The proposed ML-MFGCI designed as single stage inverter which is capable to track MPP. Thus according to Figure 4.24 if the radiation level changes

from 1000 W/m^2 to 500 W/m^2 in 0.38 *s* the *P-V* characteristics of the PV system changes as Figure 4.25.

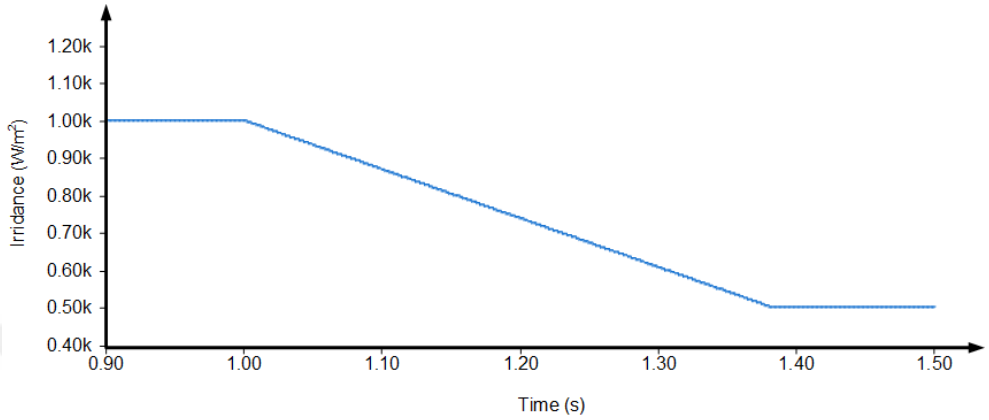

Figure 4.24. Irradiance level changing on PV panels.

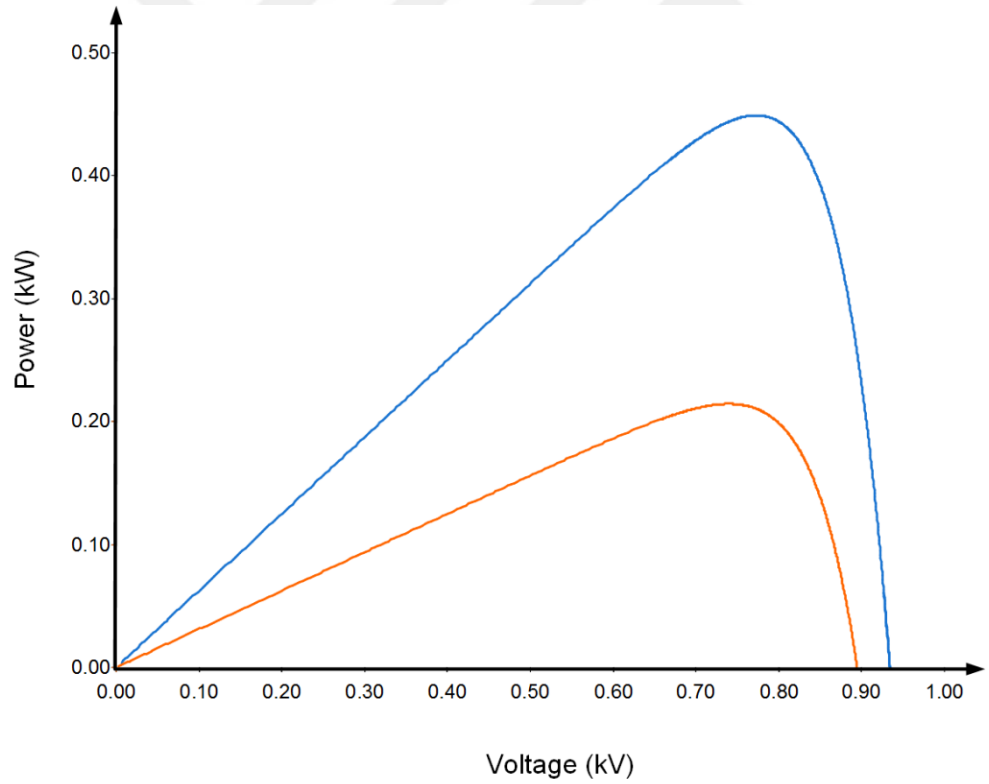

Figure 4.25. The *P-V* curves of PV system.

Figure 4.26 shows the extracted power from PV system with inverter.

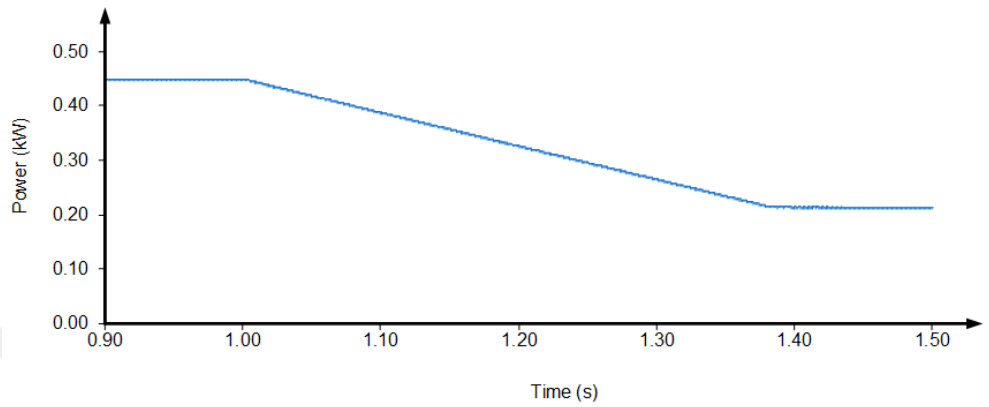

Figure 4.26. Extracted power from PV system.

Case 2: In this case, to verify the efficiency of the ML-MFGCI in the steady state conditions, the performance of the ML-MFGCI is tested for simultaneously to compensate the reactive power, current and voltage harmonics and load balancing as well as voltage regulation in the heavy loaded system. Figure 4.27 shows the PCC phase voltage waveforms of under study heavy loaded system with high level voltage and current harmonic distortion, load unbalance and voltage regulation problems. In this case, the RMS value of phase voltages for phase *A*, *B* and *C* with 205.6 V_{RMS} positive and 4.3 V_{RMS} negative sequence components are 202.4 V_{RMS}, 209.7 V_{RMS} and 205 V_{RMS}, respectively. According to phase and line voltages with 10% voltage regulation problem the loads consumes 850 kVA with 0.9 *P.F* index.

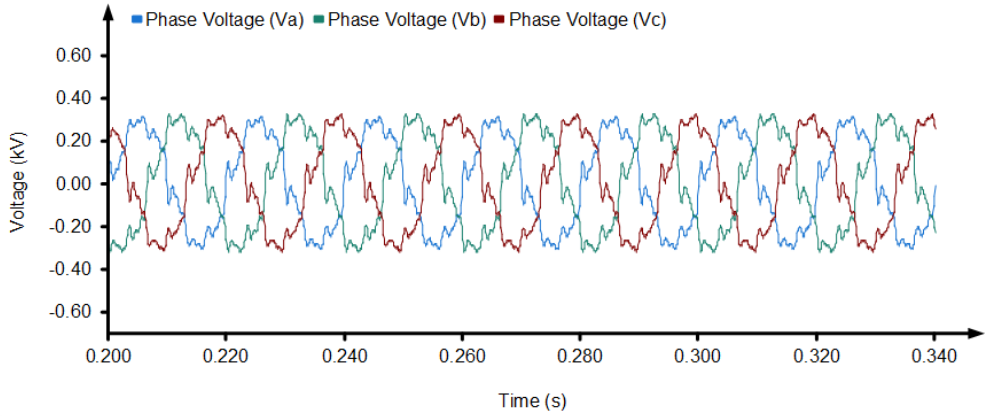

Figure 4.27. The PCC phase voltage waveforms under heavy loaded system with high harmonic distortion, load unbalance and voltage regulation problems.

The distorted PCC phase voltages have 18.28%, 17.85% and 18.82% THD's in the phase *A*, *B* and *C*, respectively. The harmonic spectrum of the PCC phase voltages show is in the Figures 4.28, 4.29 and 4.30.

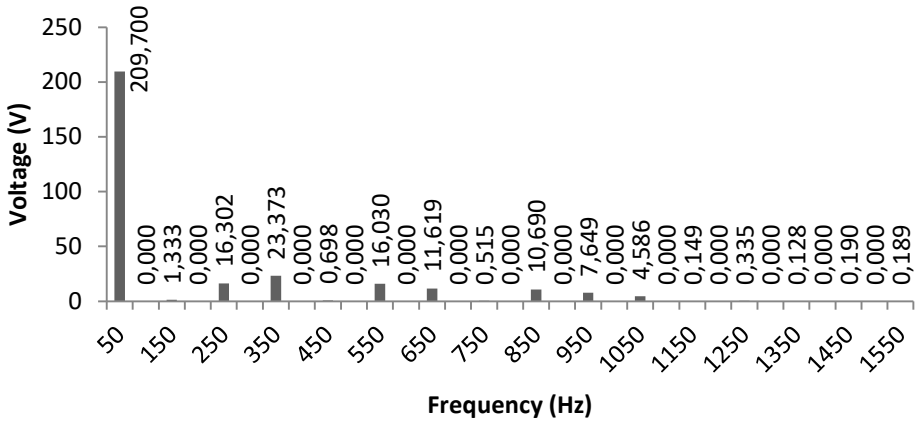

Figure 4.28. The harmonic spectrum of PCC voltage in phase *A* under heavy loaded system with high harmonic distortion, load unbalance and voltage regulation problems.

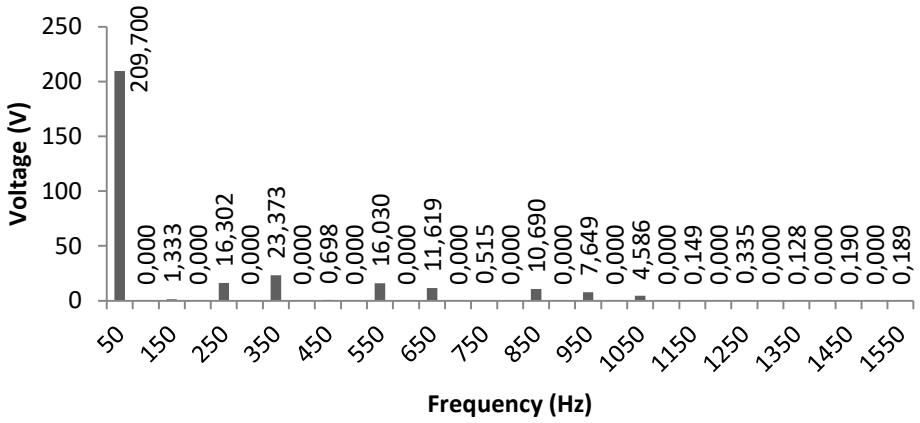

Figure 4.29. The harmonic spectrum of PCC voltage in phase *B* under heavy loaded system with high harmonic distortion, load unbalance and voltage regulation problems.

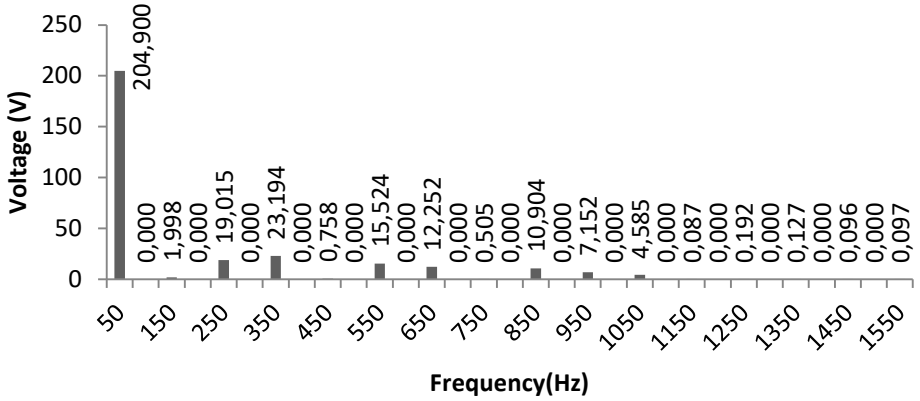

Figure 4.30. The harmonic spectrum of PCC voltage in phase *C* under heavy loaded system with high harmonic distortion, load unbalance and voltage regulation problems.

The details of the PCC phase voltages harmonic content are illustrated in Table 4.5. As seen in the Table 4.5, the dominant harmonics of the PCC phase voltages are mostly odd number harmonics.

Table 4.5. Harmonic contents of PCC phase voltages under heavy loaded system with high harmonic distortion, load unbalance and voltage regulation problems.

	Harmonic Contents of PCC Voltage					
	Phase A		Phase B		Phase C	
Order	(%)	Value (V)	(%)	Value (V)	(%)	Value (V)
1	100.000	205.600	100.000	209.700	100.000	204.900
2	0.00000	0.00000	0.00000	0.00000	0.00000	0.00000
3	0.59177	1.21668	0.63588	1.33344	0.97509	1.99796
4	0.00000	0.00000	0.00000	0.00000	0.00000	0.00000
5	9.98659	20.5324	7.77410	16.3022	9.28009	19.0149
6	0.00000	0.00000	0.00000	0.00000	0.00000	0.00000
7	9.85570	20.2633	11.1459	23.3729	11.3195	23.1938
8	0.00000	0.00000	0.00000	0.00000	0.00000	0.00000
9	0.08540	0.17558	0.33286	0.69801	0.36974	0.75760
10	0.00000	0.00000	0.00000	0.00000	0.00000	0.00000
11	7.12386	14.6466	7.64404	16.0295	7.57631	15.5238
12	0.00000	0.00000	0.00000	0.00000	0.00000	0.00000
13	6.21770	12.7835	5.54069	11.6188	5.97933	12.2516
14	0.00000	0.00000	0.00000	0.00000	0.00000	0.00000
15	0.03856	0.07927	0.24567	0.51517	0.24655	0.50519
16	0.00000	0.00000	0.00000	0.00000	0.00000	0.00000
17	5.54347	11.3973	5.09792	10.6903	5.32151	10.9037
18	0.00000	0.00000	0.00000	0.00000	0.00000	0.00000
19	3.41571	7.02270	3.64769	7.64921	3.49034	7.15171
20	0.00000	0.00000	0.00000	0.00000	0.00000	0.00000
21	2.25627	4.63890	2.18695	4.58603	2.23759	4.58482
22	0.00000	0.00000	0.00000	0.00000	0.00000	0.00000
23	0.05575	0.11463	0.07084	0.14856	0.04265	0.08739
24	0.00000	0.00000	0.00000	0.00000	0.00000	0.00000
25	0.08195	0.16848	0.15957	0.33463	0.09392	0.19245
26	0.00000	0.00000	0.00000	0.00000	0.00000	0.00000
27	0.00121	0.00249	0.06115	0.12823	0.06186	0.12675
28	0.00000	0.00000	0.00000	0.00000	0.00000	0.00000
29	0.04680	0.09622	0.09075	0.19031	0.04667	0.09562
30	0.00000	0.00000	0.00000	0.00000	0.00000	0.00000
31	0.04872	0.10017	0.09000	0.18873	0.04748	0.09729
	THD=18.28%		THD=17.85%		THD=18.82%	

In such condition the transformer's output voltage becomes as Figure 4.31 with 228.4 V_{RMS}, 228.7 V_{RMS} and 229 V_{RMS} RMS voltages for phase *A*, *B* and *C*, respectively.

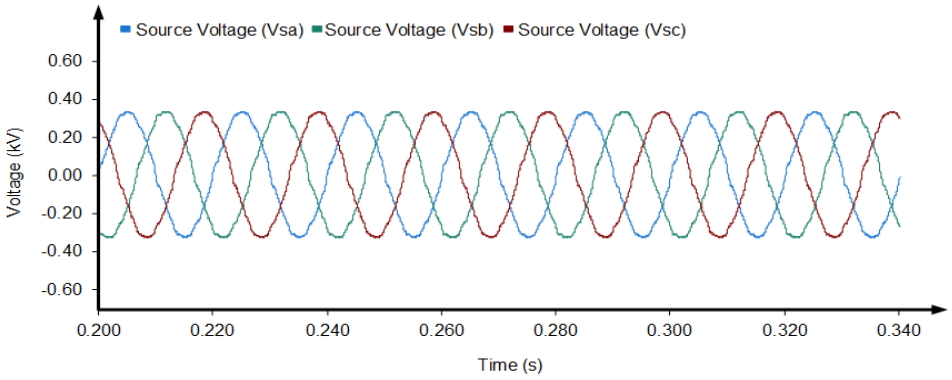

Figure 4.31. The transformer output voltage waveforms under heavy loaded system with high harmonic distortion, load unbalance and voltage regulation problems.

The distorted transformer's output voltage has 3.38%, 3.48% and 3.5% *THD*s in the phase *A*, *B* and *C*, respectively. The harmonic spectrum of the transformer's output phase voltages shown is in the Figures 4.32, 4.33 and 4.34.

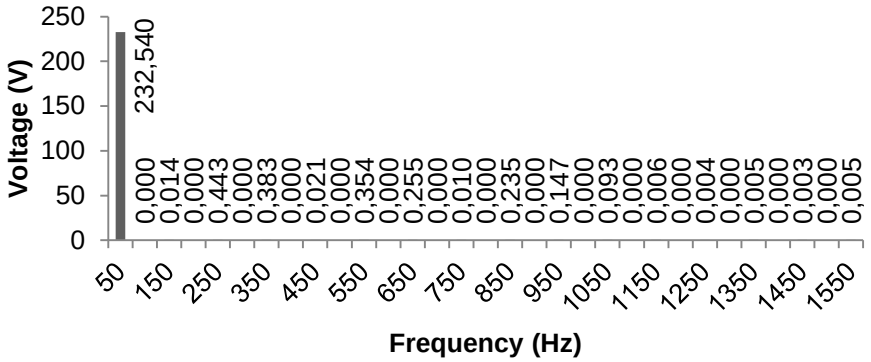

Figure 4.32. The harmonic spectrum of transformer's output voltage in phase A under heavy loaded system with high harmonic distortion, load unbalance and voltage regulation problems.

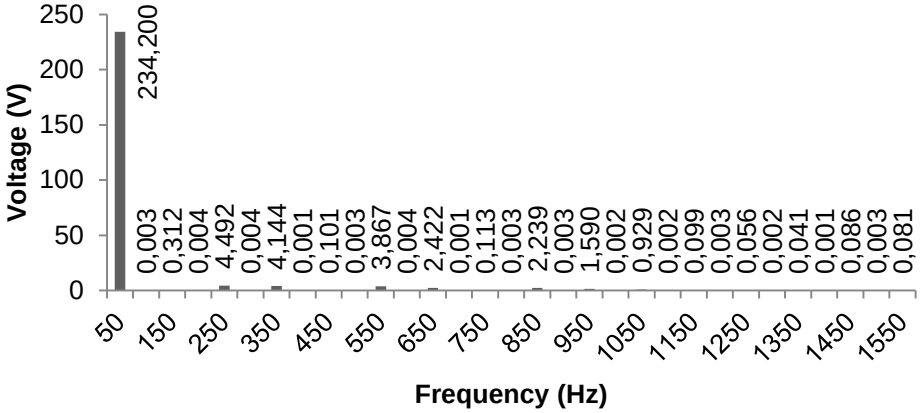

Figure 4.33. The harmonic spectrum of transformer's output voltage in phase B under heavy loaded system with high harmonic distortion, load unbalance and voltage regulation problems.

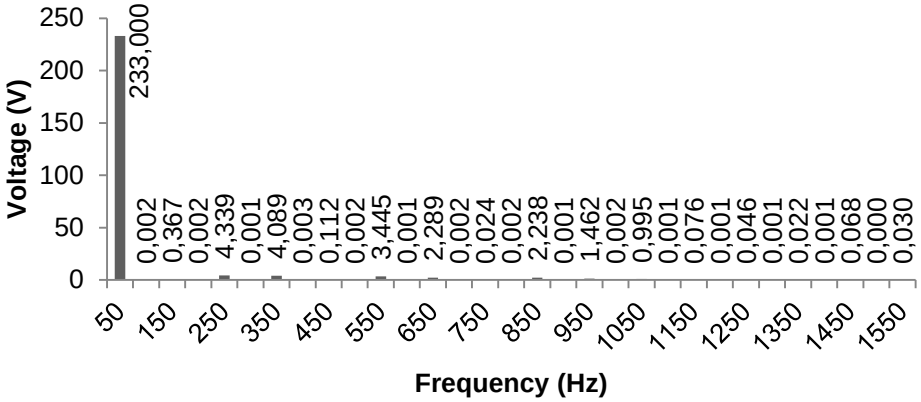

Figure 4.34. The harmonic spectrum of transformer's output voltage in phase C under heavy loaded system with high harmonic distortion, load unbalance and voltage regulation problems.

The details of the transformer's output phase voltages harmonic content are illustrated in Table 4.6.

Table 4.6. Harmonic contents of transformer's output phase voltages under heavy loaded system with high harmonic distortion, load unbalance and voltage regulation problems.

	Harmonic Contents of Transformer's Output Voltage					
	Phase A		Phase B		Phase C	
Order	(%)	Value (V)	(%)	Value (V)	(%)	Value (V)
1	100.000	232.540	100.000	234.200	100.000	233.000
2	0.00015	0.00003	0.00114	0.00268	0.00087	0.00203
3	0.05809	0.01351	0.13342	0.31246	0.15742	0.36679
4	0.00025	0.00006	0.00173	0.00404	0.00090	0.00209
5	1.90322	0.44257	1.91781	4.49151	1.86226	4.33906
6	0.00034	0.00008	0.00152	0.00355	0.00023	0.00053
7	1.64750	0.38311	1.76962	4.14444	1.75492	4.08896
8	0.00019	0.00005	0.00041	0.00095	0.00110	0.00257
9	0.09137	0.02125	0.04293	0.10054	0.04816	0.11222
10	0.00013	0.00003	0.00147	0.00345	0.00078	0.00181
11	1.52065	0.35361	1.65113	3.86694	1.47860	3.44514
12	0.00024	0.00006	0.00155	0.00363	0.00041	0.00096
13	1.09452	0.25452	1.03401	2.42166	0.98234	2.28886
14	0.00023	0.00005	0.00055	0.00128	0.00092	0.00214
15	0.04259	0.00990	0.04814	0.11275	0.01027	0.02393
16	0.00010	0.00002	0.00111	0.00260	0.00069	0.00161
17	1.01026	0.23493	0.95603	2.23903	0.96032	2.23755
18	0.00016	0.00004	0.00135	0.00316	0.00038	0.00087
19	0.63302	0.14720	0.67906	1.59036	0.62733	1.46169
20	0.00022	0.00005	0.00073	0.00171	0.00069	0.00160
21	0.40121	0.09330	0.39677	0.92924	0.42699	0.99490
22	0.00011	0.00003	0.00068	0.00160	0.00054	0.00126
23	0.02628	0.00611	0.04219	0.09881	0.03248	0.07567
24	0.00013	0.00003	0.00114	0.00267	0.00028	0.00064
25	0.01796	0.00418	0.02401	0.05624	0.01958	0.04563
26	0.00023	0.00005	0.00087	0.00205	0.00055	0.00128
27	0.02358	0.00548	0.01731	0.04053	0.00929	0.02164
28	0.00015	0.00004	0.00035	0.00082	0.00038	0.00088
29	0.01107	0.00257	0.03671	0.08597	0.02928	0.06822
30	0.00022	0.00005	0.00112	0.00263	0.00006	0.00013
31	0.02281	0.00530	0.03445	0.08069	0.01295	0.03016
	THD=3.38%		THD=3.48%		THD=3.50%	

The load draws 1.472 *kA*, 1.400 *kA* and 1.584 *kA* in phase *A*, *B* and *C*, respectively. Due to unbalance loaded the load currents becomes unbalance and

emerge a negative sequence current. The load current has 1.483 *kA* positive sequence component and 0.109 *kA* negative sequence component with 7% unbalance ratios (*UN%*) in the load current. Figure 4.35 shows the load current waveforms under same condition.

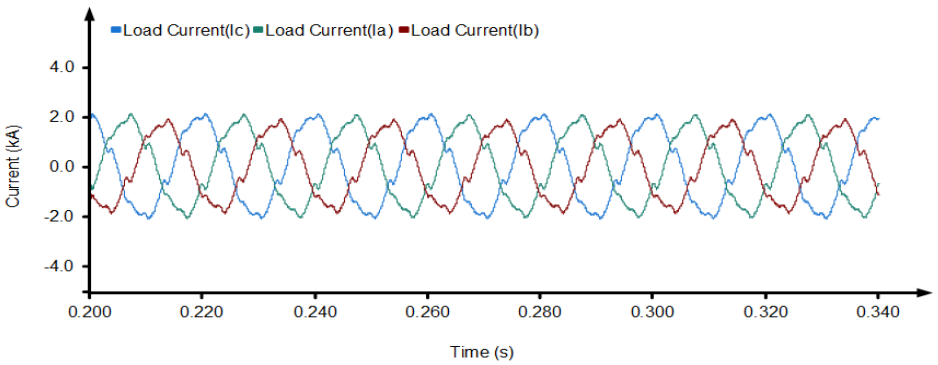

Figure 4.35. The transformer output voltage waveforms under heavy loaded system with high harmonic distortion, load unbalance and voltage regulation problems.

As seen from Figure 4.35, the load currents have high level harmonic components. The harmonic spectrum of the load currents for phases *A*, *B* and *C* are shown in the Figures 4.36, 4.37 and 4.38, respectively.

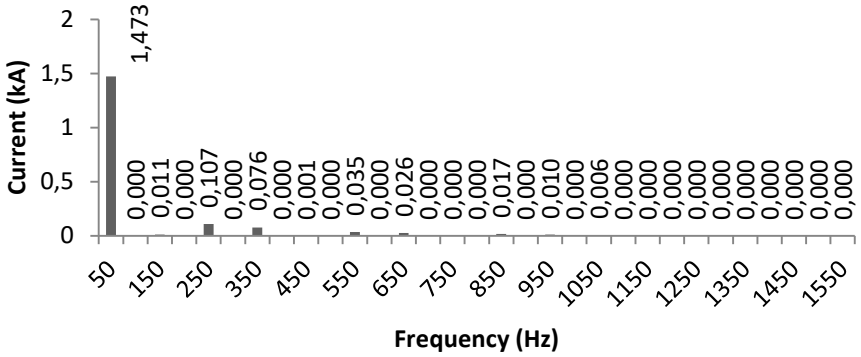

Figure 4.37. The harmonic spectrum of load current in phase *A* under heavy loaded system with high harmonic distortion, load unbalance and voltage regulation problems.

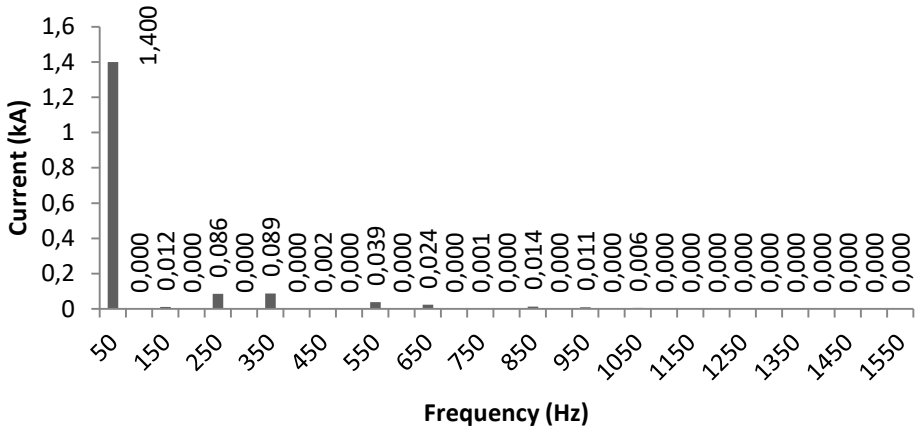

Figure 4.37. The harmonic spectrum of load current in phase *B* under heavy loaded system with high harmonic distortion, load unbalance and voltage regulation problems.

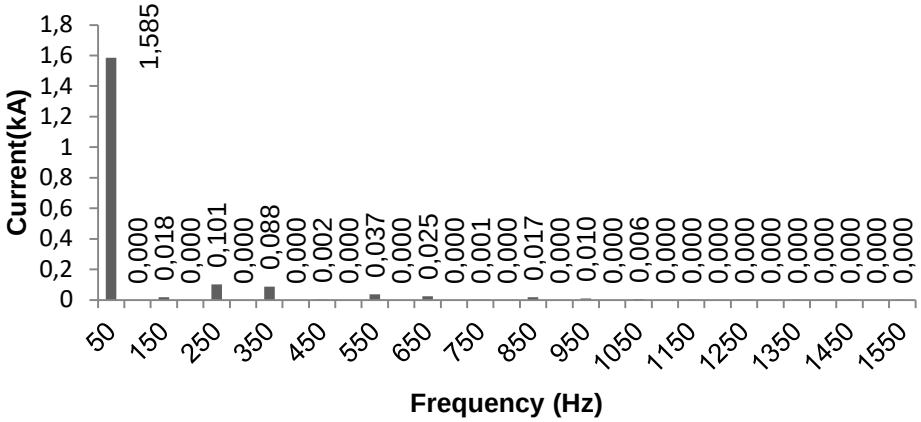

Figure 4.38. The harmonic spectrum of load current in phase C under heavy loaded system with high harmonic distortion, load unbalance and voltage regulation problems.

The details of the load currents harmonic content are illustrated in Table 4.7. The load currents *THD* are 9.5%, 9.56% and 9.05% for phase *A*, *B* and *C*, respectively.

Table 4.7. Harmonic contents of load currents under heavy loaded system with high harmonic distortion, load unbalance and voltage regulation problems.

	Harmonic Contents of Load Current					
	Phase A		Phase B		Phase C	
Order	(%)	Value (kA)	(%)	Value (kA)	(%)	Value (kA)
1	100.000	1.47260	100.000	1.40000	100.000	1.58500
2	0.00000	0.00000	0.00000	0.00000	0.00000	0.00000
3	0.71505	0.01053	0.83802	0.01173	1.10857	0.01757
4	0.00000	0.00000	0.00000	0.00000	0.00000	0.00000
5	7.26664	0.10701	6.17075	0.08639	6.35344	0.10070
6	0.00000	0.00000	0.00000	0.00000	0.00000	0.00000
7	5.12705	0.07550	6.32511	0.08855	5.54087	0.08782
8	0.00000	0.00000	0.00000	0.00000	0.00000	0.00000
9	0.03466	0.00051	0.14664	0.00205	0.14058	0.00223
10	0.00000	0.00000	0.00000	0.00000	0.00000	0.00000
11	2.35947	0.03475	2.76189	0.03867	2.36084	0.03742
12	0.00000	0.00000	0.00000	0.00000	0.00000	0.00000
13	1.74255	0.02566	1.69376	0.02371	1.57703	0.02500
14	0.00000	0.00000	0.00000	0.00000	0.00000	0.00000
15	0.00980	0.00014	0.06560	0.00092	0.05652	0.00090
16	0.00000	0.00000	0.00000	0.00000	0.00000	0.00000
17	1.18831	0.01750	1.01923	0.01427	1.07314	0.01701
18	0.00000	0.00000	0.00000	0.00000	0.00000	0.00000
19	0.65509	0.00965	0.76320	0.01068	0.62997	0.00998
20	0.00000	0.00000	0.00000	0.00000	0.00000	0.00000
21	0.39104	0.00576	0.41299	0.00578	0.36500	0.00579
22	0.00000	0.00000	0.00000	0.00000	0.00000	0.00000
23	0.00933	0.00014	0.01253	0.00018	0.00602	0.00010
24	0.00000	0.00000	0.00000	0.00000	0.00000	0.00000
25	0.01241	0.00018	0.02628	0.00037	0.01300	0.00021
26	0.00000	0.00000	0.00000	0.00000	0.00000	0.00000
27	0.00218	0.00003	0.01164	0.00016	0.00870	0.00014
28	0.00000	0.00000	0.00000	0.00000	0.00000	0.00000
29	0.00909	0.00013	0.01803	0.00025	0.00751	0.00012
30	0.00000	0.00000	0.00000	0.00000	0.00000	0.00000
31	0.00697	0.00010	0.01137	0.00016	0.00467	0.00007
	THD=9.5%		THD=9.56%		THD=9.10%	

Due to the lack of any compensator in the system, hence the source currents become as load current with same RMS value, harmonic contents and unbalance ratio.

As mentioned above the under study system has voltage regulation, voltage and current harmonic, negative sequence current and low *P.F.* index. Therefore, a system with these features and problems severity requires to a compensator. If the proposed ML-MFGCI utilized to overcome these problems the transformer output voltage waveform becomes as Figure 4.39.

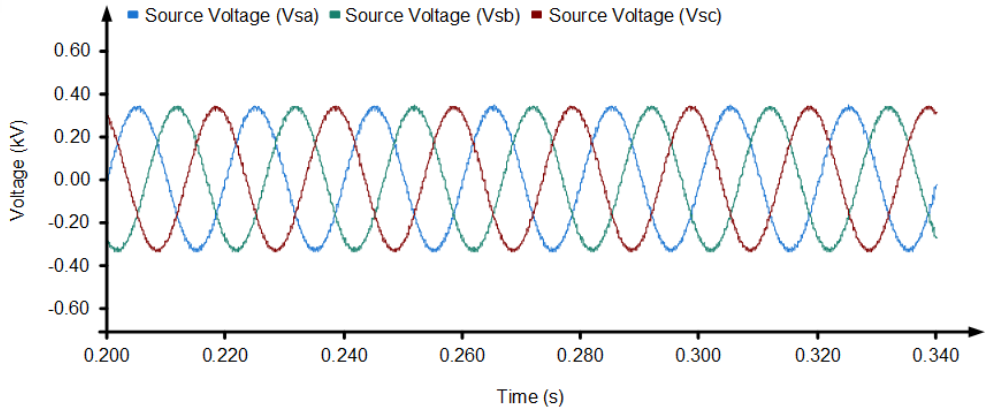

Figure 4.39. The transformer's output voltage waveforms under heavy loaded system with high harmonic distortion, load unbalance and voltage regulation problems when ML-MFGCI utilized.

By utilizing ML-MFGCI the transformer's output voltage *THD*s are decreased from 3.38% to 0.5% in phase *A*, 3.48% to 0.68% in phase *B* and 3.5% to 0.55% in phase *C*. Figures 4.40, 4.41, and 4.42 show the harmonic spectrum of the transformer's output phase voltages when the ML-MFGCI utilized to mitigate PQ problems.

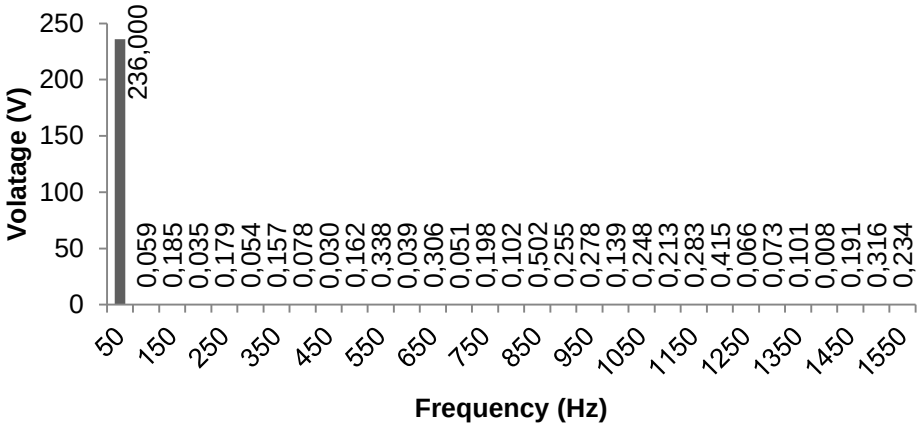

Figure 4.40. The harmonic spectrum of transformer's output voltage in phase *A* under heavy loaded system with high harmonic distortion, load unbalance and voltage regulation problems when the ML-MFGCI utilized.

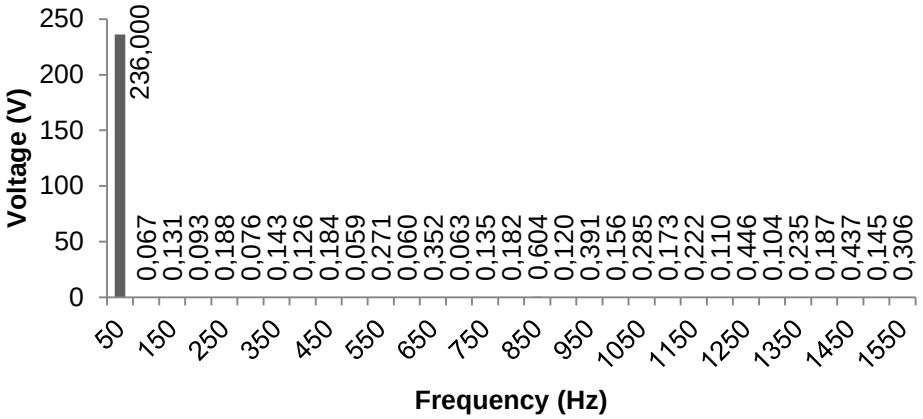

Figure 4.41. The harmonic spectrum of transformer's output voltage in phase B under heavy loaded system with high harmonic distortion, load unbalance and voltage regulation problems when the ML-MFGCI utilized.

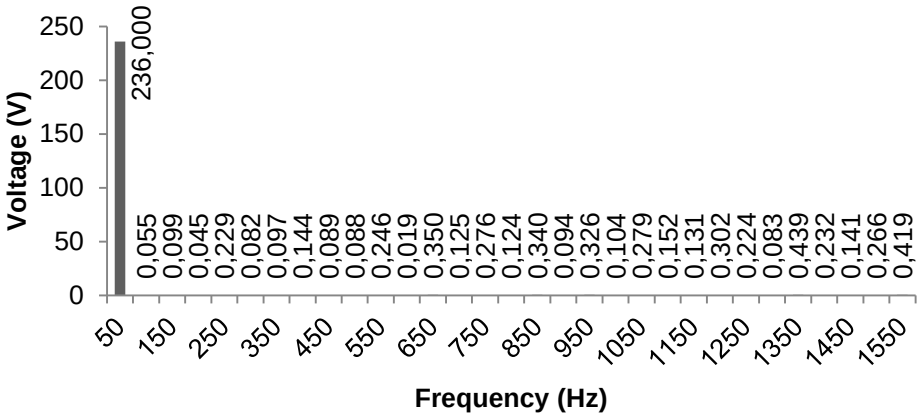

Figure 4.42. The harmonic spectrum of transformer's output voltage in phase C under heavy loaded system with high harmonic distortion, load unbalance and voltage regulation problems when the ML-MFGCI utilized.

Table 4.8 illustrate the transformer's output voltages harmonic content in details when ML-MFGCI utilized to mitigate PQ problems.

Table 4.8. Harmonic contents of transformer's output voltages under heavy loaded system with high harmonic distortion, load unbalance and voltage regulation problems when the ML-MFGCI utilized.

	Harmonic Contents of Injected Current					
	Phase A		Phase B		Phase C	
Order	(%)	Value (V)	(%)	Value (V)	(%)	Value (V)
1	100.000	236.000	100.000	236.000	100.000	236.000
2	0.02484	0.05863	0.02819	0.06652	0.02324	0.05484
3	0.07851	0.18527	0.05554	0.13107	0.04199	0.09911
4	0.01499	0.03537	0.03928	0.09269	0.01906	0.04499
5	0.07570	0.17866	0.07968	0.18805	0.09695	0.22880
6	0.02272	0.05361	0.03209	0.07574	0.03493	0.08243
7	0.06642	0.15676	0.06040	0.14255	0.04094	0.09663
8	0.03325	0.07847	0.05326	0.12568	0.06096	0.14388
9	0.01291	0.03046	0.07777	0.18353	0.03780	0.08922
10	0.06877	0.16229	0.02503	0.05906	0.03726	0.08794
11	0.14342	0.33847	0.11464	0.27054	0.10434	0.24625
12	0.01633	0.03854	0.02538	0.05989	0.00797	0.01882
13	0.12964	0.30595	0.14899	0.35162	0.14824	0.34984
14	0.02166	0.05112	0.02685	0.06338	0.05279	0.12458
15	0.08374	0.19762	0.05701	0.13455	0.11709	0.27633
16	0.04339	0.10239	0.07697	0.18164	0.05261	0.12415
17	0.21269	0.50194	0.25586	0.60383	0.14390	0.33960
18	0.10819	0.25534	0.05078	0.11984	0.03970	0.09369
19	0.11793	0.27833	0.16561	0.39084	0.13805	0.32580
20	0.05876	0.13868	0.06630	0.15647	0.04422	0.10436
21	0.10525	0.24838	0.12071	0.28488	0.11840	0.27942
22	0.09036	0.21326	0.07331	0.17300	0.06458	0.15240
23	0.11973	0.28256	0.09425	0.22242	0.05550	0.13097
24	0.17577	0.41481	0.04654	0.10984	0.12776	0.30152
25	0.02806	0.06623	0.18906	0.44618	0.09491	0.22399
26	0.03089	0.07290	0.04391	0.10363	0.03500	0.08261
27	0.04287	0.10116	0.09972	0.23534	0.18613	0.43926
28	0.00333	0.00787	0.07920	0.18691	0.09815	0.23164
29	0.08114	0.19149	0.18527	0.43724	0.05965	0.14077
30	0.13401	0.31627	0.06126	0.14457	0.11260	0.26575
31	0.09935	0.23447	0.12982	0.30638	0.17759	0.41911
	THD=0.5%		THD=0.68%		THD=0.55%	

Figure 4.43 shows the PCC phase voltages waveforms when the ML-MFGCI utilized to mitigate PQ problems. By utilizing ML-MFGCI the PCC

voltages are increased from 202.4 V_{RMS} to 225 V_{RMS}, 209.7 V_{RMS} to 225 V_{RMS} and 205 V_{RMS} to 225 V_{RMS}. Moreover, the PCC phase voltages becomes balance in 225 V_{RMS}.

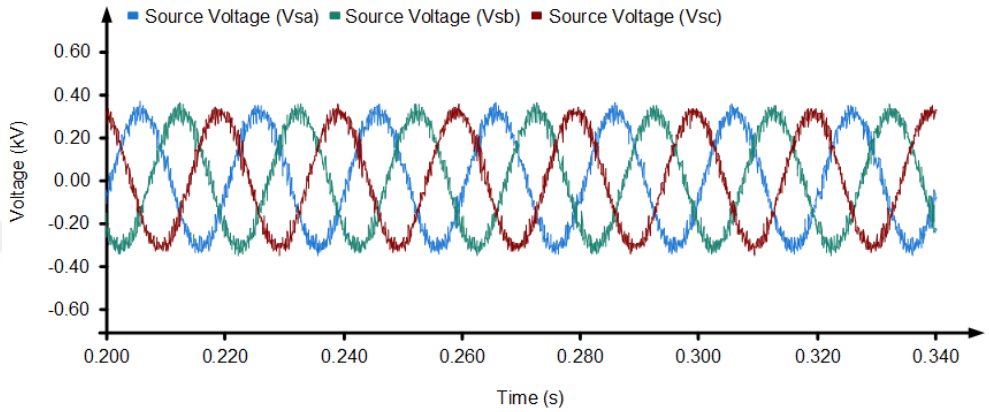

Figure 4.43. The transformer's output voltage waveforms under heavy loaded system with high harmonic distortion, load unbalance and voltage regulation problems when ML-MFGCI utilized.

When the ML-MFGCI is utilized to mitigate PQ problems the PCC voltage *THD*s are decreased from 18.28% to3.3 % in phase *A*, 17.84% to 2.7% in phase *B* and 18.82% to 2.5% in phase *C*. Figures 4.44, 4.45 and 4.46 shows the harmonic spectrum of the transformer's output phase voltages.

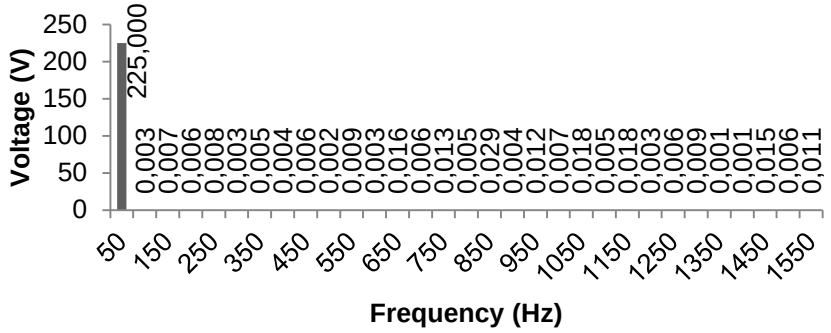

Figure 4.44. The harmonic spectrum of PCC voltage in phase *A* under heavy loaded system with high harmonic distortion, load unbalance and voltage regulation problems when the ML-MFGCI utilized.

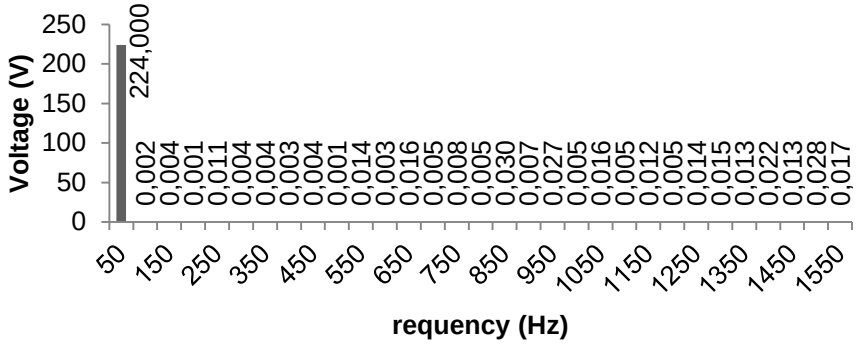

Figure 4.45. The harmonic spectrum of PCC voltage in phase *B* under heavy loaded system with high harmonic distortion, load unbalance and voltage regulation problems when the ML-MFGCI utilized.

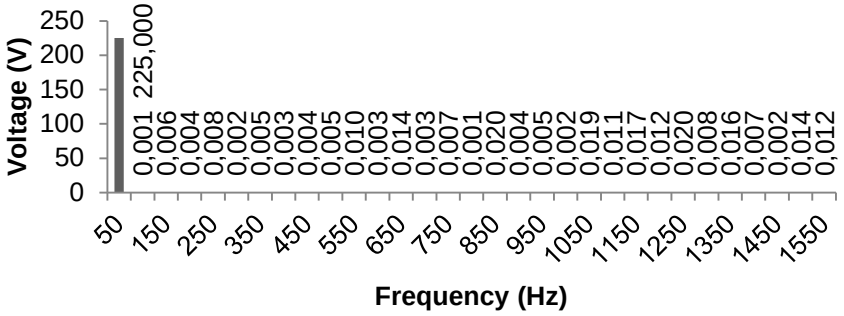

Figure 4.46. The harmonic spectrum of PCC voltage in phase *C* under heavy loaded system with high harmonic distortion, load unbalance and voltage regulation problems when the ML-MFGCI utilized.

The details of the PCC phase voltage harmonic contents are illustrated in Table 4.9. The PCC voltage *THD*s are 3.3%, 2.7% and 2.5% for phase *A*, *B* and *C*, respectively.

Table 4.9. Harmonic contents of PCC voltages under heavy loaded system with high harmonic distortion, load unbalance and voltage regulation problems when the ML-MFGCI utilized.

	Harmonic Contents of Injected Current					
	Phase A		Phase B		Phase C	
Order	(%)	Value (V)	(%)	Value (V)	(%)	Value (V)
1	100.000	225.000	100.000	224.000	100.000	225.000
2	0.12990	0.00292	0.07330	0.00164	0.06194	0.00139
3	0.32295	0.00727	0.18694	0.00419	0.27169	0.00611
4	0.26192	0.00589	0.06100	0.00137	0.19552	0.00440
5	0.35972	0.00809	0.49087	0.01100	0.34922	0.00786
6	0.13112	0.00295	0.18876	0.00423	0.08947	0.00201
7	0.21795	0.00490	0.17374	0.00389	0.22353	0.00503
8	0.17934	0.00404	0.13856	0.00310	0.14580	0.00328
9	0.26410	0.00594	0.18050	0.00404	0.15679	0.00353
10	0.09027	0.00203	0.06398	0.00143	0.21443	0.00482
11	0.40614	0.00914	0.63805	0.01429	0.45301	0.01019
12	0.14908	0.00335	0.11865	0.00266	0.11426	0.00257
13	0.69504	0.01564	0.70189	0.01572	0.61958	0.01394
14	0.28271	0.00636	0.20760	0.00465	0.14779	0.00333
15	0.57455	0.01293	0.36805	0.00824	0.29047	0.00654
16	0.23479	0.00528	0.23146	0.00518	0.05357	0.00121
17	1.27817	0.02876	1.32221	0.02962	0.90245	0.02031
18	0.16307	0.00367	0.31151	0.00698	0.19314	0.00435
19	0.52305	0.01177	1.20019	0.02688	0.22899	0.00515
20	0.30491	0.00686	0.23029	0.00516	0.09769	0.00220
21	0.78118	0.01758	0.69668	0.01561	0.86273	0.01941
22	0.23731	0.00534	0.20501	0.00459	0.50240	0.01130
23	0.77812	0.01751	0.53701	0.01203	0.76999	0.01732
24	0.11835	0.00266	0.22897	0.00513	0.55555	0.01250
25	0.24985	0.00562	0.61473	0.01377	0.87911	0.01978
26	0.40220	0.00905	0.67378	0.01509	0.37031	0.00833
27	0.06198	0.00139	0.58504	0.01310	0.69643	0.01567
28	0.05469	0.00123	0.96482	0.02161	0.30016	0.00675
29	0.68089	0.01532	0.57347	0.01285	0.07372	0.00166
30	0.25728	0.00579	1.26221	0.02827	0.63125	0.01420
31	0.48497	0.01091	0.77923	0.01745	0.53210	0.01197
	THD=3.3%		THD=2.7%		THD=2.5%	

When the PCC voltage rises to normal voltage, load draws 1.477 *kA*, 1.300 *kA* and 1.532 *kA* in phase *A*, *B* and *C*, respectively. Due to unbalance loaded the load currents becomes unbalance and emerge a negative sequence current. The load current has 1.437 *kA* positive sequence component and 0.142 *kA* negative sequence component with 10% unbalance ratios (*UN%*) in the load current. Figure 4.47 shows the load current waveforms under same condition.

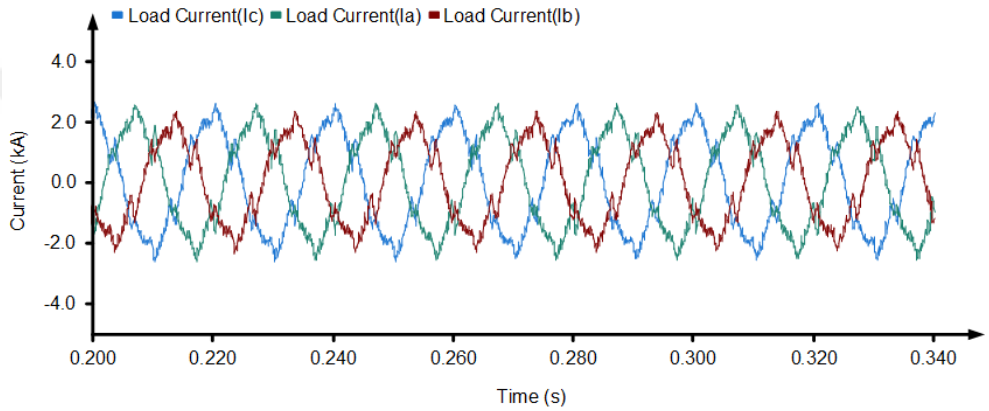

Figure 4.47. The load current waveforms under heavy loaded system with high harmonic distortion, load unbalance and voltage regulation problems when ML-MFGCI utilized.

The load current has 17.41%, 19.82% and 16.28% THD rates in phase *A*, *B* and *C*, respectively. The harmonic spectrum of the load currents show is in the Figures 4.48, 4.49 and 4.50.

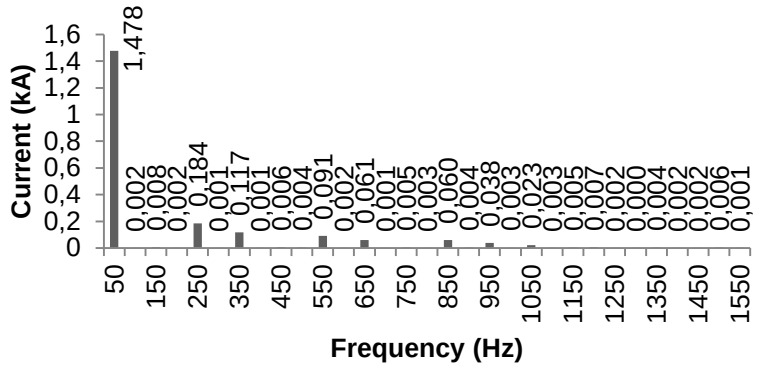

Figure 4.48. The harmonic spectrum of load current in phase A under heavy loaded system with high harmonic distortion, load unbalance and voltage regulation problems when the ML-MFGCI utilized.

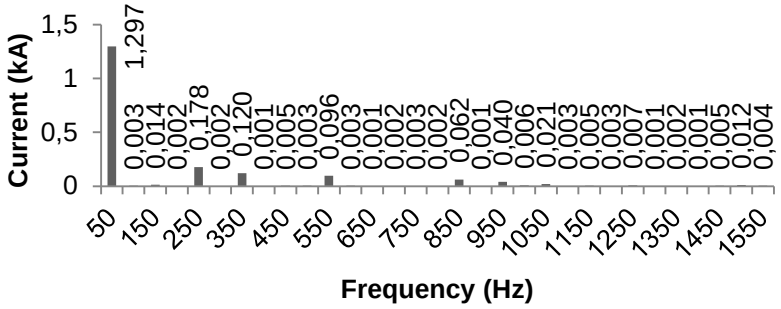

Figure 4.49. The harmonic spectrum of source current in phase B under heavy loaded system with high harmonic distortion, load unbalance and voltage regulation problems when the ML-MFGCI utilized.

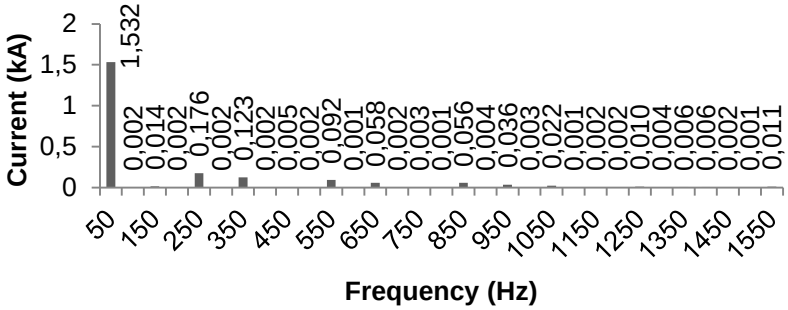

Figure 4.50. The harmonic spectrum of source current in phase C under heavy loaded system with high harmonic distortion, load unbalance and voltage regulation problems when the ML-MFGCI utilized.

The details of the source current harmonic contents are illustrated in Table 4.10.

Table 4.10. Harmonic contents of load currents under heavy loaded system with high harmonic distortion, load unbalance and voltage regulation problems when the ML-MFGCI utilized.

	Harmonic Contents of Injected Current					
	Phase A		Phase B		Phase C	
Order	(%)	Value (kA)	(%)	Value (kA)	(%)	Value (kA)
1	100.000	1.47789	100.000	1.29650	100.000	1.53230
2	0.13435	0.00199	0.26033	0.00338	0.13990	0.00214
3	0.56450	0.00834	1.06248	0.01378	0.91479	0.01402
4	0.10305	0.00152	0.11974	0.00155	0.10838	0.00166
5	12.4240	0.18361	13.7468	0.17823	11.4794	0.17590
6	0.07080	0.00105	0.17054	0.00221	0.09935	0.00152
7	7.90385	0.11681	9.29276	0.12048	7.99963	0.12258
8	0.09496	0.00140	0.09435	0.00122	0.10085	0.00155
9	0.41736	0.00617	0.35701	0.00463	0.30843	0.00473
10	0.27072	0.00400	0.24144	0.00313	0.15802	0.00242
11	6.15864	0.09102	7.36936	0.09554	5.97326	0.09153
12	0.12278	0.00181	0.25847	0.00335	0.07923	0.00121
13	4.12270	0.06093	4. 49868	0.00058	3.76144	0.05764
14	0.08857	0.00130	0.16491	0.00214	0.11718	0.00180
15	0.33196	0.00500	0.21532	0.00279	0.19367	0.00297
16	0.21377	0.00316	0.15117	0.00196	0.05722	0.00088
17	4.01882	0.06000	4.74533	0.06152	3.65303	0.05598
18	0.25645	0.00380	0.05080	0.00066	0.24807	0.00380
19	2.57565	0.03800	3.07798	0.03991	2.32997	0.03570
20	0.22747	0.00336	0.48156	0.00624	0.20140	0.00309
21	1.50685	0.02270	1.58131	0.02050	1.45084	0.02223
22	0.18932	0.00280	0.20099	0.00261	0.08329	0.00128
23	0.30796	0.00455	0.40292	0.00522	0.15660	0.00240
24	0.43915	0.00650	0.22033	0.00286	0.15279	0.00234
25	0.16027	0.00237	0.53356	0.00692	0.64623	0.00990
26	0.02972	0.00044	0.09170	0.00119	0.27797	0.00426
27	0.30123	0.00440	0.12410	0.00161	0.40279	0.00617
28	0.15453	0.00235	0.11174	0.00145	0.39409	0.00604
29	0.16399	0.00240	0.39230	0.00509	0.14558	0.00223
30	0.39934	0.00600	0.91385	0.01185	0.09354	0.00143
31	0.08388	0.00124	0.30511	0.00396	0.70561	0.01081
	THD=17.41%		THD=19.82%		THD=16.26%	

To compensate the harmonic distortions, load unbalance and reactive power as well as regulate the PCC voltage the ML-MFGCI injects the required current to system. In this case, the ML-MFGC injects 0.743 *kA* to phase *A*, 0.526 *kA* to phase *B* and 0.531 *kA* to phase *C* with 0.1455 *kA* negative sequence current into system. Figure 4.51 shows the injected current by the ML-MFGCI into system.

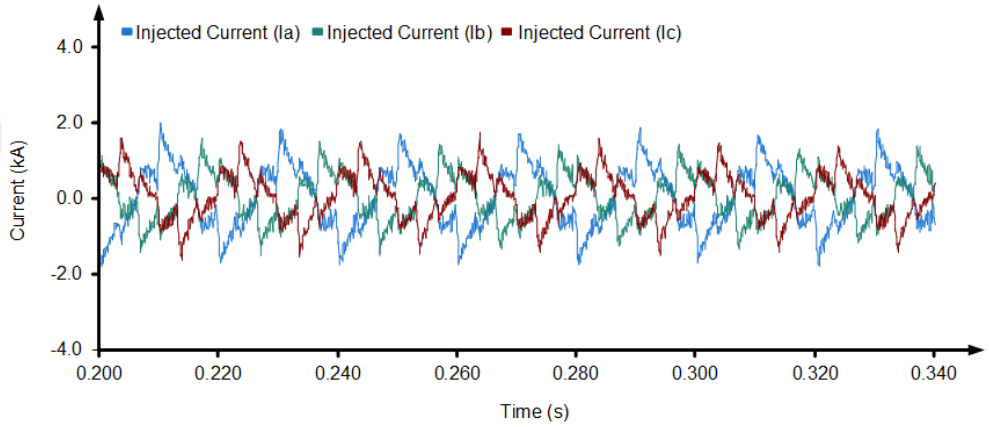

Figure 4.51. The currents waveform injected by ML-MFGCI.

As seen from figure 23, to compensate harmonics ML-MFGCI injects the required harmonic into system. Figure 4.52, 4.53 and 4.54 shows the harmonic spectrum of the injected current by ML-MFGCI in phases *A*, *B* and *C*.

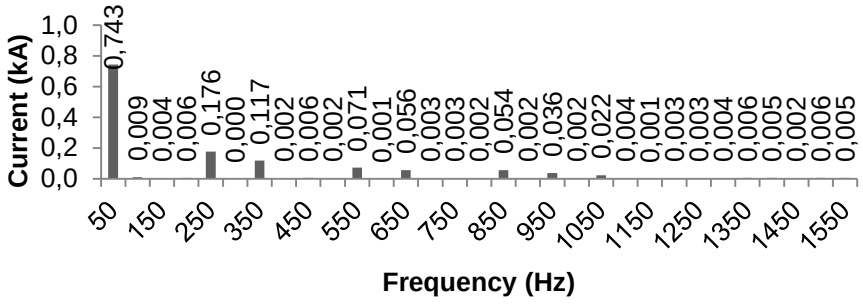

Figure 4.52. The harmonic spectrum of injected current in phase A by the ML-MFGCI under heavy loaded system with high harmonic distortion, load unbalance and voltage regulation problems.

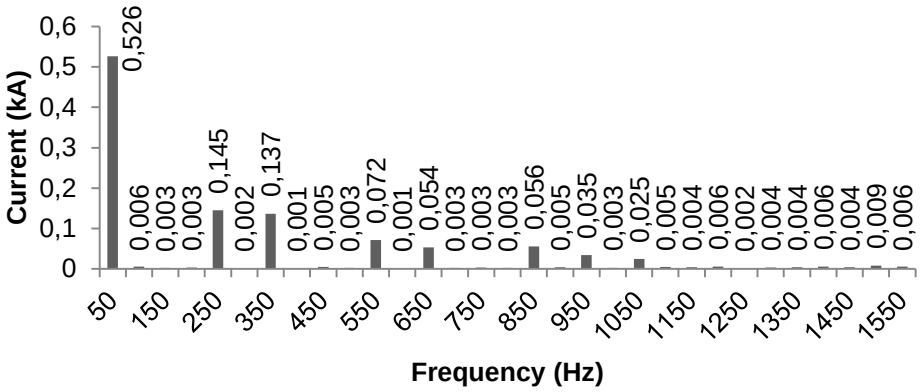

Figure 4.53. The harmonic spectrum of injected current in phase B by the ML-MFGCI under heavy loaded system with high harmonic distortion, load unbalance and voltage regulation problems.

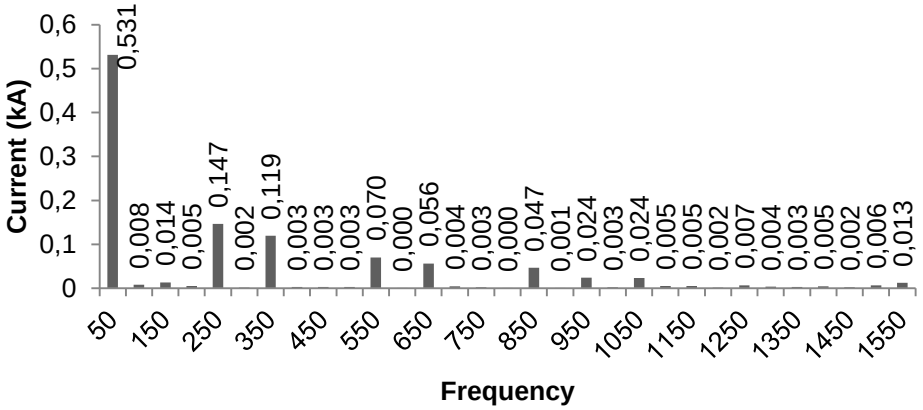

Figure 4.54. The harmonic spectrum of injected current in phase C by the ML-MFGCI under heavy loaded system with high harmonic distortion, load unbalance and voltage regulation problems.

The details of the source current harmonic contents are illustrated in Table 4.11.

Table 4.11. Harmonic contents of injected currents by ML-MFGCI under heavy loaded system with high harmonic distortion, load unbalance and voltage regulation problems.

	Harmonic Contents of Injected Current					
	Phase A		Phase B		Phase C	
Order	(%)	Value (kA)	(%)	Value (kA)	(%)	Value (kA)
1	100.000	0.74300	100.000	0.52600	100.000	0.53100
2	1.17442	0.00873	1.06059	0.00558	1.50029	0.00797
3	0.54434	0.00404	0.54371	0.00286	2.56233	0.01361
4	0.77535	0.00576	0.62086	0.00327	0.98822	0.00525
5	23.6789	0.17593	27.5546	0.14494	27.6808	0.14699
6	0.05895	0.00044	0.36383	0.00191	0.35342	0.00188
7	15.7324	0.11689	26.0308	0.13692	22.4764	0.11935
8	0.22772	0.00169	0.15318	0.00081	0.60193	0.00320
9	0.81729	0.00607	0.98942	0.00520	0.52255	0.00277
10	0.21978	0.00163	0.58016	0.00305	0.54140	0.00287
11	9.58291	0.07120	13.6608	0.07186	13.2647	0.07044
12	0.07994	0.00059	0.26242	0.00138	0.05882	0.00031
13	7.53517	0.05599	10.2018	0.05366	10.6294	0.05644
14	0.43461	0.00323	0.49587	0.00261	0.84697	0.00450
15	0.44796	0.00333	0.61760	0.00325	0.47658	0.00253
16	0.30635	0.00228	0.57919	0.00305	0.04632	0.00025
17	7.31826	0.05437	10.5823	0.05566	8.77967	0.04662
18	0.27452	0.00204	0.87173	0.00459	0.11811	0.00063
19	4.84264	0.03598	6.56938	0.03455	4.55880	0.02421
20	0.21178	0.00157	0.59596	0.00313	0.48521	0.00258
21	2.90449	0.02158	4.68024	0.02462	4.45316	0.02365
22	0.49601	0.00369	1.02695	0.00540	0.98201	0.00521
23	0.08995	0.00067	0.81751	0.00430	0.98032	0.00521
24	0.44921	0.00334	1.13199	0.00595	0.36099	0.00192
25	0.44978	0.00334	0.36960	0.00194	1.30351	0.00692
26	0.56922	0.00423	0.66874	0.00352	0.68270	0.00363
27	0.78552	0.00584	0.84979	0.00447	0.60703	0.00322
28	0.66598	0.00495	1.16137	0.00611	0.88882	0.00472
29	0.30896	0.00230	0.74998	0.00394	0.46747	0.00248
30	0.79149	0.00588	1.64545	0.00866	1.21435	0.00645
31	0.65909	0.00490	1.05499	0.00555	2.36145	0.01254

Figure 4.55 shows the source current waveforms when the ML-MFGCI utilized to mitigate PQ problems. By utilizing ML-MFGCI the source current becomes as pure sinusoidal waveform. The drown current from source with ML-

MFGCI are as 1.457 *kA* for phase *A*, 1.444 *kA* for phase *B* and 1.425 *kA* for phase *C*. Moreover negative sequence of source current decrees to 0.016 *kA* and current unbalance ration reduce to 1.2%.

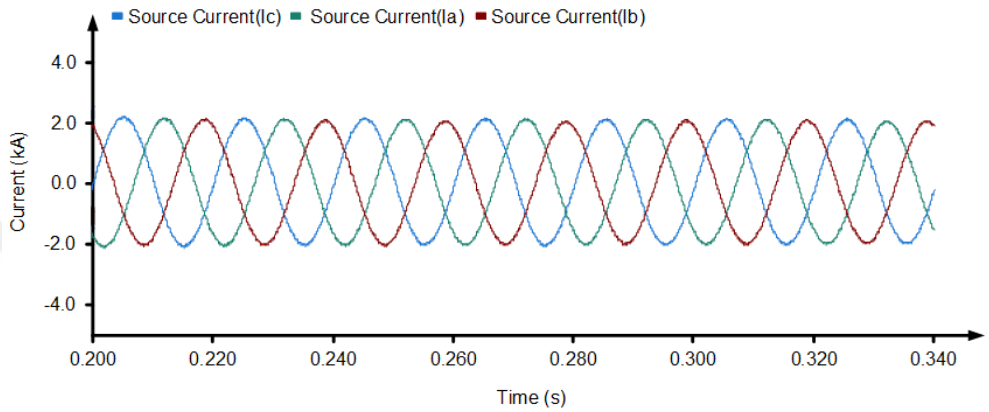

Figure 4.55. The source current waveforms under heavy loaded system with high harmonic distortion, load unbalance and voltage regulation problems when ML-MFGCI utilized.

When the ML-MFGCI is utilized to mitigate PQ problems the PCC voltage *THD*s are decreased to 1.1% in phase *A*, 0.955% in phase *B* and 1% in phase *C*. Figures 4.56, 4.57 and 4.58 show the harmonic spectrum of source current waveforms.

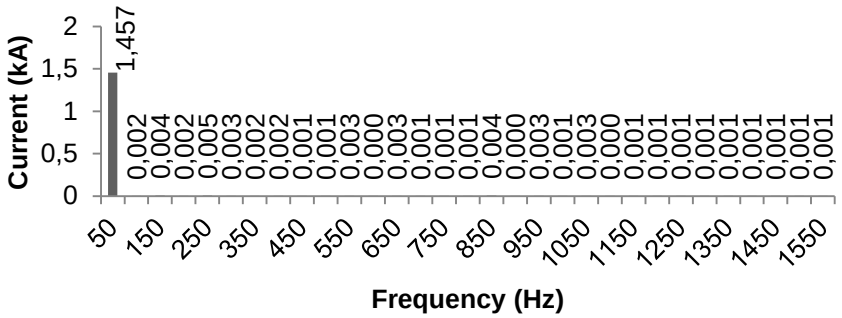

Figure 4.56. The harmonic spectrum of source current in phase A under heavy loaded system with high harmonic distortion, load unbalance and voltage regulation problems when the ML-MFGCI utilized.

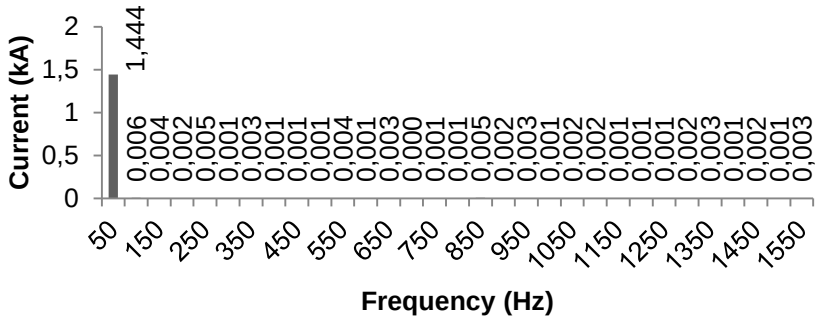

Figure 4.57. The harmonic spectrum of source current in phase B under heavy loaded system with high harmonic distortion, load unbalance and voltage regulation problems when the ML-MFGCI utilized.

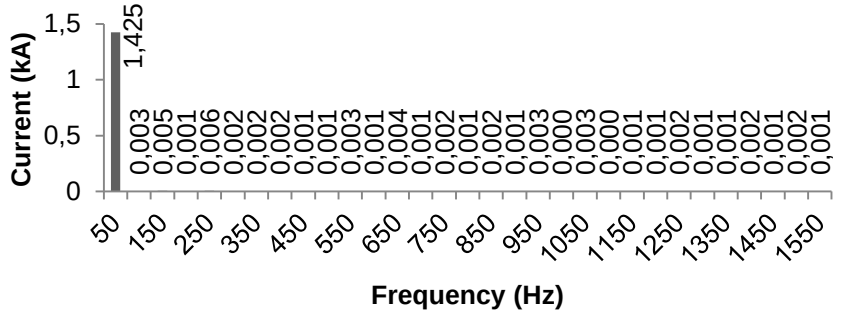

Figure 4.58. The harmonic spectrum of source current in phase C under heavy loaded system with high harmonic distortion, load unbalance and voltage regulation problems when the ML-MFGCI utilized.

The details of the source current harmonic contents are illustrated in Table 4.12.

Table 4.12. Harmonic contents of source currents under heavy loaded system with high harmonic distortion, load unbalance and voltage regulation problems when the ML-MFGCI utilized.

	Harmonic Contents of Source Current					
	Phase A		Phase B		Phase C	
Order	(%)	Value (kA)	(%)	Value (kA)	(%)	Value (kA)
1	100.000	0.74300	100.000	0.52600	100.000	0.53100
2	1.17442	0.00873	1.06059	0.00558	1.50029	0.00797
3	0.54434	0.00404	0.54371	0.00286	2.56233	0.01361
4	0.77535	0.00576	0.62086	0.00327	0.98822	0.00525
5	23.6789	0.17593	27.5546	0.14494	27.6808	0.14699
6	0.05895	0.00044	0.36383	0.00191	0.35342	0.00188
7	15.7324	0.11689	26.0308	0.13692	22.4764	0.11935
8	0.22772	0.00169	0.15318	0.00081	0.60193	0.00320
9	0.81729	0.00607	0.98942	0.00520	0.52255	0.00277
10	0.21978	0.00163	0.58016	0.00305	0.54140	0.00287
11	9.58291	0.07120	13.6608	0.07186	13.2647	0.07044
12	0.07994	0.00059	0.26242	0.00138	0.05882	0.00031
13	7.53517	0.05599	10.2018	0.05366	10.6294	0.05644
14	0.43461	0.00323	0.49587	0.00261	0.84697	0.00450
15	0.44796	0.00333	0.61760	0.00325	0.47658	0.00253
16	0.30635	0.00228	0.57919	0.00305	0.04632	0.00025
17	7.31826	0.05437	10.5823	0.05566	8.77967	0.04662
18	0.27452	0.00204	0.87173	0.00459	0.11811	0.00063
19	4.84264	0.03598	6.56938	0.03455	4.55880	0.02421
20	0.21178	0.00157	0.59596	0.00313	0.48521	0.00258
21	2.90449	0.02158	4.68024	0.02462	4.45316	0.02365
22	0.49601	0.00369	1.02695	0.00540	0.98201	0.00521
23	0.08995	0.00067	0.81751	0.00430	0.98032	0.00521
24	0.44921	0.00334	1.13199	0.00595	0.36099	0.00192
25	0.44978	0.00334	0.36960	0.00194	1.30351	0.00692
26	0.56922	0.00423	0.66874	0.00352	0.68270	0.00363
27	0.78552	0.00584	0.84979	0.00447	0.60703	0.00322
28	0.66598	0.00495	1.16137	0.00611	0.88882	0.00472
29	0.30896	0.00230	0.74998	0.00394	0.46747	0.00248
30	0.79149	0.00588	1.64545	0.00866	1.21435	0.00645
31	0.65909	0.00490	1.05499	0.00555	2.36145	0.01254
	THD=1.09%		THD=0.95%		THD=1%	

The Figure 4.59 shows the injected reactive power from ML-MFGCI into system to compensate reactive power and regulate PCC voltage.

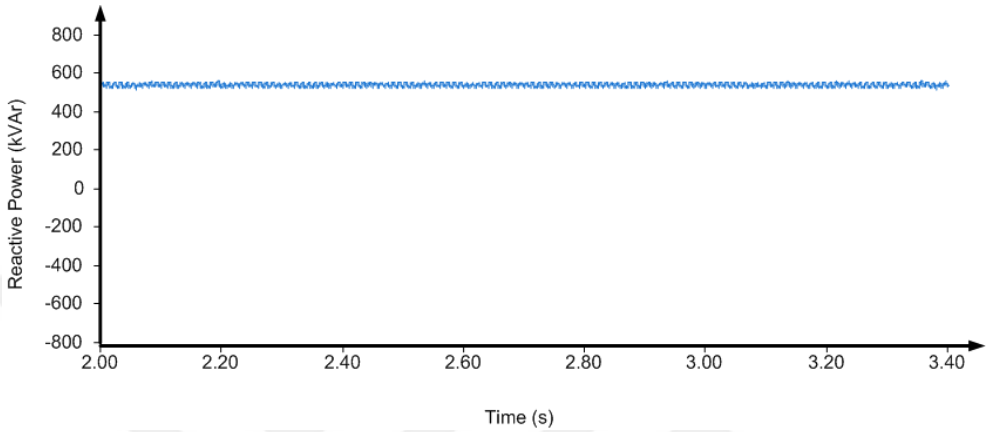

Figure 4.59. The injected reactive power from ML-MFGCI into system under heavy loaded system with high harmonic distortion, load unbalance and voltage regulation problems when the ML-MFGCI utilized.

Case3: In the presence case, to verify the efficiency of the ML-MFGCI in the transient conditions, the performance of the ML-MFGCI tested for simultaneously to compensate the reactive power, current and voltage harmonics and load balancing as well as voltage regulation during voltage sag in the heavy loaded system. Figure 4.60 shows the PCC phase voltage waveforms of under study heavy loaded system with high level voltage and current harmonic distortion, load unbalance and voltage regulation problems. In this case, the RMS value of phase voltages for phase *A, B* and *C* with 207.9 VRMS positive and 4.5 V_{RMS} negative sequence components are 204.4 V_{RMS}, 2012.7 V_{RMS} and 207 V_{RMS}, respectively. According to phase and line voltages with 10% voltage regulation problem the loads consumes 847 kVA with 0.95 *P.F* index.

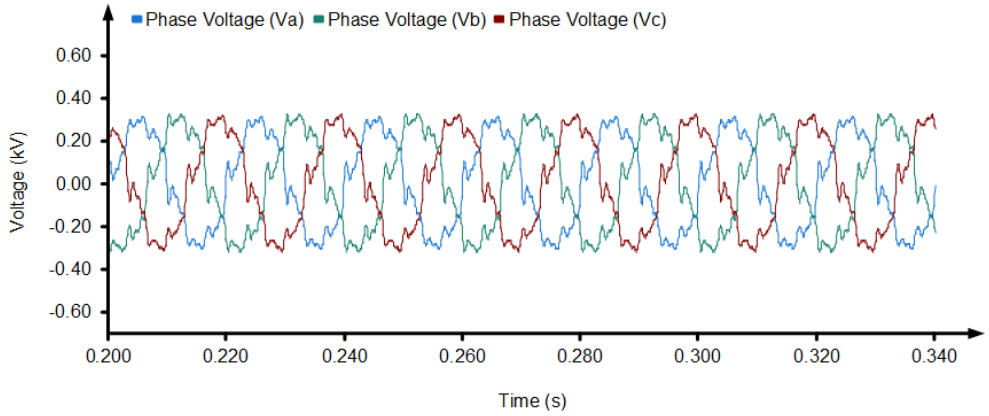

Figure 4.60. The PCC phase voltage waveforms under heavy loaded system with high harmonic distortion, load unbalance and voltage regulation problems.

The distorted PCC phase voltages have 19.5%, 19% and 20.2% *THD*'s in the phase *A*, *B* and *C*, respectively. In such condition the transformer's output voltage becomes as Figure 4.61 with 232 V_{RMS}, 233 V_{RMS} and 232 V_{RMS} RMS voltages for phase *A*, *B* and *C*, respectively.

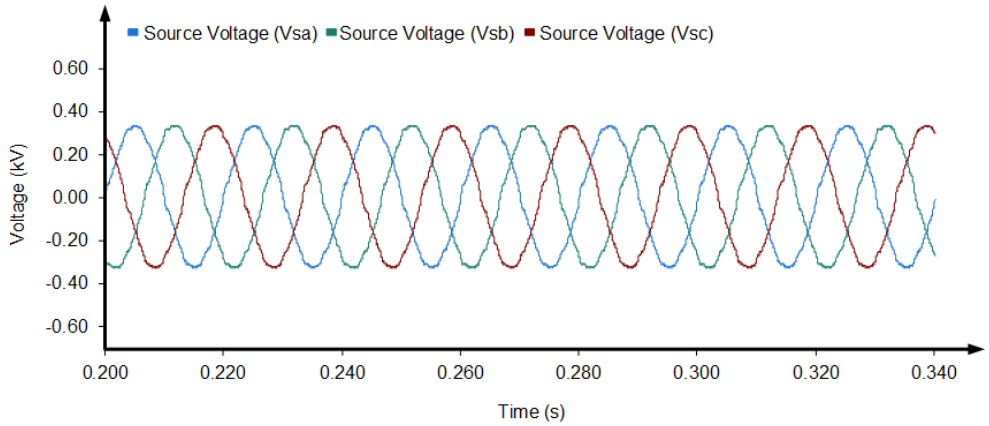

Figure 4.61. The transformer output voltage waveforms under heavy loaded system with high harmonic distortion, load unbalance and voltage regulation problems.

The distorted transformer's output voltage has 3.58%, 3.6% and 3.76% *THD*s in the phase *A*, *B* and *C*, respectively. The load draws 1.362 *kA*, 1.276 *kA* and 1.468 *kA* in phase *A*, *B* and *C*, respectively. Due to unbalance loaded the load currents becomes unbalance and emerge a negative sequence current. The load current has 1.3664 *kA* positive sequence component and 0.111 *kA* negative sequence component with 8% unbalance ratios in the load current. Figure 4.62 shows the load current waveforms under same condition. The load currents THD are 10.72%, 11% and 10.35% for phase *A*, *B* and *C*, respectively.

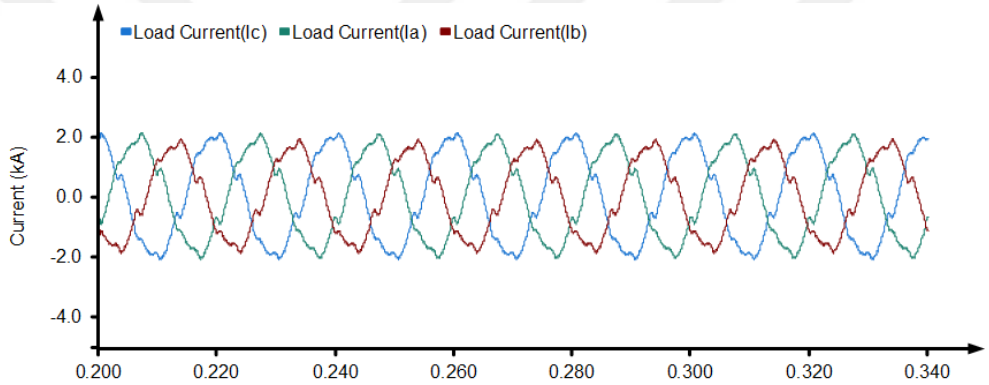

Figure 4.62. The load current waveforms under heavy loaded system with high harmonic distortion, load unbalance and voltage regulation problems.

As mentioned above the under study system has voltage regulation, voltage and current harmonic, negative sequence current and low *P.F.* index. In the previous section, the ability of the proposed ML-MFGCI has been tested to mitigate these problems. Results confirmed the effectiveness of the proposed multi-objective control method for ML-MFGCI to simultaneously eliminate voltage and currents distortions, compensate load unbalance and reactive power as well as regulate the PCC voltage. In addition to these problems if the voltage sag occurs in such system a mess condition appear in the power system. Here the effectiveness of the proposed multi-objective control method for ML-MFGCI to this condition with

15% voltage sags. Figure 4.63 shows the source voltage waveform when under study power system during voltage sag supports with ML-MFGCI.

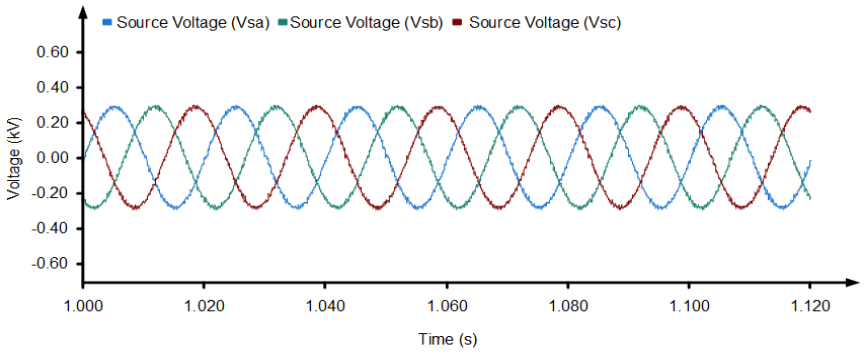

Figure 4.63. The transformer output voltage waveforms under heavy loaded system with high harmonic distortion, load unbalance and voltage regulation problems during voltage sag condition.

By utilizing ML-MFGCI the transformer's output voltage *THD*s are decreased from 3.58% to 1.1% in phase *A*, 3.6% to 1.05% in phase *B* and 3.76% to 0.84% in phase *C*. Figures 4.64, 4.65 and 4.66 show the harmonic spectrum of the transformer's output phase voltages when the ML-MFGCI utilized to mitigate PQ problems.

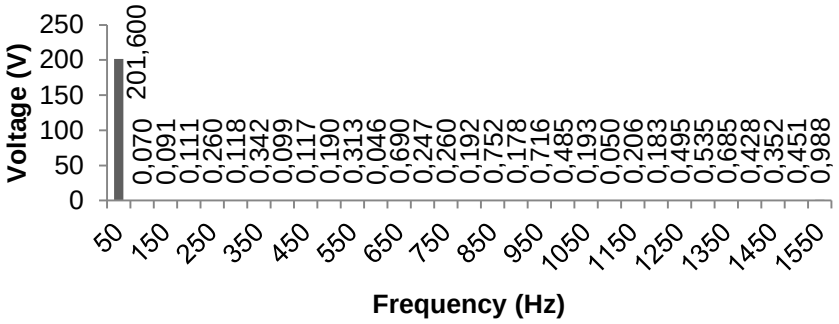

Figure 4.64. The harmonic spectrum of transformer's output voltage in phase *A* under heavy loaded system with high harmonic distortion, load unbalance and voltage regulation problems during voltage sag when the ML-MFGCI utilized.

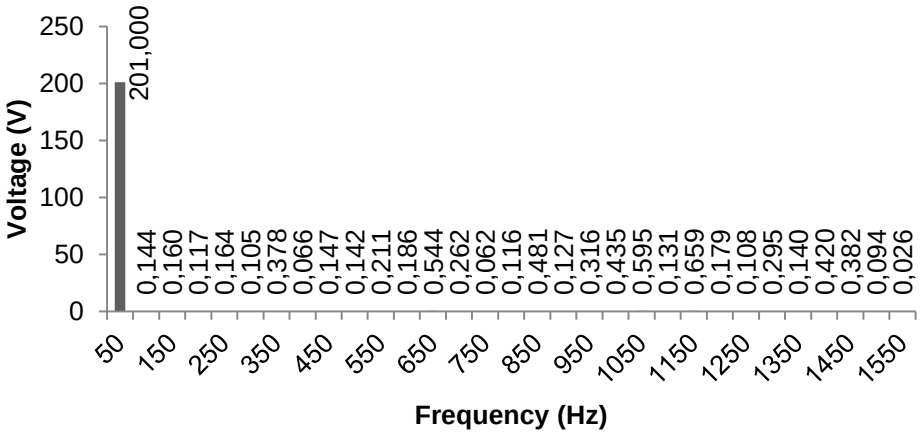

Figure 4.65. The harmonic spectrum of transformer's output voltage in phase *B* under heavy loaded system with high harmonic distortion, load unbalance and voltage regulation problems during voltage sag when the ML-MFGCI utilized.

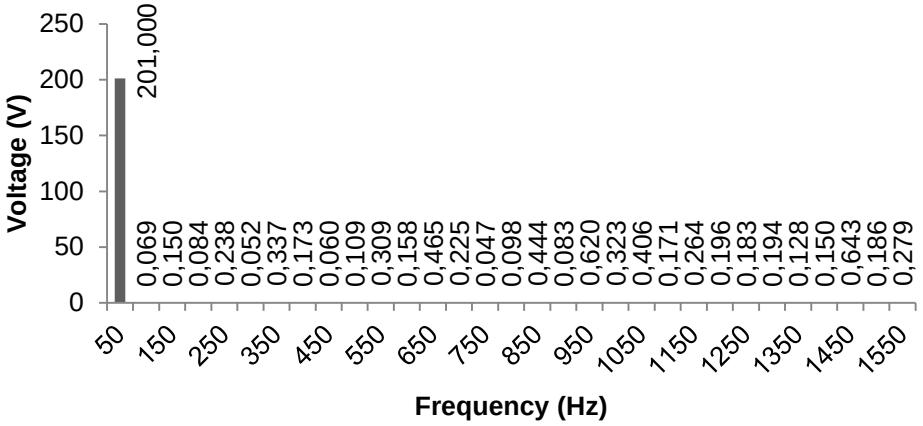

Figure 4.66. The harmonic spectrum of transformer's output voltage in phase *C* under heavy loaded system with high harmonic distortion, load unbalance and voltage regulation problems during voltage sag when the ML-MFGCI utilized.

Table 4.13illustrate the transformer's output voltages harmonic content in details when ML-MFGCI utilized to mitigate PQ problems.

Table 4.13. Harmonic contents of transformer's output voltages under heavy loaded system with high harmonic distortion, load unbalance and voltage regulation problems during voltage sag when the ML-MFGCI utilized.

	Harmonic Contents of Source Voltage					
	Phase A		Phase B		Phase C	
Order	(%)	Value (V)	(%)	Value (V)	(%)	Value (V)
1	100.000	201.600	100.000	201.000	100.000	201.000
2	0.03475	0.07005	0.07158	0.14388	0.03419	0.06873
3	0.04492	0.09056	0.07936	0.15951	0.07452	0.14978
4	0.05507	0.11102	0.05830	0.11719	0.04188	0.08418
5	0.12911	0.26029	0.08161	0.16405	0.11837	0.23792
6	0.05854	0.11802	0.05216	0.10484	0.02579	0.05184
7	0.16984	0.34240	0.18794	0.37776	0.16746	0.33660
8	0.04933	0.09945	0.03280	0.06592	0.08613	0.17313
9	0.05810	0.11714	0.07292	0.14657	0.03004	0.06038
10	0.09447	0.19045	0.07080	0.14230	0.05406	0.10866
11	0.15533	0.31315	0.10490	0.21085	0.15367	0.30887
12	0.02295	0.04626	0.09248	0.18589	0.07864	0.15806
13	0.34226	0.68999	0.27079	0.54430	0.23130	0.46490
14	0.12253	0.24701	0.13013	0.26156	0.11186	0.22483
15	0.12915	0.26036	0.03084	0.06199	0.02342	0.04707
16	0.09510	0.19173	0.05748	0.11554	0.04898	0.09844
17	0.37300	0.75197	0.23907	0.48053	0.22094	0.44408
18	0.08852	0.17845	0.06301	0.12666	0.04150	0.08341
19	0.35536	0.71641	0.15736	0.31630	0.30838	0.61984
20	0.24061	0.48506	0.21648	0.43513	0.16087	0.32335
21	0.09555	0.19264	0.29597	0.59490	0.20215	0.40632
22	0.02471	0.04982	0.06528	0.13122	0.08511	0.17107
23	0.10194	0.20550	0.32769	0.65866	0.13123	0.26377
24	0.09086	0.18317	0.08888	0.17866	0.09767	0.19632
25	0.24547	0.49488	0.05367	0.10787	0.09123	0.18337
26	0.26530	0.53484	0.14655	0.29457	0.09639	0.19374
27	0.33993	0.68530	0.06947	0.13963	0.06365	0.12793
28	0.21246	0.42833	0.20906	0.42021	0.07476	0.15027
29	0.17449	0.35176	0.18999	0.38189	0.31972	0.64263
30	0.22385	0.45128	0.04694	0.09435	0.09263	0.18619
31	0.49031	0.98847	0.01270	0.02553	0.13867	0.27872
	THD=1.10%		THD=1.05%		THD=0.84%	

Figure 4.67 shows the PCC phase voltages waveforms when the ML-MFGCI utilized to mitigate PQ problems. By utilizing ML-MFGCI the PCC voltages are increased from 172.28 V_{RMS} to 208.5 V_{RMS}, 179.3 V_{RMS} to 207.8 V_{RMS} and 175.2 V_{RMS} to 209 V_{RMS}. Moreover, the PCC phase voltages become balance in 225 V_{RMS}.

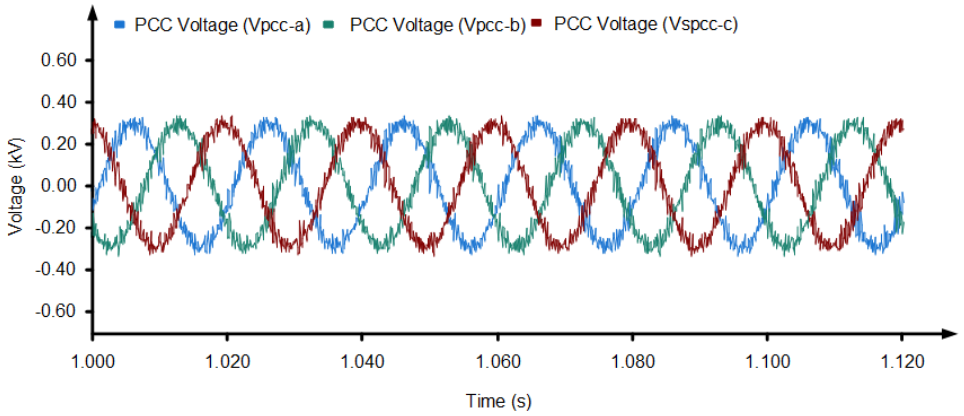

Figure 4.67. The PCC voltage waveforms under heavy loaded system with high harmonic distortion, load unbalance and voltage regulation problems during voltage sag condition.

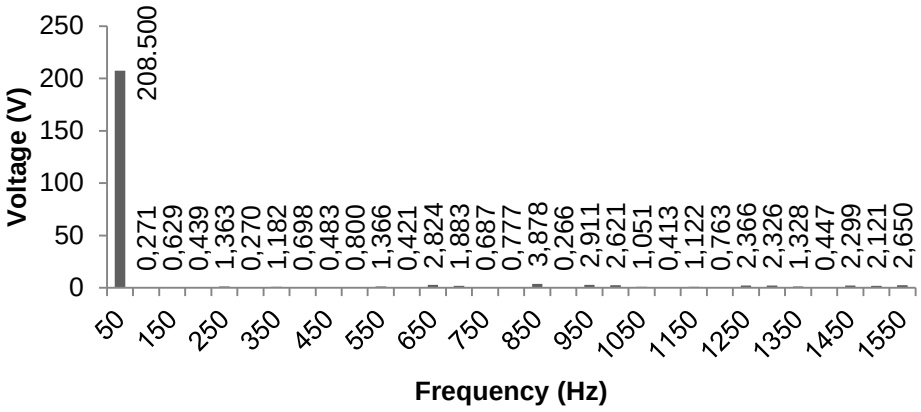

Figure 4.68. The harmonic spectrum of PCC voltage in phase *A* under heavy loaded system with high harmonic distortion, load unbalance and voltage regulation problems during voltage sag when the ML-MFGCI utilized.

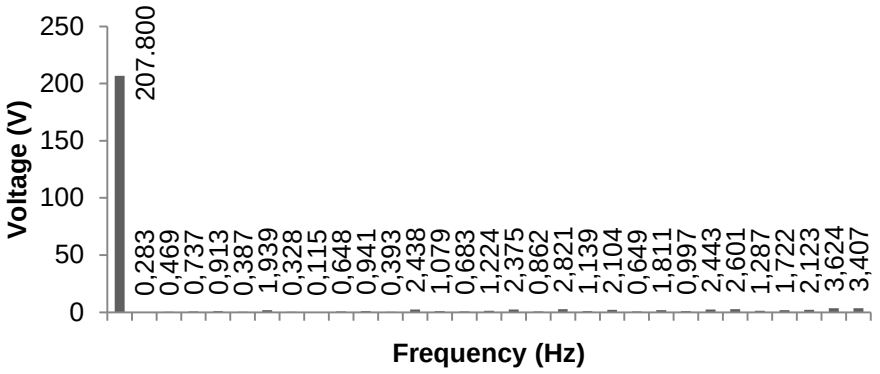

Figure 4.69. The harmonic spectrum of PCC voltage in phase *B* under heavy loaded system with high harmonic distortion, load unbalance and voltage regulation problems during voltage sag when the ML-MFGCI utilized.

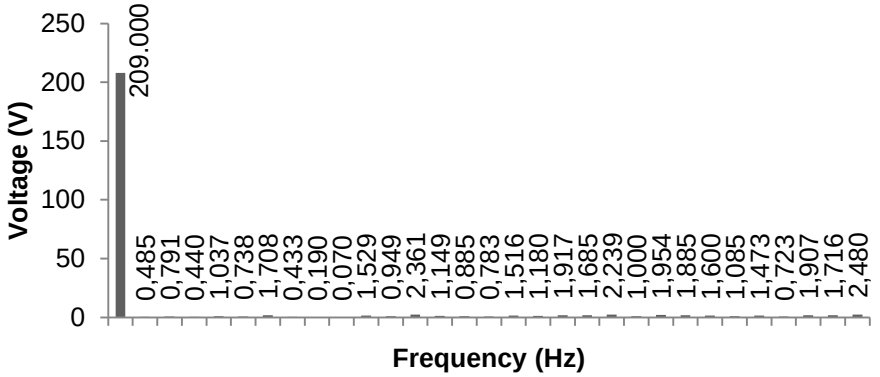

Figure 4.70. The harmonic spectrum of PCC voltage in phase *C* under heavy loaded system with high harmonic distortion, load unbalance and voltage regulation problems during voltage sag when the ML-MFGCI utilized.

The details of the PCC phase voltage harmonic contents are illustrated in Table 4.14. The PCC voltage *THD*s are 4.82%, 4.52% and 3.5% for phase *A*, *B* and *C*, respectively.

Table 4.14. Harmonic contents of PCC phase voltages under heavy loaded system with high harmonic distortion, load unbalance and voltage regulation problems during voltage sag when the ML-MFGCI utilized.

	Harmonic Contents of PCC Voltage					
	Phase A		Phase B		Phase C	
Order	(%)	Value (V)	(%)	Value (V)	(%)	Value (V)
1	100.000	208.500	100.000	207.800	100.000	209.000
2	0.13060	0.27100	0.13701	0.28334	0.23322	0.48509
3	0.30332	0.62940	0.22662	0.46865	0.38034	0.79110
4	0.21170	0.43928	0.35654	0.73732	0.21160	0.44012
5	0.65668	1.36262	0.44131	0.91263	0.49859	1.03707
6	0.13014	0.27004	0.18699	0.38669	0.35461	0.73758
7	0.56966	1.18205	0.93780	1.93937	0.82132	1.70834
8	0.33636	0.69796	0.15849	0.32775	0.20841	0.43348
9	0.23286	0.48318	0.05570	0.11518	0.09158	0.19048
10	0.38556	0.80004	0.31325	0.64780	0.03346	0.06959
11	0.65826	1.36589	0.45521	0.94138	0.73493	1.52866
12	0.20304	0.42131	0.18998	0.39288	0.45610	0.94870
13	1.36108	2.82424	1.17899	2.43815	1.13500	2.36079
14	0.90768	1.88344	0.52177	1.07902	0.55220	1.14857
15	0.33089	0.68659	0.33037	0.68321	0.42559	0.88523
16	0.37459	0.77728	0.59182	1.22387	0.37661	0.78335
17	1.86868	3.87750	1.14859	2.37527	0.72895	1.51621
18	0.12802	0.26564	0.41664	0.86161	0.56721	1.17979
19	1.40283	2.91087	1.36411	2.82098	0.92160	1.91694
20	1.26307	2.62087	0.55087	1.13920	0.80999	1.68477
21	0.50664	1.05128	1.01745	2.10408	1.07649	2.23911
22	0.19891	0.41274	0.31373	0.64880	0.48061	0.99967
23	0.54085	1.12226	0.87596	1.81149	0.93933	1.95380
24	0.36789	0.76338	0.48202	0.99682	0.90640	1.88530
25	1.14026	2.36605	1.18148	2.44331	0.76926	1.60006
26	1.12118	2.32644	1.25793	2.60139	0.52142	1.08456
27	0.63985	1.32770	0.62237	1.28706	0.70798	1.47260
28	0.21519	0.44651	0.83289	1.72243	0.34749	0.72278
29	1.10815	2.29942	1.02649	2.12278	0.91679	1.90692
30	1.02231	2.12129	1.75256	3.62429	0.82510	1.71620
31	1.27729	2.65037	1.64755	3.40712	1.19231	2.48001
	THD=4.82%		THD=4.52%		THD=3.50%	

To compensate the harmonic distortions, load unbalance and reactive power as well as control the PCC voltage the ML-MFGCI injects the required

current to system. In this case the ML-MFGC injects 1.286 kA to phase A, 1.079 kA to phase B and 1.12 kA to phase C with 0.130 kA negative sequence current into system. Figure 4.71 shows the injected current by the ML-MFGCI into system.

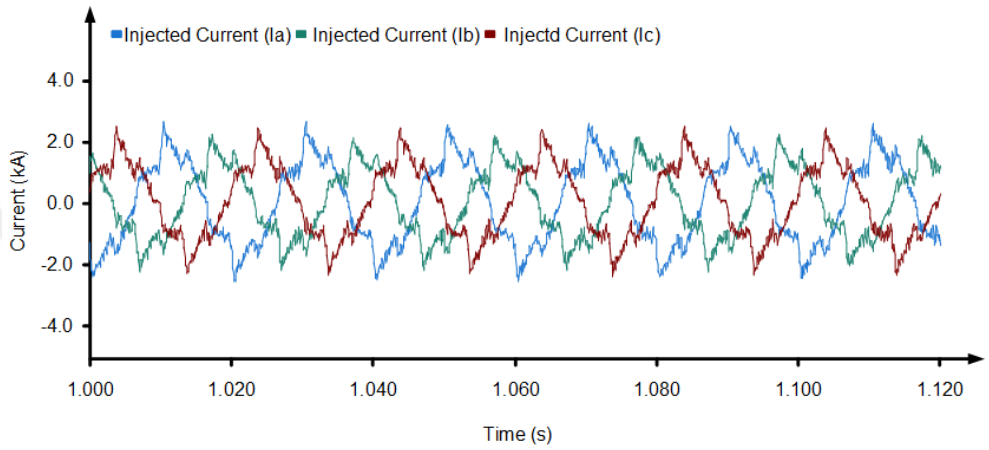

Figure 6.71. The injected current waveforms under heavy loaded system with high harmonic distortion, load unbalance and voltage regulation problems during voltage sag condition.

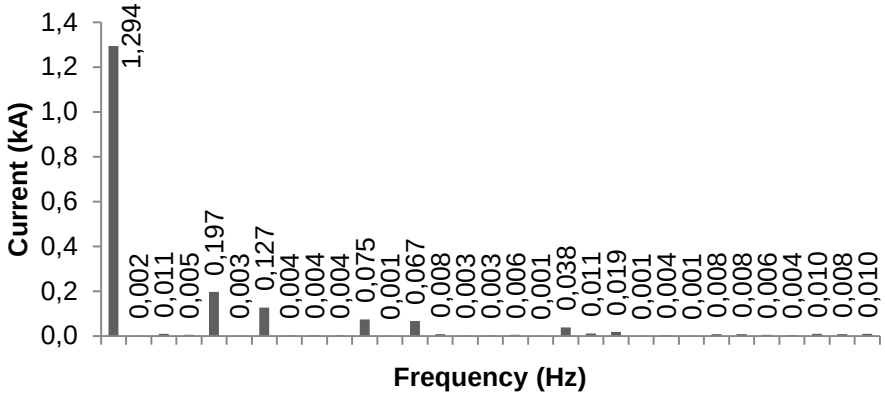

Figure 4.72. The harmonic spectrum of injected current in phase *A* by the ML-MFGCI under heavy loaded system with high harmonic distortion, load unbalance and voltage regulation problems during voltage sag condition.

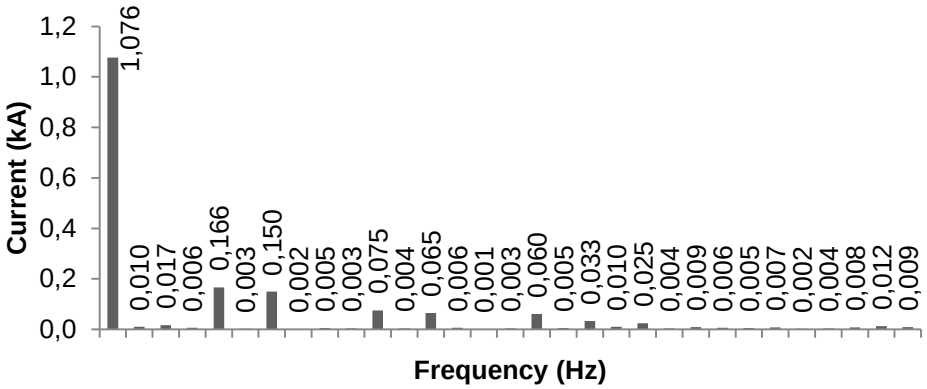

Figure 4.73. The harmonic spectrum of injected current in phase *B* by the ML-MFGCI under heavy loaded system with high harmonic distortion, load unbalance and voltage regulation problems during voltage sag condition.

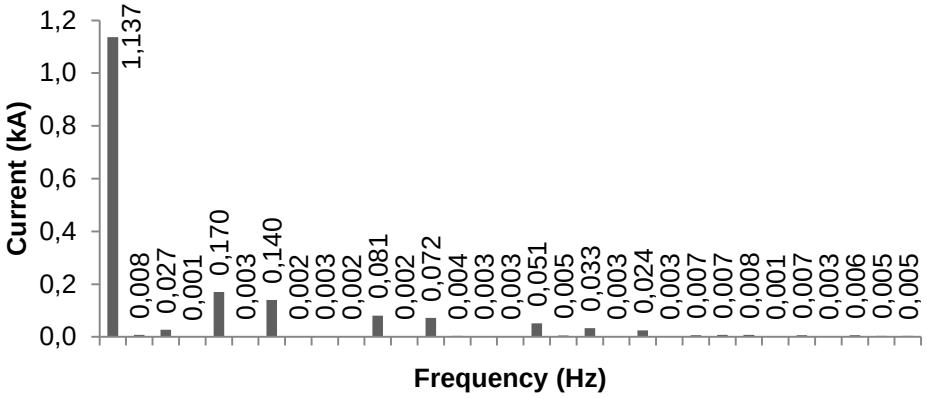

Figure 4.74. The harmonic spectrum of injected current in phase B by the ML-MFGCI under heavy loaded system with high harmonic distortion, load unbalance and voltage regulation problems during voltage sag condition.

The details of the source current harmonic contents are illustrated in Table 4.15.

Table 4.15. Harmonic contents of injected currents by ML-MFGCI under heavy loaded system with high harmonic distortion, load unbalance and voltage regulation problems.

	Harmonic Contents of Injected Current					
	Phase A		Phase B		Phase C	
Order	(%)	Value (kA)	(%)	Value (kA)	(%)	Value (kA)
1	100.000	1.29440	100.000	1.07600	100.000	1.13700
2	0.17428	0.00226	0.89822	0.00966	0.67460	0.00767
3	0.82193	0.01064	1.53861	0.01656	2.39717	0.02726
4	0.40407	0.00523	0.53563	0.00576	0.05576	0.00063
5	15.2547	0.19746	15.4737	0.16650	14.9855	0.17039
6	0.19664	0.00255	0.28276	0.00304	0.29603	0.00337
7	9.84536	0.12744	13.9032	0.14960	12.2908	0.13975
8	0.28126	0.00364	0.16806	0.00181	0.21272	0.00242
9	0.34140	0.00442	0.42279	0.00455	0.30320	0.00345
10	0.30916	0.00400	0.29391	0.00316	0.17986	0.00205
11	5.78545	0.07489	6.95840	0.07487	7.14225	0.08121
12	0.10457	0.00135	0.34522	0.00371	0.21155	0.00241
13	5.19958	0.06730	6.04399	0.06503	6.32260	0.07189
14	0.63418	0.00821	0.55324	0.00595	0.39069	0.00444
15	0.20342	0.00263	0.10578	0.00114	0.28470	0.00324
16	0.21200	0.00274	0.31394	0.00338	0.28145	0.00320
17	0.48786	0.00631	5.61572	0.06043	4.49382	0.05109
18	0.05730	0.00074	0.47318	0.00509	0.43204	0.00491
19	2.96506	0.03838	3.03589	0.03267	2.90825	0.03307
20	0.84593	0.01095	0.90617	0.00975	0.24366	0.00277
21	1.48506	0.01922	2.28029	0.02454	2.13054	0.02422
22	0.06200	0.00080	0.36890	0.00397	0.30083	0.00342
23	0.32395	0.00419	0.85405	0.00919	0.60226	0.00685
24	0.11308	0.00146	0.54061	0.00582	0.63825	0.00726
25	0.64739	0.00838	0.50316	0.00541	0.69469	0.00790
26	0.64281	0.00832	0.66862	0.00719	0.09680	0.00110
27	0.46983	0.00608	0.18532	0.00199	0.59765	0.00680
28	0.33722	0.00436	0.36264	0.00390	0.24700	0.00281
29	0.77819	0.01007	0.75452	0.00812	0.54460	0.00619
30	0.62928	0.00815	1.14335	0.01230	0.41673	0.00474
31	0.76955	0.00996	0.83139	0.00895	0.40995	0.00466

Figure 4.75 shows the source current waveforms when the ML-MFGCI utilized to mitigate PQ problems. By utilizing ML-MFGCI the source current

becomes as pure sinusoidal waveform. The drown current from source with ML-MFGCI are as 1.606 *kA* for phase *A*, 1.584 *kA* for phase *B* and 1.588 *kA* for phase *C*. Moreover negative sequence of source current decrees to 0.016 *kA* and current unbalance ration reduce to 1%.

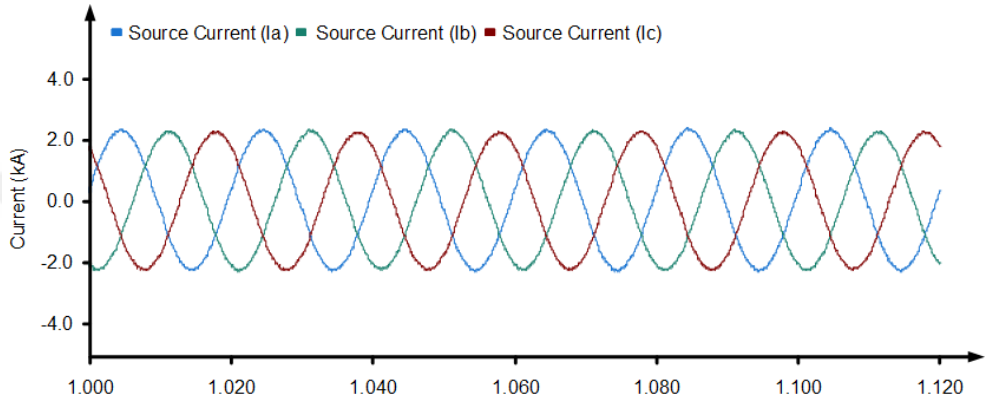

Figure 4.75. The source current waveforms under heavy loaded system with high harmonic distortion, load unbalance and voltage regulation problems during voltage sag when ML-MFGCI utilized.

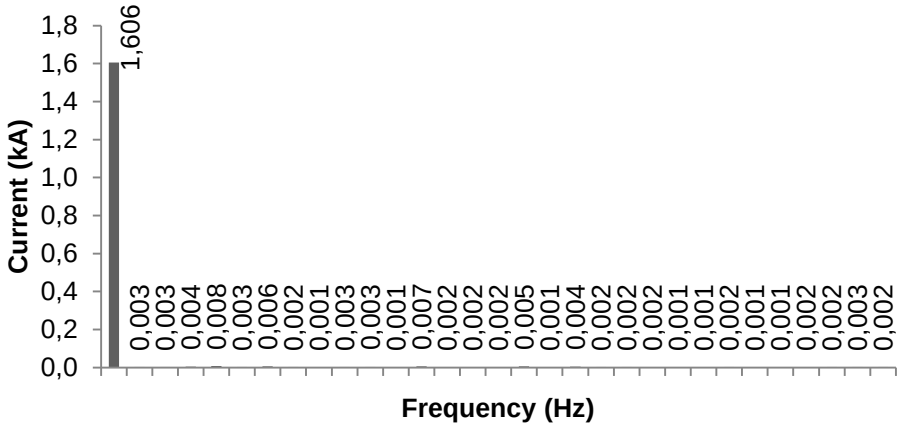

Figure 4.76. The harmonic spectrum of source current in phase *A* under heavy loaded system with high harmonic distortion, load unbalance and voltage regulation problems during voltage sag when the ML-MFGCI utilized.

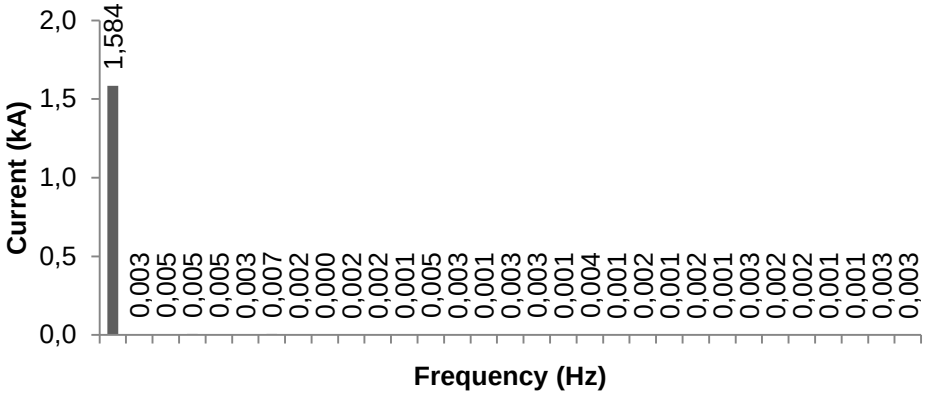

Figure 4.77. The harmonic spectrum of source current in phase *B* under heavy loaded system with high harmonic distortion, load unbalance and voltage regulation problems during voltage sag when the ML-MFGCI utilized.

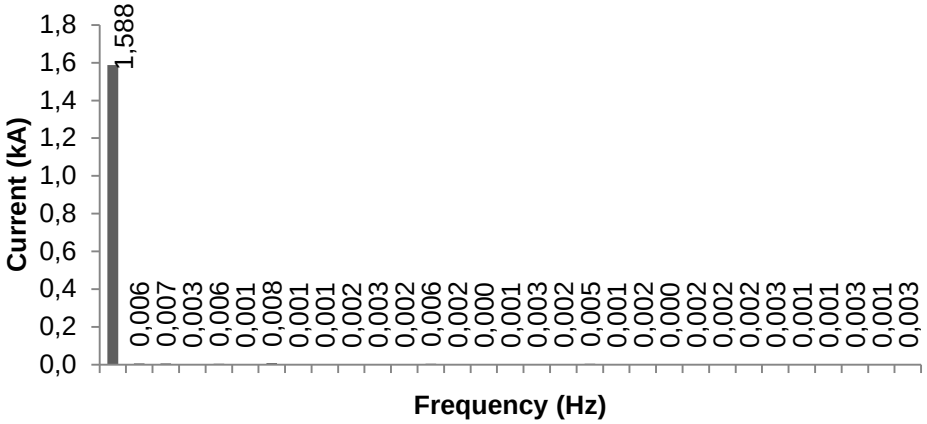

Figure 4.78. The harmonic spectrum of source current in phase *C* under heavy loaded system with high harmonic distortion, load unbalance and voltage regulation problems during voltage sag when the ML-MFGCI utilized.

The details of the source current harmonic contents are illustrated in Table 4.16.

Table 4.16. Harmonic contents of source currents under heavy loaded system with high harmonic distortion, load unbalance and voltage regulation problems when the ML-MFGCI utilized.

	Harmonic Contents of Source Current					
	Phase A		Phase B		Phase C	
Order	(%)	Value (kA)	(%)	Value (kA)	(%)	Value (kA)
1	100.000	1.60560	100.000	1.58350	100.000	1.58760
2	0.17934	0.00288	0.19800	0.00314	0.40001	0.00635
3	0.17943	0.00288	0.31726	0.00502	0.44336	0.00704
4	0.25564	0.00411	0.34663	0.00549	0.19824	0.00315
5	0.48817	0.00784	0.32986	0.00522	0.34976	0.00555
6	0.18904	0.00304	0.16720	0.00265	0.05178	0.00082
7	0.39354	0.00632	0.42457	0.00672	0.48999	0.00778
8	0.14059	0.00226	0.09511	0.00151	0.06725	0.00107
9	0.06062	0.00097	0.02950	0.00047	0.05718	0.00091
10	0.18801	0.00302	0.11949	0.00189	0.09483	0.00151
11	0.21769	0.00350	0.12875	0.00204	0.20571	0.00327
12	0.07511	0.00121	0.05665	0.00090	0.14426	0.00229
13	0.42921	0.00690	0.33025	0.00523	0.34736	0.00551
14	0.09410	0.00151	0.16891	0.00267	0.11269	0.00179
15	0.09823	0.00158	0.09468	0.00150	0.01622	0.00026
16	0.11497	0.00185	0.16546	0.00262	0.05797	0.00092
17	0.32715	0.00526	0.21195	0.00336	0.17713	0.00281
18	0.05396	0.00087	0.06285	0.00100	0.09512	0.00151
19	0.24125	0.00388	0.26399	0.00418	0.31639	0.00502
20	0.12609	0.00203	0.07188	0.00114	0.08915	0.00142
21	0.12611	0.00203	0.15369	0.00243	0.13868	0.00220
22	0.10570	0.00170	0.06132	0.00097	0.01058	0.00017
23	0.03851	0.00062	0.14534	0.00230	0.15235	0.00242
24	0.04032	0.00065	0.08640	0.00137	0.10459	0.00166
25	0.12175	0.00196	0.16756	0.00265	0.12387	0.00197
26	0.08530	0.00137	0.13614	0.00216	0.17810	0.00283
27	0.06450	0.00104	0.11636	0.00184	0.08180	0.00130
28	0.11061	0.00178	0.05173	0.00082	0.05777	0.00092
29	0.14498	0.00233	0.07035	0.00111	0.21521	0.00342
30	0.16419	0.00264	0.15845	0.00251	0.07273	0.00115
31	0.13497	0.00217	0.16470	0.00261	0.18557	0.00295
	THD=1.01%		THD=1.14%		THD=1.05%	

Figure 4.79 shows the line voltage during steady-state and voltage sag condition. The ML-MFGCI keeps the phase and line voltage within standard limits. In this condition the line voltage is 362 V.

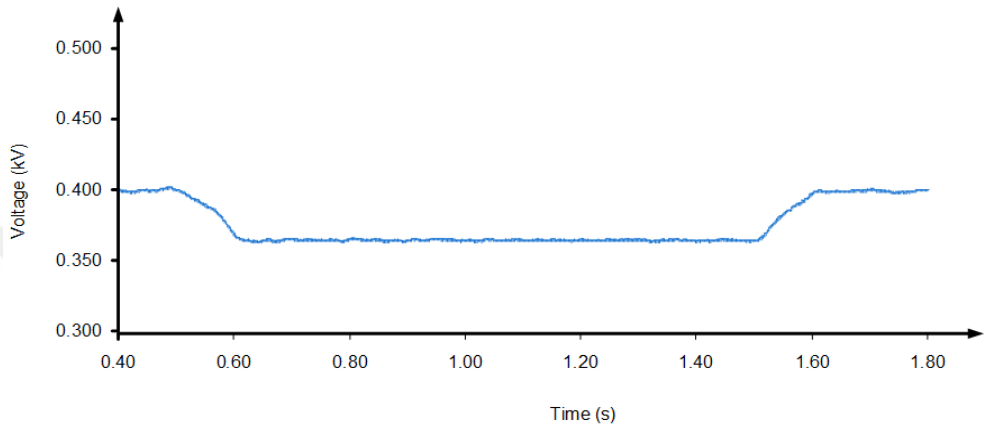

Figure 4.79. The line voltage during voltage sag when ML-MFGCI utilized.

The Figure 4.80 shows the injected reactive power from ML-MFGCI into system to compensate reactive power and regulate PCC voltage. It should be noted that to compensate voltage sag a 20% overload of ML-MFGCI allowed due to the capacity limits of the ML-MFGCI.

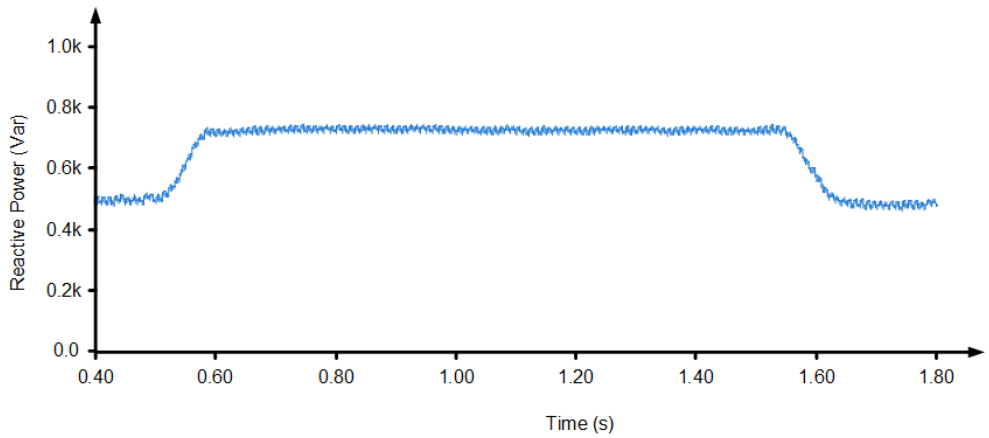

Figure 4.80. The injected reactive power from ML-MFGCI into system.

However to avoid overload of ML-MFGCI we can omit the harmonic and unbalance compensation during voltage sag or voltage swell. Figures 4.81, 4.82 and 4.83 shows the source voltage, PCC voltage and source current without harmonic and unbalance load compensation during voltage sag.

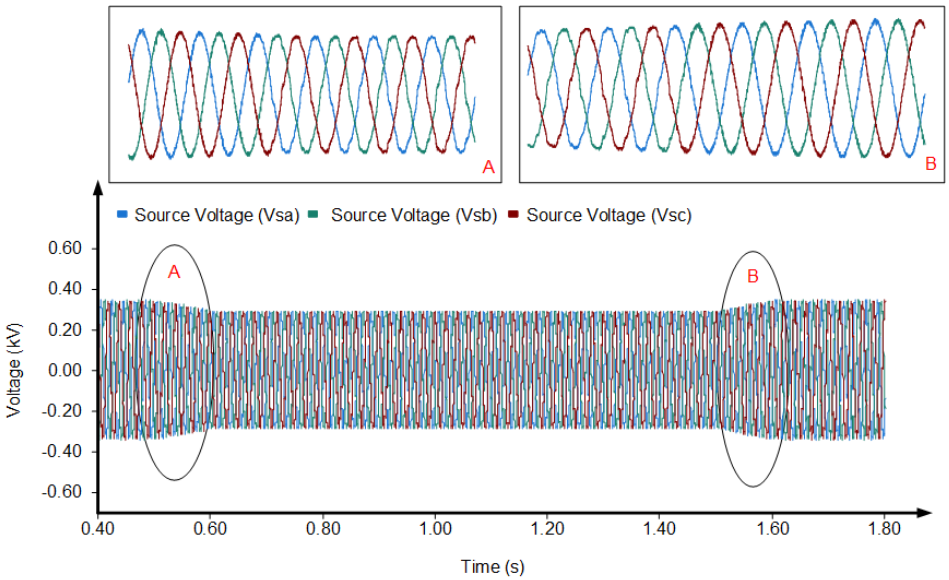

Figure 4.81. The transformer output voltage waveforms under heavy loaded system with high harmonic distortion, load unbalance and voltage regulation problems without harmonic and load unbalance compensation during voltage sag condition.

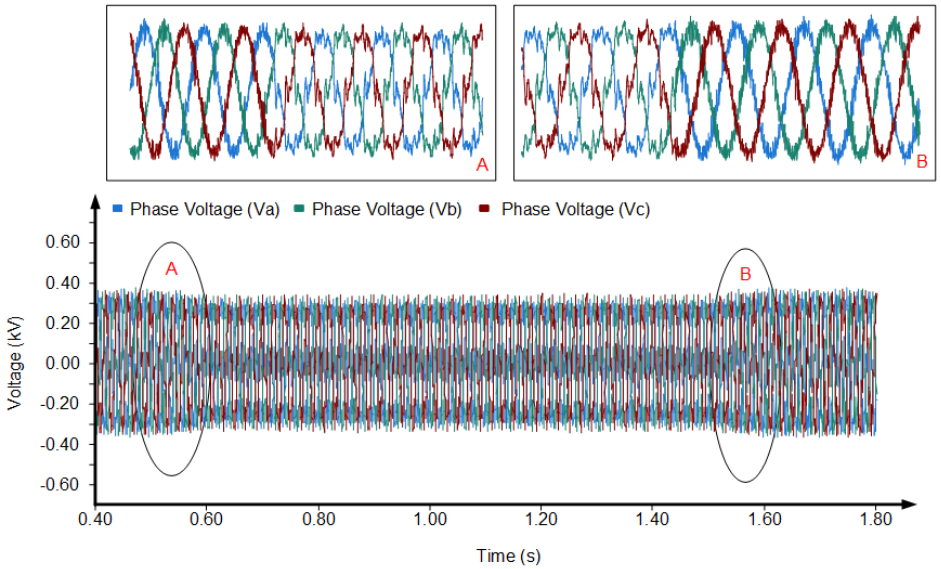

Figure 4.82. The PCC voltage waveforms under heavy loaded system with high harmonic distortion, load unbalance and voltage regulation problems without harmonic and load unbalance compensation during voltage sag condition.

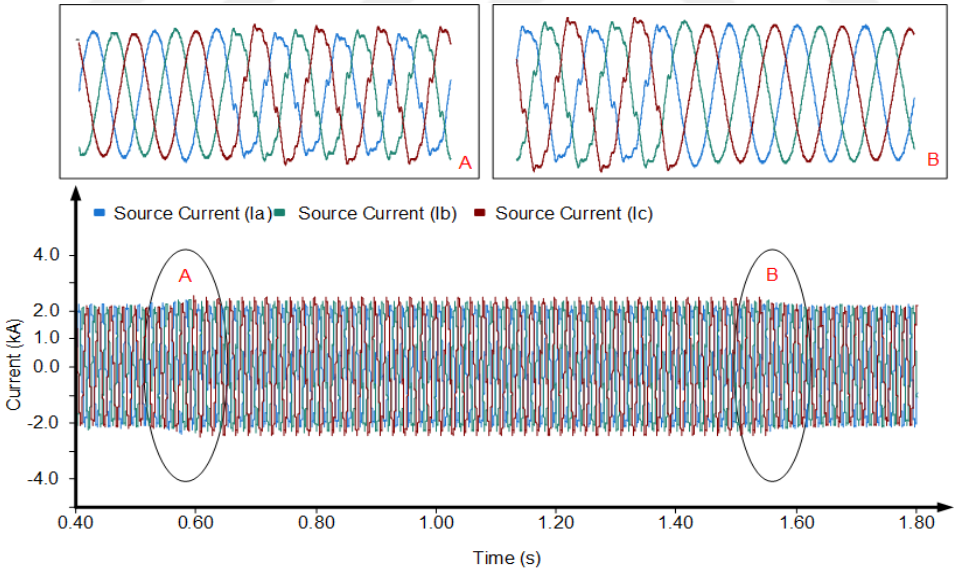

Figure 4.83. The source current waveforms under heavy loaded system with high harmonic distortion, load unbalance and voltage regulation problems without harmonic and load unbalance compensation during voltage sag condition.

The figure 4.84 shows the difference of injected reactive power for compensation of the voltage sag with and without harmonics and load unbalance compensation during voltage sag.

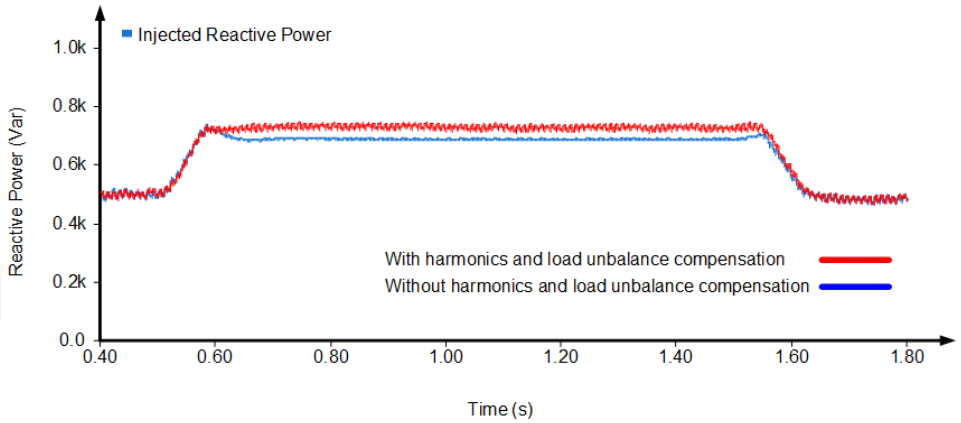

Figure 4.84. Reactive power requirement for voltage sag compensation with and without harmonics and load unbalance compensation.

Case4: In the previous sections the effectiveness of the proposed ML-MFGCI tested for harmonic elimination, load unbalance and reactive power compensation; and PCC voltage regulation as well as voltage sag compensation. Here the effectiveness of the proposed multi-objective control method for ML-MFGCI to this condition with 22.5% voltage swell. Figure 4.85 shows the source voltage waveform when under study power system supports with ML-MFGCI during voltage swell.

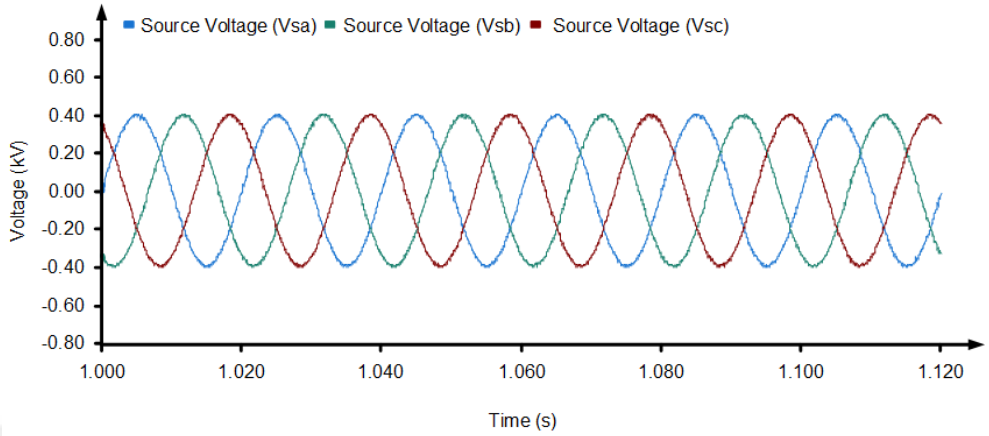

Figure 4.85. The transformer output voltage waveforms under heavy loaded system with high harmonic distortion, load unbalance and voltage regulation problems during voltage swell condition.

During voltage swell the source voltage raised to 280.5 V_{RMS} in phase *A*, 286.3 V_{RMS} in phase *B* and 284.6 V_{RMS} in phase *C*. the source voltage THDs are 3% in phase *A*, 2.96% in phase *B* and %3.12 in phase *C*. By utilizing ML-MFGCI during 22.5% voltage swell the transformer's output voltage *THD*s are decreased from 3% to 0.25% in phase *A*, 2.96% to 0.25% in phase *B* and 3.12% to 0.24% in phase *C*. Figures 4.86, 4.87 and 4.88 show the harmonic spectrum of the transformer's output phase voltages when the ML-MFGCI utilized to mitigate PQ problems.

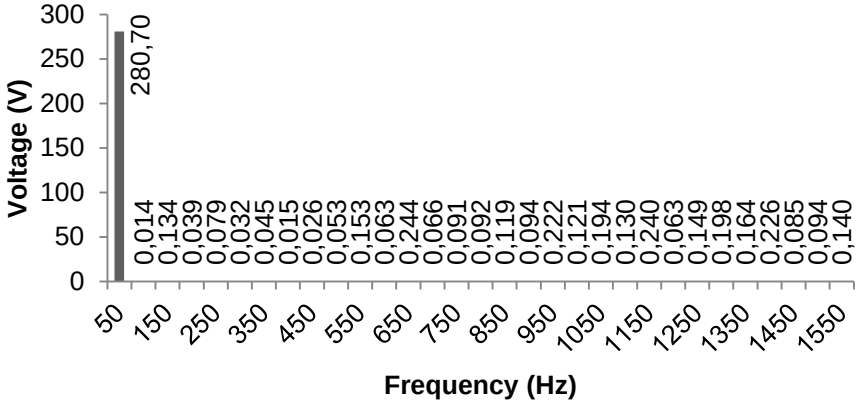

Figure 4.86. The harmonic spectrum of transformer's output voltage in phase A under heavy loaded system with high harmonic distortion, load unbalance and voltage regulation problems during voltage sag when the ML-MFGCI utilized.

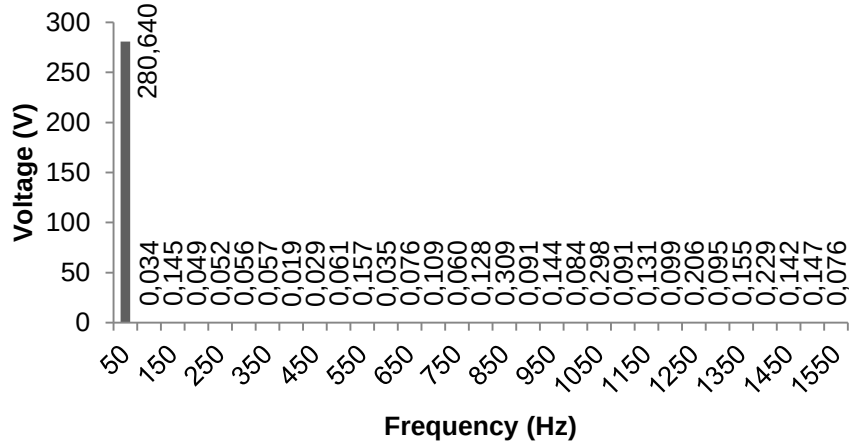

Figure 4.87. The harmonic spectrum of transformer's output voltage in phase B under heavy loaded system with high harmonic distortion, load unbalance and voltage regulation problems during voltage sag when the ML-MFGCI utilized.

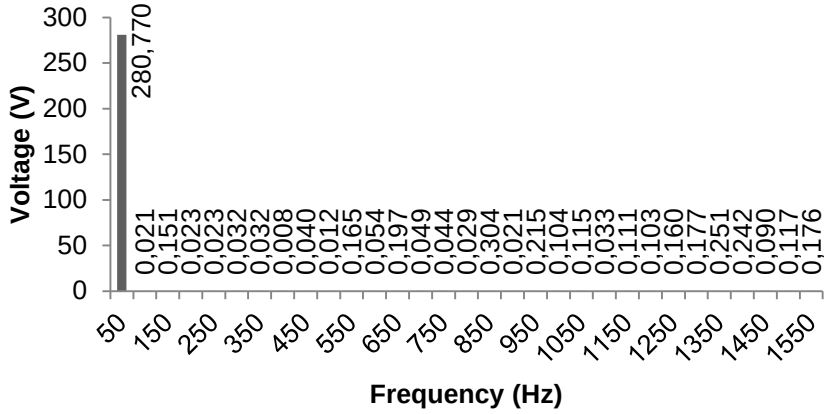

Figure 4.88. The harmonic spectrum of transformer's output voltage in phase C under heavy loaded system with high harmonic distortion, load unbalance and voltage regulation problems during voltage sag when the ML-MFGCI utilized.

Table 4.17 illustrate the transformer's output voltages harmonic content in details when ML-MFGCI utilized to mitigate PQ problems.

Table 4.17. Harmonic contents of transformer's output voltages under heavy loaded system with high harmonic distortion, load unbalance and voltage regulation problems during voltage swell when the ML-MFGCI utilized.

	Harmonic Contents of Source Voltage					
	Phase A		Phase B		Phase C	
Order	(%)	Value (V)	(%)	Value (V)	(%)	Value (V)
1	100.000	280.700	100.000	280.640	100.000	280.770
2	0.00513	0.01439	0.01216	0.03412	0.00757	0.02125
3	0.04772	0.13396	0.05168	0.14504	0.05396	0.15149
4	0.01378	0.03869	0.01730	0.04855	0.00836	0.02346
5	0.02826	0.07933	0.01871	0.05249	0.00830	0.02330
6	0.01135	0.03186	0.01990	0.05585	0.01127	0.03164
7	0.01599	0.04488	0.02032	0.05702	0.01144	0.03212
8	0.00528	0.01482	0.00690	0.01935	0.00269	0.00756
9	0.00916	0.02570	0.01040	0.02920	0.01426	0.04003
10	0.01881	0.05280	0.02191	0.06148	0.00424	0.01190
11	0.05461	0.15330	0.05609	0.15740	0.05881	0.16511
12	0.02235	0.06273	0.01230	0.03453	0.01923	0.05398
13	0.08704	0.24432	0.02700	0.07578	0.07032	0.19745
14	0.02362	0.06629	0.03868	0.10856	0.01757	0.04934
15	0.03248	0.09116	0.02126	0.05966	0.01581	0.04438
16	0.03273	0.09188	0.04569	0.12822	0.01015	0.02850
17	0.04243	0.11910	0.11000	0.30869	0.10836	0.30423
18	0.03362	0.09436	0.03235	0.09080	0.00762	0.02139
19	0.07916	0.22219	0.05148	0.14448	0.07669	0.21533
20	0.04328	0.12148	0.02980	0.08364	0.03712	0.10421
21	0.06908	0.19390	0.10618	0.29799	0.04080	0.11455
22	0.04637	0.13017	0.03245	0.09106	0.01162	0.03263
23	0.08552	0.24006	0.04662	0.13083	0.03952	0.11096
24	0.02254	0.06326	0.03512	0.09856	0.03672	0.10309
25	0.05303	0.14887	0.07323	0.20552	0.05692	0.15982
26	0.07060	0.19817	0.03372	0.09464	0.06313	0.17724
27	0.05839	0.16391	0.05507	0.15456	0.08937	0.25092
28	0.08050	0.22597	0.08173	0.22937	0.08631	0.24232
29	0.03015	0.08464	0.05046	0.14160	0.03196	0.08974
30	0.03348	0.09397	0.05225	0.14664	0.04171	0.11710
31	0.04997	0.14027	0.02708	0.07601	0.06285	0.17647
	THD=0.25%		THD=0.25%		THD=0.24%	

Figure 4.89 shows the PCC phase voltages waveforms when the ML-MFGCI utilized to mitigate PQ problems. By utilizing ML-MFGCI the PCC voltages are increased from 250.57 V_{RMS} to 230 V_{RMS}, 259.6 V_{RMS} to 230 V_{RMS} and 253.77 V_{RMS} to 230 V_{RMS}. Moreover, the PCC phase voltages become balance in 230 V_{RMS}.

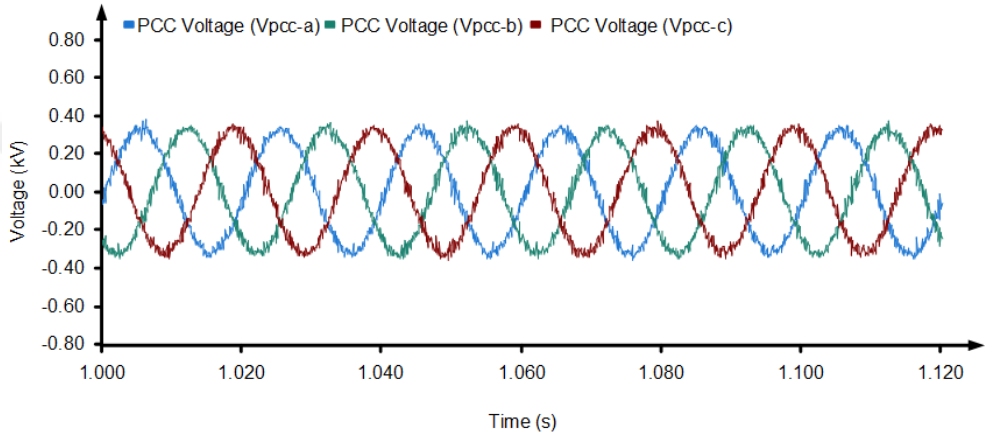

Figure 4.89. The PCC voltage waveforms under heavy loaded system with high harmonic distortion, load unbalance and voltage regulation problems during voltage swell condition.

By utilizing ML-MFGCI the PCC voltage THDs are decreased from 16.13% to 1.25% in phase *A*, 15.8% to 1.34% in phase *B* and 16.77% to 1.32% in phase *C*. Figures 4.90, 4.91 and 4.92 show the harmonic spectrum of the transformer's output phase voltages when the ML-MFGCI utilized to mitigate PQ problems.

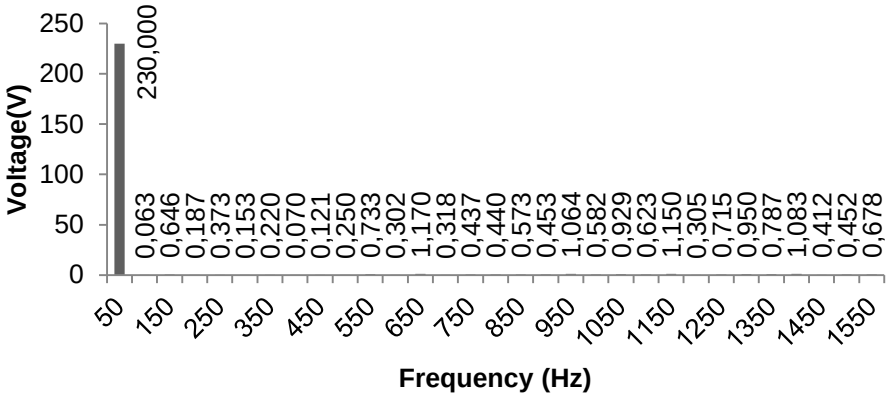

Figure 4.90. The harmonic spectrum of PCC voltage in phase A under heavy loaded system with high harmonic distortion, load unbalance and voltage regulation problems during voltage swell when the ML-MFGCI utilized.

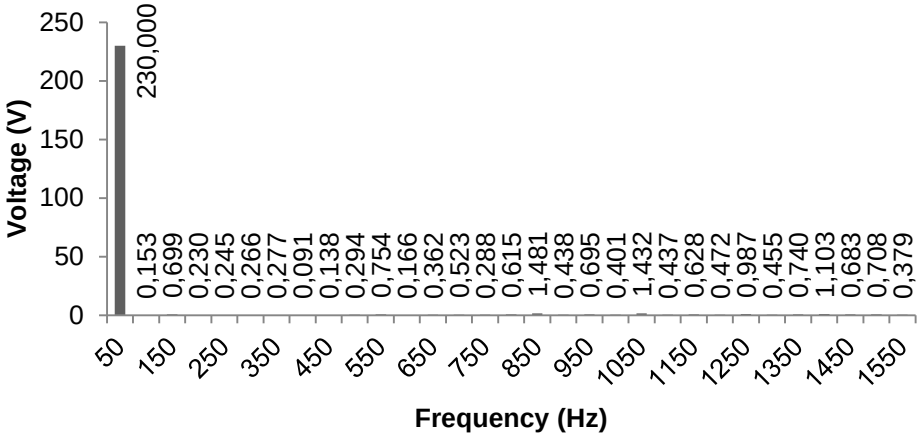

Figure 4.91. The harmonic spectrum of PCC voltage in phase *B* under heavy loaded system with high harmonic distortion, load unbalance and voltage regulation problems during voltage swell when the ML-MFGCI utilized.

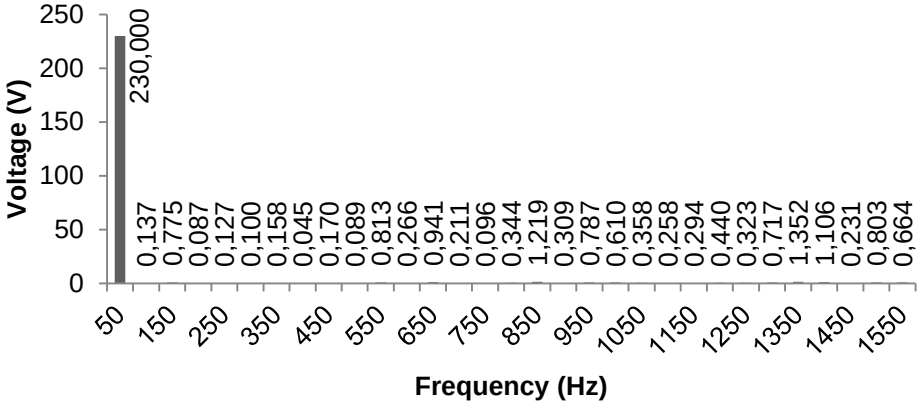

Figure 4.92. The harmonic spectrum of PCC voltage in phase *C* under heavy loaded system with high harmonic distortion, load unbalance and voltage regulation problems during voltage swell when the ML-MFGCI utilized.

The details of the PCC phase voltage harmonic contents are illustrated in Table 4.18.

Table 4.18. Harmonic contents of PCC phase voltages under heavy loaded system with high harmonic distortion, load unbalance and voltage regulation problems during voltage swell when the ML-MFGCI utilized.

	Harmonic Contents of PCC Voltage					
	Phase A		Phase B		Phase C	
Order	(%)	Value (V)	(%)	Value (V)	(%)	Value (V)
1	100.000	230.000	100.000	230.000	100.000	230.000
2	0.02733	0.06285	0.06659	0.15317	0.05966	0.13721
3	0.28086	0.64597	0.30403	0.69927	0.33684	0.77474
4	0.08132	0.18703	0.10020	0.23046	0.03791	0.08718
5	0.16235	0.37341	0.10641	0.24474	0.05522	0.12700
6	0.06640	0.15271	0.11561	0.26591	0.04361	0.10030
7	0.09585	0.22044	0.12056	0.27730	0.06851	0.15758
8	0.03025	0.06958	0.03944	0.09072	0.01977	0.04547
9	0.05279	0.12141	0.05998	0.13797	0.07400	0.17019
10	0.10890	0.25048	0.12761	0.29351	0.03882	0.08929
11	0.31881	0.73326	0.32781	0.75397	0.35365	0.81340
12	0.13143	0.30229	0.07197	0.16553	0.11570	0.26612
13	0.50868	1.16997	0.15724	0.36166	0.40922	0.94121
14	0.13840	0.31832	0.22749	0.52324	0.09184	0.21124
15	0.19017	0.43739	0.12510	0.28772	0.04176	0.09604
16	0.19138	0.44016	0.26756	0.61538	0.14944	0.34371
17	0.24892	0.57253	0.64401	1.48122	0.52979	1.21851
18	0.19707	0.45327	0.19025	0.43758	0.13438	0.30908
19	0.46272	1.06425	0.30213	0.69489	0.34211	0.78685
20	0.25288	0.58162	0.17426	0.40080	0.26504	0.60960
21	0.40378	0.92870	0.62240	1.43153	0.15573	0.35818
22	0.27070	0.62262	0.19012	0.43728	0.11205	0.25771
23	0.49987	1.14971	0.27316	0.62826	0.12762	0.29352
24	0.13268	0.30516	0.20530	0.47219	0.19111	0.43955
25	0.31070	0.71461	0.42931	0.98741	0.14057	0.32332
26	0.41310	0.95014	0.19778	0.45490	0.31163	0.71676
27	0.34234	0.78737	0.32190	0.74038	0.58796	1.35232
28	0.47087	1.08301	0.47978	1.10349	0.48065	1.10550
29	0.17899	0.41168	0.29705	0.68322	0.10023	0.23052
30	0.19663	0.45226	0.30782	0.70798	0.34935	0.80350
31	0.29458	0.67753	0.16485	0.37916	0.28854	0.66364
	THD=1.25%		THD=1.34%		THD=1.32%	

To compensate the harmonic distortions, load unbalance and reactive power as well as control the PCC voltage the ML-MFGCI injects the required

current to system. In this case the ML-MFGC injects 0.667 *kA* to phase *A*, 0.922 *kA* to phase *B* and 0.844 *kA* to phase *C* with 0.143 *kA* negative sequence current into system. Figure 4.93 shows the injected current by the ML-MFGCI into power system.

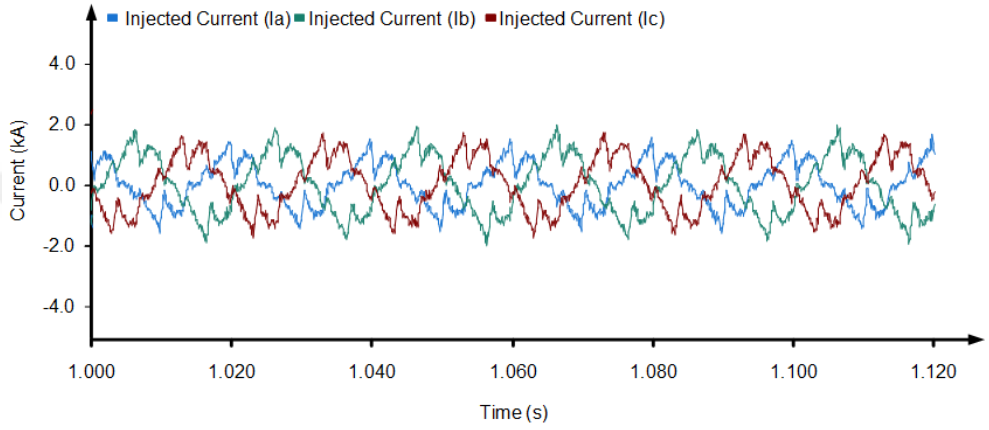

Figure 4.93. The injected current waveforms under heavy loaded system with high harmonic distortion, load unbalance and voltage regulation problems during voltage swell condition.

Figures 4.94, 4.95 and 4.96 show the harmonic spectrum of the transformer's output phase voltages when the ML-MFGCI utilized to mitigate PQ problems.

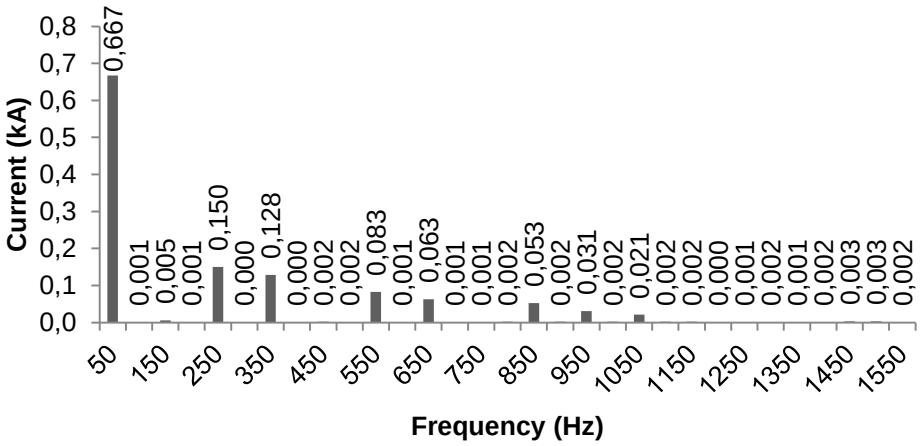

Figure 4.94. The harmonic spectrum of injected current in phase *A* by the ML-MFGCI under heavy loaded system with high harmonic distortion, load unbalance and voltage regulation problems during voltage swell condition.

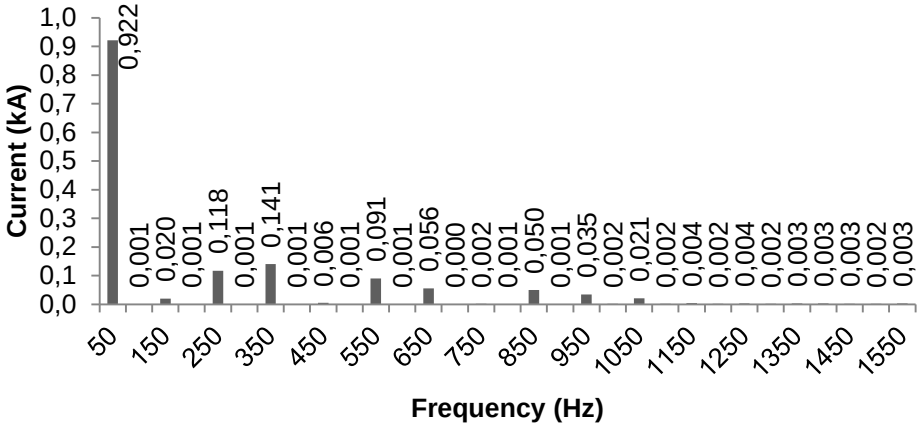

Figure 4.95. The harmonic spectrum of injected current in phase *B* by the ML-MFGCI under heavy loaded system with high harmonic distortion, load unbalance and voltage regulation problems during voltage swell condition.

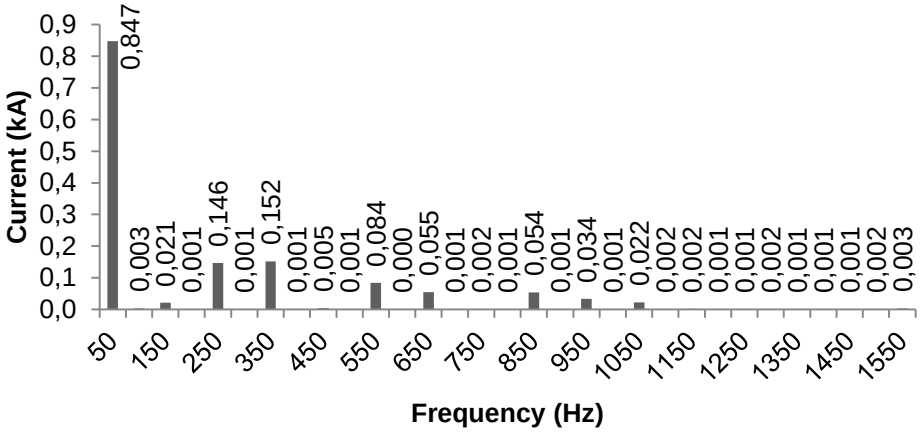

Figure 4.96. The harmonic spectrum of injected current in phase *C* by the ML-MFGCI under heavy loaded system with high harmonic distortion, load unbalance and voltage regulation problems during voltage swell condition.

The details of the source current harmonic contents are illustrated in Table 4.19.

Table 4.19. Harmonic contents of injected currents by ML-MFGCI under heavy loaded system with high harmonic distortion, load unbalance and voltage regulation problems.

	Harmonic Contents of Injected Current					
	Phase A		Phase B		Phase C	
Order	(%)	Value (kA)	(%)	Value (kA)	(%)	Value (kA)
1	100.000	0.66700	100.000	0.92200	100.000	0.84700
2	0.22208	0.00148	0.06045	0.00056	0.37108	0.00314
3	0.82188	0.00548	2.20781	0.02036	2.52054	0.02135
4	0.17666	0.00118	0.12193	0.00112	0.15139	0.00128
5	22.5452	0.15038	12.7685	0.11773	17.2870	0.14642
6	0.05970	0.00040	0.07507	0.00069	0.17173	0.00145
7	19.2587	0.12846	15.3098	0.14116	17.9173	0.15176
8	0.03188	0.00021	0.09826	0.00091	0.16249	0.00138
9	0.34958	0.00233	0.64454	0.00594	0.54883	0.00465
10	0.23044	0.00154	0.13717	0.00126	0.12828	0.00109
11	12.3799	0.08257	9.85712	0.09088	9.95350	0.08431
12	0.21054	0.00140	0.06113	0.00056	0.05546	0.00047
13	9.45392	0.06306	6.10820	0.05632	6.45784	0.05470
14	0.12617	0.00084	0.03643	0.00034	0.06620	0.00056
15	0.13688	0.00091	0.20921	0.00193	0.18479	0.00157
16	0.29120	0.00194	0.15050	0.00139	0.08854	0.00075
17	7.88343	0.05258	5.41466	0.04992	6.39852	0.05420
18	0.35205	0.00235	0.13620	0.00126	0.10159	0.00086
19	4.60690	0.03073	3.79554	0.03499	4.02165	0.03406
20	0.28100	0.00187	0.21081	0.00194	0.14525	0.00123
21	3.19052	0.02128	2.27568	0.02098	2.64929	0.02244
22	0.27030	0.00180	0.23247	0.00214	0.18757	0.00159
23	0.34485	0.00230	0.44252	0.00408	0.26090	0.00221
24	0.03332	0.00022	0.21581	0.00199	0.16822	0.00142
25	0.18182	0.00121	0.41332	0.00381	0.14634	0.00124
26	0.25080	0.00167	0.21369	0.00197	0.17909	0.00152
27	0.22101	0.00147	0.31635	0.00292	0.06386	0.00054
28	0.22629	0.00151	0.35662	0.00329	0.08551	0.00072
29	0.48134	0.00321	0.28141	0.00259	0.16413	0.00139
30	0.43535	0.00290	0.20079	0.00185	0.21030	0.00178
31	0.23896	0.00159	0.35584	0.00328	0.35470	0.00300

Figure 4.97 shows the source current waveforms when the ML-MFGCI utilized to mitigate PQ problems. By utilizing ML-MFGCI the source current

becomes as pure sinusoidal waveform. The drown current from source with ML-MFGCI are as 1.931 *kA* for phase *A*, 1.939 *kA* for phase *B* and 1.919 *kA* for phase *C*. Moreover negative sequence of source current decrees from 0.133 to 0.010 *kA* and current unbalance ration reduce to 0.5%.

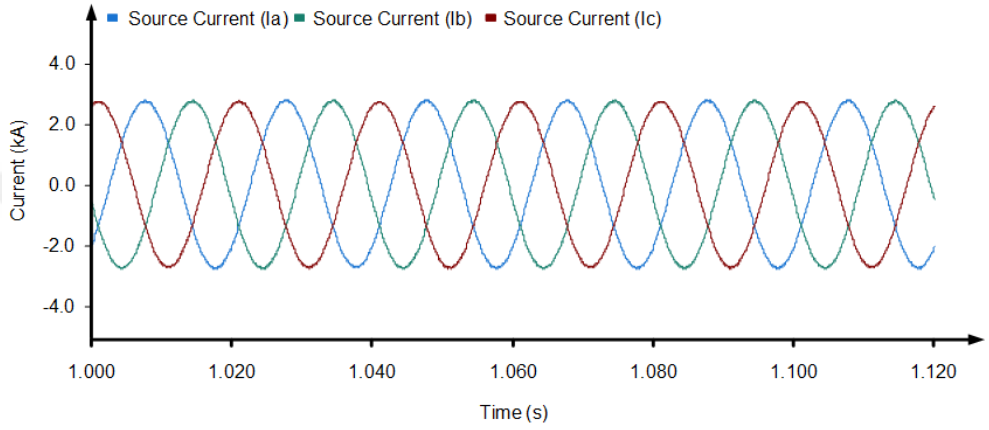

Figure 4.97. The source current waveforms under heavy loaded system with high harmonic distortion, load unbalance and voltage regulation problems during voltage swell when ML-MFGCI utilized.

In the voltage swell compensation duration the source current THDs are decreased from 9% to 0.38% in phase *A*, 9.1% to 0.5% in phase *B* and 8.67% to 0.44% in phase *C* versus without compensation situation. Figures 4.98, 4.99 and 4.100 show the harmonic spectrum of source current when the ML-MFGCI utilized to mitigate PQ problems.

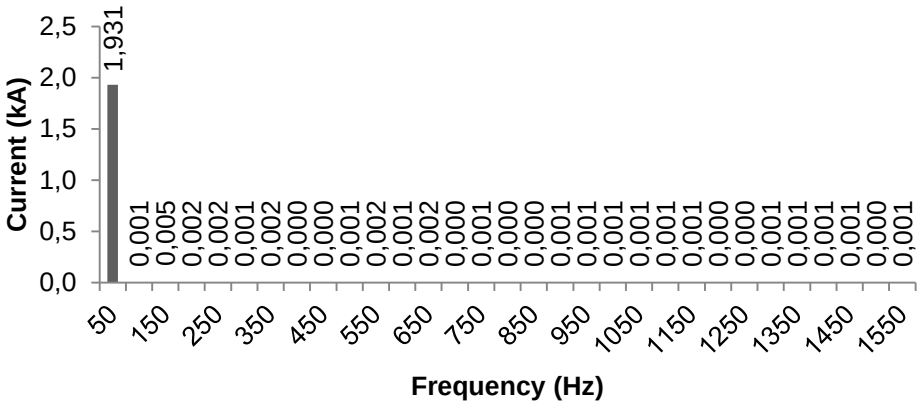

Figure 4.98. The harmonic spectrum of source current in phase A under heavy loaded system with high harmonic distortion, load unbalance and voltage regulation problems during voltage swell when the ML-MFGCI utilized.

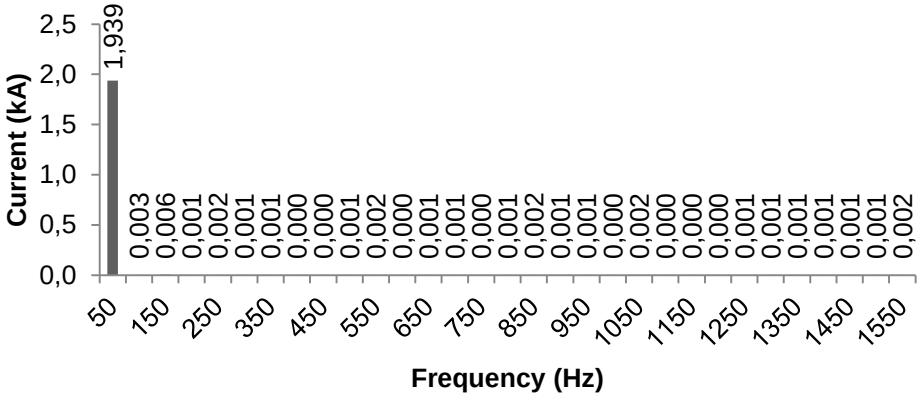

Figure 4.99. The harmonic spectrum of source current in phase B under heavy loaded system with high harmonic distortion, load unbalance and voltage regulation problems during voltage swell when the ML-MFGCI utilized.

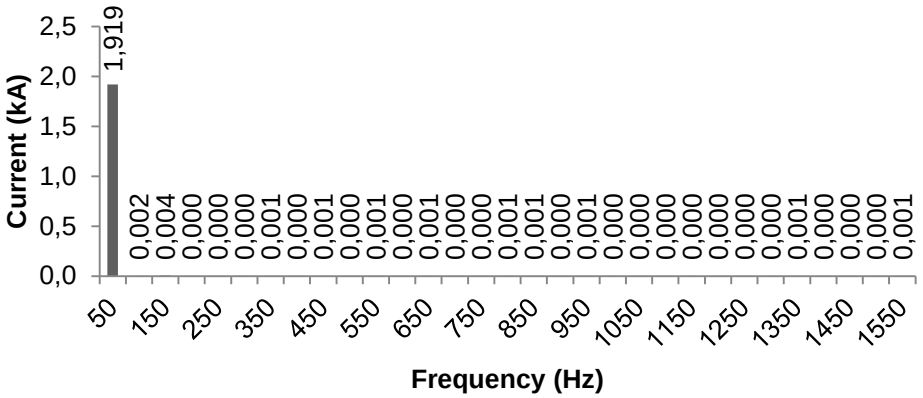

Figure 4.100. The harmonic spectrum of source current in phase C under heavy loaded system with high harmonic distortion, load unbalance and voltage regulation problems during voltage swell when the ML-MFGCI utilized.

The details of the source current harmonic contents are illustrated in Table 4.20.

Table 4.20. Harmonic contents of source currents under heavy loaded system with high harmonic distortion, load unbalance and voltage regulation problems when the ML-MFGCI utilized.

	Harmonic Contents of Source Current					
	Phase A		Phase B		Phase C	
Order	(%)	Value (kA)	(%)	Value (kA)	(%)	Value (kA)
1	100.000	1.93100	100.000	1.93930	100.000	1.91850
2	0.06534	0.00126	0.14389	0.00279	0.17676	0.00211
3	0.27729	0.00535	0.28582	0.00554	0.29741	0.00354
4	0.08359	0.00161	0.06984	0.00135	0.03616	0.00043
5	0.10269	0.00198	0.11329	0.00220	0.03189	0.00038
6	0.03623	0.00070	0.04583	0.00089	0.01297	0.00015
7	0.09239	0.00178	0.04696	0.00091	0.05692	0.00068
8	0.01463	0.00028	0.01763	0.00034	0.02862	0.00034
9	0.01067	0.00021	0.02034	0.00039	0.06003	0.00072
10	0.04564	0.00088	0.03202	0.00062	0.01596	0.00019
11	0.09640	0.00186	0.09149	0.00177	0.09087	0.00108
12	0.03538	0.00068	0.01162	0.00023	0.03840	0.00046
13	0.08922	0.00172	0.03767	0.00073	0.07949	0.00095
14	0.02474	0.00048	0.03856	0.00075	0.02468	0.00029
15	0.04528	0.00087	0.02189	0.00042	0.00437	0.00005
16	0.00946	0.00018	0.03428	0.00066	0.04405	0.00053
17	0.02488	0.00048	0.12314	0.00239	0.11381	0.00136
18	0.03369	0.00065	0.03027	0.00059	0.01010	0.00012
19	0.07537	0.00146	0.04591	0.00089	0.07819	0.00093
20	0.03287	0.00063	0.02270	0.00044	0.02582	0.00031
21	0.04894	0.00095	0.08177	0.00159	0.02776	0.00033
22	0.03524	0.00068	0.01616	0.00031	0.01203	0.00014
23	0.06788	0.00131	0.01671	0.00032	0.03645	0.00043
24	0.01517	0.00029	0.01873	0.00036	0.03183	0.00038
25	0.02359	0.00046	0.05071	0.00098	0.02537	0.00030
26	0.04140	0.00080	0.02947	0.00057	0.01632	0.00019
27	0.03956	0.00076	0.02633	0.00051	0.04549	0.00054
28	0.04566	0.00088	0.05664	0.00110	0.01468	0.00017
29	0.06579	0.00127	0.06194	0.00120	0.00612	0.00007
30	0.01537	0.00030	0.02804	0.00054	0.03358	0.00040
31	0.06799	0.00131	0.10257	0.00199	0.07368	0.00088
	THD=0.38%		THD=0.5%		THD=0.44%	

Figure 4.101 and 4.102 shows the line and fundamental components of phase voltage at PCC with ML-MFGCI versus without compensation situation

during steady-state and voltage sag condition. As see from figures the ML-MFGCI keeps the phase and line voltages within standard limits.

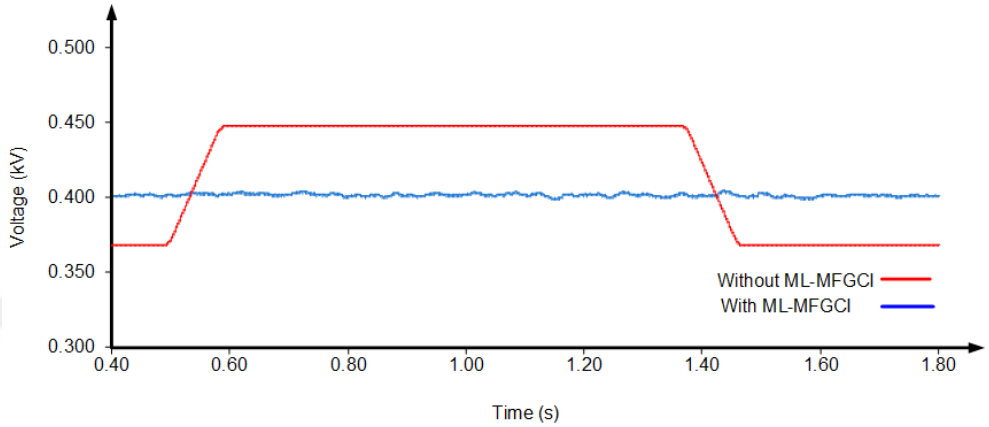

Figure 4.101. The line voltage during voltage swell with and without ML-MFGCI utilized.

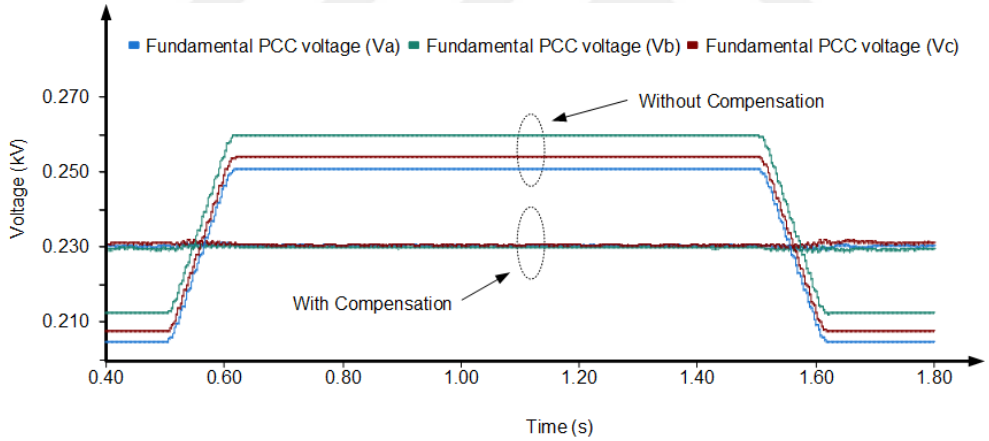

Figure 4.102. The fundamental components of PCC voltage during voltage swell with and without ML-MFGCI utilized.

The Figure 4.103 shows the injected reactive power from ML-MFGCI into system to compensate voltage swell in PCC.

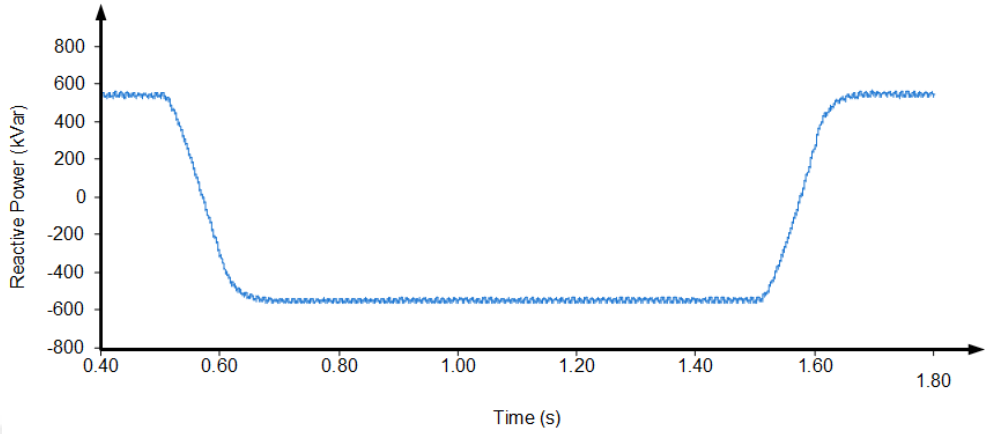

Figure 4.103. The injected reactive power from ML-MFGCI into system under heavy loaded system with high harmonic distortion, load unbalance and voltage regulation problems during voltage swell when the ML-MFGCI utilized.

Case5: In this case, to verify the efficiency of the ML-MFGCI in the third mode, the performance of the ML-MFGCI equipped by 500 *kW* nominal rating PV system, is tested for simultaneously to exchange active power with utility grid and to compensate the reactive power, current and voltage harmonics and load balancing as well as voltage regulation during voltage sag in the heavy loaded system. As mentioned above, the studied system has voltage regulation, voltage and current harmonic, negative sequence current and low *P.F.* index problems. Figure 4.104 shows the active power injected from ML-MFGCI into utility grid when used in third mode.

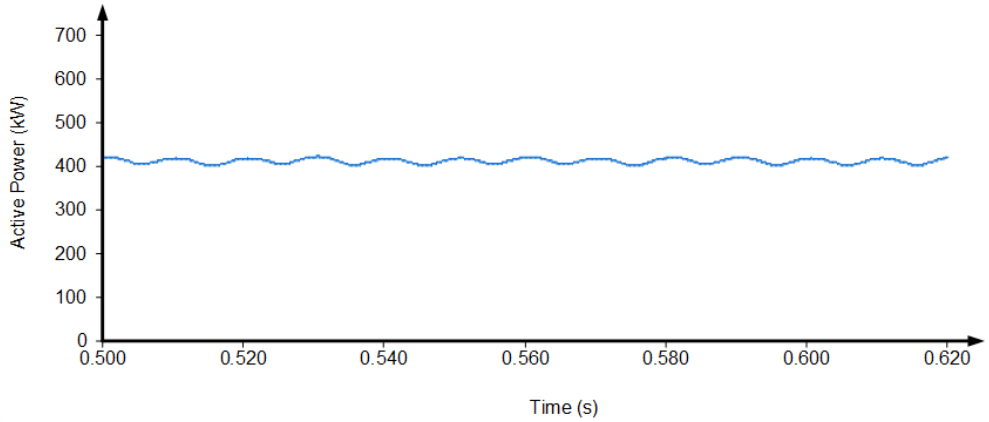

Figure 4.104. The injected active power from ML-MFGCI into power system produced by PV system under heavy loaded system with high harmonic distortion, load unbalance and voltage regulation problems.

Figure 4.105 shows the load current where has 15.7% THD in phase *A*, 16.05% THD in phase *B* and 14.95% THD in phase *C*.

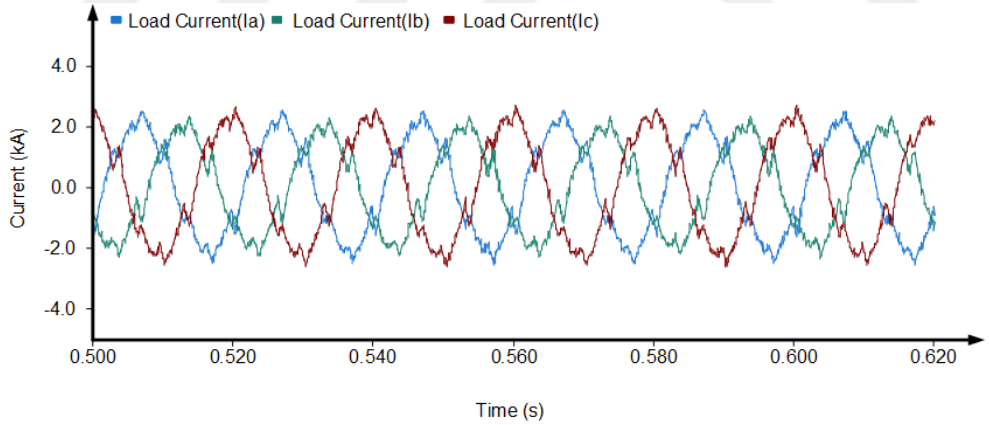

Figure 4.105. The load current under heavy loaded system with high harmonic distortion, load unbalance and voltage regulation problems when ML-MFGCI equipped by PV system is utilized.

Figures 4.106, 4.107 and 4.108 show the harmonic spectrum of the load current where has 15.7% THD in phase *A*, 16.05% THD in phase *B* and 14.95% THD in phase *C*.

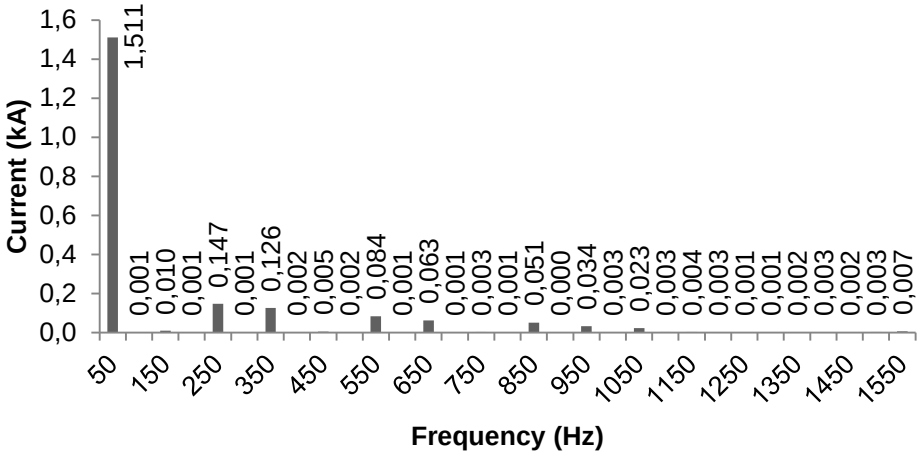

Figure 4.106. The harmonic spectrum of distorted and unbalance load current in phase A when ML-MFGCI equipped by PV system.

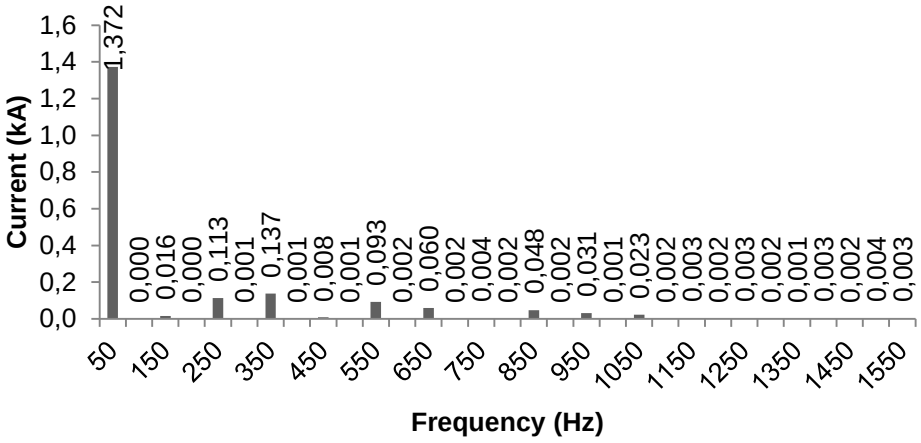

Figure 4.107. The harmonic spectrum of distorted and unbalance load current in phase B when ML-MFGCI equipped by PV system.

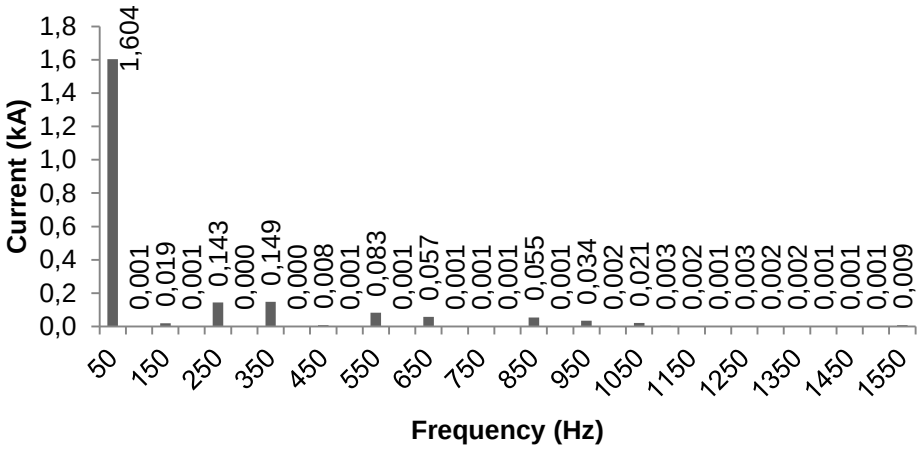

Figure 4.108. The harmonic spectrum of distorted and unbalance load current in phase C when ML-MFGCI equipped by PV system.

Table 4.21 illustrates the load current harmonic content in details when ML-MFGCI by PV system.

Table 4.21. The harmonic spectrum of distorted and unbalance load currents when ML-MFGCI equipped by PV system.

	Harmonic Contents of Load Current					
	Phase A		Phase B		Phase C	
Order	(%)	Value (kA)	(%)	Value (kA)	(%)	Value (kA)
1	100.000	1.51100	100.000	1.37200	100.000	1.60400
2	0.05006	0.00076	0.03287	0.00045	0.03148	0.00050
3	0.66225	0.01001	1.15059	0.01579	1.17472	0.01884
4	0.05818	0.00088	0.02690	0.00037	0.04156	0.00067
5	9.74266	0.14721	8.26163	0.11335	8.92986	0.14324
6	0.06000	0.00091	0.05254	0.00072	0.02393	0.00038
7	8.32905	0.12585	10.0104	0.13734	9.26572	0.14862
8	0.10087	0.00152	0.09807	0.00135	0.02483	0.00040
9	0.33502	0.00506	0.58308	0.00800	0.48255	0.00774
10	0.10664	0.00161	0.05967	0.00082	0.05057	0.00081
11	5.57503	0.08424	6.76990	0.09288	5.19626	0.08335
12	0.07403	0.00112	0.13984	0.00192	0.06504	0.00104
13	4.15254	0.06274	4.38659	0.06018	3.58198	0.05745
14	0.07188	0.00109	0.15863	0.00218	0.07455	0.00120
15	0.22948	0.00347	0.26237	0.00360	0.04223	0.00068
16	0.07569	0.00114	0.14267	0.00196	0.07001	0.00112
17	3.40554	0.05146	3.48305	0.04779	3.41177	0.05472
18	0.00469	0.00007	0.10965	0.00150	0.09108	0.00146
19	2.21849	0.03352	2.26492	0.03107	2.15007	0.03449
20	0.16961	0.00256	0.07730	0.00106	0.09408	0.00151
21	1.54316	0.02332	1.65581	0.02272	1.28498	0.02061
22	0.19053	0.00288	0.12237	0.00168	0.19235	0.00309
23	0.29373	0.00444	0.23614	0.00324	0.15236	0.00244
24	0.17363	0.00262	0.13091	0.00180	0.06034	0.00097
25	0.05718	0.00086	0.24333	0.00334	0.17408	0.00279
26	0.09823	0.00148	0.14246	0.00195	0.11703	0.00188
27	0.12702	0.00192	0.08930	0.00123	0.12418	0.00199
28	0.18132	0.00274	0.19051	0.00261	0.07957	0.00128
29	0.11233	0.00170	0.15864	0.00218	0.03184	0.00051
30	0.21023	0.00318	0.29518	0.00405	0.05670	0.00091
31	0.45208	0.00683	0.23449	0.00322	0.53215	0.00854
	THD=15.35%		THD=16.05%		THD=14.95%	

To compensate the harmonic distortions, load unbalance and reactive power as well as regulate the PCC voltage the ML-MFGCI injects the required current to system. In this case the ML-MFGC injects 0.743 *kA* to phase *A*, 0.526 *kA*

to phase *B* and 0.531 *kA* to phase *C* with 0.1455 *kA* negative sequence current into system. Figure 4.109 shows the injected current by the ML-MFGCI into system.

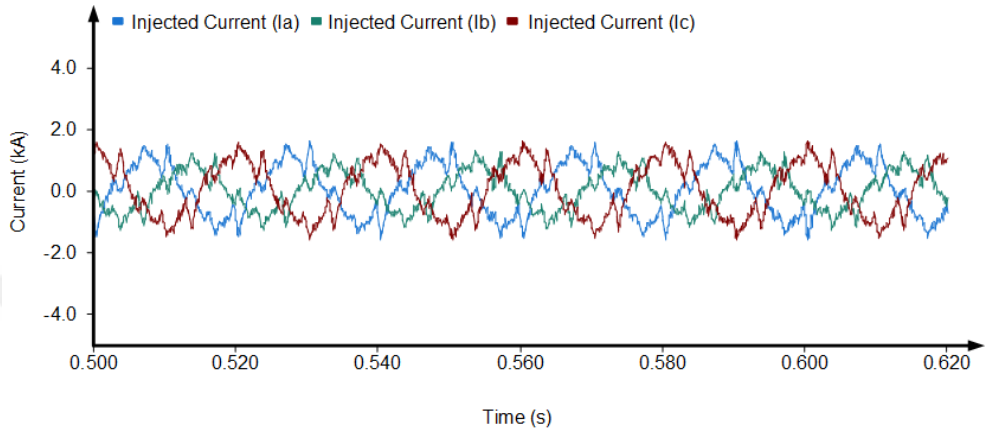

Figure 4.109. The currents waveform injected by ML-MFGCI equipped by PV system.

As seen from figure 4.109, to compensate harmonics ML-MFGCI injects the required harmonic into system. Figure 4.110, 4.111 and 4.112 shows the harmonic spectrum of the injected current by ML-MFGCI in phases *A*, *B* and *C*.

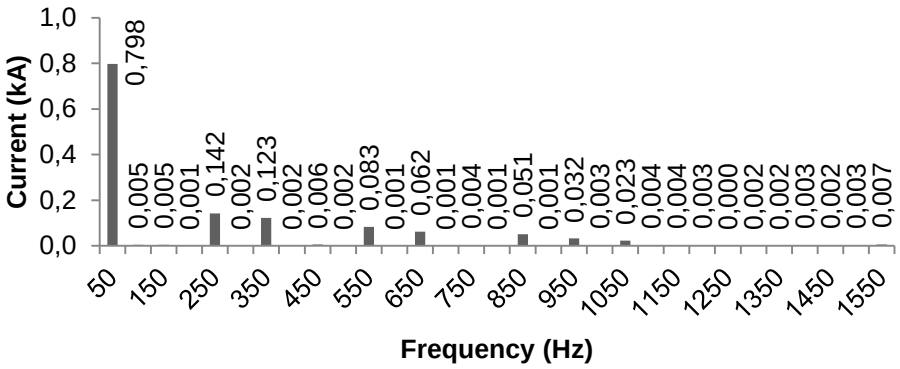

Figure 4.110. The harmonic spectrum of injected current in phase *A* by the ML-MFGCI equipped by PV system under heavy loaded system with high harmonic distortion, load unbalance and voltage regulation problems.

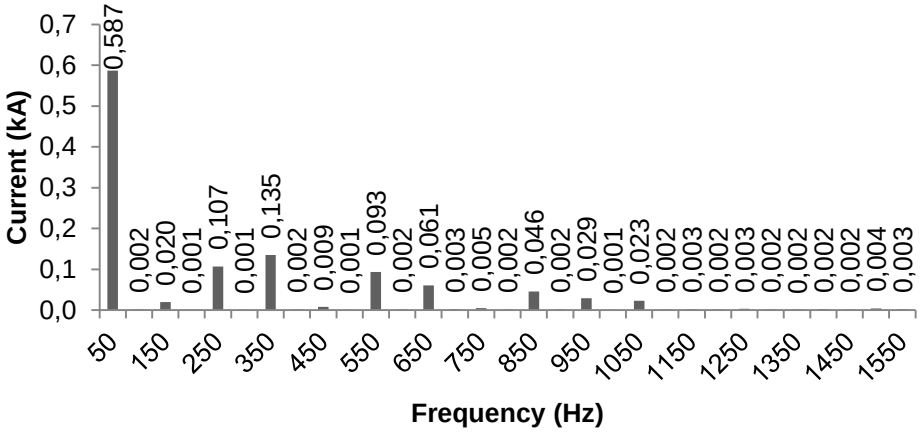

Figure 4.111. The harmonic spectrum of injected current in phase *B* by the ML-MFGCI equipped by PV system under heavy loaded system with high harmonic distortion, load unbalance and voltage regulation problems.

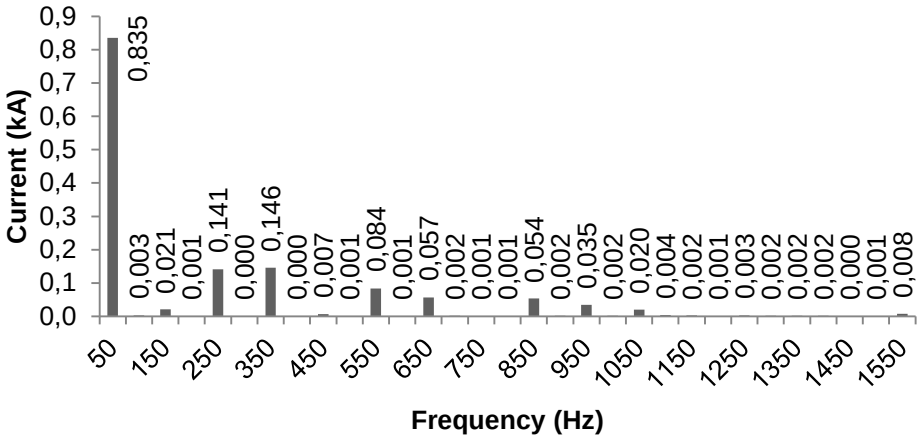

Figure 4.112. The harmonic spectrum of injected current in phase *C* by the ML-MFGCI equipped by PV system under heavy loaded system with high harmonic distortion, load unbalance and voltage regulation problems.

The details of the source current harmonic contents are illustrated in Table 4.22.

Table 4.22. Harmonic contents of injected currents by ML-MFGCI equipped by PV system under heavy loaded system with high harmonic distortion, load unbalance and voltage regulation problems.

	Harmonic Contents of Injected Current					
	Phase A		Phase B		Phase C	
Order	(%)	Value (kA)	(%)	Value (kA)	(%)	Value (kA)
1	100.000	0.79800	100.000	0.58700	100.000	0.83500
2	0.60010	0.00473	0.32204	0.00189	0.39025	0.00326
3	0.67781	0.00535	3.37846	0.01983	2.48594	0.02076
4	0.15760	0.00124	0.11410	0.00067	0.06997	0.00058
5	18.0350	0.14230	18.2589	0.10718	16.8824	0.14097
6	0.21787	0.00172	0.24340	0.00143	0.03634	0.00030
7	15.5554	0.12273	23.0235	0.13515	17.4711	0.14588
8	0.22649	0.00179	0.30709	0.00180	0.02249	0.00019
9	0.78498	0.00619	1.44932	0.00851	0.85596	0.00715
10	0.25411	0.00200	0.16114	0.00095	0.14395	0.00120
11	10.5750	0.08344	15.9050	0.09336	10.0429	0.08386
12	0.14574	0.00115	0.37984	0.00223	0.13391	0.00112
13	7.84714	0.06191	10.3494	0.06075	6.81437	0.05690
14	0.14754	0.00116	0.43978	0.00258	0.22263	0.00186
15	0.46887	0.00370	0.85673	0.00503	0.15802	0.00132
16	0.15298	0.00121	0.36864	0.00216	0.11548	0.00096
17	6.40739	0.05055	7.81549	0.04588	6.42747	0.05367
18	0.06859	0.00054	0.30214	0.00177	0.20866	0.00174
19	4.08416	0.03222	4.99834	0.02934	4.17301	0.03484
20	0.32517	0.00257	0.16290	0.00096	0.19604	0.00164
21	2.86982	0.02264	3.90967	0.02295	2.41146	0.02014
22	0.45429	0.00358	0.33914	0.00199	0.45971	0.00384
23	0.49149	0.00388	0.49310	0.00289	0.29389	0.00245
24	0.41590	0.00328	0.34088	0.00200	0.15701	0.00131
25	0.04909	0.00039	0.59579	0.00350	0.40354	0.00337
26	0.19062	0.00150	0.37456	0.00220	0.21171	0.00177
27	0.22139	0.00175	0.27151	0.00159	0.21627	0.00181
28	0.40765	0.00322	0.40006	0.00235	0.18968	0.00158
29	0.30478	0.00240	0.36373	0.00214	0.04870	0.00041
30	0.41545	0.00328	0.71554	0.00420	0.10989	0.00092
31	0.85060	0.00671	0.50498	0.00296	0.96628	0.00807

Figure 4.113 shows transformer's output voltage under heavy loaded system with high harmonic distortion, load unbalance and voltage regulation problems when PV supported ML-MFGCI is utilized.

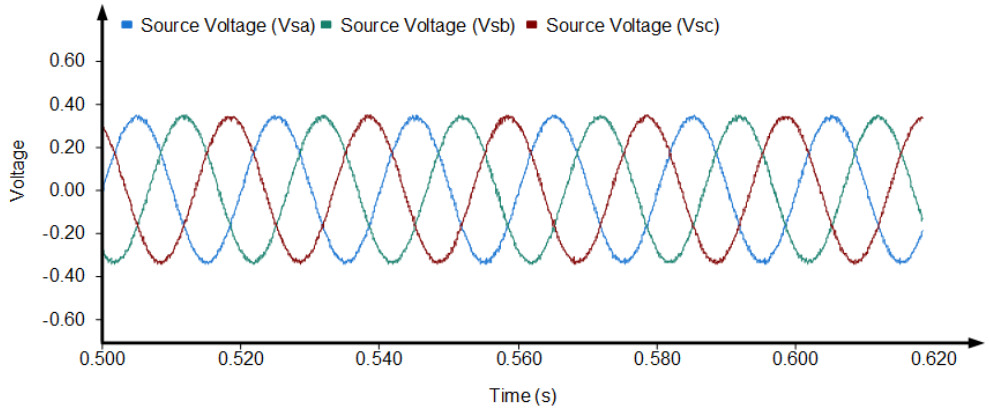

Figure 4.113. The transformer's output voltage under heavy loaded system with high harmonic distortion, load unbalance and voltage regulation problems when PV supported ML-MFGCI is utilized.

By utilizing ML-MFGCI, the transformer's output voltage *THD*s are decreased from 3.58% to 0.35% in phase *A*, 3.6% to 1.05% in phase *B* and 3.76% to 0.84% in phase *C*. Figures 4.114, 4.115 and 4.116 show the harmonic spectrum of the transformer's output phase voltages when the ML-MFGCI is utilized to mitigate PQ problems.

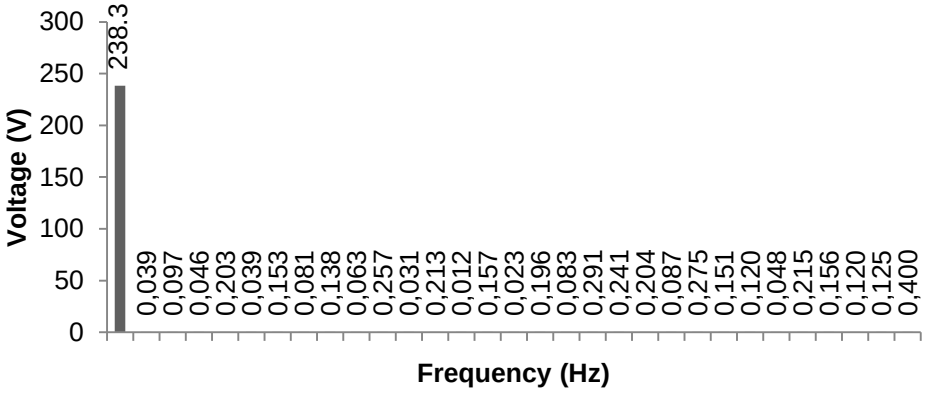

Figure 4.114. The harmonic spectrum of transformer's output voltage in phase *A* under heavy loaded system with high harmonic distortion, load unbalance and voltage regulation problems when PV supported ML-MFGCI is utilized.

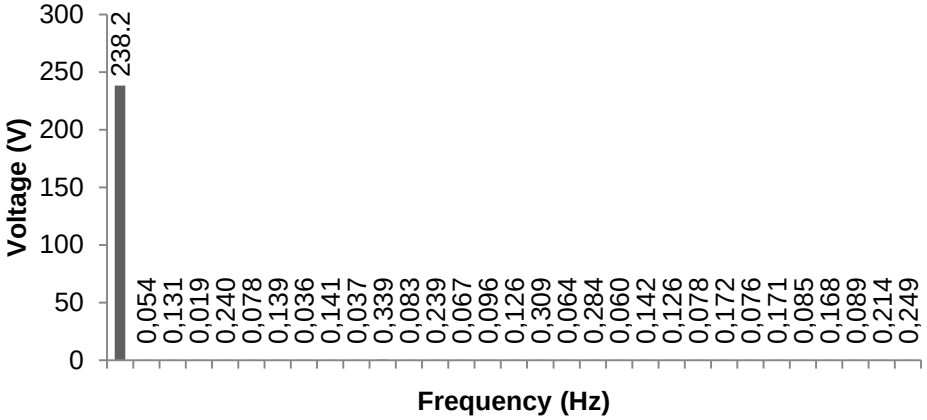

Figure 4.115. The harmonic spectrum of transformer's output voltage in phase *B* under heavy loaded system with high harmonic distortion, load unbalance and voltage regulation problems when PV supported ML-MFGCI is utilized.

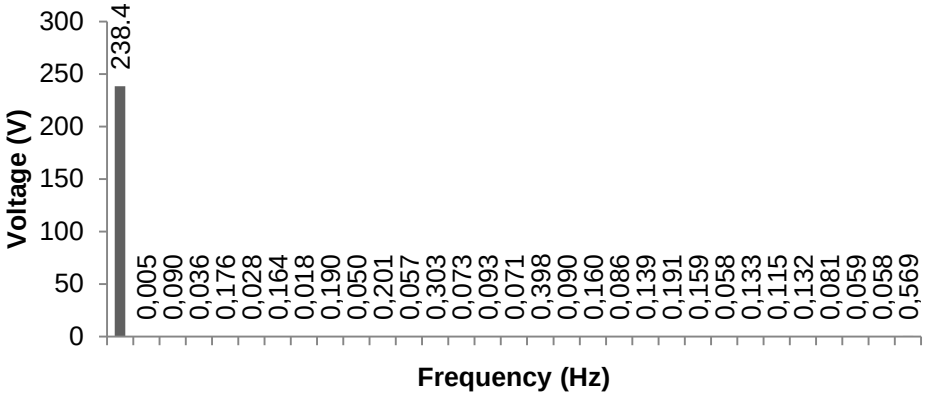

Figure 4.116. The harmonic spectrum of transformer's output voltage in phase *C* under heavy loaded system with high harmonic distortion, load unbalance and voltage regulation problems when PV supported ML-MFGCI is utilized.

The details of the transformer's output voltage harmonic contents are illustrated in Table 4.23.

Table 4.23. Harmonic contents of transformer's output voltage under heavy loaded system with high harmonic distortion, load unbalance and voltage regulation problems when PV supported ML-MFGCI is utilized

	Harmonic Contents of Source Voltage					
	Phase A		Phase B		Phase C	
Order	(%)	Value (V)	(%)	Value (V)	(%)	Value (V)
1	100.000	238.300	100.000	238.400	100.000	238.400
2	0.01645	0.03921	0.02281	0.00454	0.00190	0.00454
3	0.04078	0.09717	0.05508	0.08997	0.03774	0.08997
4	0.01934	0.04608	0.00795	0.03592	0.01507	0.03592
5	0.08528	0.20323	0.10057	0.17597	0.07381	0.17597
6	0.01650	0.03932	0.03266	0.02823	0.01184	0.02823
7	0.06428	0.15319	0.05833	0.16389	0.06874	0.16389
8	0.03385	0.08065	0.01529	0.01824	0.00765	0.01824
9	0.05776	0.13764	0.05925	0.19026	0.07981	0.19026
10	0.02639	0.06288	0.01557	0.04979	0.02089	0.04979
11	0.10790	0.25713	0.14240	0.20148	0.08451	0.20148
12	0.01291	0.03076	0.03501	0.05748	0.02411	0.05748
13	0.08922	0.21260	0.10051	0.30333	0.12724	0.30333
14	0.00500	0.01192	0.02804	0.07259	0.03045	0.07259
15	0.06588	0.15700	0.04016	0.09261	0.03885	0.09261
16	0.00974	0.02320	0.05298	0.07108	0.02981	0.07108
17	0.08227	0.19605	0.12969	0.39796	0.16693	0.39796
18	0.03480	0.08293	0.02686	0.09013	0.03781	0.09013
19	0.12194	0.29058	0.11918	0.16044	0.06730	0.16044
20	0.10116	0.24107	0.02524	0.08575	0.03597	0.08575
21	0.08572	0.20427	0.05961	0.13930	0.05843	0.13930
22	0.03661	0.08724	0.05310	0.19058	0.07994	0.19058
23	0.11533	0.27482	0.03263	0.15864	0.06654	0.15864
24	0.06350	0.15133	0.07233	0.05778	0.02424	0.05778
25	0.05041	0.12013	0.03189	0.13299	0.05578	0.13299
26	0.02028	0.04833	0.07181	0.11470	0.04811	0.11470
27	0.09029	0.21517	0.03559	0.13151	0.05516	0.13151
28	0.06540	0.15585	0.07063	0.08068	0.03384	0.08068
29	0.05015	0.11951	0.03725	0.05936	0.02490	0.05936
30	0.05266	0.12548	0.09004	0.05771	0.02421	0.05771
31	0.16798	0.40031	0.10473	0.56880	0.23859	0.56880
	THD=0.39%		THD=0.36%		THD=0.39%	

Figure 4.117 shows the PCC phase voltages waveforms when the ML-MFGCI equipped by PV system utilized to mitigate PQ problems. By utilizing

ML-MFGCI equipped by PV system the PCC voltages are increased from 172.28 V_{RMS} to 208.5 V_{RMS}, 179.3 V_{RMS} to 207.8 V_{RMS} and 175.2 V_{RMS} to 209 V_{RMS}. Moreover, the PCC phase voltages become balance in 225 V_{RMS}.

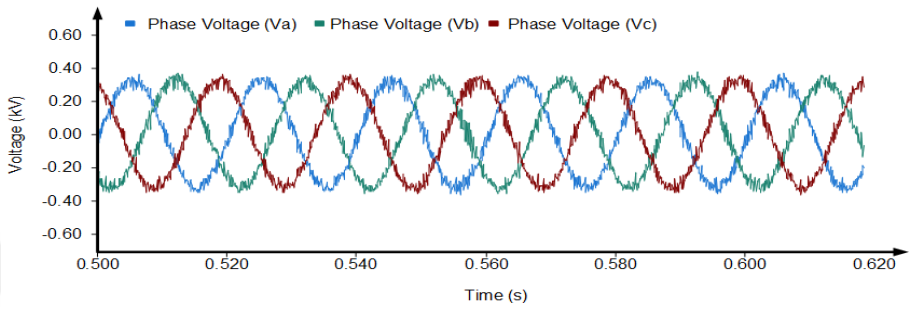

Figure 4.117. The PCC voltage under heavy loaded system with high harmonic distortion, load unbalance and voltage regulation problems when ML-MFGCI equipped by PV system is utilized.

When the ML-MFGCI is utilized to mitigate PQ problems the PCC voltage *THD*s are decreased to 1.69% in phase *A*, 1.53% in phase *B* and 1.80% in phase *C*. Figures 4.116, 4.117 and 4.118 show the harmonic spectrum of source current waveforms.

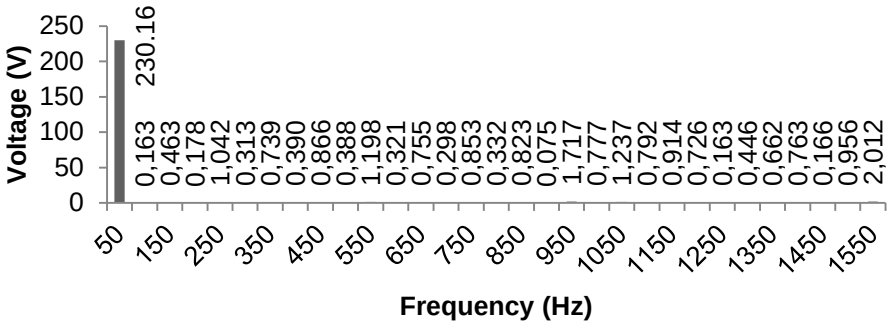

Figure 4.118. The harmonic spectrum of PCC voltage in phase *A* under heavy loaded system with high harmonic distortion, load unbalance and voltage regulation problems when PV supported ML-MFGCI is utilized.

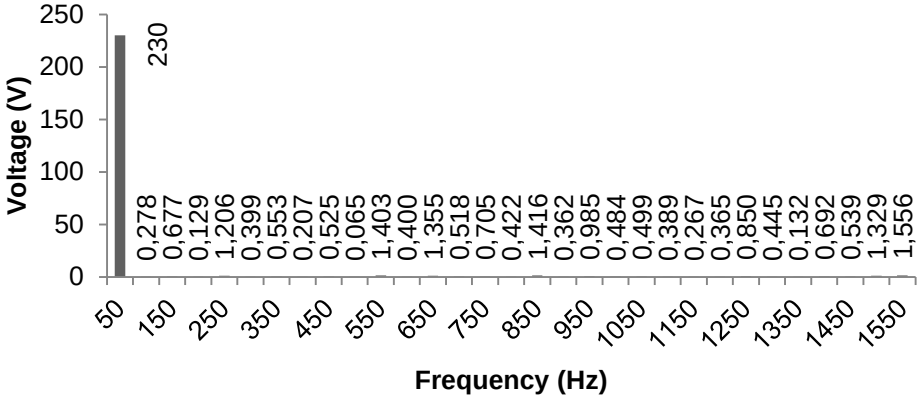

Figure 4.119. The harmonic spectrum of PCC voltage in phase *B* under heavy loaded system with high harmonic distortion, load unbalance and voltage regulation problems when PV supported ML-MFGCI is utilized.

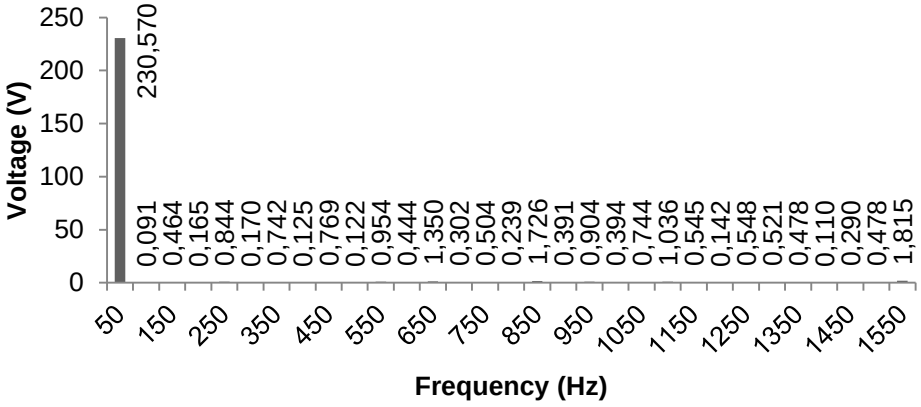

Figure 4.120. The harmonic spectrum of PCC voltage in phase *C* under heavy loaded system with high harmonic distortion, load unbalance and voltage regulation problems when PV supported ML-MFGCI is utilized.

The details of the PCC voltage harmonic contents are illustrated in Table 4.24.

Table 4.24. Harmonic contents of PCC voltage under heavy loaded system with high harmonic distortion, load unbalance and voltage regulation problems when PV supported ML-MFGCI is utilized

	Harmonic Contents of PCC Voltage					
	Phase A		Phase B		Phase C	
Order	(%)	Value (V)	(%)	Value (V)	(%)	Value (V)
1	100.000	230.160	100.000	230.000	100.000	230.570
2	0.07080	0.16296	0.12095	0.27818	0.03953	0.09114
3	0.20134	0.46341	0.29415	0.67654	0.20113	0.46375
4	0.07749	0.17836	0.05625	0.12938	0.07139	0.16460
5	0.45280	1.04216	0.52416	1.20556	0.36616	0.84425
6	0.13604	0.31311	0.17332	0.39863	0.07370	0.16992
7	0.32111	0.73907	0.24037	0.55284	0.32177	0.74190
8	0.16934	0.38976	0.09001	0.20701	0.05427	0.12512
9	0.37626	0.86601	0.22820	0.52487	0.33345	0.76884
10	0.16862	0.38810	0.02823	0.06492	0.05310	0.12244
11	0.52033	1.19759	0.60982	1.40259	0.41377	0.95404
12	0.13964	0.32139	0.17390	0.39997	0.19249	0.44383
13	0.32818	0.75534	0.58912	1.35497	0.58552	1.35003
14	0.12929	0.29757	0.22505	0.51762	0.13088	0.30177
15	0.37052	0.85279	0.30658	0.70513	0.21868	0.50422
16	0.14417	0.33182	0.18365	0.42240	0.10364	0.23897
17	0.35763	0.82313	0.61552	1.41569	0.74857	1.72598
18	0.03272	0.07531	0.15722	0.36161	0.16954	0.39091
19	0.74587	1.71669	0.42832	0.98514	0.39201	0.90386
20	0.33760	0.77702	0.21047	0.48409	0.17095	0.39416
21	0.53759	1.23732	0.21717	0.49949	0.32284	0.74436
22	0.34412	0.79202	0.16910	0.38893	0.44944	1.03627
23	0.39730	0.91443	0.11613	0.26710	0.23643	0.54514
24	0.31538	0.72588	0.15879	0.36521	0.06151	0.14183
25	0.07084	0.16304	0.36964	0.85018	0.23757	0.54776
26	0.19396	0.44641	0.19333	0.44465	0.22577	0.52056
27	0.28775	0.66227	0.05745	0.13214	0.20739	0.47818
28	0.33149	0.76296	0.30079	0.69182	0.04784	0.11031
29	0.07222	0.16623	0.23434	0.53898	0.12574	0.28993
30	0.41557	0.95647	0.57768	1.32866	0.20729	0.47795
31	0.87418	2.01201	0.67656	1.55608	0.78732	1.81532
	THD=1.69%		THD=1.53%		THD=1.80%	

Figure 4.121 shows the source current waveforms when the ML-MFGCI utilized to mitigate PQ problems. By utilizing ML-MFGCI the source current

becomes as pure sinusoidal waveform. The drawn current from source with ML-MFGCI are 1.457 *kA* for phase *A*, 1.444 *kA* for phase *B* and 1.425 *kA* for phase *C*. Moreover, negative sequence of source current is decreased to 0.016 *kA* and current unbalance ration is reduced to 1.2%.

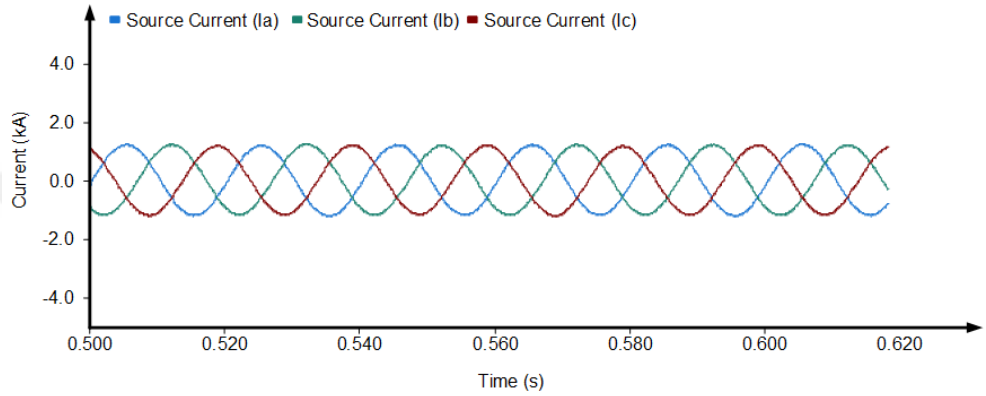

Figure 4.121. The source current under heavy loaded system with high harmonic distortion, load unbalance and voltage regulation problems when ML-MFGCI equipped by PV system is utilized.

When the ML-MFGCI is utilized to mitigate PQ problems, the PCC voltage *THD*s are decreased to 1.1% in phase *A*, 0.955% in phase *B* and 1% in phase *C*. Figures 4.122, 4.123 and 4.124 show the harmonic spectrum of source current waveforms.

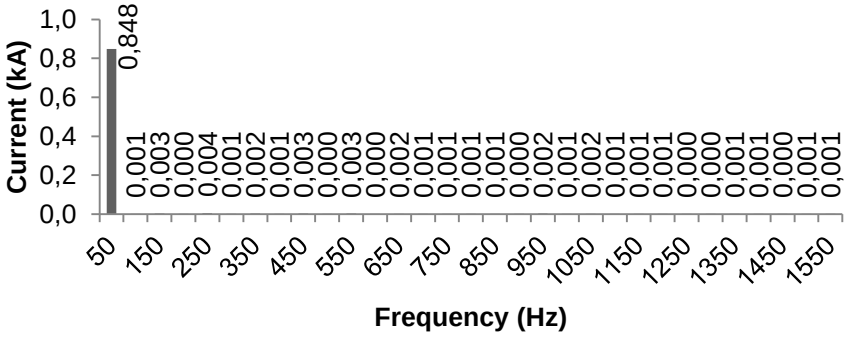

Figure 4.122. The harmonic spectrum of source current in phase *A* under heavy loaded system with high harmonic distortion, load unbalance and voltage regulation problems when PV supported ML-MFGCI is utilized.

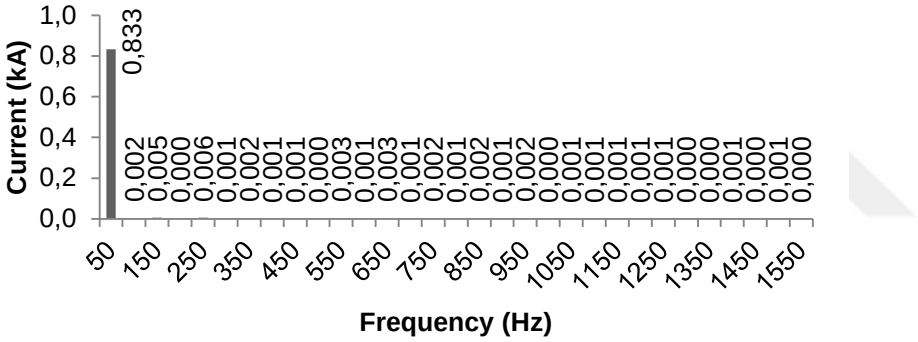

Figure 4.123. The harmonic spectrum of source current in phase *B* under heavy loaded system with high harmonic distortion, load unbalance and voltage regulation problems when PV supported ML-MFGCI is utilized.

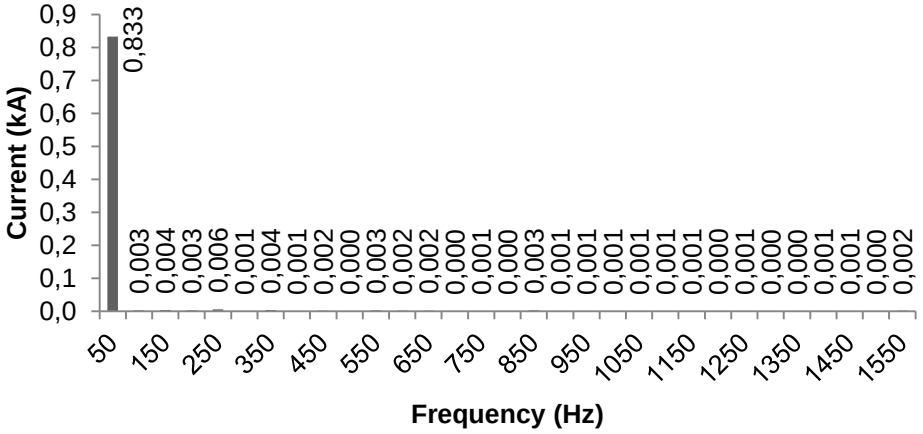

Figure 4.124. The harmonic spectrum of source current in phase *C* under heavy loaded system with high harmonic distortion, load unbalance and voltage regulation problems when PV supported ML-MFGCI is utilized.

The details of the source current harmonic contents are illustrated in Table 4.25.

Table 4.25. Harmonic contents of source currents under heavy loaded system with high harmonic distortion, load unbalance and voltage regulation problems when PV supported ML-MFGCI is utilized.

	Harmonic Contents of Source Current					
	Phase A		Phase B		Phase C	
Order	(%)	Value (kA)	(%)	Value (kA)	(%)	Value (kA)
1	100.000	0.84800	100.000	0.83300	100.000	0.83300
2	0.12154	0.00103	0.20678	0.00172	0.39594	0.00330
3	0.33545	0.00284	0.65064	0.00542	0.49497	0.00412
4	0.03957	0.00034	0.05219	0.00043	0.32445	0.00270
5	0.50344	0.00427	0.69649	0.00580	0.69127	0.00576
6	0.10204	0.00087	0.13152	0.00110	0.15904	0.00132
7	0.27298	0.00231	0.23608	0.00197	0.42449	0.00354
8	0.13021	0.00110	0.12277	0.00102	0.08846	0.00074
9	0.34591	0.00293	0.15656	0.00130	0.24169	0.00201
10	0.05891	0.00050	0.05529	0.00046	0.03487	0.00029
11	0.33830	0.00287	0.38415	0.00320	0.32049	0.00267
12	0.04984	0.00042	0.13349	0.00111	0.19271	0.00161
13	0.20988	0.00178	0.35027	0.00292	0.26335	0.00219
14	0.08459	0.00072	0.14034	0.00117	0.03640	0.00030
15	0.16376	0.00139	0.18297	0.00152	0.10658	0.00089
16	0.09384	0.00080	0.10575	0.00088	0.01895	0.00016
17	0.13802	0.00117	0.27094	0.00226	0.31220	0.00260
18	0.04337	0.00037	0.07238	0.00060	0.11566	0.00096
19	0.27965	0.00237	0.19541	0.00163	0.12237	0.00102
20	0.06283	0.00053	0.02134	0.00018	0.07485	0.00062
21	0.18145	0.00154	0.06815	0.00057	0.10259	0.00085
22	0.11632	0.00099	0.06738	0.00056	0.09782	0.00081
23	0.11841	0.00100	0.06014	0.00050	0.07019	0.00058
24	0.11680	0.00099	0.06671	0.00056	0.05671	0.00047
25	0.03452	0.00029	0.07439	0.00062	0.08609	0.00072
26	0.04838	0.00041	0.05857	0.00049	0.02973	0.00025
27	0.10633	0.00090	0.04641	0.00039	0.02690	0.00022
28	0.06497	0.00055	0.06362	0.00053	0.07391	0.00062
29	0.03387	0.00029	0.04342	0.00036	0.06859	0.00057
30	0.14559	0.00123	0.10633	0.00089	0.04855	0.00040
31	0.11764	0.00100	0.02918	0.00024	0.20241	0.00169
	THD=1.1%		THD=0.95%		THD=1.00%	

The Figure 4.125 shows the injected reactive power from ML-MFGCI into system to compensate reactive power and regulate PCC voltage.

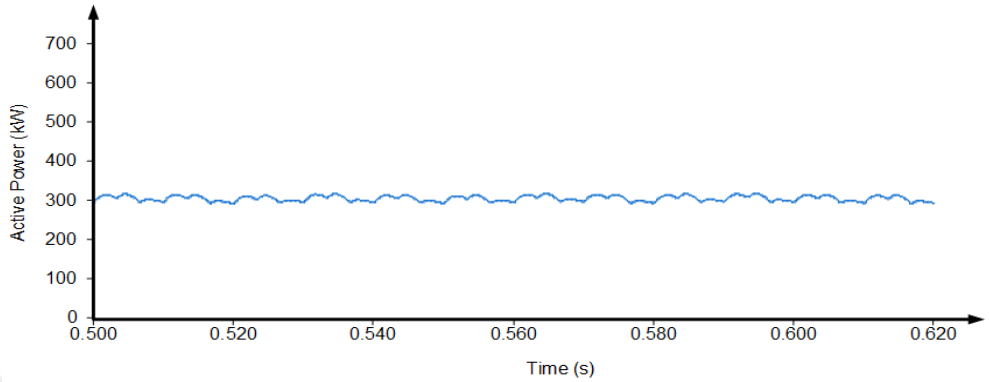

Figure 4.125. The injected reactive power from ML-MFGCI into when the ML-MFGCI equipped by PV system is utilized.

Case6: In the presence case, to verify the efficiency of the ML-MFGCI equipped by PV system in the transient conditions, the performance of the ML-MFGCI is tested for simultaneously to compensate the reactive power, current and voltage harmonics and load balancing as well as voltage regulation during voltage sag in the heavy loaded system. Figure 4.126 and 4.127 shows the injected active and reactive power in the voltage sag during. As seen from Figure 4.126 the injected active power from ML-MFGCI does not change and reactive power is increased to compensate voltage sag.

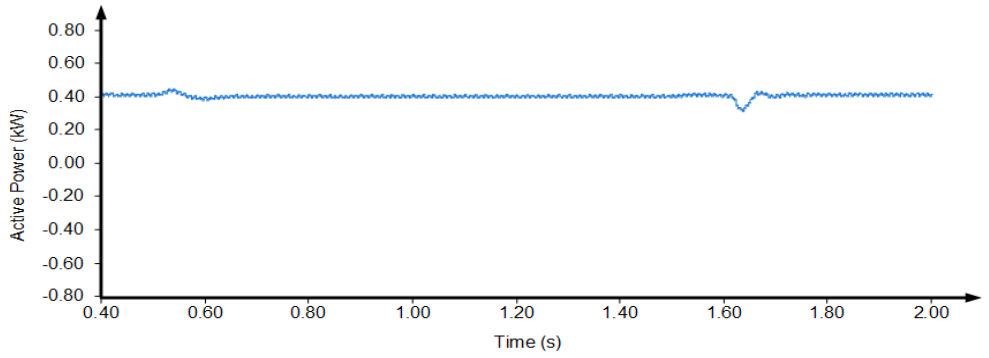

Figure 4.126. The injected active power from PV supported ML-MFGCI into power system during voltage sag condition.

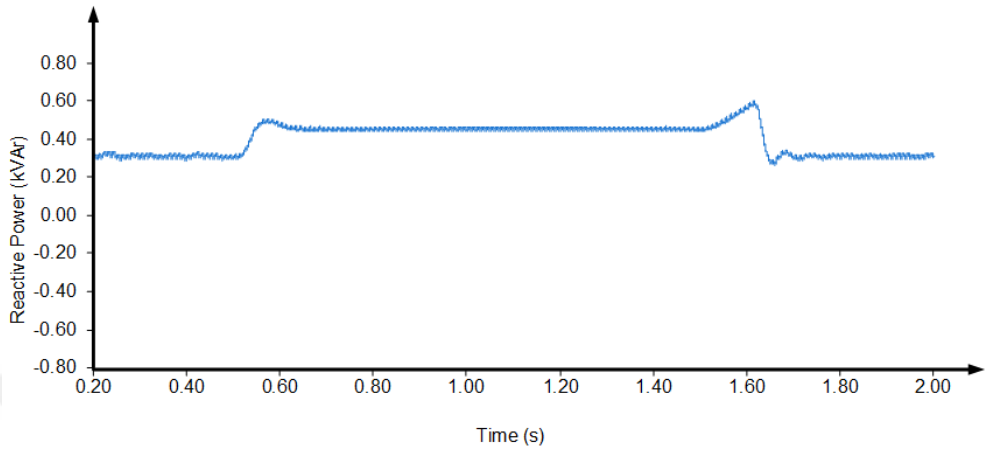

Figure 4.127. The injected reactive power from PV supported ML-MFGCI into power system during voltage sag condition.

Figure 4.128 shows the fundamental component of load current during voltage sag.

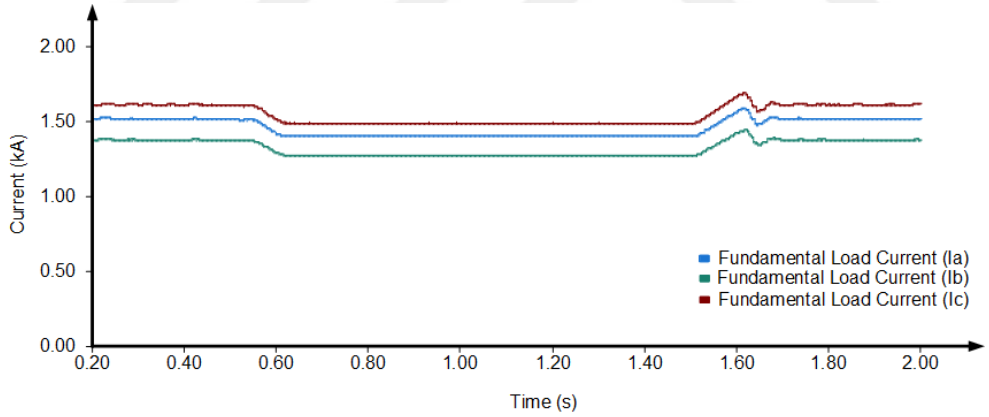

Figure 4.128. The fundamental component of load current in the voltage sag duration when PV supported ML-MFGCI is utilized.

Figure 4.129 shows the fundamental component of ınjected current by ML-MFGCI in voltage sag duration. In the voltage sag condition, the injected current from ML-MFGCI is increased to 1.1 *kA* in phase *A*, 1.2 *kA* in phase *B* and 1.2 *kA* in phase *C*.

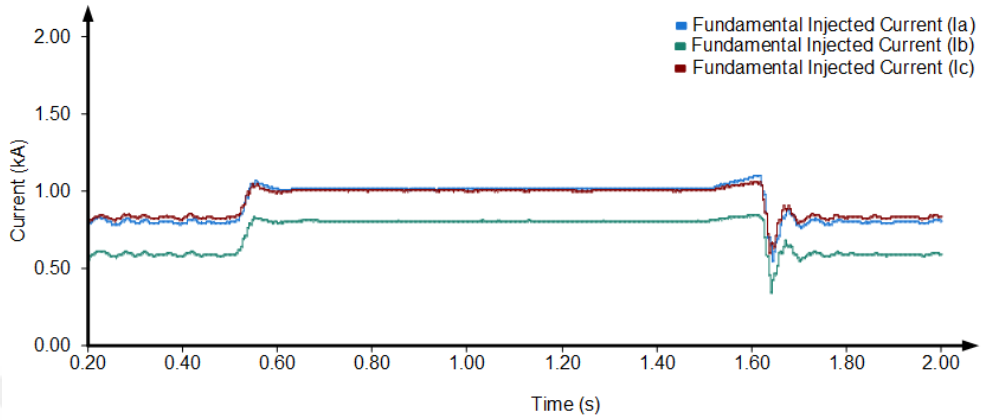

Figure 4.129. The fundamental component of injected current by ML-MFGCI into power system in the voltage sag duration.

Figure 4.130 shows the fundamental component of source current during voltage sag. As seen from Figure 4.130 the source current in both steady-state and transient condition is balance.

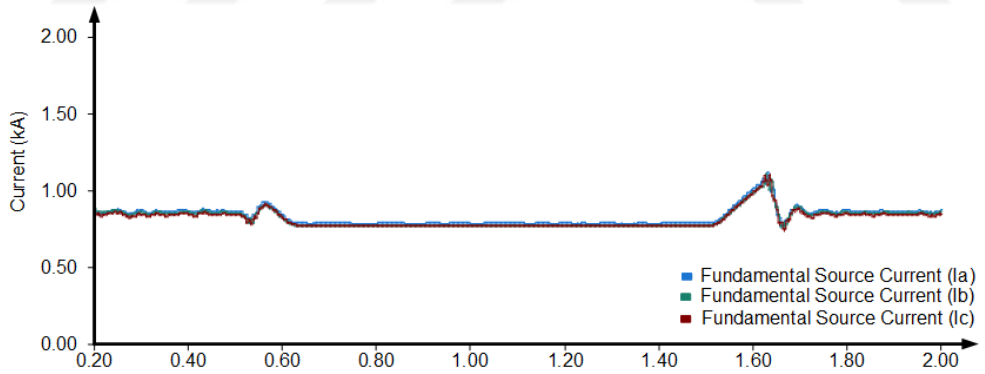

Figure 4.128. The fundamental component of source current during voltage sag when PV supported ML-MFGCI is utilized.

Figure 4.131 shows the THD of load current during voltage sag. The load current has 16.5% THD in phase *A*, 16.2% THD in phase *B* and 15.5% in phase *C*.

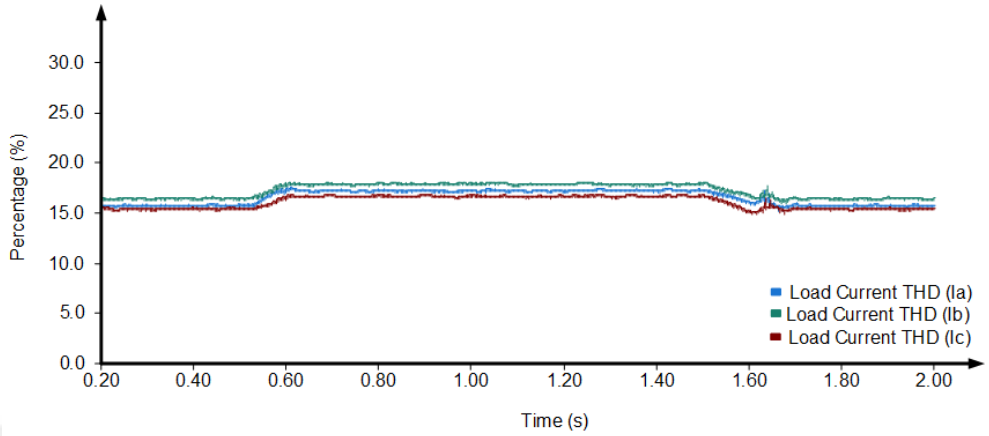

Figure 4.131. The load current THDs during voltage sag when PV supported ML-MFGCI is utilized.

Figure 4.132 shows the THD of PCC voltage during voltage sag. As seen from Figure 4.132 the THD of phase voltages in PCC is below than 5% and is in the within of standard limits.

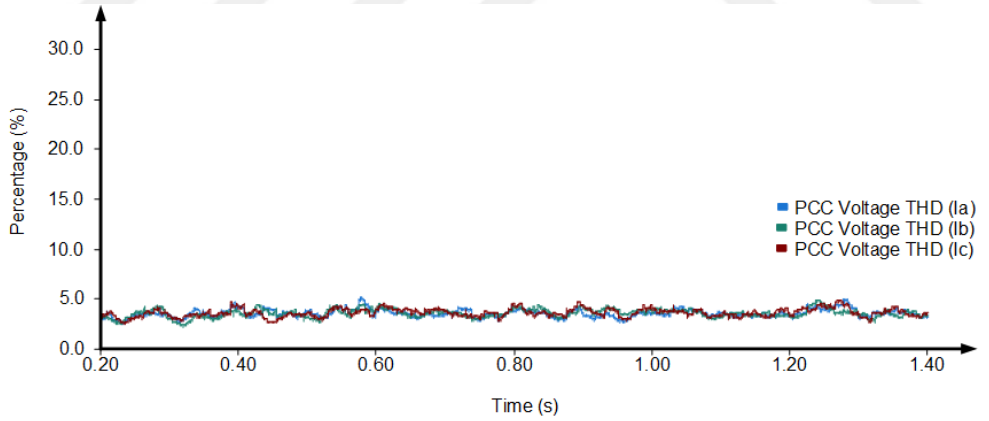

Figure 4.132. PCC phase voltage THDs during voltage sag when PV supported ML-MFGCI is utilized.

Figure 4.133 shows the THD of source current during voltage sag. As seen from Figure 4.133 the THD of source current is below than 5% and is in the within of standard limits.

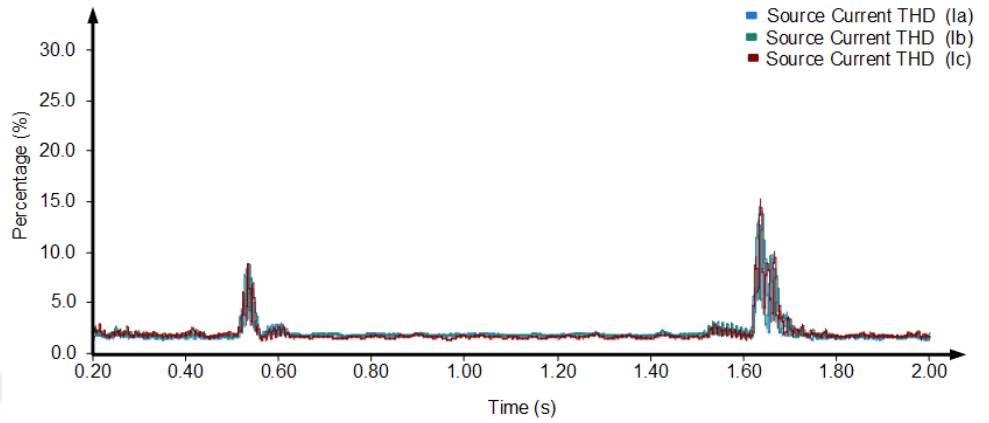

Figure 4.133. The source current THDs during voltage sag when PV supported ML-MFGCI is utilized.

Figure 4.134 shows the THD of source voltage during voltage sag. As seen from Figure 4.134 the THD of source voltage is below than 5% and is in the within of standard limits.

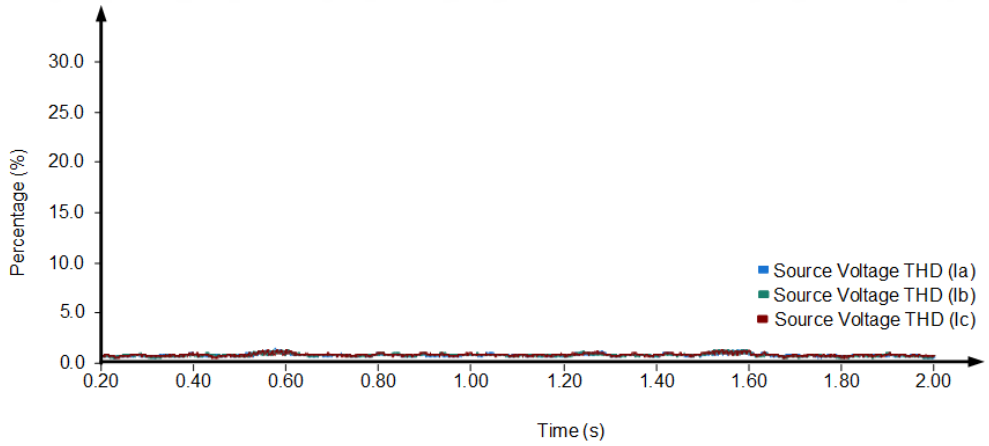

Figure 4.134. The source voltage THDs during voltage sag when PV supported ML-MFGCI is utilized.

Case7: In the previous sections the effectiveness of the proposed PV supported ML-MFGCI was tested for harmonic elimination, load unbalance and

reactive power compensation; and PCC voltage regulation as well as voltage sag compensation. Here the effectiveness of the proposed multi-objective control method for ML-MFGCI to this condition with 22.5% voltage swell. Figure 4.135 shows the fundamental component of load current during voltage swell.

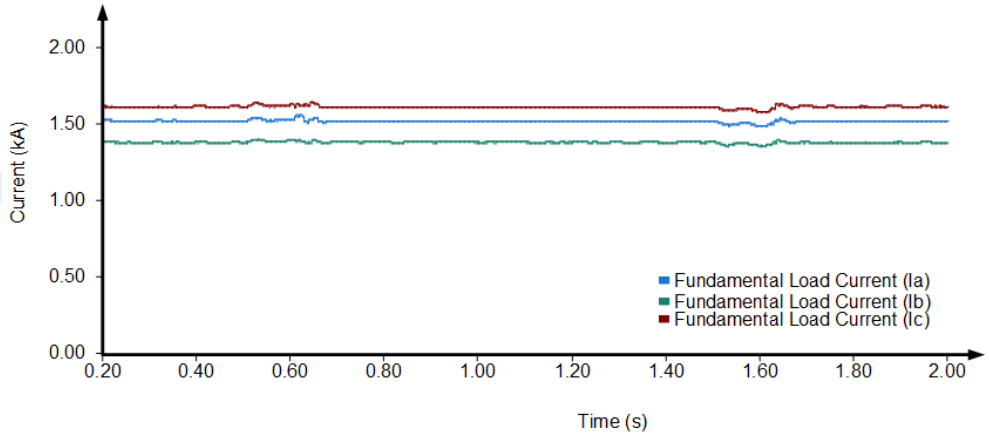

Figure 4.135. The fundamental component of load current during voltage swell when PV supported ML-MFGCI is utilized.

As mentioned above, in the proposed control algorithm an active power control was introduced to compensate voltage swell. To compensate voltage swell, it's necessary to reduce the injected active power and to increase the injected reactive power from ML-MFGCI into power system. For this goal, the active power controller adjusts the DC link voltage to control the injected active power from ML-MFGCI into power system. Figure 4.136 shows the DC voltages during voltage swell.

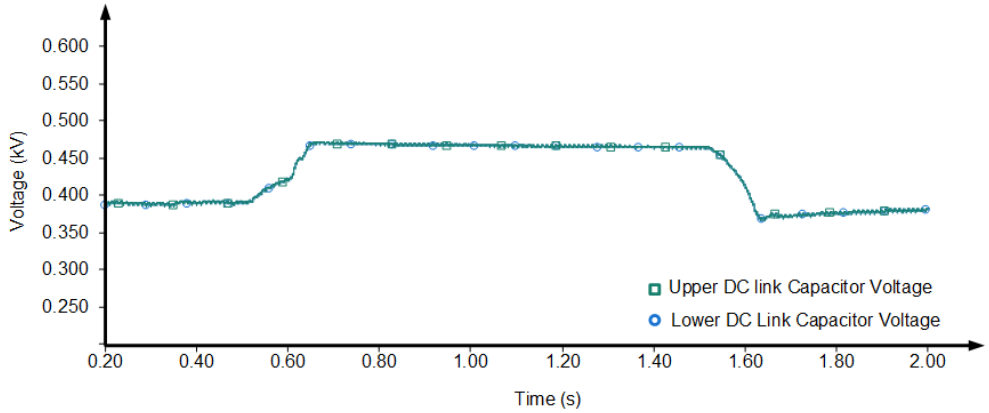

Figure 4.136. The DC link voltages of ML-MFGCI during voltage swell.

As shown in Figure 4.137 in order to release the overall capacity of ML-MFGCI to inject reactive power during voltage swell the output active power from ML-MFGCI decrease to zero according to DC link voltage control.

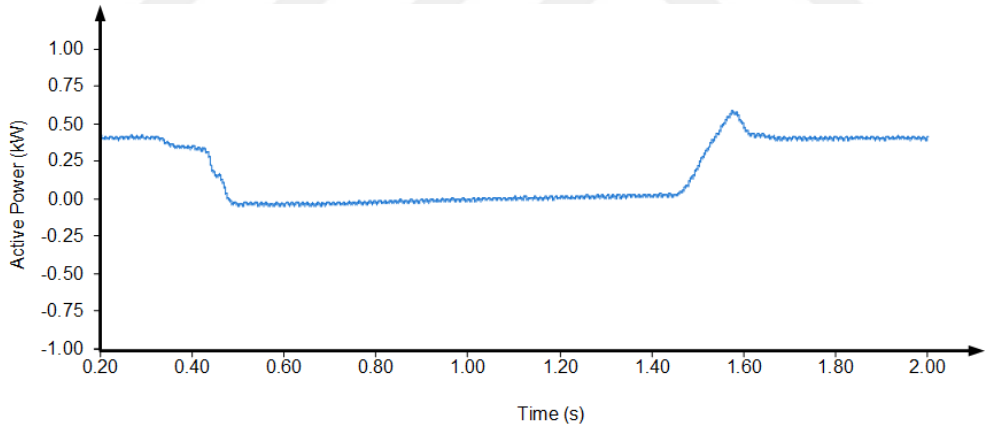

Figure 4.137. The injected active power from PV supported ML-MFGCI into power system during voltage swell.

As seen from Figure 4.138 to compensate the voltage swell, the injected current from ML-MFGCI is decreased from 0.8 to 0.65 *kA* in phase *A* and increased from 0.65 to 0.85 *kA* in phase *B*.

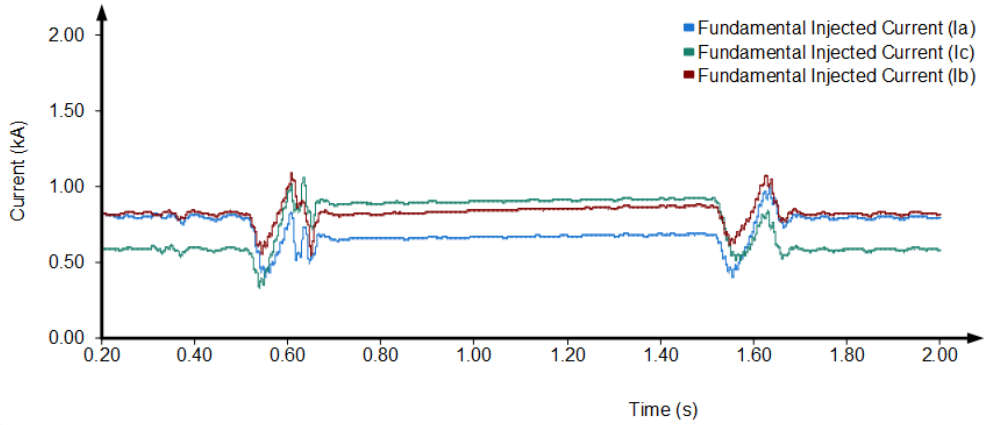

Figure 4.138. The injected current from PV supported ML-MFGCI into power system during voltage swell.

Figure 4.139 shows the fundamental of PCC phase voltages during voltage swell. As seen from Figure 4.139 the ML-MFGCI can compensate the voltage swell and keep the PCC voltage to nominal value.

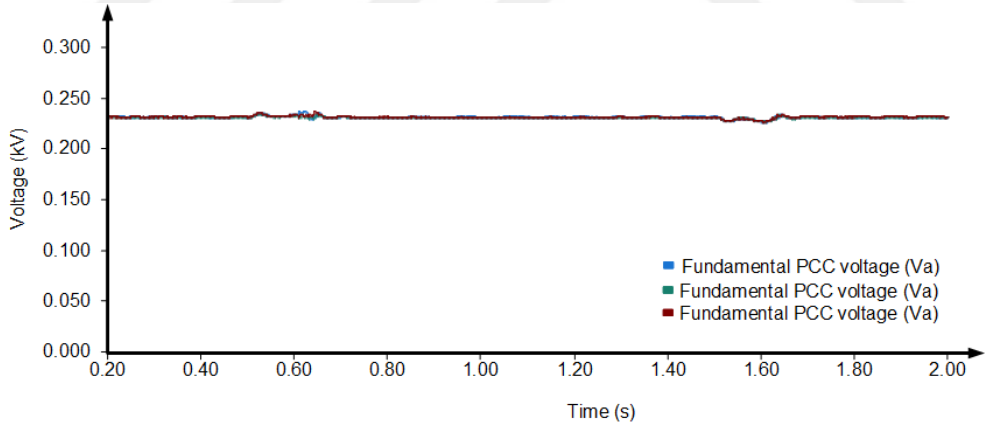

Figure 4.139. The PCC phase voltages during voltage swell.

Case8: In the presence case, to verify the performance of the PV supported ML-MFGCI system tests for simultaneously to compensate the reactive power, current and voltage harmonics, load balancing and neutral line current as well as to regulate voltage in the heavy loaded system are achieved. Figure 4.140 shows the

load current waveforms where between 0.5 s and 0.65 s become unbalance. In this condition, load current reaches from 1.733 *kA* to 1.172 *kA* in phase *A* and remains constant with 1.733 *kA* value in phase *B* and *C*. In this situation, load current has 0.2 *kA* negative sequence component and 0.19 *kA* zero sequence component.

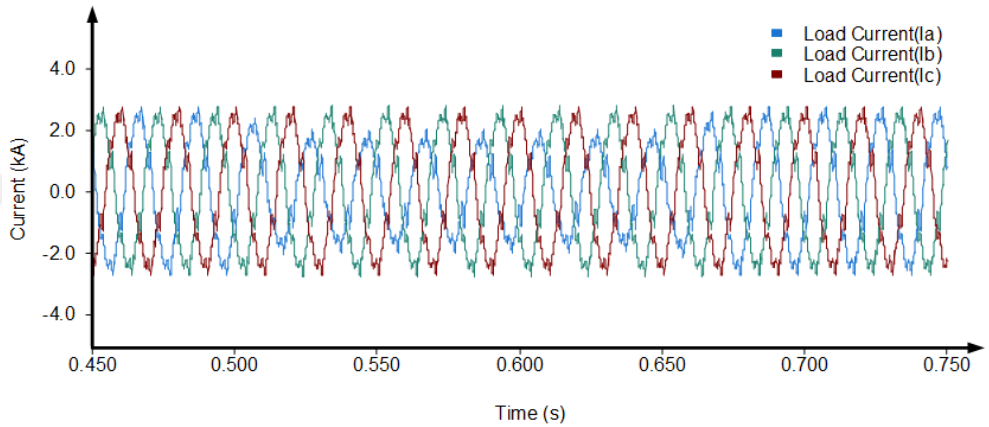

Figure 4.140. The load current waveforms with high level negative and zero sequence components, harmonic distortion, and voltage regulation problems.

As seen from Figure 4.140, the load currents have high level harmonic components. The harmonic spectrums of the load currents for phase *A*, phase *B* and phase *C* are shown in the Figures 4.141, 4.142 and 4.143, respectively.

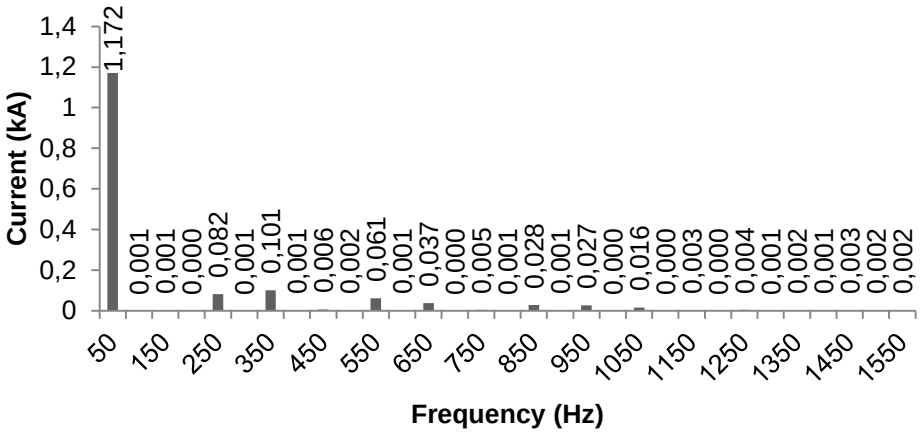

Figure 4.141. The harmonic spectrum of load current in phase *A* with high level negative and zero sequence components, harmonic distortion, and voltage regulation problems.

.

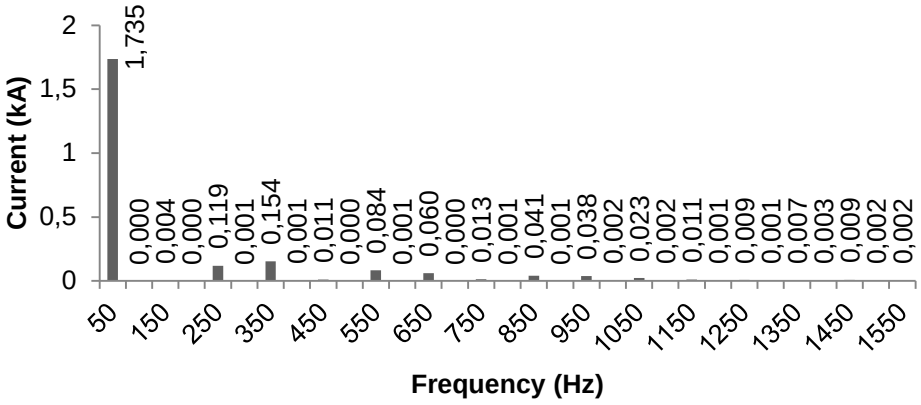

Figure 4.142. The harmonic spectrum of load current in phase *B* with high level negative and zero sequence components, harmonic distortion, and voltage regulation problems.

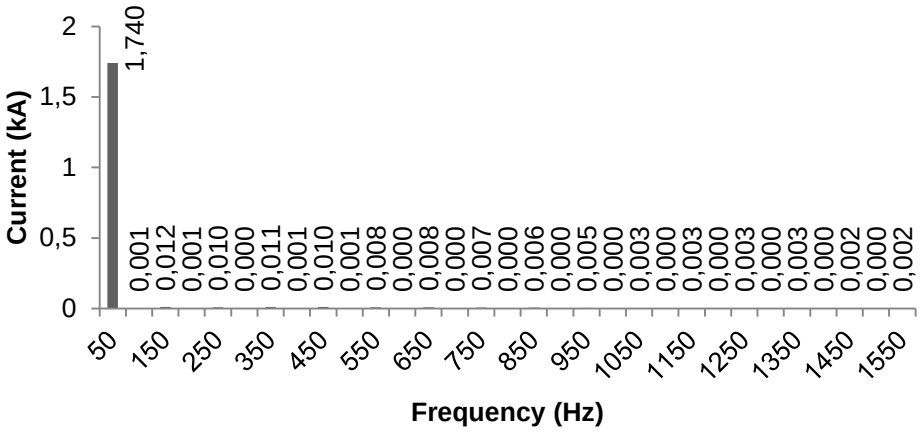

Figure 4.143. The harmonic spectrum of load current in phase *C* with high level negative and zero sequence components, harmonic distortion, and voltage regulation problems.

The load current has 18.6%, 12.6% and 12.8% THD rates in phase *A*, *B* and *C*, respectively. The details of load current harmonic contents are illustrated in Table 4.26.

Table 4.26. Harmonic contents of load currents with high level negative and zero sequence components, harmonic distortion, and voltage regulation problems

	Harmonic Contents of Source Current					
	Phase A		Phase B		Phase C	
Order	(%)	Value (kA)	(%)	Value (kA)	(%)	Value (kA)
1	100.000	1.17150	100.000	1.73500	100.000	1.74000
2	0.05172	0.00061	0.02785	0.00048	0.03099	0.00054
3	0.09498	0.00111	0.21474	0.00373	0.66985	0.01166
4	0.02493	0.00029	0.02609	0.00045	0.03642	0.00063
5	7.02505	0.08230	6.85742	0.11898	0.55781	0.00971
6	0.05716	0.00067	0.05562	0.00096	0.01350	0.00023
7	8.62553	0.10105	8.89609	0.15435	0.60806	0.01058
8	0.12310	0.00144	0.08305	0.00144	0.05068	0.00088
9	0.53085	0.00622	0.61382	0.01065	0.58343	0.01015
10	0.17058	0.00200	0.01771	0.00031	0.03527	0.00061
11	5.20852	0.06102	4.86905	0.08448	0.45352	0.00789
12	0.12486	0.00146	0.06520	0.00113	0.02685	0.00047
13	3.15804	0.03700	3.45033	0.05986	0.43131	0.00750
14	0.02480	0.00029	0.01728	0.00030	0.01960	0.00034
15	0.43356	0.00508	0.76935	0.01335	0.40979	0.00713
16	0.05114	0.00060	0.03727	0.00065	0.00833	0.00014
17	2.35915	0.02764	2.35191	0.04081	0.33621	0.00585
18	0.08554	0.00100	0.06008	0.00104	0.00998	0.00017
19	2.26962	0.02659	2.21392	0.03841	0.27141	0.00472
20	0.03851	0.00045	0.08877	0.00154	0.01942	0.00034
21	1.34685	0.01578	1.35387	0.02349	0.15627	0.00272
22	0.01862	0.00022	0.12531	0.00217	0.01701	0.00030
23	0.22871	0.00268	0.65191	0.01131	0.14761	0.00257
24	0.03160	0.00037	0.08349	0.00145	0.01820	0.00032
25	0.37035	0.00434	0.50772	0.00881	0.15428	0.00268
26	0.06440	0.00075	0.07291	0.00126	0.01358	0.00024
27	0.16877	0.00198	0.39806	0.00691	0.15737	0.00274
28	0.11980	0.00140	0.16518	0.00287	0.00653	0.00011
29	0.28405	0.00333	0.51136	0.00887	0.12780	0.00222
30	0.15541	0.00182	0.08781	0.00152	0.00914	0.00016
31	0.17404	0.00204	0.11416	0.00198	0.09255	0.00161
	THD=18.6%		THD=12.6%		THD=12.8%	

Figure 4.144 shows the injected current in phase *A*, *B* and *C* to compensate reactive power, harmonics and load unbalance with high level negative sequence as

well as voltage regulation in PCC by PV supported ML-MFGCI. In this case, the ML-MFGCI injects 0.415 *kA*, 0.896 and 0.880 *kA* in phase *A*, *B* and *C*, respectively with 0.21 kA negative and 0.195 zero sequence components.

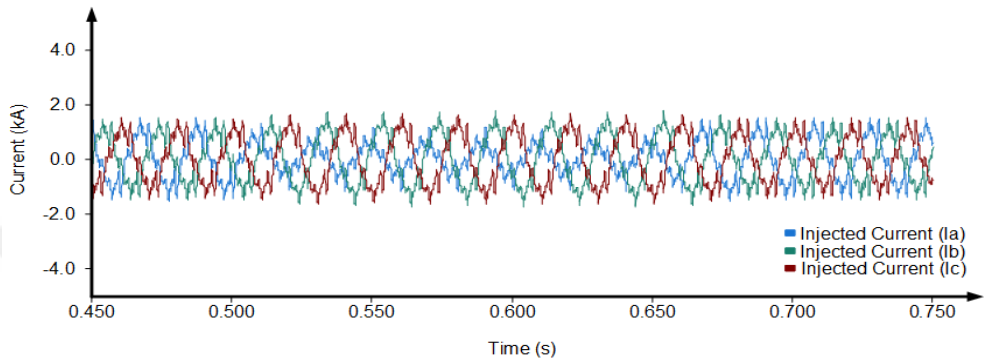

Figure 4.144. The injected current waveforms by PV supported ML-MFGCI to compensate negative and zero sequence components, harmonic distortion and reactive power as well as regulate the PCC voltage.

The harmonic spectrum of the injected currents by PV supported ML-MFGCI into phases *A*, *B* and *C* are shown in the Figures 4.145, 4.146 and 4.147, respectively.

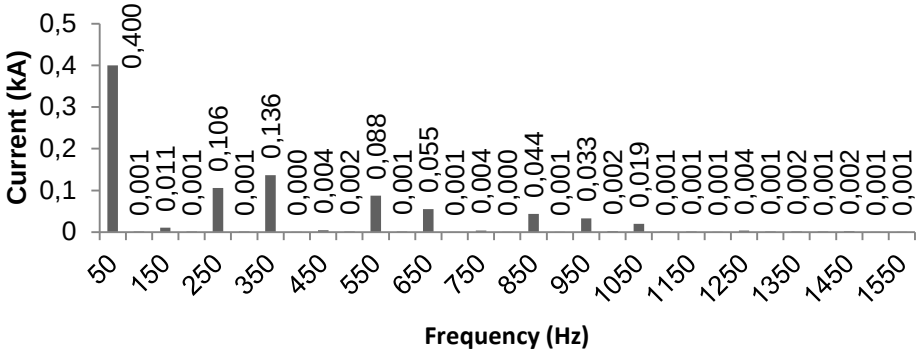

Figure 4.145. The harmonic spectrum of injected current in phase *A* by PV supported ML-MFGCI to compensate negative and zero sequence components, harmonic distortion and reactive power as well as regulate the PCC voltage.

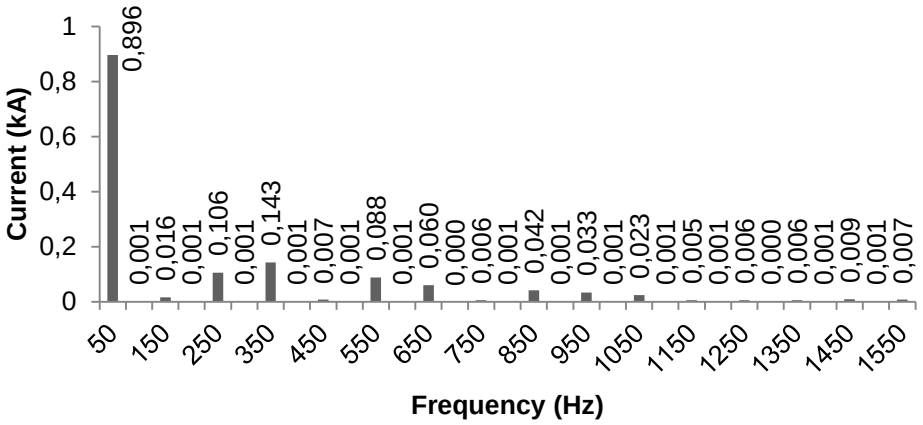

Figure 4.146. The harmonic spectrum of injected current in phase *B* by PV supported ML-MFGCI to compensate negative and zero sequence components, harmonic distortion and reactive power as well as regulate the PCC voltage.

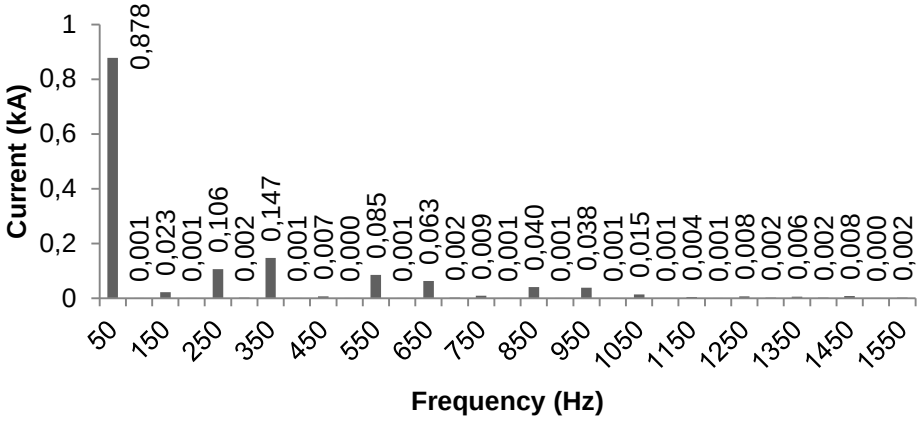

Figure 4.147. The harmonic spectrum of injected current in phase *C* by PV supported ML-MFGCI to compensate negative and zero sequence components, harmonic distortion and reactive power as well as regulate the PCC voltage.

The details of load current harmonic contents are illustrated in Table 4.27.

Table 4.27. Harmonic contents of injected currents by PV supported ML-MFGCI into power system to compensate negative and zero sequence components, harmonic distortion and reactive power as well as regulate the PCC voltage.

	Harmonic Contents of Injected Current					
	Phase A		Phase B		Phase C	
Order	(%)	Value (kA)	(%)	Value (kA)	(%)	Value (kA)
1	100.000	0.40000	100.000	0.89600	100.000	0.87800
2	0.27663	0.00111	0.06892	0.00062	0.13847	0.00122
3	2.63758	0.01055	1.81471	0.01626	2.58421	0.02269
4	0.26303	0.00105	0.07721	0.00069	0.08702	0.00076
5	26.4553	0.10582	11.8116	0.10583	12.1229	0.10644
6	0.25914	0.00104	0.07032	0.00063	0.20345	0.00179
7	34.0822	0.13633	15.9616	0.14302	16.7152	0.14676
8	0.11447	0.00046	0.16355	0.00147	0.07746	0.00068
9	1.11440	0.00446	0.81460	0.00730	0.77954	0.00684
10	0.40711	0.00163	0.08897	0.00080	0.05689	0.00050
11	21.8942	0.08758	9.80547	0.08786	9.71905	0.08533
12	0.35280	0.00141	0.12242	0.00110	0.11877	0.00104
13	13.8275	0.05531	6.74424	0.06043	7.20104	0.06323
14	0.19953	0.00080	0.03410	0.00031	0.23646	0.00208
15	0.95145	0.00381	0.65044	0.00583	1.02247	0.00898
16	0.06174	0.00025	0.05980	0.00054	0.15901	0.00140
17	10.9128	0.04365	4.66463	0.04180	4.61211	0.04049
18	0.23931	0.00096	0.05887	0.00053	0.11069	0.00097
19	8.27278	0.03309	3.73460	0.03346	4.36764	0.03835
20	0.50454	0.00202	0.13646	0.00122	0.12249	0.00108
21	4.84934	0.01940	2.60888	0.02338	1.65523	0.01453
22	0.24219	0.00097	0.07854	0.00070	0.05817	0.00051
23	0.35131	0.00141	0.56979	0.00511	0.50056	0.00439
24	0.14496	0.00058	0.12551	0.00112	0.06117	0.00054
25	0.91638	0.00367	0.64360	0.00577	0.85868	0.00754
26	0.36591	0.00146	0.05377	0.00048	0.22460	0.00197
27	0.40361	0.00161	0.64506	0.00578	0.70679	0.00621
28	0.33170	0.00133	0.05805	0.00052	0.25500	0.00224
29	0.56831	0.00227	1.03010	0.00923	0.89282	0.00784
30	0.13661	0.00055	0.16678	0.00149	0.04543	0.00040
31	0.16618	0.00066	0.79537	0.00713	0.20099	0.00176

Figure 4.148 shows the load and source currents unbalance ratio. As seen from Figure 4.148, the ML-MFGCI reduced unbalance ratio from 12.86% in load

current to 2.85% in source current. Thus the negative sequence component of source current reduced to 0.024 *kA* versus load current where contains 0.2 *kA* negative sequence.

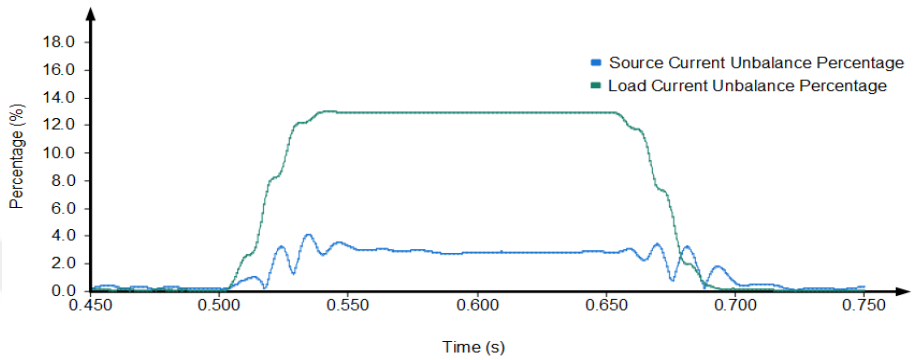

Figure 4.148. The load and source currents unbalance ratio when PV supported ML-MFGCI is utilized to compensate negative and zero sequence components, harmonic distortion and reactive power as well as regulate the PCC voltage.

Figure 4.149 shows the load and source currents zero sequence components. As seen from Figure 4.149 the ML-MFGCI reduced zero sequence from 0.19 *kA* in load current almost to zero in the source current.

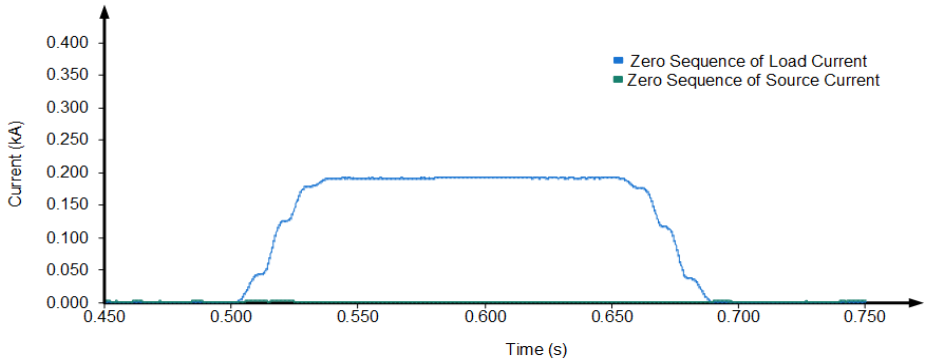

Figure 4.149. The zero sequence components of load and source currents when PV supported ML-MFGCI is utilized to compensate negative and zero sequence components, harmonic distortion and reactive power as well as regulate the PCC voltage.

Figure 4.150 shows the load and source neutral line currents with injected current into neutral line by PV supported ML-MFGCI. As seen from Figure 4.150, the ML-MFGCI is able to completely clear current in neutral line. In this context the neutral line current in load side is reduced from 0.6 *kA* nearly to zero in source side.

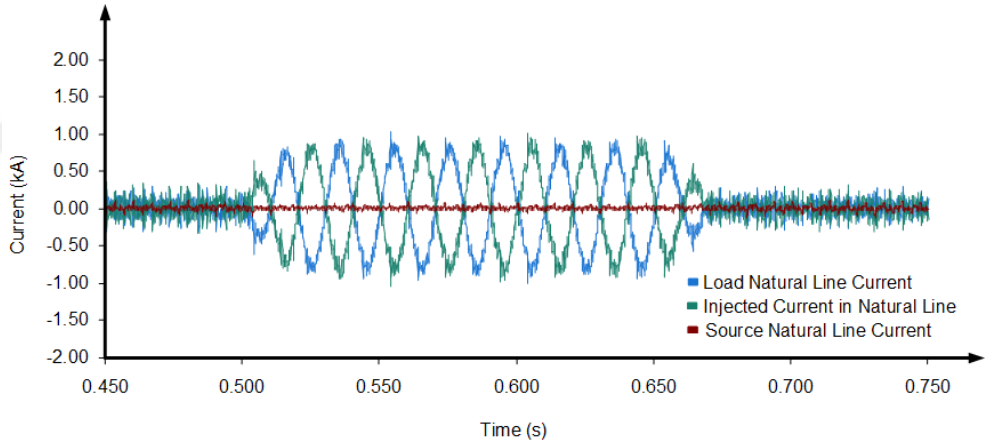

Figure 4.150. The line load and source neutral current when PV supported ML-MFGCI is utilized to compensate negative and zero sequence components, harmonic distortion and reactive power as well as regulate the PCC voltage.

Figure 4.151 shows the source current where free upon from harmonics and zero sequence component and diminished negative sequence component with 0.925 *kA*, 0.9 *kA* and 0,928 *kA* in phase *A*, *B* and *C*, respectively.

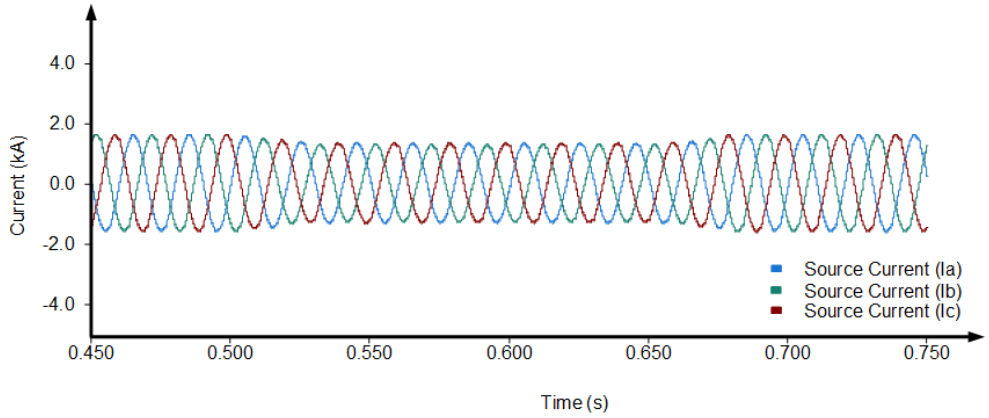

Figure 4.151. The source current waveforms when PV supported ML-MFGCI utilized to compensate negative and zero sequence components, harmonic distortion and reactive power as well as regulate the PCC voltage.

The harmonic spectrum of the source currents for phases *A*, *B* and *C* are shown in the Figures 4.152, 4.153 and 4.154, respectively when PV supported ML-MFGCI is utilized to compensate high level of negative and zero sequence components, voltage/current harmonics and reactive power as well as to regulate PCC voltage.

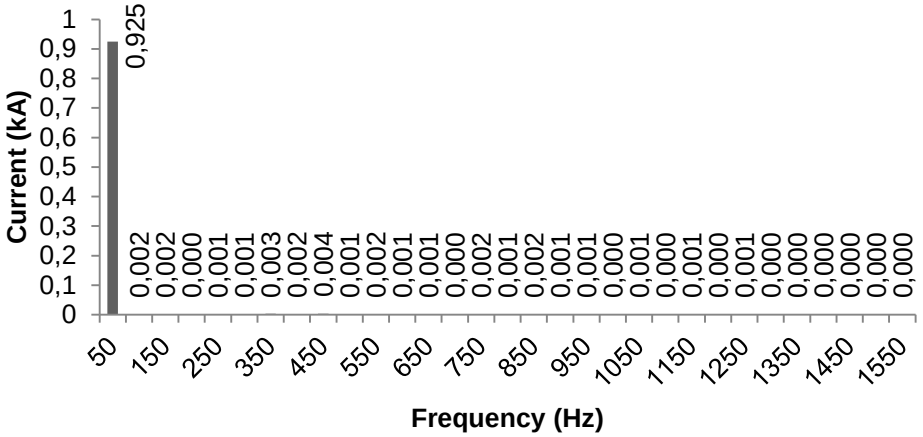

Figure 4.152. The harmonic spectrum of source current in phase *A* when PV supported ML-MFGCI is utilized to compensate negative and zero sequence components, harmonic distortion and reactive power as well as regulate the PCC voltage.

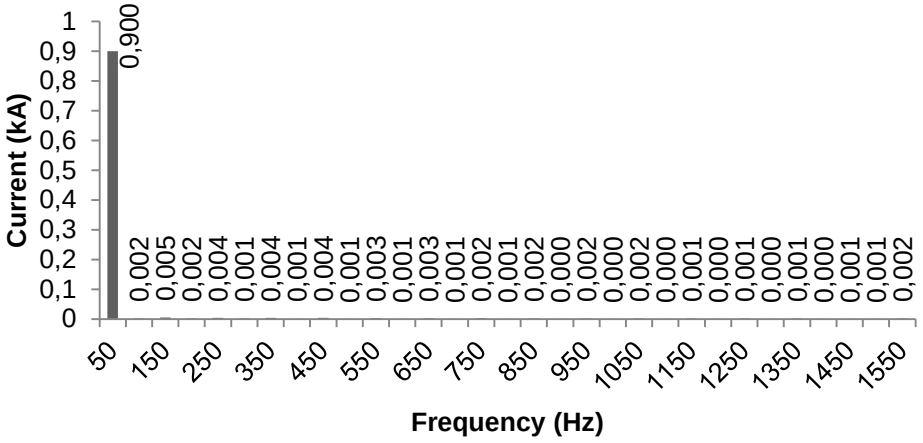

Figure 4.153. The harmonic spectrum of source current in phase *B* when PV supported ML-MFGCI is utilized to compensate negative and zero sequence components, harmonic distortion and reactive power as well as regulate the PCC voltage.

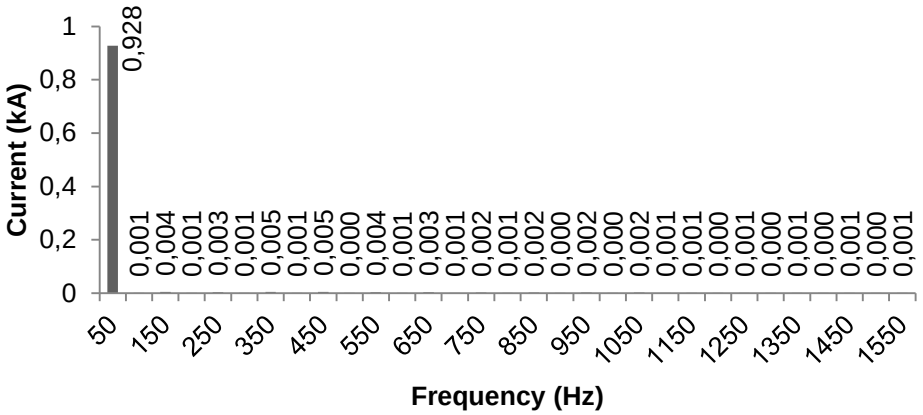

Figure 4.154. The harmonic spectrum of source current in phase *C* when PV supported ML-MFGCI is utilized to compensate negative and zero sequence components, harmonic distortion and reactive power as well as regulate the PCC voltage.

The source current has 1.2%, 1.6% and 1.6% THD rates in phase *A*, *B* and *C*, respectively. The details of source current harmonic contents are illustrated in Table 4.28.

Table 4.28. Harmonic contents of source currents when PV supported ML-MFGCI utilized to compensate negative and zero sequence components, harmonic distortion and reactive power as well as regulate the PCC voltage

	Harmonic Contents of Source Current					
	Phase A		Phase B		Phase C	
Order	(%)	Value (kA)	(%)	Value (kA)	(%)	Value (kA)
1	100.000	0.92470	100.000	0.90000	100.00000	0.92800
2	0.19637	0.00182	0.16892	0.00152	0.12542	0.00116
3	0.19007	0.00176	0.50113	0.00451	0.46320	0.00430
4	0.03507	0.00032	0.16857	0.00152	0.15840	0.00147
5	0.10943	0.00101	0.43245	0.00389	0.33177	0.00308
6	0.12138	0.00112	0.12777	0.00115	0.15283	0.00142
7	0.37083	0.00343	0.46202	0.00416	0.49045	0.00455
8	0.19549	0.00181	0.11202	0.00101	0.11463	0.00106
9	0.39855	0.00369	0.46337	0.00417	0.49134	0.00456
10	0.14550	0.00135	0.07541	0.00068	0.00438	0.00004
11	0.26291	0.00243	0.34629	0.00312	0.39165	0.00363
12	0.05552	0.00051	0.06043	0.00054	0.07304	0.00068
13	0.09560	0.00088	0.31086	0.00280	0.31533	0.00293
14	0.03863	0.00036	0.06020	0.00054	0.11991	0.00111
15	0.17300	0.00160	0.26125	0.00235	0.25584	0.00237
16	0.06920	0.00064	0.07235	0.00065	0.10718	0.00099
17	0.17087	0.00158	0.22302	0.00201	0.21963	0.00204
18	0.06443	0.00060	0.05226	0.00047	0.04281	0.00040
19	0.12508	0.00116	0.23483	0.00211	0.26453	0.00245
20	0.04380	0.00041	0.02107	0.00019	0.04738	0.00044
21	0.08412	0.00078	0.17574	0.00158	0.18701	0.00174
22	0.02960	0.00027	0.00483	0.00004	0.07525	0.00070
23	0.12825	0.00119	0.15283	0.00138	0.13807	0.00128
24	0.01956	0.00018	0.04509	0.00041	0.03530	0.00033
25	0.10453	0.00097	0.15459	0.00139	0.10564	0.00098
26	0.02583	0.00024	0.05003	0.00045	0.01823	0.00017
27	0.05289	0.00049	0.13122	0.00118	0.14081	0.00131
28	0.03576	0.00033	0.01956	0.00018	0.00343	0.00003
29	0.03282	0.00030	0.08603	0.00077	0.13291	0.00123
30	0.01928	0.00018	0.06377	0.00057	0.01420	0.00013
31	0.04160	0.00038	0.18238	0.00164	0.13745	0.00128
	THD=1.21%		THD=1.64%		THD=1.46%	

Figure 4.155 shows the source voltage where free upon from harmonics and zero sequence component and diminished negative sequence component with 238 *V*, 238.2 *V* and 238.2 *V* in phase *A*, *B* and *C*, respectively.

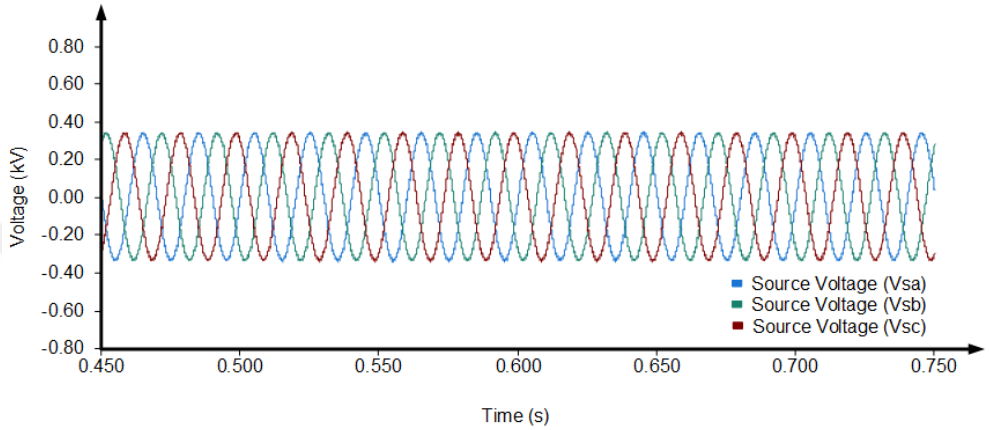

Figure 4.155. The source voltage waveforms when PV supported ML-MFGCI is utilized to compensate negative and zero sequence components, harmonic distortion and reactive power as well as regulate the PCC voltage.

The harmonic spectrum of the source voltages for phases *A*, *B* and *C* are shown in the Figures 4.156, 4.157 and 4.158, respectively when PV supported ML-MFGCI is utilized to compensate high level of negative and zero sequence components, voltage/current harmonics and reactive power as well as to regulate PCC voltage.

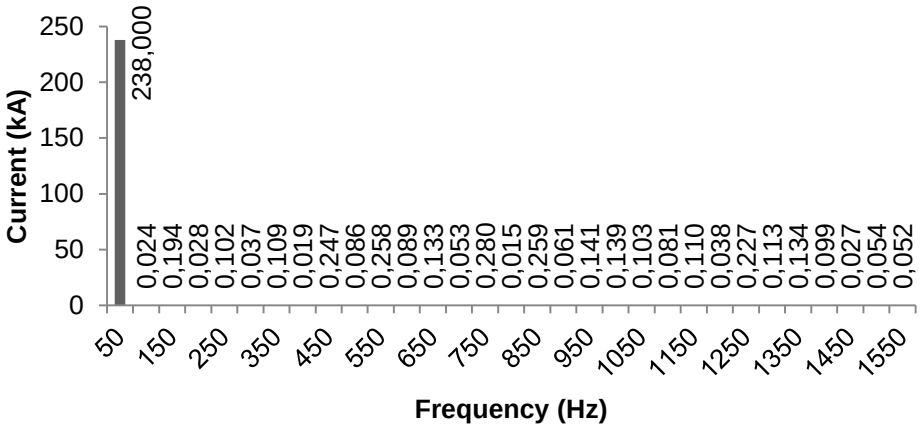

Figure 4.156. The harmonic spectrum of source voltage in phase *A* when PV supported ML-MFGCI is utilized to compensate negative and zero sequence components, harmonic distortion and reactive power as well as regulate the PCC voltage.

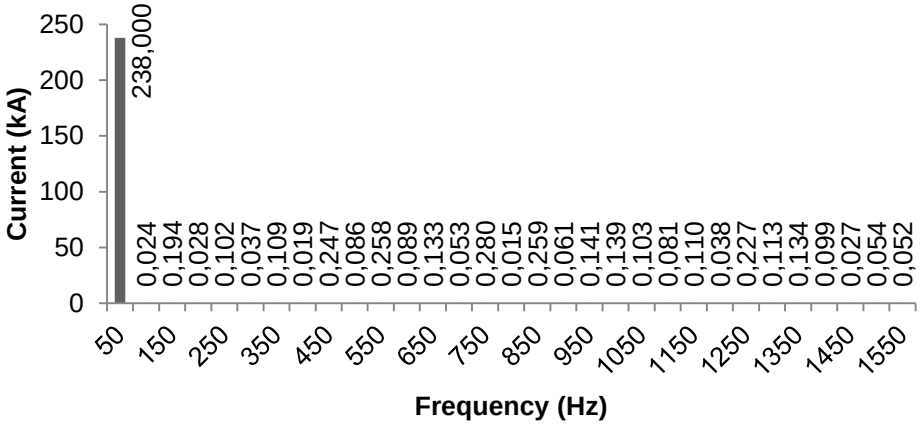

Figure 4.157. The harmonic spectrum of source voltage in phase *B* when PV supported ML-MFGCI is utilized to compensate negative and zero sequence components, harmonic distortion and reactive power as well as regulate the PCC voltage.

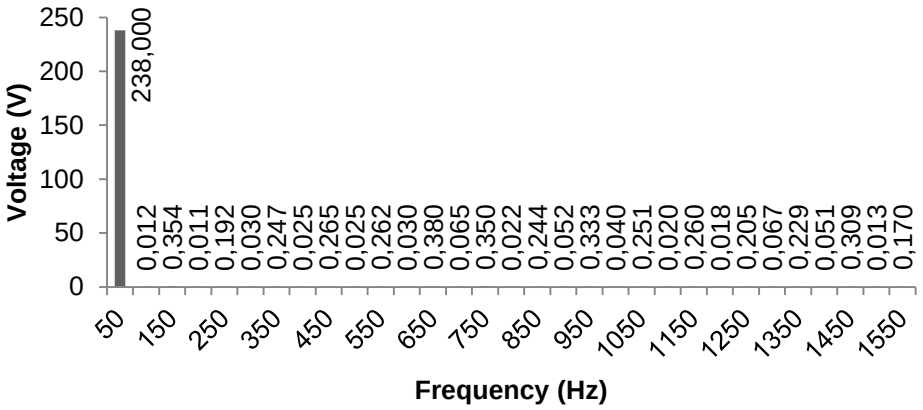

Figure 4.158. The harmonic spectrum of source voltage in phase *C* when PV supported ML-MFGCI is utilized to compensate negative and zero sequence components, harmonic distortion and reactive power as well as regulate the PCC voltage.

The source voltage has 0.31%, 0.36% and 0.42% THD rates in phase *A*, *B* and *C*, respectively. The details of source voltage harmonic contents are illustrated in Table 4.29.

Table 4.29. Harmonic contents of source voltage when PV supported ML-MFGCI utilized to compensate negative and zero sequence components, harmonic distortion and reactive power as well as regulate the PCC voltage

	Harmonic Contents of Source Voltages					
	Phase A		Phase B		Phase C	
Order	(%)	Value (V)	(%)	Value (V)	(%)	Value (V)
1	100.000	238.000	100.000	238.000	100.000	238.000
2	0.01010	0.02405	0.00725	0.01725	0.00515	0.01226
3	0.08170	0.19445	0.11443	0.27234	0.14887	0.35431
4	0.01172	0.02788	0.00229	0.00546	0.00455	0.01083
5	0.04291	0.10212	0.04603	0.10954	0.08067	0.19200
6	0.01561	0.03715	0.00798	0.01899	0.01265	0.03010
7	0.04596	0.10937	0.07499	0.17847	0.10387	0.24721
8	0.00782	0.01862	0.02013	0.04792	0.01067	0.02538
9	0.10392	0.24733	0.09382	0.22328	0.11133	0.26496
10	0.03621	0.08618	0.01317	0.03135	0.01055	0.02512
11	0.10848	0.25819	0.06872	0.16355	0.11017	0.26220
12	0.03723	0.08860	0.01334	0.03175	0.01276	0.03037
13	0.05590	0.13305	0.09706	0.23100	0.15964	0.37994
14	0.02230	0.05307	0.00972	0.02314	0.02735	0.06509
15	0.11745	0.27953	0.10231	0.24350	0.14703	0.34993
16	0.00612	0.01456	0.00628	0.01494	0.00945	0.02250
17	0.10880	0.25893	0.07030	0.16730	0.10267	0.24437
18	0.02559	0.06090	0.00663	0.01579	0.02181	0.05190
19	0.05940	0.14137	0.09686	0.23052	0.13976	0.33264
20	0.05851	0.13925	0.01996	0.04750	0.01674	0.03983
21	0.04315	0.10269	0.13153	0.31303	0.10540	0.25085
22	0.03423	0.08146	0.01608	0.03827	0.00833	0.01984
23	0.04622	0.11000	0.12322	0.29327	0.10921	0.25992
24	0.01598	0.03804	0.02003	0.04767	0.00767	0.01827
25	0.09525	0.22668	0.07052	0.16785	0.08604	0.20477
26	0.04768	0.11348	0.00474	0.01129	0.02819	0.06710
27	0.05620	0.13375	0.09770	0.23254	0.09602	0.22852
28	0.04160	0.09902	0.01281	0.03048	0.02130	0.05068
29	0.01125	0.02678	0.14449	0.34390	0.12990	0.30917
30	0.02285	0.05439	0.02501	0.05952	0.00555	0.01320
31	0.02193	0.05219	0.15113	0.35969	0.07123	0.16954
	THD=0.31%		THD=0.36%		THD=0.42%	

Figure 4.159 shows the DC link capacitors voltage when the PV supported ML-MFGCI injects current into neutral line to compensate load neutral line current. As seen from Figure 4.159, the control algorithm can keep the DC voltages balance when the high level of neutral line current injection is required. In this situation the reference DC link voltage is obtained by MPPT algorithm.

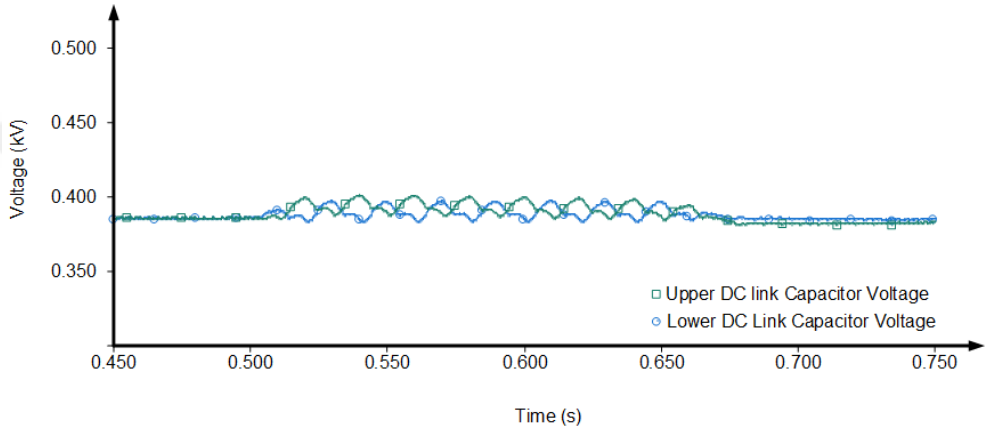

Figure 4.159. The DC link capacitors voltage of PV supported ML-MFGCI when ML-MFGCI utilized to compensate high level negative and zero sequence components, harmonic distortion and reactive power as well as regulate the PCC voltage.

Figures 4.160 and 4.161 shows the injected active and reactive power from PV supported ML-MFGCI into power system when ML-MFGCI utilized to compensate high level negative and zero sequence components, harmonic distortion and reactive power as well as regulate the PCC voltage. In this instance ML-MFGCI injects 420 *kW* and 270 *kVAr* into power system, respectively.

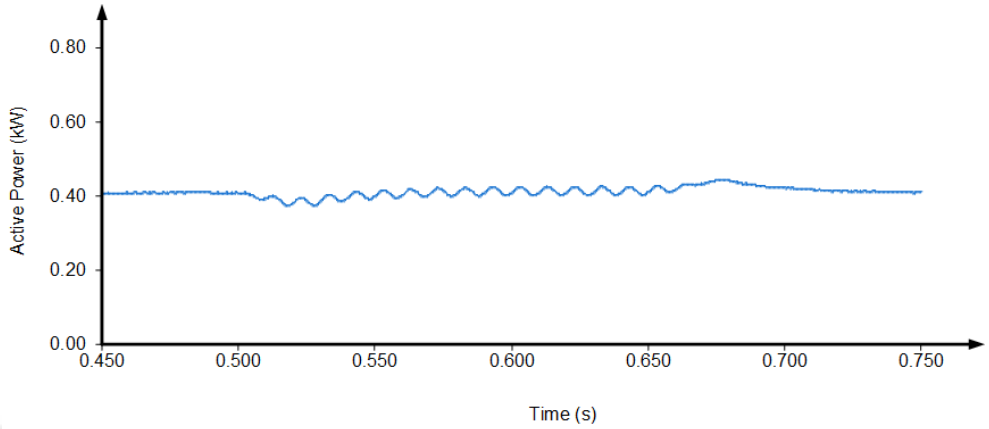

Figure 4.160. The injected active power from PV supported ML-MFGCI into power system in case 8.

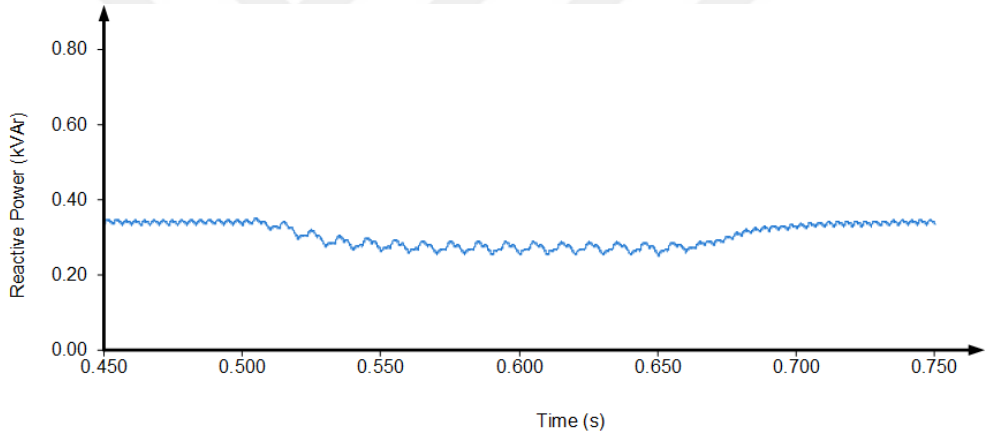

Figure 4.161. The injected reactive power from PV supported ML-MFGCI into power system in case 8.

Case9: In the presence case, to verify the performance of the PV supported ML-MFGCI is tested for simultaneously to exchange bidirectional power and to compensate the reactive power, current and voltage harmonics, load balancing and neutral line current with PCC voltage regulation. Figure 4.162 shows the DC/AC subgrid arrangement which ML-MFGCI configure as interlinked inverter. The interlinked inverter should be able to transfer power in both direction.

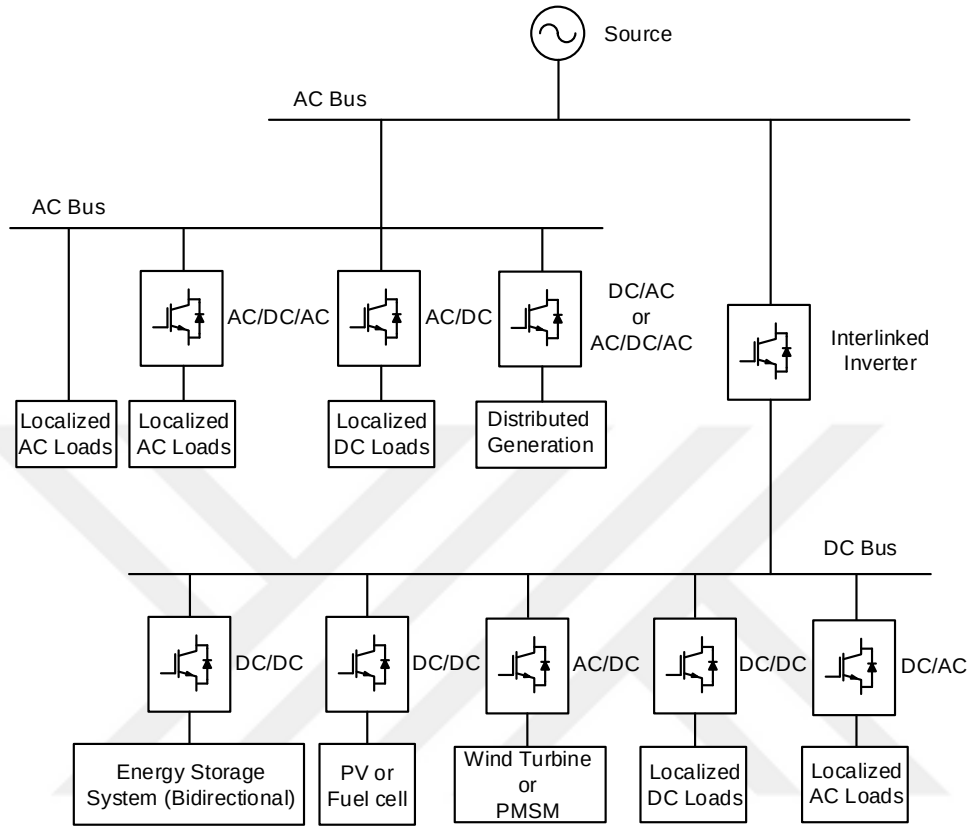

Figure 4.162. The scheme of DC/AC subgrid arrangement.

Figure 4.163 shows the DC line current where produced power from PV system is larger than consumed power by DC load until 0.5 *s*. Thus the produced extra power injected into AC power system by interlinked inverter. In this instance the produced DC current from PV system is 0.575 *kA* and drawn current from DC loads is 0.078 *kA*. Therefore interlinked inverter injects 0.497 *kA* into AC power system. When the consumed DC current by DC loads increase to 0.760 *kA* between 0.5 *s* and 1.5 *s* the interlinked inverter injects 0.185 *kA* DC current into DC link and acts as rectifier.

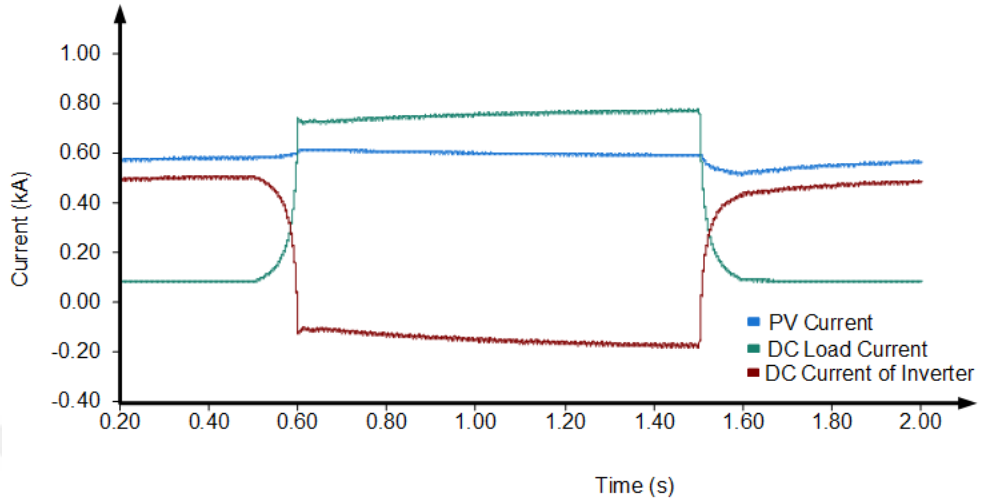

Figure 4.163. The DC load, PV system and DC link current of ML-MFGCI for various DC load condition when ML-MFGCI configured as interlinked inverter.

Figure 4.164 shows the exchanged active power by ML-MFGCI between DC and AC bus when ML-MFGCI configure as interlinked inverter. As seen from Figure 4.164, the ML-MFGCI injects 355 *kW* from DC bus into AC power system until 0.5 *s* and injects 180 *kW* in vise versa between 0.5 *s* and 1.5 *s*.

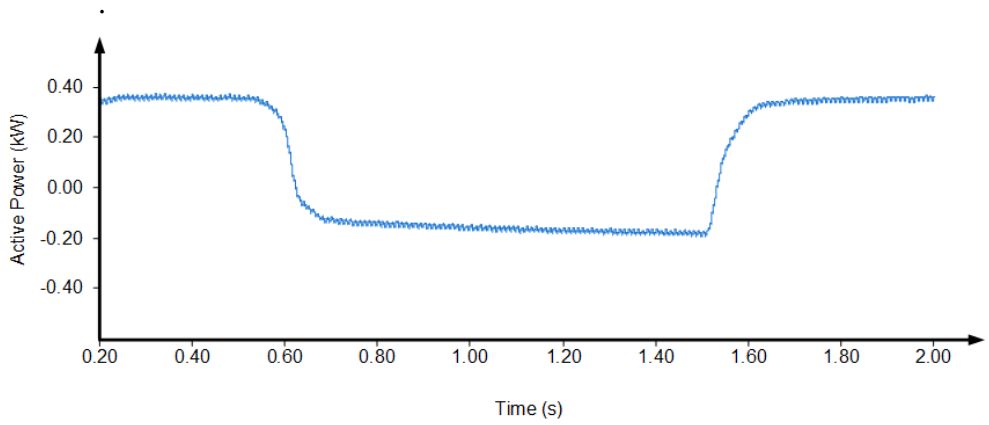

Figure 4.164. The exchanged active power between DC and AC bus by ML-MFGCI for various DC load condition in case 9 when ML-MFGCI configured as interlinked inverter.

Figure 4.165 shows the injected reactive power by ML-MFGCI into AC system when configure as interlinked inverter. As seen from Figure 4.163, the ML-MFGCI injects 270 *kVAr* into AC power system until 0.5 *s*. Between 0.5 s and 1.5 s due to increase the source current a voltage drop occur in PCC owing to line impedance. Thus the ML-MFGCI to regulate PCC voltage injects more reactive power into system. In this instance the ML-MFGCI injects 555 *kVAr* reactive power into system to regulate PCC voltage and to compensate load reactive power.

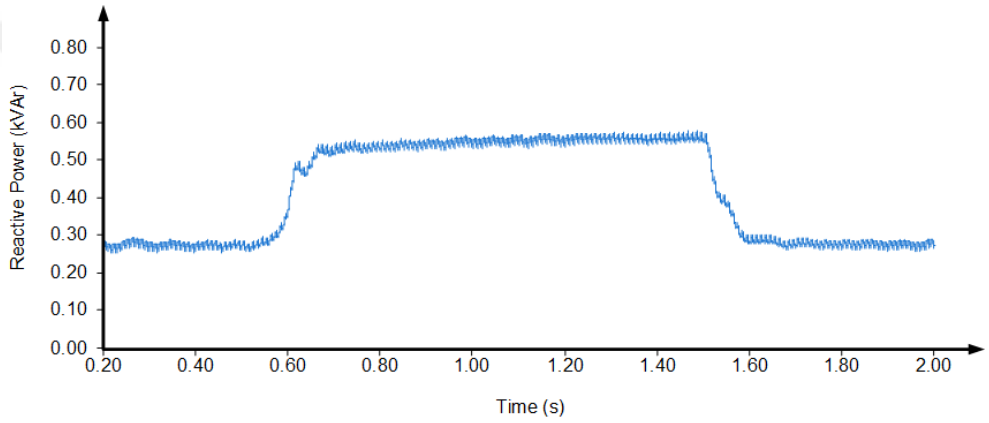

Figure 4.165. The injected reactive power by ML-MFGCI for various DC load condition in case 9 when ML-MFGCI configured as interlinked inverter.

Figure 4.166 shows the ML-MFGCI current in various DC load condition in the studied case 9. The ML-MFGCI has 0.706 *kA*, 0,495 *kA* and 0.730 *kA* in phase A, B and C, respectively when injecting active power into AC grid and has 0,986 *kA*, 0.790 *kA* and 0.775 *kA* in phase A, B and C, respectively when injecting active power into DC grid.

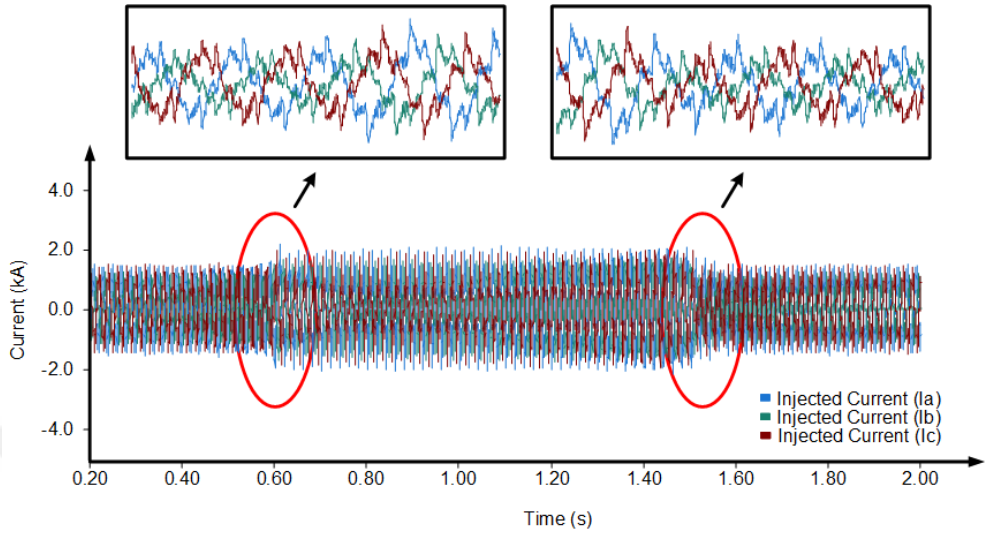

Figure 4.166. The ML-MFGCI current for various DC load condition in case 9 when ML-MFGCI is configured as interlinked inverter.

The ML-MFGCI is able to compensate the load unbalance in both condition. Figure 4.167 shows the load and source currents unbalance ratio where ML-MFGCI is reduced the current unbalance from 10.5% in load current to below 2% in source current for both DC load situation.

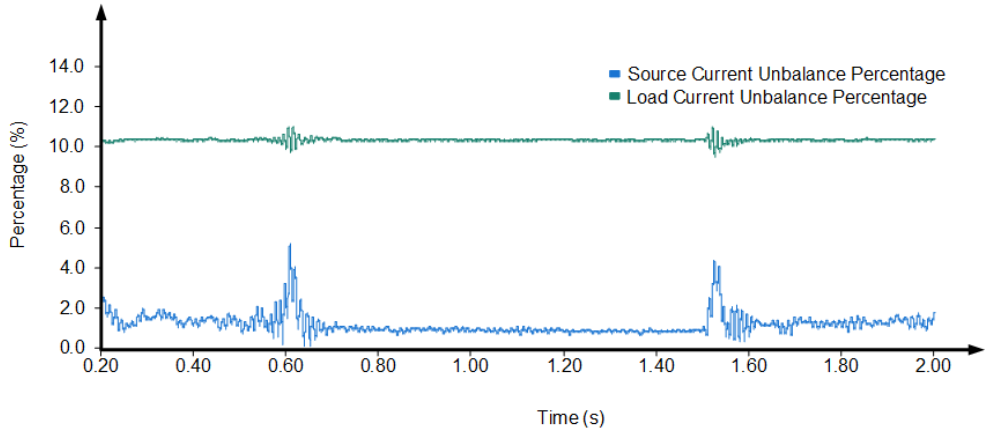

Figure 4.167. The load and source currents unbalance ratio for various DC load condition in case 9 when ML-MFGCI is configured as interlinked inverter.

As well as ML-MFGCI is able to eliminate the voltage/current harmonics for both DC load condition when used as interlinked inverter. Figure 4.168 shows the source current for various DC load condition in studied case when ML-MFGCI is utilized as interlinked inverter. The source current has 0.754 *kA*, 0.747 *kA* and 0.734 *kA* in phase *A*, *B* and *C*, respectively until 0.5 *s* when ML-MFGCI injects extra active power produced by PV system into AC power system. In this instance the source current has 0.735 *kA* and 0.01 *kA* positive and negative sequence components, respectively. Likewise source current has 1.56 *kA*, 1.54 *kA* and 1.54 *kA* in phase *A*, *B* and *C*, respectively between 0.5 *s* and 1.5 *s* when ML-MFGCI injects active power from AC power system into DC grid. In last instance the source current has 1.53 *kA* and 0.014 *kA* positive and negative sequence components, respectively.

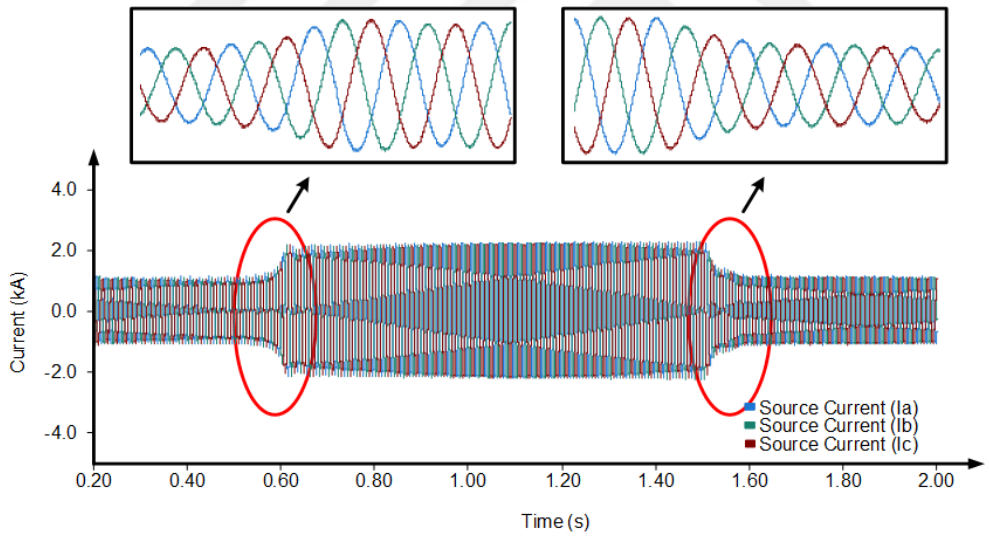

Figure 4.168. The source current waveforms for various DC load condition in case 9 when ML-MFGCI configure as interlinked inverter.

Bu utilizing ML-MFGCI as interlinked inverter the source current THDs are decreased from12.6% to 3.17% in phase *A*, 2.85% in phase *B* and 13.26 to 2.62% in phase *C* until 0.5 *s* when ML-MFGCI injects extra active power produced

by PV system into AC power system and decrease from12.6% to 2.80% in phase *A*, 13.26 to 2.75% in phase *B* and 13.26 to 2.85% in phase *C* between 0.5 *s* and 1.5 *s* when ML-MFGCI injects active power from AC power system into DC grid. Figures 4.169, 4.170, and 4.171 shows the harmonic spectrum of the source currents when the ML-MFGCI is utilized as interlinked inverter to mitigate PQ problems with bidirectional active power exchange capability. It should be noted that in Figures 4.169, 4.170, and 4.171 the red and blue highlights denote the components of source current for various frequency when ML-MFGCI injects extra active power produced by PV system into AC power system and when ML-MFGCI injects active power from AC power system into DC grid, respectively.

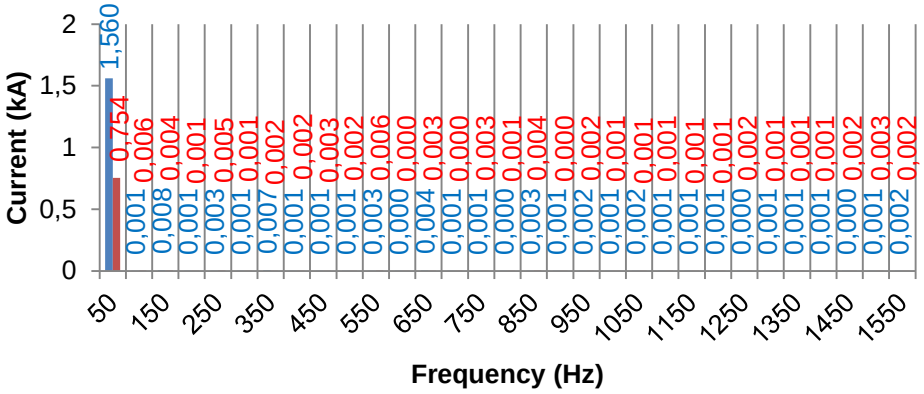

Figure 4.169. The harmonic spectrum of source current in phase *A* for various DC load condition in case 9 when ML-MFGCI is configured as interlinked inverter.

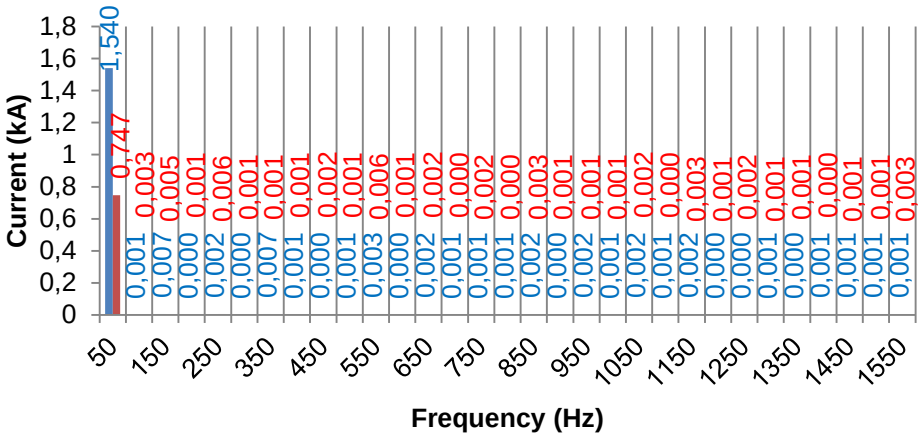

Figure 4.170. The harmonic spectrum of source current in phase *B* for various DC load condition in case 9 when ML-MFGCI is configured as interlinked inverter.

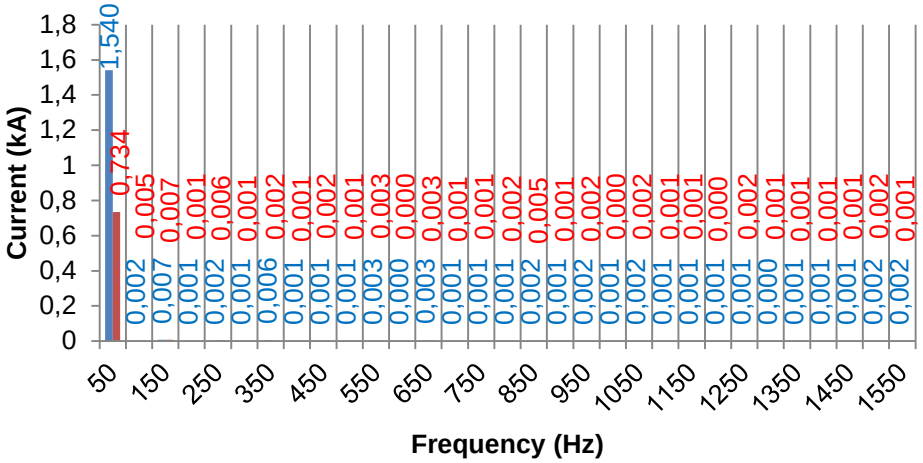

Figure 4.171. The harmonic spectrum of source current in phase *C* for various DC load condition in case 9 when ML-MFGCI is configured as interlinked inverter.

Figure 4.172 shows the PCC phase voltages for various DC load condition in studied case when ML-MFGCI utilized as interlinked inverter. By utilizing ML-MFGCI as interlinked inverter the PCC phase voltages are increased from 207

V_{RMS} in phase *A*, 214.8 V_{RMS} in phase *B* and 210 V_{RMS} in phase *C* to 230 V_{RMS} in all three phases and regulate to nominal voltage.

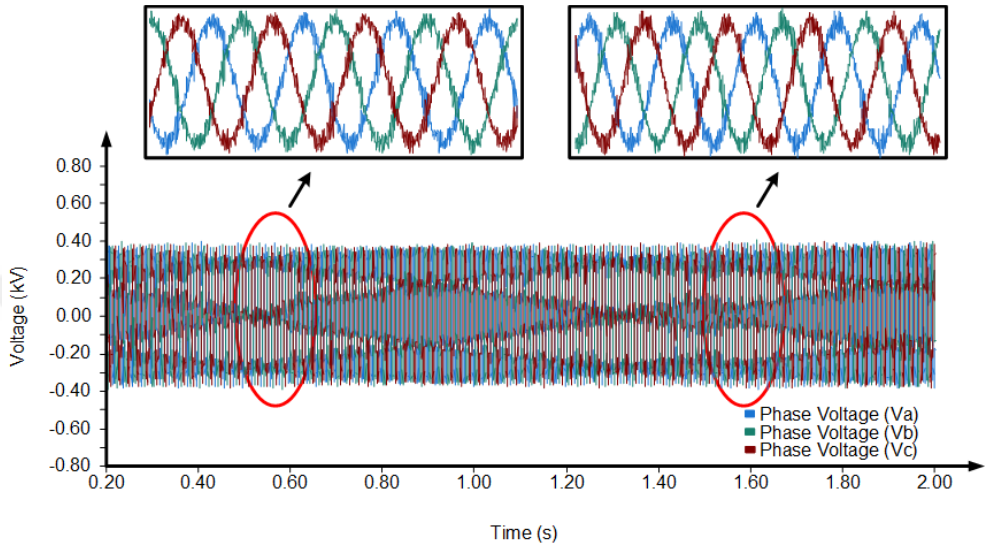

Figure 4.172. The PCC phase voltage waveforms for various DC load condition in case 9 when ML-MFGCI is configured as interlinked inverter.

By utilizing ML-MFGCI as interlinked inverter, the PCC phase voltage THDs are decreased from 21.38% to 1.55% in phase *A*, 21% to 1.7% in phase *B* and 22.25% to 1.7% in phase *C* until 0.5 *s* when ML-MFGCI injects extra active power produced by PV system into AC power system and decrease from 21.38% to 0.77% in phase *A*, 21% to 0.77% in phase *B* and 22.25% to 0.8% in phase *C* between 0.5 *s* and 1.5 *s* when ML-MFGCI injects active power from AC power system into DC grid. Figures 4.173, 4.174, and 4.175 shows the harmonic spectrum of the PCC phase voltages when the ML-MFGCI is utilized as interlinked inverter to mitigate PQ problems with bidirectional active power exchange capability. It should be noted that in Figures 4.173, 4.174, and 4.175, the red and blue highlights denote the components of source current for various frequency when ML-MFGCI injects extra active power produced by PV system into AC power system and when

ML-MFGCI injects active power from AC power system into DC grid, respectively.

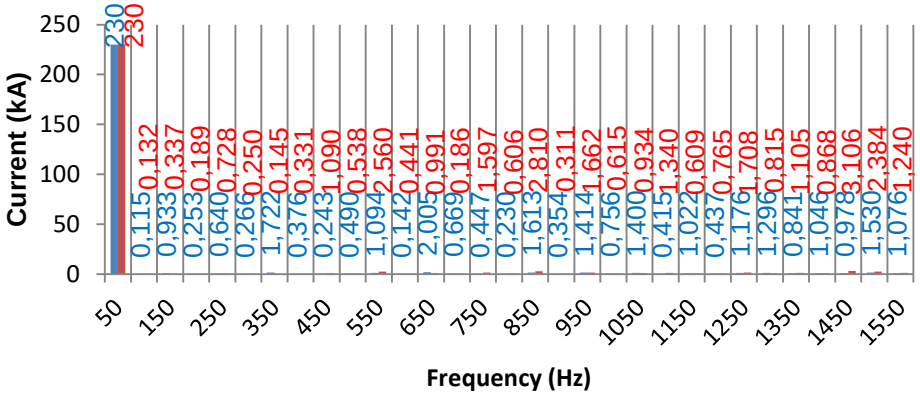

Figure 4.173. The harmonic spectrum of PCC voltage in phase *A* for various DC load condition in case 9 when ML-MFGCI is configured as interlinked inverter.

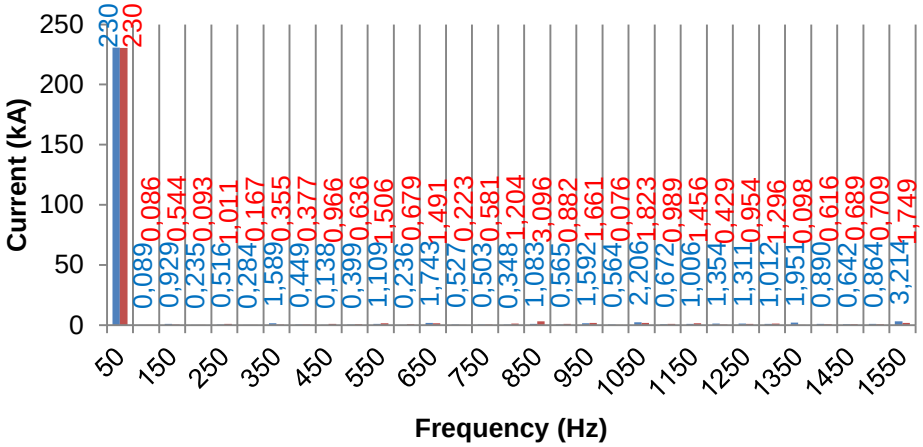

Figure 4.174. The harmonic spectrum of PCC voltage in phase *B* for various DC load condition in case 9 when ML-MFGCI is configured as interlinked inverter.

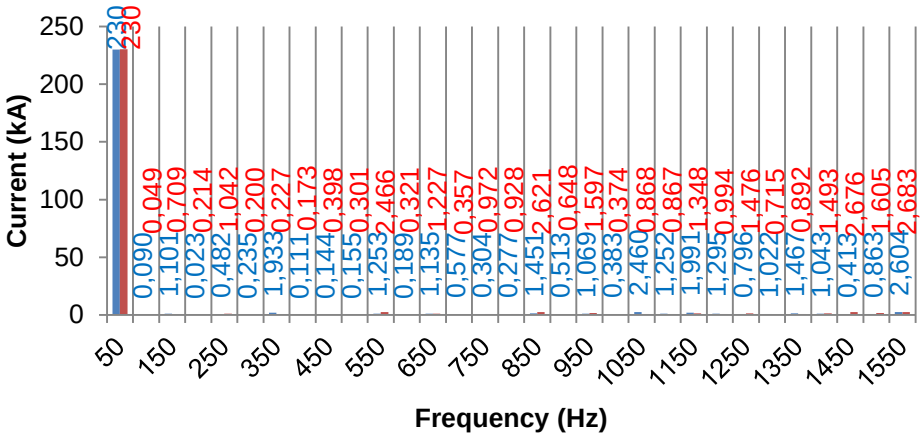

Figure 4.175. The harmonic spectrum of PCC voltage in phase *C* for various DC load condition in case 9 when ML-MFGCI is configured as interlinked inverter.

Figure 4.176 shows the source phase voltages for various DC load condition in studied case when ML-MFGCI is utilized as interlinked inverter. By utilizing ML-MFGCI as interlinked inverter, the PCC phase voltage balanced from 233 V_{RMS} in phase *A*, 235V_{RMS} in phase *B* and 235 V_{RMS} in phase *C* to 238 V_{RMS} in all three phases.

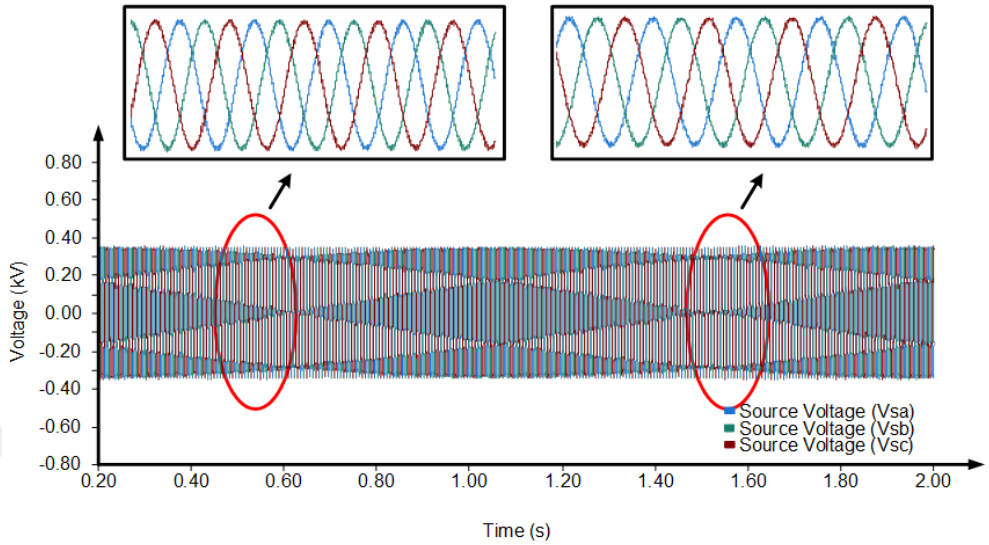

Figure 4.176. The source phase voltage waveforms for various DC load condition in case 9 when ML-MFGCI is configured as interlinked inverter.

By utilizing ML-MFGCI as interlinked inverter, the source phase voltages THD is decreased from 3.95% to 0.60% in phase *A*, 4.00% to 0.54% in phase *B* and 4.00% to 0.49% in phase *C* until 0.5 *s* when ML-MFGCI injects extra active power produced by PV system into AC power system and decrease from 3.95% to from 4.00% to 0.47% in phase *A*, 4.00% to % 0.39% in phase *B* and 4% to 0.46% in *C* between 0.5 *s* and 1.5 *s* when ML-MFGCI injects active power from AC power system into DC grid. Figures 4.177, 4.178, and 4.179 show the harmonic spectrum of the source phase voltages when the ML-MFGCI is utilized as interlinked inverter to mitigate PQ problems with bidirectional active power exchange capability. It should be noted that in Figures 4.177, 4.178, and 4.179, the red and blue highlights denote the components of source current for various frequency when ML-MFGCI injects extra active power produced by PV system into AC power system and when ML-MFGCI injects active power from AC power system into DC grid, respectively.

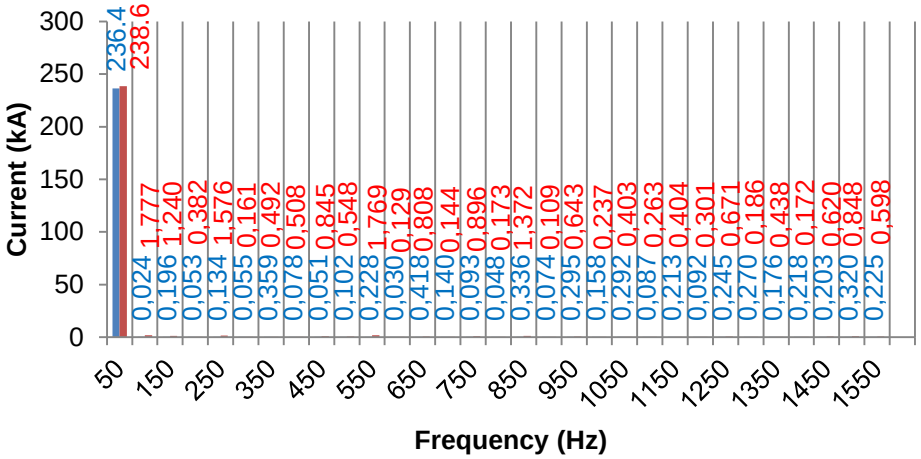

Figure 4.177. The harmonic spectrum of source voltage in phase *A* for various DC load condition in case 9 when ML-MFGCI is configured as interlinked inverter.

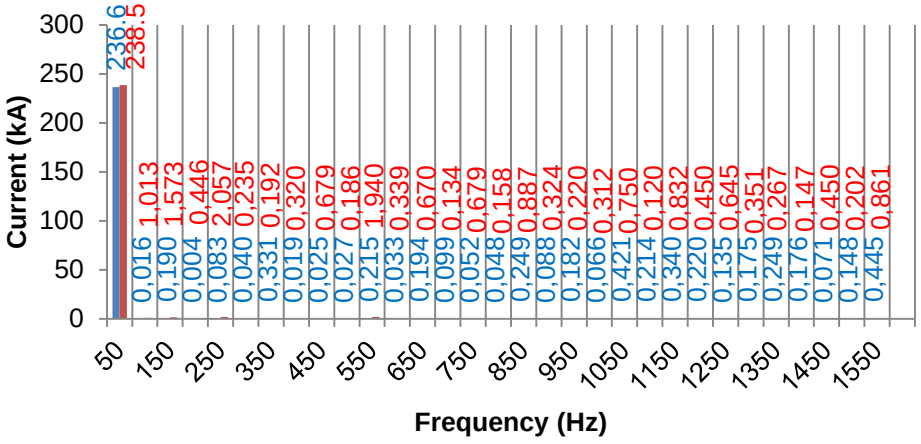

Figure 4.178. The harmonic spectrum of source voltage in phase *B* for various DC load condition in case 9 when ML-MFGCI is configured as interlinked inverter.

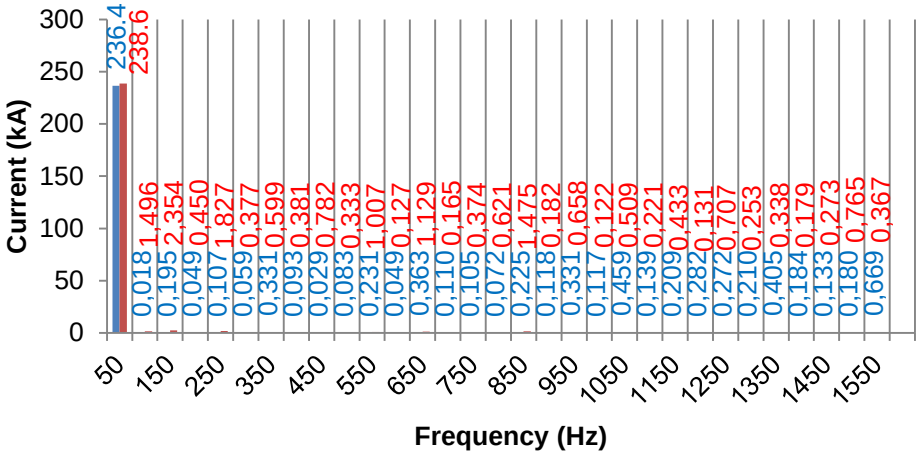

Figure 4.179. The harmonic spectrum of source voltage in phase *C* for various DC load condition in case 9 when ML-MFGCI is configured as interlinked inverter.

4.4. Summary

Simulation results confirm the effectiveness of the proposed multi-objective control method for ML-MFGCI to simultaneously eliminate voltage and currents distortions, compensate load unbalance and reactive power as well as regulate the PCC voltage. The case results shows that the system operates stable in the studied case and meets the regulations of standards.

5. WAVELET TRANSFORM BASED VOLTAGE SAG/SWELL DETECTION ALGORITHM

The significant increase in the amount of activity in the PQ area has been observed from literature since 1990s. Due to increasing usage of devices which are more sensitive to voltage/current disturbances and high frequency transients, the end users are affected and exposed to the unexpected misoperation and outage (Bollen and Gu, 2006). PQ problems can be defined as any variation in the electrical power supply such as voltage sags/swell, interruptions, flickers, harmonics and notches. Also, The International Electrotechnical Commission (IEC) defines the PQ in IEC 61000-4-30 as: ‘‘Characteristics of the electricity at a given point on an electrical system, evaluated against a set of reference technical parameters’’. This definition is related to the possibility of measuring and quantifying the performance of the power system. Another standardized PQ definition is given by IEEE standard 1100 as: ‘‘The concept of powering and grounding sensitive equipment in a matter that suitable to the operation of that equipment’’ (Subasi et al., 2011).

The voltage sag/swells are short duration variations of the RMS value of the voltage from the nominal value. The voltage sag/swells are characterized by their magnitude and duration. Depending on their duration they can be instantaneous, momentary or temporary. The different definitions and limits of magnitude and duration of voltage sag/swells are given in European Standard EN50160 and in IEEE Std. 1159–2009. The voltage sag/swells are usually associated with system faults or with switching or heavy loads. They constitute one of the most important PQ disturbances because of their detrimental effect on equipment, their detection and analysis being one of the most important problems in modern power systems (Barros et al., 2012).

However there is no standard method defined for detection and analysis of voltage sag/swells. There are different methods proposed in the literature that can

be applied to this end, although none of them is dominant. Standard IEC 61000-4-7 report some of the most common methods applied. They can be divided into two categories: time-domain and frequency-domain methods. The time-domain methods are the comparative method, the envelope method, the sliding window method, the *dv/dt* method and the RMS method. In the comparative method the transient is detected when a fixed absolute threshold is exceeded. The envelop method is similar to the comparative method, but after removing the fundamental component of the signal. In the sliding window method the instantaneous values are compared to the corresponding values in the previous cycle, directly or after removing the fundamental component. In the *dv/dt* method a transient disturbance is detected when a fixed absolute value of *dv/dt* is exceeded. In the RMS method the RMS value is computed for intervals less than one fundamental period and compared to a threshold. The time-domain methods are easy to implement than the frequency-domain methods but they can present worse detection performance than the frequency-domain methods. The most common frequency-domain methods are FFT, Kalman filter, wavelets and S-transform. The use of wavelets allows the decomposition of a signal into components as a function of time and frequency, providing a more precise time location of a transient than other frequency-domain methods (Apráiz et al., 2014).

In the previous studies, to classify the PQ disturbances and to detect the voltage sags/swells, the effect of disturbances was analyzed individually and the effectiveness of system under different combinations of PQ disturbances was not analyzed. But in real power systems the voltage waveform is non-stationery and distorted with flicker and harmonics. In this paper, a new algorithm to detect the voltage sag/swell in harmonics and flicker distorted non-stationary voltage signals is proposed.

The hybrid discrete wavelet transform (DWT) is developed to detect fast changes in the voltage signals, which allows time localization of differences frequency components of a signal with different frequency wavelets.

5.1. Theoretical background of discrete wavelet transform

The application of wavelet transform was first carried out in the area of geophysics in 1980 by the French geophysicist J. Morlet of the French oil company Elf Aquitaine and his coworkers. In electrical engineering, it was popular for some time under the various names of multirate-sampling, quadrature mirror filters (QMFs) and etc, (Hanif et al., 2012). The term “wavelet” means a small wave and the wave refers to the condition that this function is an oscillatory.

Wavelet functions are generated by using a prototype wavelet named as mother wavelet. In other words, the functions used in the transformation process are derived from a main function or the mother wavelet. WT has also another term “Translation (τ)”. This term is used in the same sense as it was used in FFT. It is related with the location of the window, as the window is shifted through the signal as visualized in Figure 5.1 (Hanif et al., 2012; Sarkar et al., 1998).

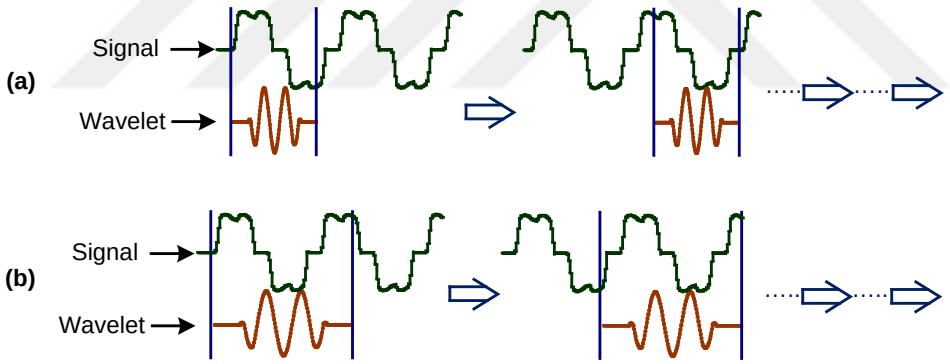

Figure 5.1. Translated versions of Wavelet function.

Discrete Wavelet Transform (DWT) is the form of WT that uses the discrete values of the signal in the time-domain. The mathematical expression of DWT is given in Eq. 5.1.

$$\psi_{m,n}(t) = \frac{1}{\sqrt{{a_0}^m}}\left(\frac{t - nb_0{a_0}^m}{{a_0}^m}\right) \tag{5.1}$$

where the integers m and n control the wavelet dilation and translation respectively, a_0 is a specified fixed dilation step parameter which should be greater than one and b_0 is the location parameter which should be greater than zero (Zafar and Morsi, 2013).

The control parameters m and n contain the set of positive and negative integers. WT of a continuous signal *x(t)* gives the decomposition wavelets by using the discrete form of Eq. 5.2. In other words, the scale-location of the signal in the time-frequency-domain is determined by using Eq. 5.3.

$$\psi(\tau, s) = \frac{1}{\sqrt{|s|}}\int x(t)\psi^*\left(\frac{t-\tau}{s}\right)dt \tag{5.2}$$

$$T_{m,n} = \int_{-\infty}^{\infty} x(t){a_0}^{-m/2}\psi\left({a_0}^{-m}t - nb_0\right)dt \tag{5.3}$$

where the values of *T* are the scale-location grid of the signal in the time-frequency-domain according to indexes *m* and *n*.

For DWT, the values of $T_{m,n}$ are known as wavelet coefficients or detail coefficients. Common choices for DWT parameters, a_0 and b_0 are selected as two and one, respectively. The term “power of two” is emerged for the practical application. This power of two is known as the dyadic grid arrangement for dilation and translation steps. The dyadic grid is perhaps the simplest and most efficient discretization for practical purposes and lends itself to the construction of an orthonormal wavelet basis (Aboufadel and Schlicker, 1999), (Addison, 2002).

$$\psi_{m,n}(t) = 2^{-m/2}\psi\left(2^{-m}t - n\right) \tag{5.4}$$

By choosing an orthonormal wavelet basis $\psi_{m,n}(t)$, the original signal can be reconstructed by utilizing the wavelet coefficients $T_{m,n}$ by using inverse discrete wavelet transform (IDWT) given in Eq. 5.5.

$$x(t) = \sum_{m=-\infty}^{\infty} \sum_{n=-\infty}^{\infty} T_{m,n} \psi_{m,n}(t) \tag{5.5}$$

There are many wavelet functions defined by the mathematician. Haar wavelet proposed firstly, Meyer wavelet, Morlet wavelet and Daubechies wavelet are the most common wavelets adapted to the applications of WT in the power system applications.

Each wavelet includes the high-pass and low-pass filters in the decomposition process. The decomposition can be implemented using filtering and down-sampling, and can be iterated, with successive approximations subsequently decomposed. Finally, one signal is broken down into lower resolution components. For each decomposition stage, the approximations are the low-frequency signal components that are obtained from the low-pass filter. The details are the high-frequency components, which are obtained from the high- pass filter. Finally, the low-pass filter is related to the scaling function and the high-pass filter is related to the mother wavelet. The low-frequency content represents the identity of the signal from the approximations (Aktas and Turkmenoglu, 2010). This decomposition halves the time resolution since only half the number of samples characterizes the entire signal. However, this operation doubles the frequency resolution, since the frequency band of the signal spans only half the previous frequency band, effectively reducing the uncertainty in the frequency by half. The above procedure, also called as the subband coding, can be repeated for further decomposition. At every level, the filtering and subsampling will result in half the number of samples (and hence half the time resolution) and half the frequency band spanned (and hence double the frequency resolution). Figure 5.2 illustrates this procedure, where

F(n) is the original signal to be decomposed, and cA_1 and cD_1 are low pass and high pass filters, respectively. In each resolution level, the input signal in the upper resolution n level is split into the approximation by a low-pass filter and the detail by the high-pass filter in the lower resolution level. Both the output approximation and detail signals are then decimated by two (Polikar, 2001).

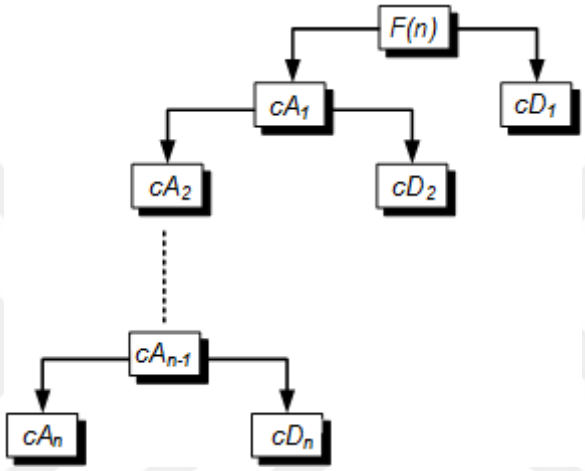

Figure 5.2. The filtering process of Wavelet transforms.

As an example, suppose that the original signal *F(n)* has 1024 sample points, spanning a frequency band of 0 to π *rad/s*. At the first decomposition level, the signal is passed through the high pass and low pass filters, followed by subsampling by 2. The output of the high pass filter has 512 points (hence half the time resolution), but it only spans the frequencies π/2 to π *rad/s* (hence double the frequency resolution). These 512 samples constitute the first level of DWT coefficients. The output of the low pass filter also has 512 samples, but it spans the other half of the frequency band, frequencies from 0 to π/2 *rad/s*. This signal is then passed through the same low pass and high pass filters for further decomposition. The output of the second low pass filter followed by subsampling has 256 samples spanning a frequency band of 0 to π/4 *rad/s*, and the output of the

second high pass filter followed by subsampling has 256 samples spanning a frequency band of $\pi/4$ to $\pi/2$ *rad/s*. The second high pass filtered signal constitutes the second level of DWT coefficients. This signal has half the time resolution, but twice the frequency resolution of the first level signal. The low pass filter output is then filtered once again for further decomposition. This process continues until two samples are left. For this specific example there would be 9 levels of decomposition, each having half the number of samples of the previous level. The DWT of the original signal is then obtained by concatenating all coefficients starting from the last level of decomposition (remaining two samples, in this case). DWT will then have the same number of coefficients as the original signal (Polikar, 2001).

5.2. Proposed voltage sag/swell detection method

The proposed voltage sag/swell detection process of the improved WT algorithm is realized in two steps. The decomposition process is applied to the input voltage (VA) without using any discretization process. In other words, the sampling process of the input signal is eliminated in this algorithm. The filter types of the decomposition process are very important due they can slow down the response of the voltage sag/swell detection unit. The types of filters that the number of the coefficients is less are preferred to use in the voltage sag/swell detection algorithm.

The high-pass filter output (high) of the first decomposition gives the impulses, during any disturbances are occurred. This situation can be utilized in the improved voltage sag/swell detection algorithm as Figure 5.3 of Haar wavelet transform in Figure 5.4, db2 wavelet transform in Figure 5.5, db4 wavelet transform in Figure 5.6, db8 wavelet transform in Figure 5.7 and Dmey wavelet transform in Figure 5.8.

The output of the first decomposition process (high) consists of both the positive and negative pulses. Then, an algorithm is written by using the FORTRAN code to compare the impulse values with the threshold value.

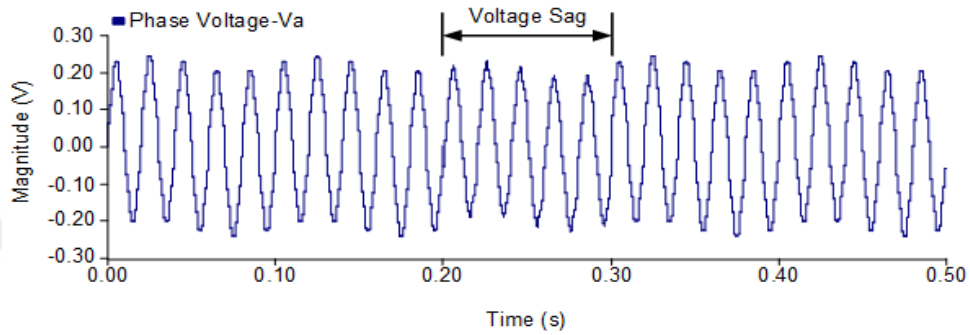

Figure 5.3. Phase voltage signal with sag.

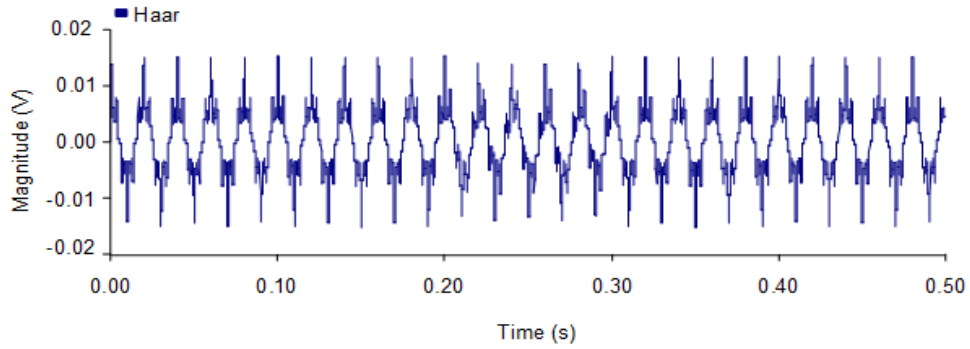

Figure 5.4. WT decomposition process for Haar wavelet transforms.

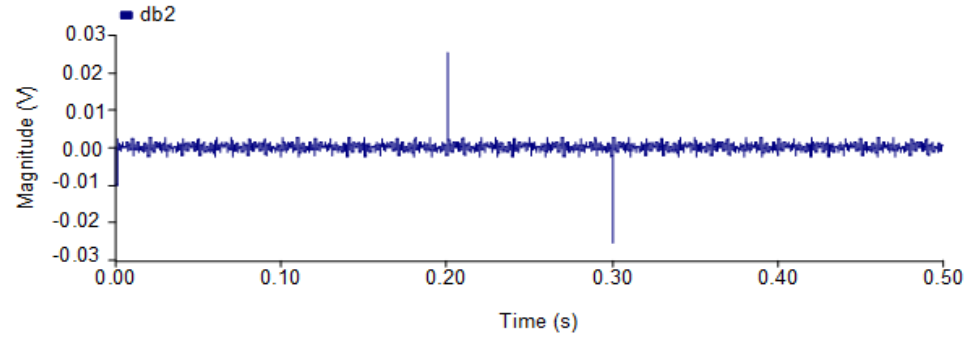

Figure 5.5. WT decomposition process db2 Wavelet transforms.

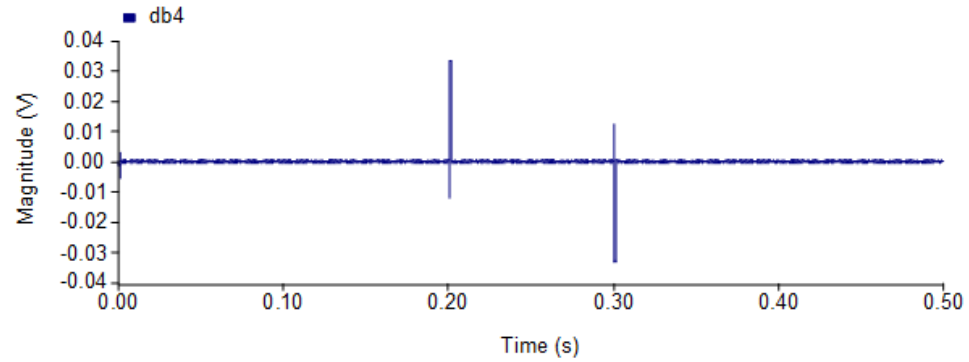

Figure 5.6. WT decomposition process for db4 wavelet transforms.

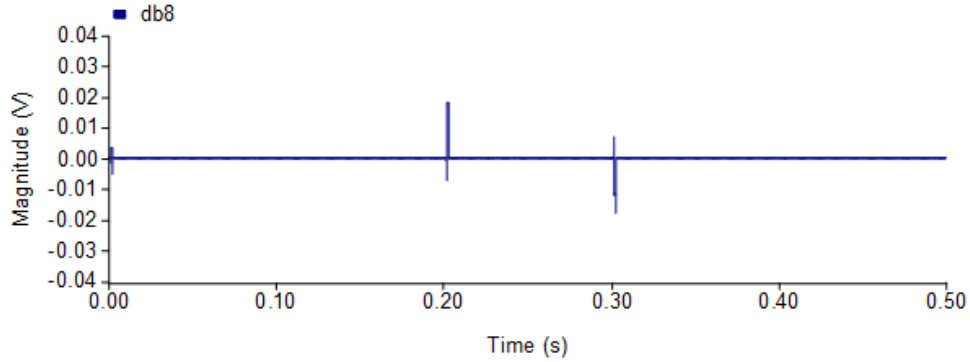

Figure 5.7. WT decomposition process for db8 wavelet transforms.

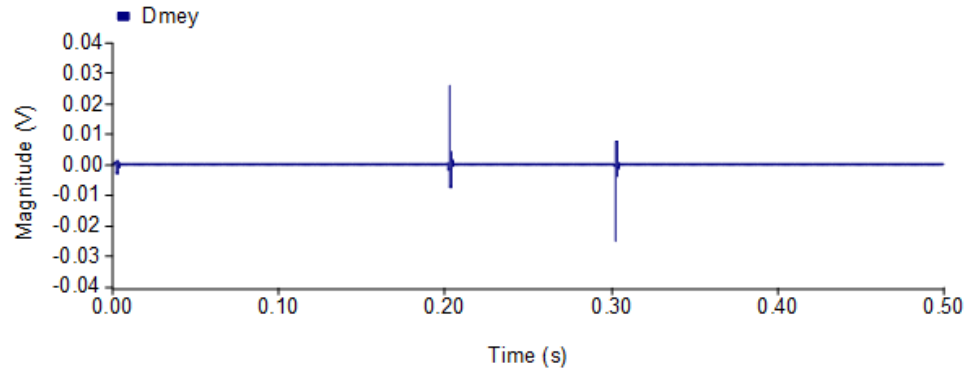

Figure 5.8. WT decomposition process Dmey Wavelet transforms.

Selecting an adequate wavelet filter is very important to identify the features of the fault voltage signals. However, if the filters are not ideal half band, then perfect reconstruction cannot be achieved. Although it is not always possible to realize ideal filters, under certain conditions it is possible to use filters that provide perfect reconstruction. The most famous one is known as Daubechies wavelets (Polikar, 2001). To minimize the delay time of the voltage sag/swell detection response, the second level of db2 can be used. As shown in Figure 4.9, the db2 shows different behaviors during voltage sag with positive/negative and without phase jump. Note that due to successive subsampling by 2, the signal length should be a power of 2 or at least a multiple of power of 2. The length of the signal determines the number of levels that the signal can be decomposed to.

As seen from Figure 5.9, the voltage sag with positive and negative phase jump can be exactly detected by db2. But the db2 does not give any peak at the start and end of the voltage sag without phase jump. So the voltage sag without phase jump cannot be detected by db2.

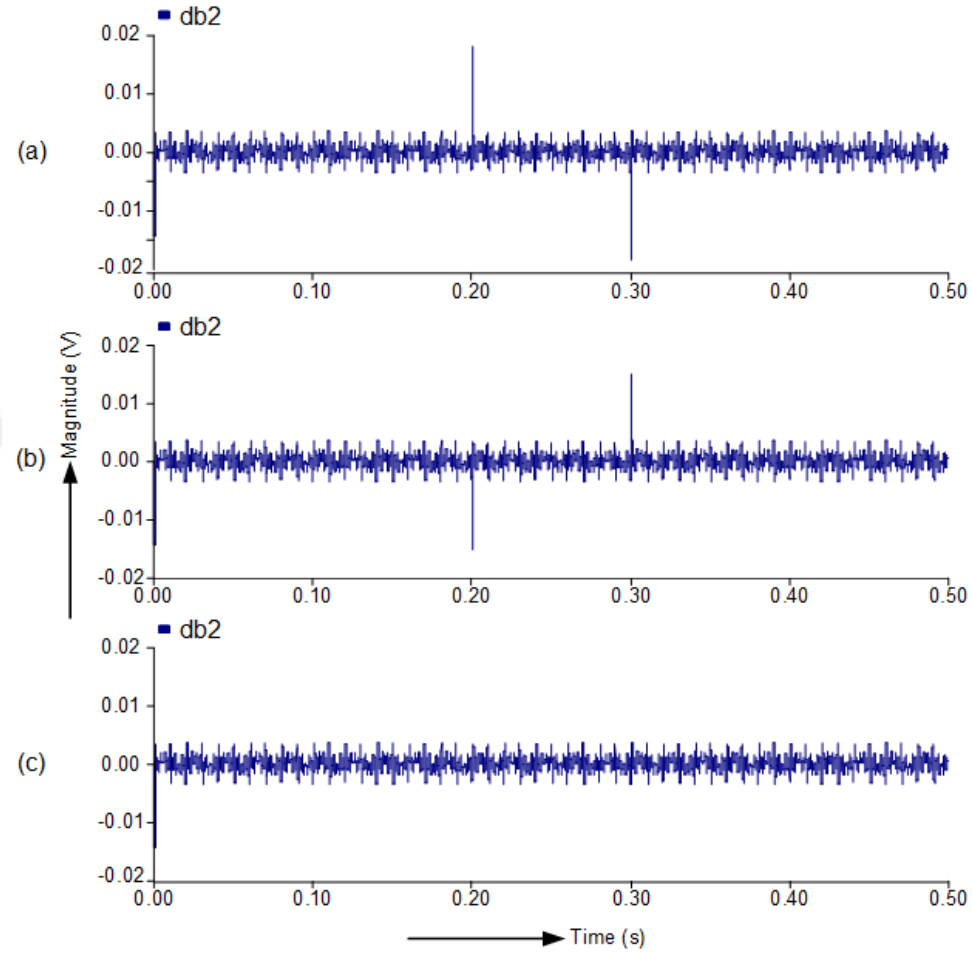

Figure 5.9. WT decomposition with Db2 wavelet for voltage sag with (a) negative phase jump, (b) positive phase jump and (c) without phase jump.

Thus, as shown in Figure 5.10, the voltage sag with and without phase jump can be detected by db8. However, the performance of db8 to detect the voltage sag/swell with phase jump is worse than that of db2. Due to this reasons, an algorithm is developed by combining the superior properties of db2 which quickly detects the voltage sag/swell with positive and negative phase jump and db8 to detect the voltage sag/swell without phase jump. The voltage swells with and

without phase jump has same characteristics with voltage sag and can be detected using this type of method.

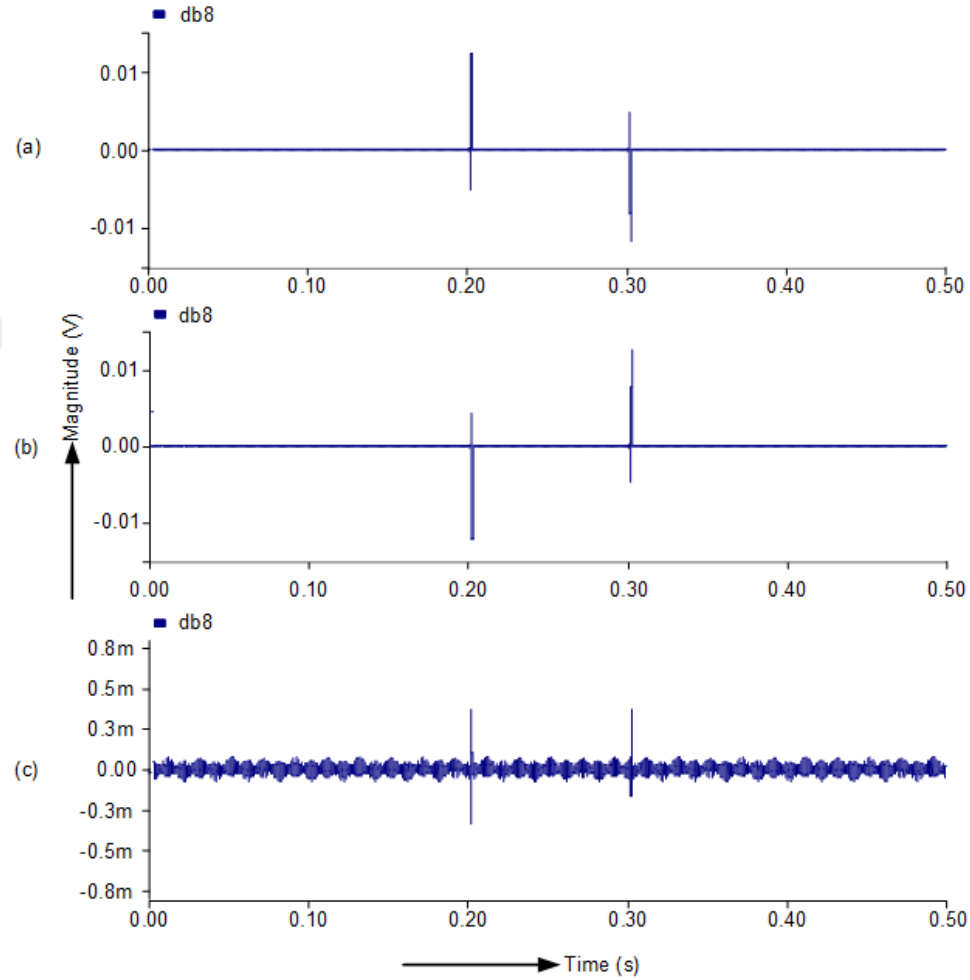

Figure 5.10. WT decomposition with Db8 wavelet for voltage sag with (a) negative phase jump, (b) positive phase jump and (c) without phase jump.

Figure 5.11 illustrates the software structure of the hybrid detection method consisting of db2 using 128 sampling numbers and db8 using 512 sampling numbers. The algorithm consists of three hysteresis bands. The first hysteresis band is used to detect the voltage sag/swell with negative phase jump. The second hysteresis band detects the voltage sag/swell with positive phase jump. The third

hysteresis band is used to detect the voltage sag/swell without phase jump. In Figure 5.11, the H(1), H(2) and H(3) denote the input of hysteresis bands 1, 2 and 3, respectively. The input of H(1) and H(2) is the output of db2 and the input of H(3) is the output of db8. The hysteresis bands, especially H(1) and H(2), have the inverse characteristic to detect the voltage sag/swell. So, at the end of voltage sag/swell, one of the hysteresis bands detects the end point of sag/swell however; this can be a starting point of sag/swell for another hysteresis band. For this reason, if one of this hysteresis bands detect the voltage sag/swell, the input of two others hysteresis bands becomes zero. Also due the db2 detects the voltage sag/swell with less time delay than db8, if ether of H(1) or H(2) detects the voltage sag/swell, the H(3) becomes zero and the H(3) cannot detect the voltage sag /swell with phase jump. Thus it is satisfied that, the hysteresis bands cannot detect the voltage sag/swells at the same time.

The desired value of DWT should be defined to detect the voltage sag/swell. This desired value is the DWT response to voltage sag/swell between ±%10 $V_{nominal}$ and predetermined level. With the use of this method, the effectiveness of impulse and oscillatory transients can be eliminated from voltage sag/swell detection process.

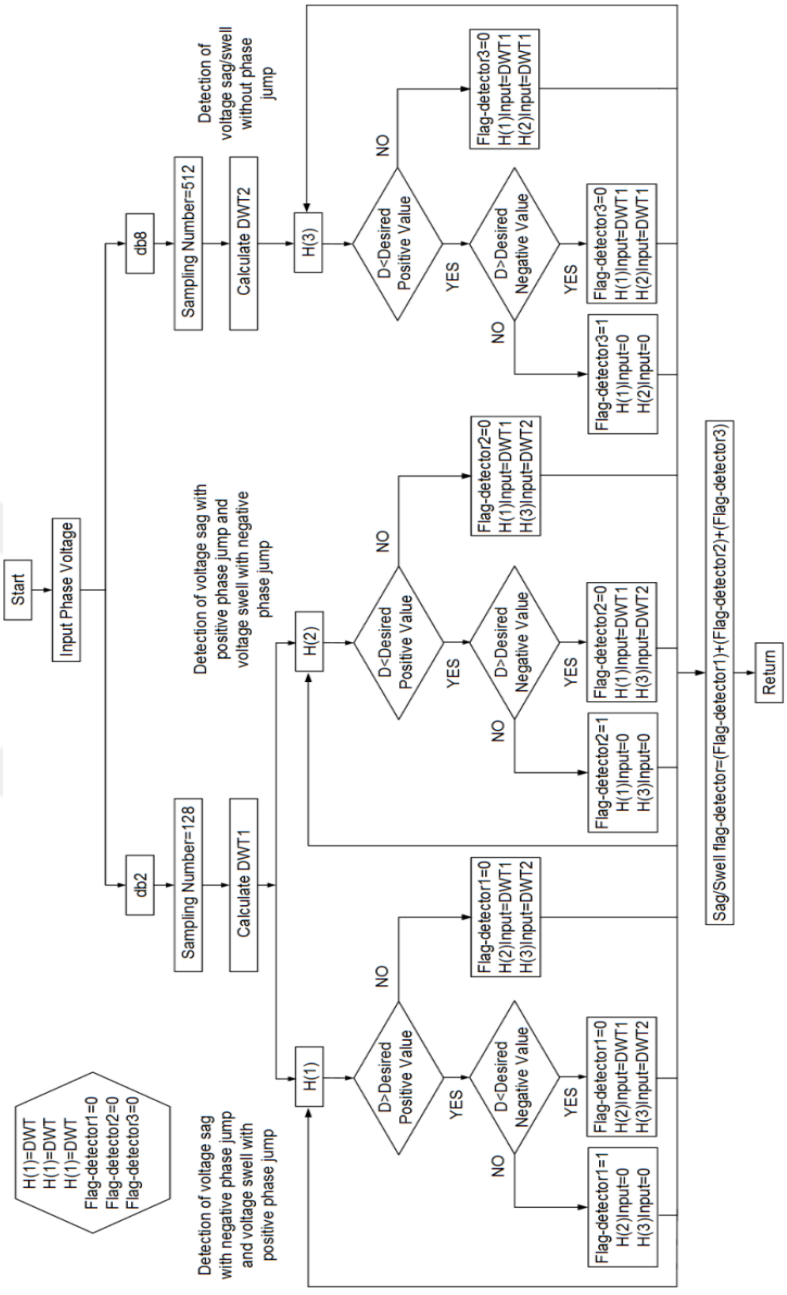

Figure 5.11. The flowchart of proposed sag/swell detection algorithm

5.3. Conventional sag/swell detection methods

The proposed sag/swell detection method is compared with dq-transformation, EPLL and Fast Fourier (FFT) transform methods to show the superiority of the proposed detection method. In the dq-transformation based sag/swell detection method, the phase voltages V_A, V_B and V_C are transformed to the dq plane as given in Eq. (5.6).With the use of Eq. (5.7), the sag/swell depth is obtained (Teke et al., 2009).

$$\begin{bmatrix} V_d \\ V_q \end{bmatrix} = \frac{2}{3}\begin{bmatrix} \cos\theta & \cos(\theta-\frac{2\pi}{3}) & \cos(\theta+\frac{2\pi}{3}) \\ \sin\theta & \sin(\theta-\frac{2\pi}{3}) & \sin(\theta+\frac{2\pi}{3}) \end{bmatrix} \tag{5.6}$$

$$S_{dq} = \left|1-\sqrt{V_d{}^2+V_q{}^2}\right| \tag{5.7}$$

In Figure 5.12(a) the block diagram of the dq-transformation based sag/swell detection method is illustrated. After the three-phase set of voltages is transformed into and components, the square root of the sum of squares of these components is obtained. The obtained value is subtracted from 1 (reference value) and then the absolute value of the resulting variable is filtered out with a 100-Hz low-pass filter to extract the positive-sequence component of voltage. If a negative sequence is generated by voltage sag and/or unbalance, it appears as an oscillating error in the dq-based sag detection method. To measure the positive sequence separately from the negative sequence, the dq–based method normally uses a low-pass filter that has a narrow bandwidth. But this type of filter causes some phase delay or measurement delay; thus, the response time of the system tends to be lengthened.

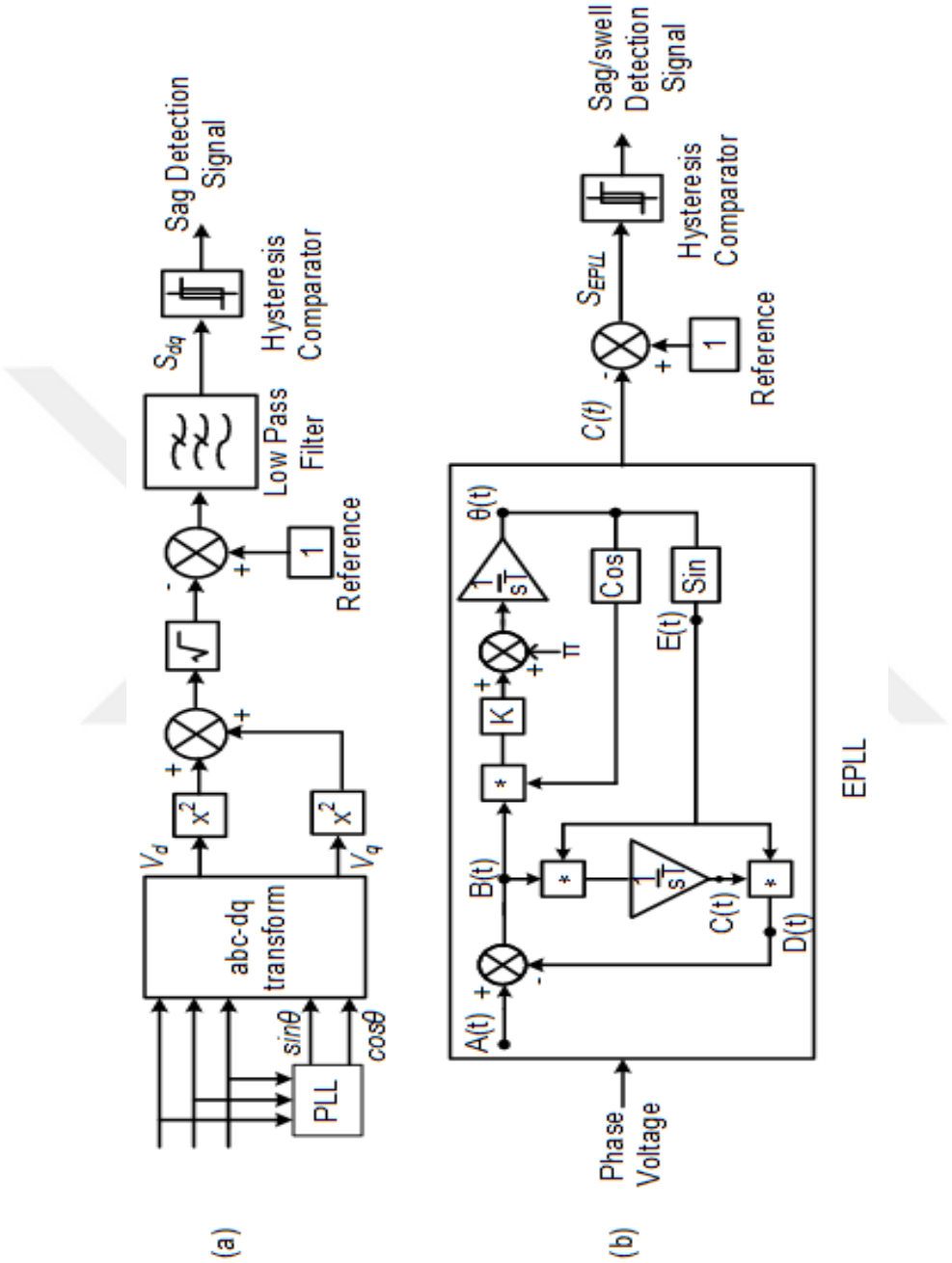

Figure 5.12. Block diagram of (a) dq-transformation and (b) EPLL based voltage sag/swell detection method.

The filtered output is subjected to a hysteresis comparator, and the output of this comparator generates the sag/swell detection signal. The signal is high when sag/swell occurs and is low otherwise. The detection method is able to detect the three-phase balanced voltage sag/swell with acceptable performance. However, the most important disadvantage of this method is that it uses three-phase voltage measurements for the detection.

The method is unable to detect the voltage sag lower than a definite depth. As an instance, a single-phase-to-ground fault resulting in 18% of voltage sag cannot be determined by this method because the method uses the average of the three-phase voltage and perceives the single-phase voltage sag as an average value of 6% if the voltage sag detection limit is selected to be 10%.

To overcome the disadvantages of the dq sag/sell detection method, EPLL based sag/swell detection method can be used to detect balanced and unbalanced voltage sags/swells, except that the EPLL is applied to each supply phase independently and is tuned to respond to phase jumps in the supply quickly as shown in Figure 5.11(b).

The system receives the input signal *A(t)* (supply voltage or load current) and provides an on-line estimate of the following signals:

(1) *B(t)*, the difference of input and the synchronized fundamental component.

(2) *C(t)*, the amplitude of D(t).

(3) *D(t)*, the synchronized fundamental component.

(4) *E(t)*, PLL signal.

(5) $\theta(t)$, the phase angle of D(t).

$$B(t) = A(t) - k_2 t \tag{5.8}$$

$$\theta(t) = \cos\theta(t)\left(-\frac{A}{\omega}\cos\omega t - \frac{k_2}{2}t\right) \tag{5.9}$$

$$E(t) = \sin\left(\cos\theta(t)\left(-\frac{A}{\omega}\cos\omega t - \frac{k_2}{2}t\right) + \pi t\right) \tag{5.10}$$

$$C(t) = -\frac{k_3 A}{\omega}\cos\omega t - \frac{k_2 k_3}{2}t^2 \tag{5.11}$$

$$D(t) = C(t)\sin\left(-\frac{C(t)}{k_3}\pi t\right) \tag{5.12}$$

There exists a compromise between speed and accuracy. For large K_1, K_2 and K_3, the convergence of the estimated values to actual values is faster and the steady state misadjustment is higher. This is an inherent characteristic of an adaptive algorithm. Parameters K_1, K_2 and K_3 ought to be selected appropriately according to the application. If only the total "flicker content" of a signal is to be extracted, then the filter can be set to operate in an alternative mode. In this mode, the filter is set to operate at a low speed to track only the fundamental signal and not the flicker. The result is that the smooth "averaged" fundamental is extracted on the output and the total distortion signal at the error terminal (Karimi-Ghartemani and Iravani, 2002).

In EPLL the *C(t)* gives the amplitude of the tracked signal *A(t)*. For example, if the amplitude of the measured Phase-A supply voltage is 220 V_{rms}, the *C(t)* signal is obtained as continuous 1 p.u. If the amplitude falls to 165 V_{rms}, the

amplitude of the *C(t)* signal falls to 0.75 p.u. Figure 5.11(b) presents the block diagram of voltage sag/swell detection method using EPLL.

By subtracting the *C(t)* signal from the ideal voltage magnitude (1 p.u.), the voltage sag/swell depth (S_{EPLL}) can be detected. The comparison of this value with the limit value of 10% (0.1 p.u.) gives information as to whether a voltage sag occurred.

$$S_{EPLL} = \left|1 - C(t)\right| \tag{5.13}$$

Another technique that can return information regarding the state of a system supply is the Fourier transform to each supply phase. The advantage of this method is that it can return magnitude and phase of each frequency component within the supply, which is particularly important if there are harmonics present, such as the fifth or seventh. In order to prevent errors occurring with the information returned regarding the fundamental (50 Hz) the previous methods effectively filter out harmonics other than the fundamental. The effect of doing so can be to introduce transient delays in detecting changes in the phase of the fundamental. The Fourier transform or the practical digital implementation of it, the "windowed fast Fourier transform" (WFFT) automatically accounts for all frequencies (bearing in mind the Nyquist Criterion). Depending on the type of controller the information regarding frequencies other than the fundamental can either be used or ignored.

Although the WFFT can return accurate steady-state information about the supply phases, the WFFT kernel is itself an averaging function. Thus, it can take up to one cycle of the fundamental when a sag/swell has commenced before information regarding the magnitude and phase can be assumed accurate (Fitzer et al., 2002), (Fitzer et al., 2004). In FFT based algorithm, the RMS variation of input voltage is measured to judge the voltage sag/swell. And a discrete Fourier

transform (DFT) algorithm is used to calculate the RMS value of the fundamental component (Bae et al., 2010). The source voltage *V(t)* can be expressed as Eq. (5.14) using the Fourier series:

$$v(t) = \frac{a_0}{2} + \sum_{n=0}^{\infty} a_n \cos n\omega_0 t + \sum_{n=0}^{\infty} b_n \sin n\omega_0 t \tag{5.14}$$

The fundamental component for n-1 is obtained as in Eq. (5.15) and Eq. (5.16), separating the real part and imaginary part

$$a_1 = \frac{2}{T}\int_0^T v(t)\cos\omega_0 t dt \tag{5.15}$$

$$b_1 = \frac{2}{T}\int_0^T v(t)\sin\omega_0 t dt \tag{5.16}$$

Applying the DFT for Eqs. (5.15) and (5.16), (5.17) and (5.18) are obtained

$$a_1 = \frac{\sqrt{2}}{N}\sum_{i=0}^{N} v\left(t - i\frac{T}{N}\right)\cos\left(2\pi\frac{i}{N}\right) \tag{5.17}$$

$$b_1 = \frac{\sqrt{2}}{N}\sum_{i=0}^{N} v\left(t - i\frac{T}{N}\right)\sin\left(2\pi\frac{i}{N}\right) \tag{5.18}$$

Using the value of a_1 and b_1, the RMS value of the fundamental component can be easily obtained as the following:

$$V_{RMS} = \sqrt{a_1^2 + b_1^2} \tag{5.19}$$

By subtracting the V_{RMS} signal from the ideal voltage RMS (1 p.u.), the voltage sag/swell depth (S_{FFT}) can be detected.

$$S_{FTT} = \left|1 - \sqrt{a_1^2 + b_1^2}\right| \tag{5.20}$$

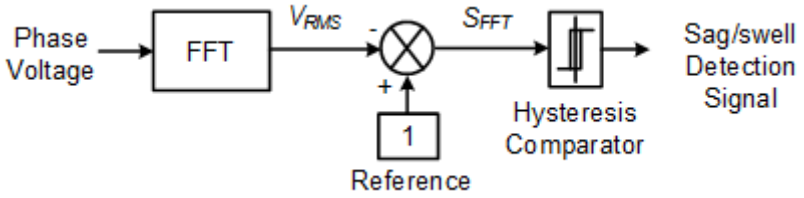

Figure 5.13. Block diagram of FFT based voltage sag/swell detection method.

5.4. Results and Discussions

The performance of the proposed algorithm is compared with different case studies. The results of test cases are summarized in Table I. It should be noted that in flowing cases the sag occur between 0.2 and 0.3 seconds.

Case 1: In this case, the performance of proposed sag/swell algorithm is compared with conventional sag/swell detection method for three phase balance (without phase jump) 13% voltage sag. As seen from Figure 5.14 and Table 5.1, the proposed algorithm has superior performance to detect the start and end times of voltage sag. FFT based method has the worst detection performance to detect the start and end time of voltage sag due large computation time.

Table 5.1. The performance comparison of proposed and conventional sag detection methods in the case 1.

Methods	**Case1**	
	Start of Voltage Sag (s)	End of Voltage Sag (s)
dq	0.20368	0.30348
EPLL	0.20300	0.30200
FFT	0.21400	0.30438
Proposed	0.20115	0.20100

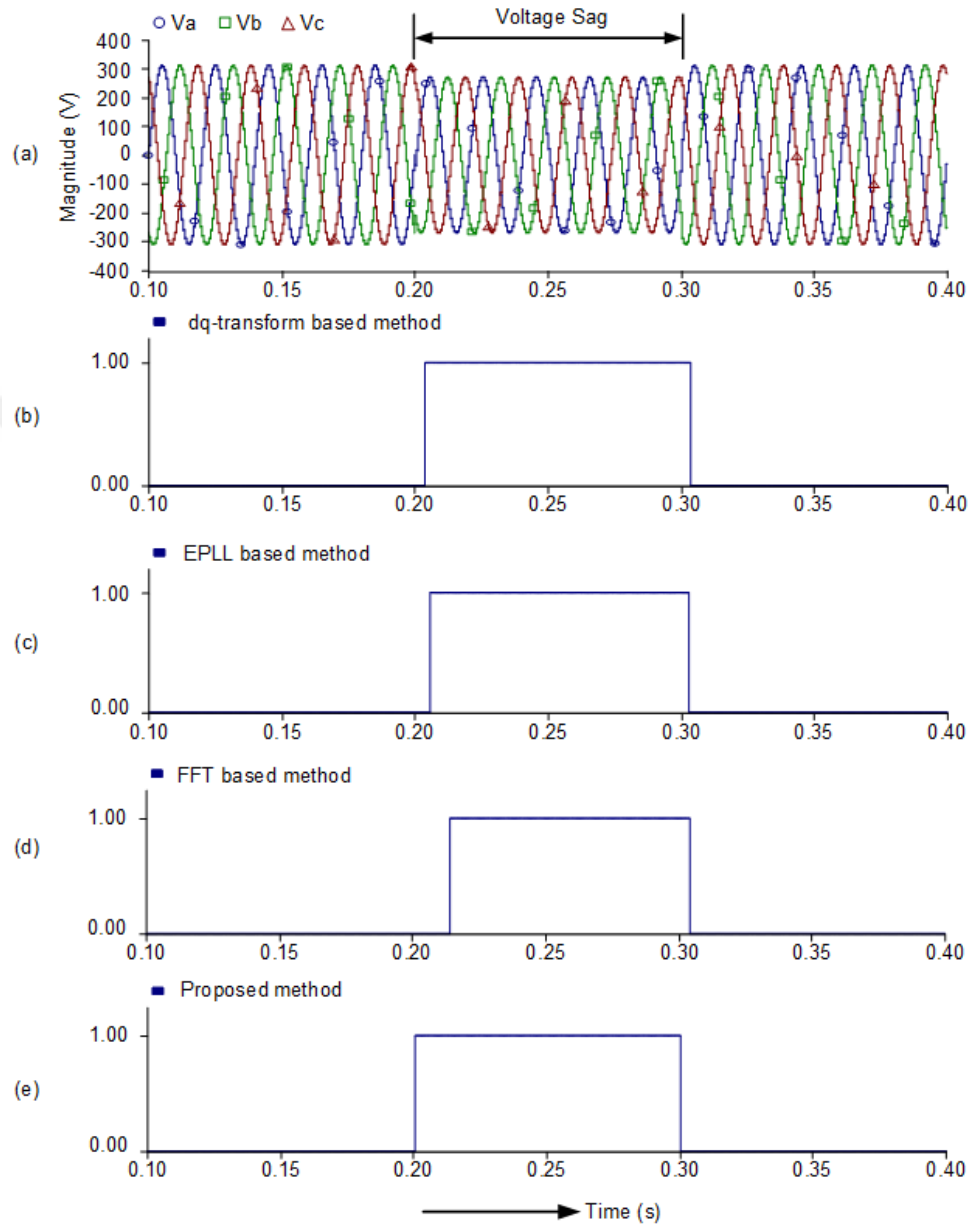

Figure 5.14. The performance of sag detection methods for three phase to ground fault without phase jump.

Case 2: In this case, the performance of proposed sag/swell algorithm is compared with conventional sag/swell detection method for single phase 13%

voltage sag with -10° phase jump. As seen from Figure 5.15 and Table 5.2, the proposed algorithm has superior performance to detect the voltage sag with minimum time delay. In this case, the dq-transformation based method has the worst detection performance. Also, due to the presence of phase jump the EPLL based method has low accuracy to detect voltage sag. FFT based method also has large time delay to detect the voltage sag.

Table 5.2. The performance comparison of proposed and conventional sag detection methods in the case 2.

Methods	**Case 2**	
	Start of Voltage Sag (s)	End of Voltage Sag (s)
dq	0.20664	0.21015
EPLL	0.20312	0.30204
FFT	0.21406	0.30439
Proposed	0.20030	0.20015

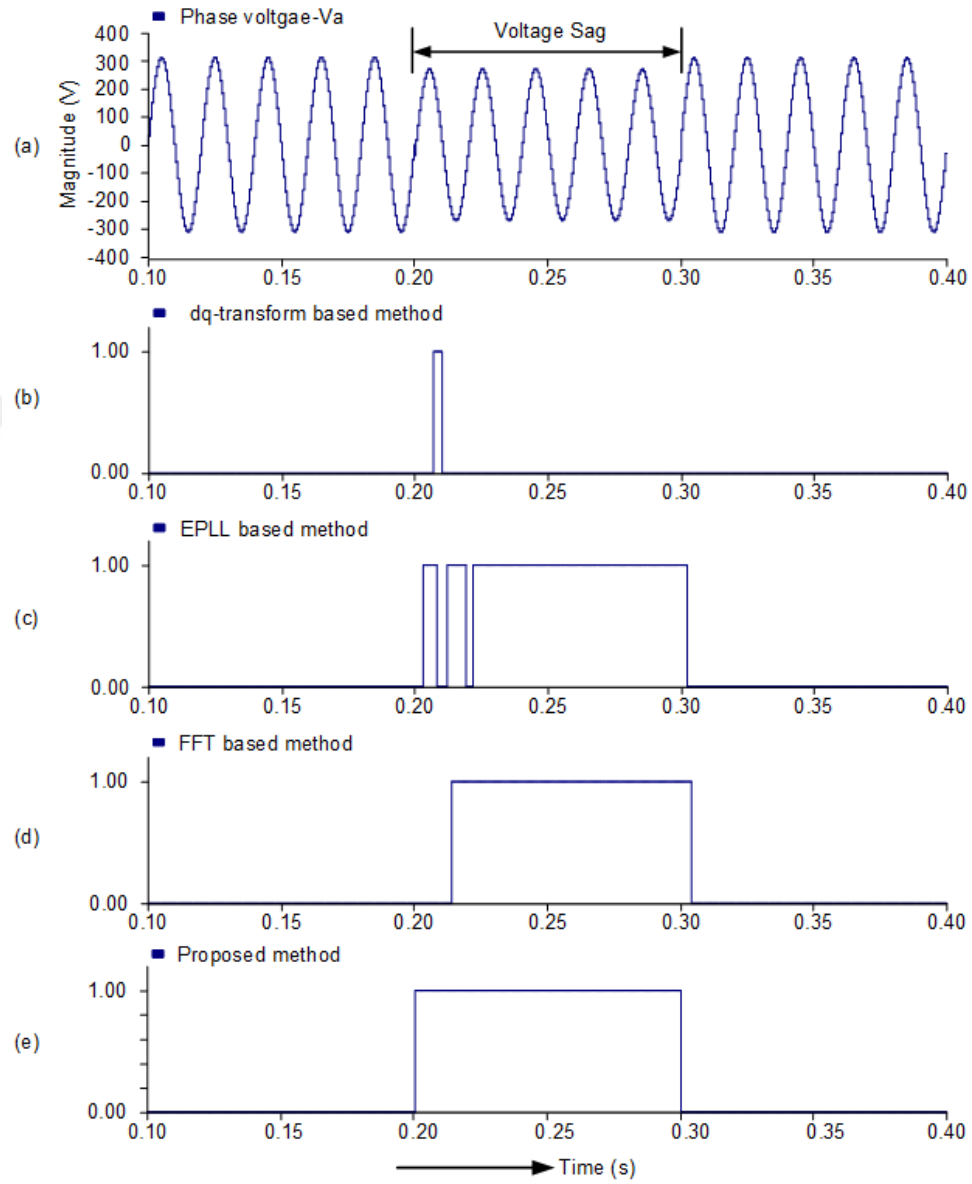

Figure 5.15. The performance of sag detection methods for single phase to ground fault with -10° phase jump.

Case 3: In this case, the performance of proposed sag/swell algorithm is compared with conventional sag/swell detection method for single phase %13 voltage sag with -20° phase jump.

As seen from Figure 5.16 and Table 5.3, the proposed algorithm has superior performance to detect the voltage sag with minimum delay. The dq-transformation based method has the worst detection performance. Comparing with the previous case (a voltage sag with -10° phase jump), FFT and EPLL based methods have the poor detection performance

Table 5.3. The performance comparison of proposed and conventional sag detection methods in the case 3.

Methods	**Case 3**	
	Start of Voltage Sag (s)	End of Voltage Sag (s)
dq	0.20460	0.30120
EPLL	0.20223	0.31245
FFT	0.20624	0.30407
Proposed	0.20030	0.20015

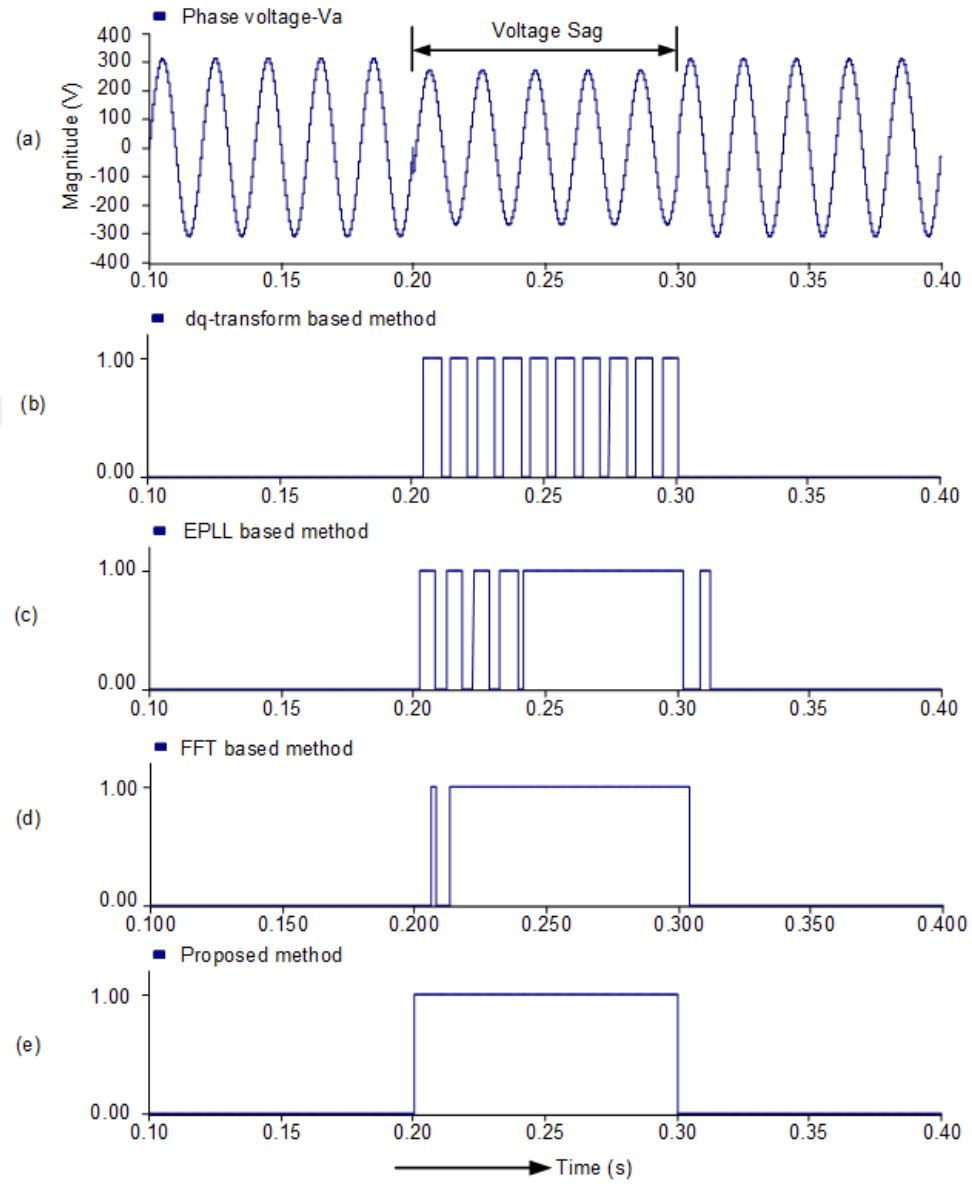

Figure 5.16. The performance of sag detection methods for single phase to ground fault with -20° phase jump.

Case 4: In this case, the performance of proposed sag/swell algorithm is compared with conventional sag/swell detection method for single phase 13% voltage sag with -20° phase jump condition for distorted phase voltage with harmonic. The distorted phase voltage contains 5%, 4%, 2% and 1.5% p.u. in 5^{th}, 7^{th}, 11^{th} and 13^{th} harmonic orders, respectively. As seen from Figure 5.17 and Table 5.4, the proposed algorithm has superior performance to detect the voltage sag with minimum time delay. In this case, due the EPLL and FFT based detection methods extract the harmonics from fundamental components, they are not affected by harmonics. The harmonics in the system can cause an increase on the RMS value of reference signal. In this condition, the dq-transformation based method can detect the voltage sag wrongly because this method cannot extract the harmonic component. This situation can cause the incorrect detection of sag or swells when the magnitude of voltage is within the standard limits.

Table 5.4. The performance comparison of proposed and conventional sag detection methods in the case 4.

Methods	**Case 4**	
	Start of Voltage Sag (s)	End of Voltage Sag (s)
dq	0.20459	0.30172
EPLL	0.20230	0.31240
FFT	0.20625	0.30406
Proposed	0.20030	0.20015

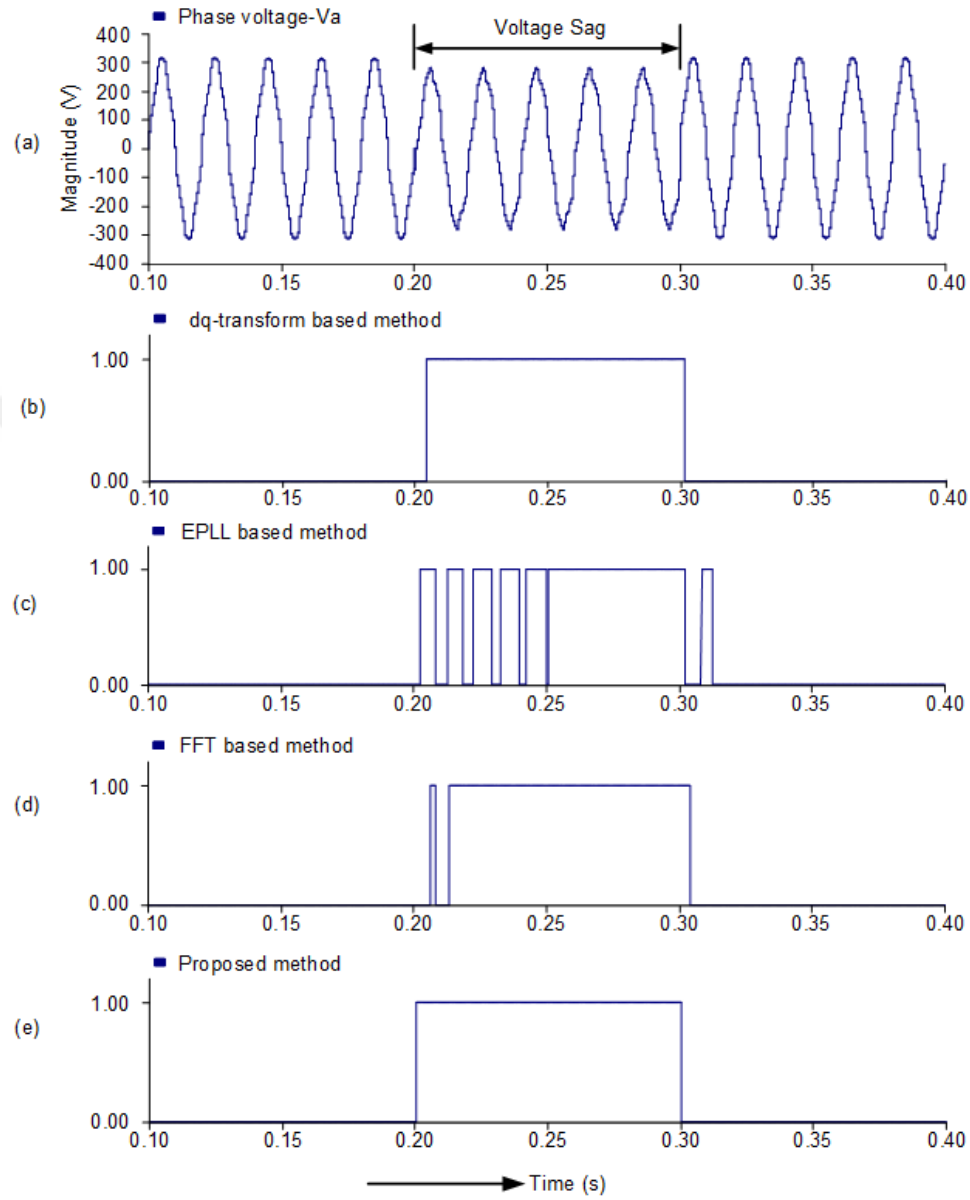

Figure 5.17. The performance of sag detection methods for single phase to ground fault with -20° phase jump when the source voltage includes harmonic orders.

Case 5: In this case, the performance of proposed sag/swell algorithm is compared with conventional sag/swell detection method for single phase %13 voltage sag with -20° phase jump condition for distorted phase voltage with harmonic.

The distorted phase voltage contains 10% p.u. at 8 Hz flicker with %5, %4, %2 and %1.5 p.u. in 5^{th}, 7^{th}, 11^{th} and 13^{th} harmonic orders, respectively. As seen from Figure 5.18 and Table 5.5, the proposed algorithm has superior performance to detect the voltage sag with less time delay. In this case, due the dq-transformation based detection method cannot extract the flicker and harmonic orders from signals, so in normal operation condition it also detects voltage sag or swell. In EPLL based detection method, the EPLL parameters should be adjusted to extract the flicker and harmonic orders from phase voltage waveform in steady state. So this can cause a large time delay for detection process. The accuracy of EPLL based detection method is related with its parameters, voltage sag/swell level and phase jump degree. FFT based detection method cannot completely extracts the flicker and harmonics from fundamental components. This method can operate incorrectly especially within the standard limits.

Table 5.5. The performance comparison of proposed and conventional sag detection methods in the case 5.

Methods	**Case 5**	
	Start of Voltage Sag (s)	End of Voltage Sag (s)
dq	-	-
EPLL	0.21500	0.32105
FFT	0.21440	0.30470
Proposed	0.20031	0.20016

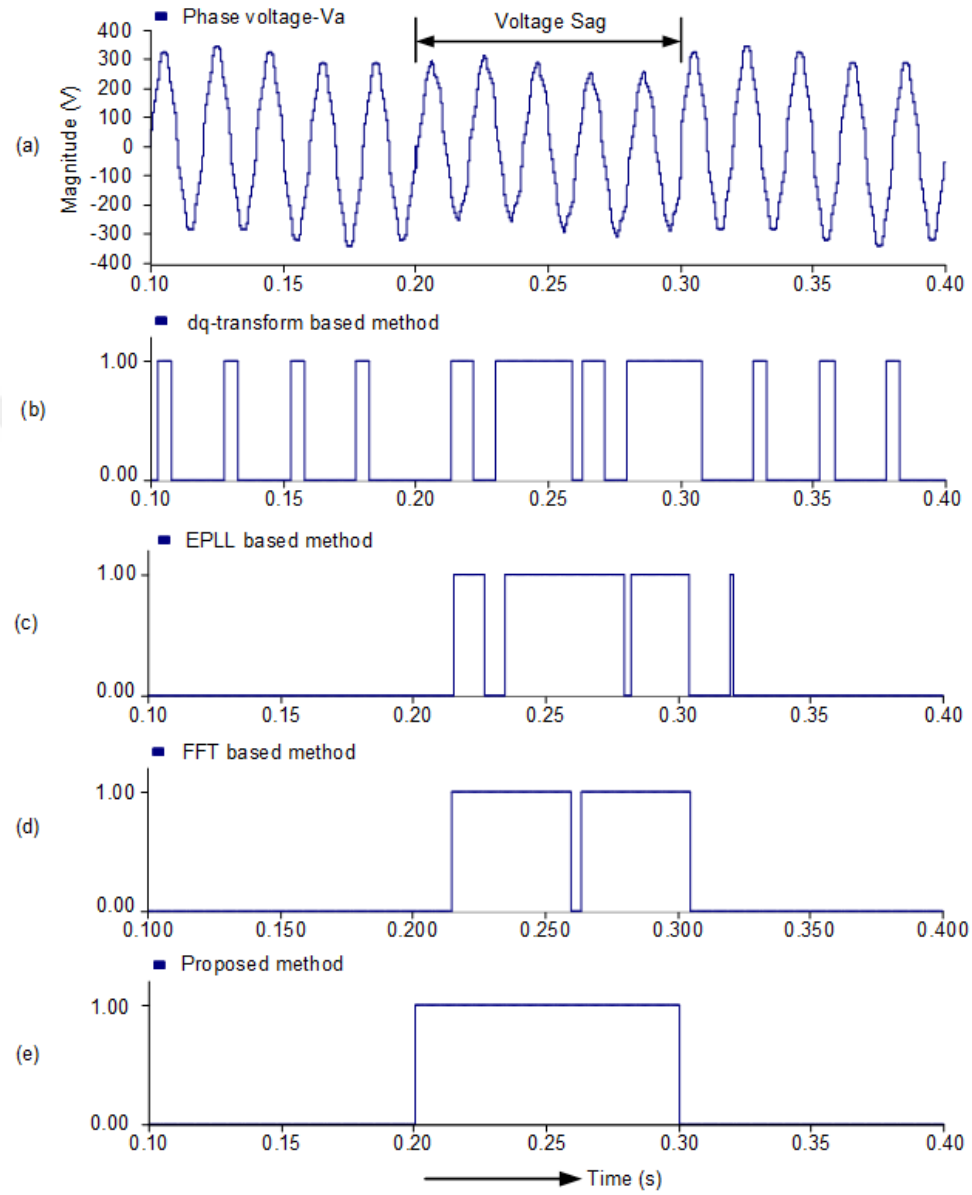

Figure 5.18. The performance of sag detection methods for single phase to ground fault with -20° phase jump when the source voltage includes flicker and harmonic orders.

5.5. Summary

A new wavelet transform based voltage sag/swell detection algorithm in flicker and harmonic polluted source voltage is proposed. The proposed detection algorithm has the advantage of being a hybrid structure consisting of a db2 and a db8 to detect sag/swell with or without phase jump. The proposed algorithm can detect the voltage sag/swell with and without phase jump within 0.5-ms and 1.15-ms, respectively. The feasibility of proposed algorithm was verified through test cases using the PSCAD/EMTDC. The performance of voltage sag/swell detection method is compared with dq-transformation, FFT and EPLL based voltage sag/swell detection methods. Compared with conventional detection methods, the case results reveal good robustness, accuracy and faster processing time to detect balanced and unbalanced voltage sag/swells.

The solution step of the simulation model is adjusted at 10 ms which can be easily adapted to future hardware implementations. The developed sag/swell detection algorithm can be effectively utilized in series connected custom power devices for fast compensation of voltage sag/swell in the sensitive loads.

5. WAVELET TRANSFORM BASED VOLTAGE SAG/SWELL DETECTION ALGORITHM Mohammed BARGHI LATRAN

6. CONCLUSIONS AND RECOMMENDATIONS

One of the main objectives of this thesis is to perform a VSS-MPPT algorithm. The output power of PV arrays is changing with weather conditions such as solar radiance and atmospheric temperature. Therefore, in PV generation systems utilization of the MPPT control strategy becomes indispensable condition to extract maximum power from the PV arrays. The conventional MPPT techniques are generally utilized with a fixed perturbation step size identified by the tradeoff between tracking speed and efficiency necessities. The extracted power from PV arrays with a lager step size perturbation tends faster dynamics behavior but excessive oscillations in steady state conditions and results a low efficiency. This situation will be reversed with smaller step size MPPT strategy. To overcome to tradeoff between tracking speed and efficiency dilemma problem the variable step size iteration can be utilized. Moreover to maximize the efficiency of the PV system, a GMPPT algorithm proposed to track maximum power during PS conditions. During PS conditions conventional MPPT algorithms are likely to be trapped at one of the local peak, simply because its algorithm could not differentiate the local with the global peak.

In chapter 3, a detailed analysis of the physical structure of solar cells and their *I-V* and *P-V* characteristics has been presented. The proposed modified variable step size IncCond MPPT algorithm to extract maximum power from PV system under sharply shifty and unpredictable weather conditions presented in this chapter. Moreover chapter 3 comprises the proposed PS condition detection method and search algorithm to tracks the GMPPT. The proposed algorithms and techniques used to improve MPPT efficiency especially under unstable atmospheric conditions presented in this chapter. It starts by introducing a new rule for modifying the step size in MPPT algorithm. Then, it describes the methods used to overcome the problems of rapidly as well as slowly changing atmospheric

conditions and PS. Furthermore, simulation results of the proposed modified variable step size IncCond MPPT algorithm have been presented. The simulations were run in EMTDC/PSCAD environment, where the response of the proposed algorithm has been analyzed under several irradiation schemes. The results have been compared to the responses of conventional IncCond MPPT algorithm, showing the improvements in transient, dynamic, and steady-state responses. Moreover, the dynamic performance of the proposed algorithm is obviously faster than that of fixed step size method. Also, the proposed algorithm tested in the PS condition. Finally it presents the simulation results which are illustrates the significantly improvements in the GMPPT process in comparison to conventional algorithm under different atmospheric conditions. The proposed MPPT algorithm improves the efficiency of the entire system through increasing the tracking speed and reducing the power loss under uniform and non-uniform or under PS condition. The extensive simulation test results show that in the fast solar radiation changing condition where radiation level increases from 500 W/m^2 to 1000 W/m^2 in 0.163 *s*, the proposed MPPT algorithm can convergence to exact MPPT voltage in the 0.65 *s*. However, the conventional IncCond MPPT algorithm with 2V and 5V step size tracks the MPP voltage in 2.7 *s* and 1.14 *s*, respectively. In the slow solar radiation changing condition where radiation level increases from 500 W/m^2 to 1000 W/m^2 in 7.45 *s* the proposed MPPT method and conventional IncCond with 2 *V* and 5 *V* convergence to MPP voltage pretty much at same time. However, convergence to MPP voltage by proposed method is smoothly than conventional method. In the presence of ripple, when the operating voltage convergence to MPP voltage it causes a power flicker or power oscillation in the output power from PV system when the conventional method is used. This situation hazards the stability, reliability and quality of power system. This problem can be eliminated by using the proposed method. Another test case was at the sharply radiation changing condition where radiation changed as sinusoidal function where the period of this

sinusoidal function was 2 s and oscillate between 500 W/m^2 and 1000 W/m^2. The test result shows that the proposed method can tracks the MPP voltage where conventional IncCond method is not capable to tracks MPP voltage.

Another main objective of this thesis is to optimal design a multi objective control strategy for multilevel multifunctional inverter in large scale grid connected photovoltaic system. A comprehensive review on the topologies and control strategies of multilevel multifunctional inverters are performed. The development of new control strategies and execution of multifunctional compensation capabilities in large scale PV systems are the main research trends related to both active power flow control and mitigation of various PQ disturbances using multilevel multifunctional inverters. The different aspects of multilevel multifunctional inverters, the novel developments and practical applications in this field of research were discussed in details in chapter 2. The detailed classification, challenges and future trends on ML-MFGCIs are presented.

A detailed analysis and discussion on the PQ problems mitigation in new power systems which are supported by renewable energy resources based distributed generation systems presented in this thesis. Due to installing of non-controllable and stochastic nature of renewable energy sources on power systems and closed to consumers as well as existing of severely PQ problems in week power systems the utilization of the compensators becomes indispensable condition to maintain quality, reliability and stability of the power system have been represented. The benefits of the multilevel inverters in high power rating application have been remarked. Moreover, the capability of the interlinked inverters to use as multifunctional inverter with modifying the control strategy of the interlinked inverters has been outlined. Thus, proposed control algorithm for a PV based multifunctional neutral point clamped multilevel inverter to simultaneously maintain high-quality power exchange between PV systems and the utility grid in disturbed grids and perform simultaneous mitigation of PQ problems

in steady-state and transient conditions are presented in chapter 4. It starts by introducing a new rule for modifying the PV based interlinked neutral point clamped multilevel inverter's control algorithm. Then, it describes the methods used to transfer high quality power from PV systems into power networks and overcome the PQ problems. This chapter is concluded by proposed control algorithm formulation and scheme. Finally it presents the simulation results in PSCAD/EMTDC program which are illustrates the significantly improvements in the quality of power system in steady-state and transient conditions and transfer high quality power from PV system into system with maximum power tracking capability.

The proposed control procedure can be explained as flows:

1) Implement a PLL structure to extract the phase angles of point of common coupling voltage and line current which are used to synchronize the PV based interlinked neutral point clamped multilevel inverter with utility grid, to generate reference signals, to compute the compensation signal and reactive power compensation.
2) Implement a strategy for the current and voltage reference signal extraction method under non-sinusoidal and unbalance voltage and current conditions with Enhanced Phase Locked Loop Quadrature Signals Generator based Positive-sequence Component Detector algorithm.
3) Implement a strategy for the compensation signal calculation under non-sinusoidal and unbalance voltage and current conditions based on the synchronous reference frame theory concepts.
4) Implement a strategy for control the common DC link inverter as single phase inverter with single phase synchronous reference frame theory concept to compensate single and tow phase voltage sag and swells.

5) Implement an optimal DC voltage control strategy to give efficient compensation performance especially during voltage sag/swells faults.
6) Implement an optimal AC voltage control strategy to compensate the voltage sag/swells as well as regulate the PCC voltage.
7) Implement an optimal active power control strategy to compensate the voltage swell and over voltage disturbances.
8) Implement an optimal DC link voltage balance strategy to eliminate common mode voltage and to prevent the injection of leakage current into power system.

The proposed ML-MFGCI can exchange active power between AC and DC subgrid and enhance the quality of AC power system by compensate the voltage/current harmonics, load unbalance, neutral line current and reactive power as well as regulate the PCC voltage to nominal value. The ML-MFGCI also can compensate the voltage unbalance as well as compensate the three, two and single phase voltage sag/swells. The extensive simulation test results show that ML-MFGCI eliminates the voltage and current harmonics and keeps the supply current, PCC voltage and source voltage almost sinusoidal and below 5% THD. The test results also show that according to rated capacity of ML-MFGCI and voltage sag or swell levels the ML-MFGCI mitigates the voltage sag and swells and keeps the RMS of load voltage nearly 0.9-1 per unit for voltage sags and 1-1.1 for voltage swells. Moreover, test results show that the ML-MFGCI compensates the current unbalance and eliminates the negative sequence current from source current and keeps the unbalance ratio less than 3%. The test results also show that the ML-MFGCI completely eliminates the neutral line current.

Another main objective of this thesis is to propose a new wavelet transform based voltage sag/swell detection algorithm in flicker and harmonic polluted source voltage. Due to increasing usage of devices which are more sensitive to voltage

sag/swell the implementation of fast voltage sag/swell detection method becomes indispensable condition to protect end users from exposed to the unexpected mis-operation and outage have been represented. The difficulties of voltage sag/swell detection in the existing of harmonics and flicker have been outlined. The complexity of the situation when a voltage sag/swell with phase jumps occurs in unbalanced system has been remarked. Thus, the proposed algorithm and details the techniques used to improve the efficiency of fast voltage sag/swell detection especially under distorted system with harmonics and flicker presented in this chapter. The proposed algorithm can detect the voltage sag/swell with and without phase jump within 0.5-ms and 1.15-ms, respectively. The feasibility of proposed algorithm was verified through test cases using the PSCAD/EMTDC. The performance of voltage sag/swell detection method is compared with dq-transformation, FFT and EPLL based voltage sag/swell detection methods. Compared with conventional detection methods, the case results reveal good robustness, accuracy and faster processing time to detect balanced and unbalanced voltage sag/swells.

In the future, field researches will concentrate on reliability of electric power, energy conservation, efficient energy use and maximum use of renewable energy sources. Further research can be carried out in the following areas:

- Research on the new power quality aspects by growing interest on the vehicle to grid services which plug-in electric vehicles; inverter based renewable energy resources and active power quality conditioners.
- Research on the DC power quality aspects by growing interest on hybrid AC/DC micro and nano-grids.
- Research on the energy internet concept to maximize energy efficiency and future power network challenges where the numerous of energy consumers

produce their own energy from renewable energy resources and share it with each other.

REFERENCES

Aboufadel, E., Schlicker, S., Discovering wavelets. Wiley-Interscience, 1st edition. 1999.

Addison, N., 2002. The illustrated wavelet transform handbook, Taylor & Francis. 1st edition.

Agüera-Pérez, A., Palomares-Salas, J.C., González de la Rosa, J.J., Sierra-Fernández, J.M., Ayora-Sedeño, D., Moreno-Muñoz, A., 2011. Characterization of electrical sags and swells using higher-order statistical estimators. Measurement, 44, (8), 1453–1460.

Ahmed, J., Salam, Z., 2015. An improved method to predict the position of maximum power point during partial shading for PV arrays. IEEE Transactions on Industrial Informatics, 11, (6), 1378 – 1387.

Ahmed, J., Salam, Z., 2015. A critical evaluation on maximum power point tracking methods for partial shading in PV systems. Renewable and Sustainable Energy Reviews 47, 933-953.

Akagi, H., Kanazawad, Y., Nabae, A., 1984. Instantaneous reactive power compensators comprising switching devices without energy storage components. IEEE Trans Ind Appl, 20, (3), 6, 25–30.

Alepuz, S., Busquets-Monge, S., Bordonau, J., Gago, J., Gonzalez, D., Balcells, J., 2006, Interfacing renewable energy sources to the utility grid using a three-level inverter. IEEE Trans Ind. Electron., 53, (5), 15, 04–11.

Aktas, M., Turkmenoglu, V., 2010. Wavelet-based switching faults detection in direct torque control induction motor drives. IET Science, Measurement & Technology, 4, (6), 303-310.

Akorede, M.F., Hizam, H., Aris, I., Kadir, M.Z.A., 2010. A critical review of strategies for optimal allocation of distributed generation units in electric power systems. IREE, 5, (2), 593-600.

Alonso, O., Sanchis, P., Gubia, E., Marroyo, L., 2003. Cascaded H-bridge multilevel converter for grid connected photovoltaic generators with independent maximum power point tracking of each solar array", 34th IEEE Power Electronics Specialist Conference, 731-735.

Alonso-Martı´nez, J., Eloy-Garcı´a, J., Arnaltes, S., 2010. Direct power control of grid connected PV systems with three level NPC inverter. Sol Energy, 84, (7), 1175–86.

Altin, N., Ozdemir, S., 2013. Three-phase three-level grid interactive inverter with fuzzy logic based maximum power point tracking controller. Energy Convers Manage, 69, 17–26.

Aly, M., Ahmed, E.M., Shoyama, M., 2017, Thermal and reliability assessment for wind energy systems with DSTATCOM functionality in resilient microgrids, IEEE Transactions on Sustainable Energy, 8, (3), 953 – 965.

Appen, J., Braun, M., Stetz, T., Diwold, K., Geibel, D., 2013, The challenge of high PV penetration in the german electric grid, IEEE Power and Energy Magazine, 11, (2), 55 – 64.

Apráiz, M., Barros, J., Diego, R. I., 2014. A real-time method for time–frequency detection of transient disturbances in voltage supply systems. Electric Power Systems Research, 108, 103–112.

Arai, J., Iba, K., Funabashi, T., Nakanishi, Y., Koyanagi, K., Yokoyama, R., 2008. Power electronics and its applications to renewable energy in Japan. IEEE Circuits and Systems Magazine, 8, 52-66.

Azmi, S.A., Adam, G.P., Ahmed, K.H., Finney, S.J., Williams, B.W., 2013, Grid interfacing of multimegawatt photovoltaic inverters, IEEE Transactions on Power Electronics, 28, (6), 2770 – 2784.

Bae, B., Lee, J., Jeong, J., Han, B., 2010. Line-interactive single-phase dynamic voltage restorer with novel sag detection algorithm. IEEE Trans Power Delivery, 25, (4), 2–9.

Bai, Z., Zhang, Z., Zhang, Y., 2007. A generalized three-phase multilevel current source inverter with carrier phase-shifted SPWM. In: IEEE conference on power electronics specialists. 2055–2060.

Balamurugan, M., Sahooa, S.K., Sukchai, S., 2017, Application of soft computing methods for grid connected PV system: A technological and status review, Renewable and Sustainable Energy Reviews, 75, 1493–1508.

Bandara, K., Sweet, T., Ekanayake, J., 2012. Photovoltaic applications for off-grid electrification using novel multi-level inverter technology with energy storage. Renewable Energy Jan., 37, (1), 82–8.

Barghi-Latran, M., and Teke, A., 2015, Investigation of multilevel multifunctional grid connected inverter topologies and control strategies used in photovoltaic systems, Renewable and Sustainable Energy Reviews, 42, 361–376.

Barros, J., Diego, R.I., Apráiz M., 2012. Applications of wavelets in electric power quality: Voltage events. Electric Power Systems Research, 88, 130–136.

Belkaid, A., Gaubert, J.P., Gherbi, A., 2017. Design and implementation of a high-performance technique for tracking PV peak power. IET Renewable Power Generation, 11, (1), 92 – 99.

Biswal, B., Mishra, S., 2014. Power signal disturbance identification and classification using a modified frequency slice wavelet transform. IET Generation, Transmission & Distribution, 8, (2), 353-362.

Bollen MHJ, Gu YH. Signal processing of power quality, disturbances. Wiley Interscience & IEEE Press; 2006.

Beser, E., Arifoglu, B., Camur, S., Kandemir-Beser, E., 2010. A grid-connected photovoltaic power conversion system with single-phase multilevel inverter. Sol Energy, 2056–67.

Bhattacharya, S., Divan, D., 1995. Synchronous frame based controller implementation for a hybrid series active filter system. In: Proceedings of 30th industry applications society annual meeting, industry applications conference, 2531–2540.

Bhusal, P., Zahnd, A., Eloholma, M., Halonen, L., 2007, Energy-efficient innovative lighting and energy supply solutions in developing countries. IREE, 2. (1), 665-670.

Blaabjerg, F., Koutroulis, E., 2011, Methods for the optimal design of grid-connected PV inverters. Int J Renewable Energy Res, 1, (2), 54–64.

Blaabjerg, F., Yang, Y., Mam K., 2013. Power electronics – key technology for renewable energy systems – status and future. In: Third international conference on electric power and energy conversion systems. Istanbul, 1–6.

Bollen, M.H.J., Das, R., Djokic, S, Ciufo, P, Meyer, J., Rönnberg, S.K., Zavodam, F., 2017, Power quality concerns in implementing smart distribution-grid applications, IEEE Transactions on Smart Grid, 8, (1), 391 – 399.

Braun, M., Stetz, T., 2008, Multifunctional photovoltaic inverters - economic potential of grid-connected multifunctional PV-battery-systems in industrial environments, European Photovoltaic Solar Energy Conference and Exhibition, 3268– 3275.

Busquets-Monge, S., Rocabert, J., Rodriguez, P., Alepuz, S., Bordonau, J., 2008. Multilevel diode-clamped converter for photovoltaic generators with independent voltage control of each solar array. IEEE Trans. Ind. Electron., 55, (7), 27, 13–23.

Caamaño-Martín, E., Laukamp, H., Jantsch, M., Erge, T., Thornycroft, J., De Moor, H., Cobben, S., Suna, D., Gaiddon, B., 2008, Interaction between photovoltaic distributed generation and electricity networks, Prog. Photovolt: Res. Appl., 16, (7), 629 – 643.

Calderaro, V., Lattarulo, V., Piccolo A., Siano, P., 2012, Optimal switch placement by alliance algorithm for improving microgrids reliability, IEEE Transactions on Industrial Informatics, 8, (4), 925 – 934.

Campbell, M., Blunden, J., Smeloff, E., Aschenbrenner, P., 2009. Minimizing utility-scale PV power plant LCOE through the use of high capacity factor configurations. In: 34th IEEE conference on photovoltaic specialists, 7–12, 421–426.

Campbell, M., Blunden, J., Smeloff, E., Aschenbrenner, P., 2009. Minimizing utility-scale PV power plant LCOE through the use of high capacity factor configurations. In: 34th IEEE conference on photovoltaic specialists. 421–426.

Carrasco, J.M., Franquelo, LG, Bialasiewicz, J.T., Galván, E., Guisado, R.C.P., Prats, M.Á.M., León, J.I., Alfonso, N.M.. 2006. Power-electronic systems for the grid integration of renewable energy sources: a survey. IEEE Trans Ind Electron, 53, (4), 1002 – 1016.

Cavalcanti, MC., Farias, AM., Oliveira, KC., Neves, FAS., Afonso, JL., 2012, Eliminating leakage currents in neutral point clamped inverters for photovoltaic systems. IEEE Trans Ind Electron Jan., 59, (1), 435–43.

Chavarria, J., Biel, D., Guinjoan, F., Meza, C., Negroni, JJ., 2013. Energy-balance control of PV cascaded multilevel grid-connected inverters under level-shifted and phase-shifted PWMs. IEEE Trans Ind Electron Jan., 60, (1), 98–111.

Cecati, C., Ciancetta, F., Siano, P., 2010, A multilevel inverter for photovoltaic systems with fuzzy logic control. IEEE Trans. Ind. Electron., 57, (12), 41, 15–25.

Chen, K., Tian, S., Cheng, Y., Bai, L., 2014, An improved MPPT controller for photovoltaic system under partial shading condition, IEEE Transactions on Sustainable Energy, 5, (3), 978 – 985.

Cheng, L., Chang, Y., Huang, R., 2015, Mitigating voltage problem in distribution system with distributed solar generation using electric vehicles, 6, (4), 1475 – 1484.

Chiang Loh, P. Li, D., Kang Chai, Y., Blaabjerg, F., 2012, Hybrid AC–DC microgrids with energy storages and progressive energy flow tuning, Proceedings of The 7th International Power Electronics and Motion Control Conference, 1, 120 – 127.

Chiang Loh, P., Li, D., Kang Chai, Y., Blaabjerg, F., 2013, Autonomous Operation of Hybrid Microgrid with AC and DC Subgrids, IEEE Transactions on Power Electronics, 28, (5), 2214 – 2223.

Costa, F.B., Souza, B.A., Brito, N.S.D., 2010. Real-time detection of voltage sags based on wavelet transform. Latin America Conference and Exposition on Transmission and Distribution, 537–542.

Dash, PP., Kazerani, M., 2011. A multilevel current-source inverter based gridconnected photovoltaic system. In: North American power symposium, 1–6.

Dash, PP., Kazerani, M., 2012. Harmonic elimination in a multilevel current-source inverter-based grid-connected photovoltaic system. In: proceedings of the 38th IEEE annual conference on industrial electronics society, 1–6.

Dehghani, H., Vahidi, B., Naghizadeh, R.A., Hosseinian, S.H., 2013. Power quality disturbance classification using a statistical and wavelet-based Hidden Markov Model with Dempster–Shafer algorithm. International Journal of Electrical Power & Energy Systems, 47, 368–377.

Dwivedi, U.D., Singh, S.N., 2010. Enhanced detection of power-quality events using intra and interscale dependencies of wavelet coefficients. IEEE Transactions on Power Delivery, 25, (1), 358 – 366.

Electric Power Quality, IEEE, Inc., NY, USA, 2009.

Erişti, H., Demir, Y., 2010. A new algorithm for automatic classification of power quality events based on wavelet transform and SVM. Expert Systems with Applications, 37, (6), 4094–4102.

European Standard EN 50160, Voltage characteristics of electricity supplied by public electricity networks, CENELEC (2010).

Fennich, M., 2013. Tracking the global maximum power point of PV arrays under partial shading conditions. MSc thesis The University of Texas at San Antonio, 57.

Fitzer, C., Barnes, M., Peter-Green, G., 2002. Voltage sag detection technique for a dynamic voltage restorer. IEEE Ind Appl Conf., 2, 17–24.

Fitzer, C., Barnes, M., Green, P., 2004, Voltage sag detection technique for a dynamic voltage restorer. IEEE Trans Ind Appl, 40, (1), 3–12.

Flores, P., Dixon, J., Ortuzar, M., Carmi, R., Barriuso, P., Morán, L., 2009. Static Var compensator and active power filter with power injection capability, using 27-level inverters and photovoltaic cells. IEEE Trans Ind Electron Jan., 56, (1), 130–8.

Gencer, Ö., Öztürk, S., Erfidan, T., 2010. A new approach to voltage sag detection based on wavelet transform. International Journal of Electrical Power & Energy Systems, 32, (2), 133–140.

Ghaemi, A.H., Abyaneh, H.A., Mazlumi, K., 2011. Harmonic indices assessment by Wavelet Transform. International Journal of Electrical Power & Energy Systems, 33, (8), 1399–1409.

Grandi, G., Ostojic, D., 2009. Dual-inverter-based MPPT algorithm for grid-connected photovoltaic systems. In: International conference on clean electrical power, 393–398.

Grandi, G., Rossi, C., Ostoji,c D., Casadei, D., 2009, A new multilevel conversion structure for grid-connected PV applications. IEEE Trans Ind Electron., 56, (11), 44, 16–26.

Granados-Lieberman, D., Romero-Troncoso, R.J., Osornio-Rios, R.A., Garcia-Perez, A., Cabal-Yepez, E., 2011. Techniques and methodologies for power quality analysis and disturbances classification in power systems: a review. IET Generation, Transmission & Distribution, 5, (4), 519-529.

Graps, A., 1995. An introduction to wavelets. IEEE Computational Science & Engineering, 2, (2), 50-61.

González, R., Gubía, E., López, J., Marroyo, L., 2008. Transformerless single-phase multilevel-based photovoltaic inverter. IEEE Trans Ind Electron, 55, (7), 2694–702.

Guerrero, J.M., Loh, P.C., Lee; T.L., Chandorkar, M., 2013, Advanced control architectures for intelligent microgrids—part II: power quality, energy storage, and AC/DC microgrids, IEEE Transactions on Industrial Electronics, 60, (4), 1263 – 1270.

Habibi, A., Nayeripour, M., Aghaei, J., 2013, Secure multi-objective distributed generation planning in distribution network, 21st Iranian Conference on Electrical Engineering, 1 – 6.

Hämäläinen, J., 2015. Comparison of output harmonics between two- and three-level three-phase space vector PWM inverters. Tampere University of technology, MSc Thesis, 53.

Hamzaouia, I., Bouchafaaa, .F, Hadjammar, A., 2011, Investigation of the behavior of a three phase grid-connected photovoltaic system to control active and reactive power with DPC. Energy Procedia, 6, 493–502.

Hanif, M., Basu, M., Gaughan, K., 2012. Development of EN50438 compliant wavelet-based islanding detection technique for three-phase static distributed generation systems. IET Renewable Power Generation, 6, (4), 289-301.

Hansen, A.D., Sørensen, P., Hansen, L.H., Bindner, H., 2000. Models for a stand-alone PV system. Risø-R-1219(EN)/SEC-R-12, Risø National Laboratory, Roskilde, 79.

Hatziadoniu, CJ., Chalkiadakis, FE., Feiste, VK., 1999. A power conditioner for a gridconnected photovoltaic generator based on the 3-level inverter. IEEE Trans Energy Convers., 14, (4), 16, 05–10.

He, F., Zhao, Z., Yuan, L., 2012. Impact of inverter configuration on energy cost of gridconnected photovoltaic systems. Renewable Energy May, 41, 328–35.

Holz, R., 2013. Central inverters for utility-scale applications, SOLARPRO, 6.1, 11–12.

Hongtu, Z., Dongmei, X., 2012. Algorithm analysis on measuring the begin-end time of voltage sag based on biorthogonal wavelet. Energy Procedia, 17, Part A, 18–23,

Hung, CH., Gilmore, J., Huang, CP., Dai, PG., Zhu, W.. 2010. BoS cost savings and LCOE reduction for a 10 MW PV system with the 500 kW transformerless inverter. In: Second IEEE international symposium on power electronics for distributed generation systems, 924–928.

IEC Electromagnetic compatibility (EMC), Part 4, Section 30: Testing and measurement techniques – Power quality measurement methods. Standard IEC 61000-4-30; 2003.

IEEE recommended practice for powering and grounding sensitive electronic equipment. IEEE standard 1100; 1992.

IEEE Std. 1159-2009, IEEE Recommended Practice for Monitoring

Ishaque, K., Salam, Z., Syafaruddin, 2011. A comprehensive MATLAB Simulink PV system simulator with partial shading capability based on two-diode model. Solar Energy, 85, (9), 2217-2227.

Ishaque, K., Salam, Z., Taheri, H., 2011. Simple, Fast and accurate two diode model for photovoltaic modules. Solar Energy Mater. Solar Cells, 95, 586–594.

Ishaque, K., Salam, Z., Shamsudin, M.A., Amjad, M., 2012. A direct control based maximum power point tracking method for photovoltaic system under partial shading conditions using particle swarm optimization algorithm. Applied Energy, 99, 414-422.

Ishaque, K. Salam, Z,. 2013. A deterministic particle swarm optimization maximum power point tracker for photovoltaic system under partial shading condition. IEEE Trans. Ind. Electron., 60, (8), 3195 – 3206.

Joshia, P., Arora, S., 2017, Maximum power point tracking methodologies for solar PV systems – A review, Renewable and Sustainable Energy Reviews, 70, 1154–1177.

Justo, J.J., Mwasilu, F., Lee, J., Jung, J.W., 2013, AC-microgrids versus DC-microgrids with distributed energy resources: A review, Renewable and Sustainable Energy Reviews, 24, 387–405.

Kapoor, R., Saini, M. K., 2011. Hybrid demodulation concept and harmonic analysis for single/multiple power quality events detection and classification. International Journal of Electrical Power & Energy Systems, 33, (10), 1608–1622.

Karimi-Ghartemani, M., Iravani, MR., 2002. A nonlinear adaptive filter for online signal analysis in power systems: applications. IEEE Trans Power Delivery, 17, (2), 1, 7–22.

Kermadi, M., Berkouk, El,M., 2017, Artificial intelligence-based maximum power point tracking controllers for Photovoltaic systems: Comparative study, Renewable and Sustainable Energy Reviews, 69, 369–386.

Khadkikar, V., 2012. Enhancing electric power quality using UPQC: a comprehensive overview. IEEE Trans Power Electron, 27, (5), 84–97.

Khalid, M., Ahmadi, A.,Savkin, A.V., Agelidis, V.G., 2016, Minimizing the energy cost for microgrids integrated with renewable energy resources and conventional generation using controlled battery energy storage, Renewable Energy, 97, 646-655.

Khaligh, A., Onar, O.C., 2009. Energy harvesting: solar, wind, and ocean energy conversion systems. CRC Press, 1 edition, 382.

Killi, M., Samanta, S., 2015. An Adaptive Voltage-sensor-based MPPT for photovoltaic systems with SEPIC converter including steady-state and drift analysis. IEEE Transactions on Industrial Electronics, 62, (12), 7609 – 7619.

Knopf, H., 1999. Analysis, Simulation, and Evaluation of Maximum Power point tracking (MPPT) methods for a solar powered vehicle. MS thesis Portland State University, 332.

Koizumi, H., Kurokawa, K., 2005. A novel maximum power point tracking method for PV module integrated converter. Proceedings of the IEEE 36th Power Electronics Specialists Conference, 2081–2086.

Konstantopoulos, C., Koutroulis, E., 2014. Global maximum power point tracking of flexible photovoltaic modules. IEEE Transactions on Power Electronics, 29, (6), 2817 – 2828.

Kornelakis, A., Koutroulis, E.. 2009. Methodology for the design optimisation and the economic analysis of grid-connected photovoltaic systems. Renewable Power Gener, 3, (4), 476–92.

Koziy, K., Gou, B., Aslakson, J., 2013. A low-cost power-quality meter with series arc-fault detection capability for smart grid. IEEE Transactions on Power Delivery, 28, (3), 1584-1591.

Kumar, A.A., Rao, J.S., 2012. Power quality improvement of grid interconnected 3-phase 4-wire distribution system using fuzzy logic control. IJERT, 1, (4).

Laaksonen, H., Mohamed, A., 2008. Stability of microgrid with different configurations after islanding due to fault in the utility grid, IREE, 3. (3), 498-512.

Lee, SJ., Bae, HS., Cho, BH., 2009. Modeling and control of the single-phase photovoltaic grid-connected cascaded h-bridge multilevel inverter. In: IEEE energy conversion congress and exposition, 43–47.

Li, D., Zhu, Z.Q., 2015, A novel integrated power quality controller for microgrid, IEEE Transactions on Industrial Electronics, 62, (5), 2848 – 2858.

Liu, L., Li, H., Xue, Y., 2013. A coordinated active and reactive power control strategy for grid-connected cascaded photovoltaic (pv) system in high voltage high power applications. In: 28th IEEE annual conference and exposition on applied power electronics, 1301–1308.

Liu, F., Duan, S., Liu, F., Liu, B., Kang, Y., 2008. A variable step size INC MPPT method for PV systems. IEEE Transactions on Industrial Electronics, 55, (7), 2622 – 2628.

Malki, S., 2011. Maximum power point tracking (MPPT) for photovoltaic system" MS thesis Université M'Hamed Bougara Boumerdès. Algeria, 115.

Manimala, K., Selvi, K., Ahila, R., 2012. Optimization techniques for improving power quality datamining using wavelet packet based support vector machine. Neurocomputing, 77, (1), 36–47.

Masoum, M.A.S., Jamali, S., Ghaffarzadeh, N., 2010. Detection and classification of power quality disturbances using discrete wavelet transform and wavelet networks. IET Science, Measurement & Technology, 4, (4), 193-205.

Mehera, S.K., 2010. Pradhanb, A.K., Fuzzy classifiers for power quality events analysis, Electric Power Systems Research, 80, (1), 71–76.

Mei, J., Xiao, B., Shen, K., Tolbert, LM., Zheng, JY., 2013. Modular multilevel inverter with new modulation method and its application to photovoltaic grid-connected generator. IEEE Trans Power Electron Nov., 28, (11), 50, 63–73.

Melin, PE., Espinoza, JR., Zargari, NR., Moran, LA., Guzman, JI., 2008. A novel multi-level converter based on current source power cell. In: IEEE conference on power electronics specialists. 2084–2089.

Meng-Yeong, L., 2009. Three-level neutral-pointclamped matrix converter topology. University of Nottingham, PhD thesis, 254.

Meyer, J., Klatt, M., Schegner, P., 2011, Power quality challenges in future distribution networks, 2nd IEEE PES International Conference and Exhibition on Innovative Smart Grid Technologies, 1-6.

Miñambres-Marcos, V., Romero-Cadaval, E., Milanes-Montero, MI., GuerreroMartínez, MA., Barrero-González, F., Castrillo, PG., 2010. Power injection system for photovoltaic plants based on a multiconverter topology with dc-link capacitor voltage balancing. In: 12th International conference on optimization of electrical and electronic equipment. 1121–1130.

Mi~nambres-Marcos, V., Romero-Cadaval, E., Guerrero-Martínez, MA., MilanésMontero, MI., 2013. Cooperative operation of inverters for grid-connected photovoltaic generation systems. Electr Power Syst Res., 96, 47–55.

Moradi-Shahrbabak, Z., Tabesh, A., Yousefi, G.R., 2014. Economical design of utility-scale photovoltaic power plants with optimum availability. IEEE Transactions on Industrial Electronics, 61, (7), 3399–3406.

Mortezaei, A., Simões, M.G., Bubshait, A.S., Busarello, T.D.C., Marafão, F.P., Al-Durra, A., 2017, Multifunctional control strategy for asymmetrical cascaded H-bridge inverter in microgrid applications, IEEE Transactions on Industry Applications, 53, (2), 1538 – 1551.

Nath, S., Sinha, P., Goswami, S. K., 2012. A wavelet based novel method for the detection of harmonic sources in power systems. International Journal of Electrical Power & Energy Systems. 40, (1), 54–61.

Olalla, C., Clement, D., Rodriguez, M., Maksimovic, D., 2013. Architectures and control of submodule integrated DC–DC converters for photovoltaic applications. IEEE Trans. Power Electron., 28, (6), 2980–2997.

Oliveira, KC., Cavalcanti, MC., Afonso, JL., Farias, AM., Neves, FAS., 2010. Transformerless photovoltaic systems using neutral point clamped multilevel inverters. In: IEEE international symposium on industrial electronics, 1131–1136.

Paridari, K., Hamzeh, M., Emamian, S., Karimi, H., Bakhshai, A., 2013, A new decentralized voltage control scheme of an autonomous microgrid under unbalanced and nonlinear load conditions, IEEE International Conference on Industrial Technology 1812 – 1817.

Perpinias, I.I., Papanikolaou, N.P., Tatakis, 2015, E.C., Fault ride through concept in low voltage distributed photovoltaic generators for various dispersion and penetration scenarios, Sustainable Energy Technologies and Assessments, 12, 15-25.

Petinrin, J.O., Shaaban, M., 2016, Impact of renewable generation on voltage control in distribution systems, Renewable and Sustainable Energy Reviews, 65, 770-783.

Pilawa-Podgurski, R.C.N., Perreault, D. J., 2013. Submodule integrated distributed maximum power point tracking for solar photovoltaic applications. IEEE Trans. Power Electron., 28, (6), 2957–2967.

Pimentel, SP., Martinez, RMM., Pomilio, JA., 2009. Single-phase distributed generation system based on asymmetrical cascaded multilevel inverter. In: Brazilian power electronics conference, 346–353.

Pires, VF., Martins, JF., Hao, C., 2012. Dual-inverter for grid-connected photovoltaic system: modeling and sliding mode control. Sol Energy, 86, (7), 21, 06–15.

Patrao, I., Figueres, E., González-Espín, F., Garcerá G. 2011. Transformerless topologies for grid-connected single-phase photovoltaic inverters. Renewable Sustainable Energy Rev Sep., 15, (7), 34, 23–31.

Petinrin, J.O., Shaaban, M., 2016, Impact of renewable generation on voltage control in distribution systems, Renewable and Sustainable Energy Reviews, 65, 770–783.

Polikar, R., Wavelet transform tutorials, 2012. (http://users.rowan.edu/~polikar/ wavelets/ wttutorial.html).

Polikar, R., The Wavelet Tutorial, Part IV, Jun. 2001 (http://users.rowan.edu/~polikar/WAVELETS/WTpart4.html).

Poshtkouhi, S., Palaniappan, V., Fard, M., Trescases, O., 2012. A general approach for quantifying the benefit of distributed power electronics for fine grained MPPT in photovoltaic applications using 3-D modeling. IEEE Trans. Power Electron., 27, (11), 4656–4666.

Pregeij, A., Begovic, M., Rohatgi, A.,. 2002. Impact of inverter configuration on PV system reliability and energy production. In: 29th IEEE conference on photovoltaic specialists, 1388–1391.

Rahim, NA., Selvaraj, J., 2010. Multistring five-level inverter with novel PWM control scheme for PV application. IEEE Trans Ind. Electron., 57, (6), 21, 11–23.

Rahim, NA., Selvaraj, J., Krismadinata, C., 2010, Five-level inverter with dual reference modulation technique for grid-connected PV system. Renewable Energy March, 35, (3), 7, 12–20.

Rajasekar, S., Gupta, R., 2011. Photovoltaic array based multilevel inverter for power conditioning. In: International conference on power and energy systems, 1–6.

Rajkumar, MV., Manoharan. PS,. 2013. FPGA based multilevel cascaded inverters with SVPWM algorithm for photovoltaic system. Sol Energy, 87, 2, 29–45.

Rajkumar, MV., Manoharan, PS., Ravi A. 2013. Simulation and an experimental investigation of SVPWM technique on a multilevel voltage source inverter for photovoltaic systems. Int Journal Electr Power Energy Syst., 52, 1, 16–31.

Ramli, M.Z., Salam, Z., 2014. A simple energy recovery scheme to harvest the energy from shaded photovoltaic modules during partial shading. IEEE Trans.Power Electron., 29, (12), 6458 – 6471.

Ravi, A., Manoharan, PS., Vijay-Anand, J., 2011, Modeling and simulation of three phase multilevel inverter for grid connected photovoltaic systems. Sol Energy, 85, (11), 281, 1–8.

Ray, P.K., Kishor, N., Mohanty, S.R., 2012. Islanding and power quality disturbance detection in grid-connected hybrid power system using wavelet and S-transform. IEEE Transactions on Smart Grid, 3, (3), 1082-1094.

Rezaei, MA., Farhangi, S., Iman-Eini, H., 2011. Enhancing the reliability of single-phase CHB-based grid-connected photovoltaic energy systems. Second conference on power electronics, 1, 17–22.

Rivera, S., Wu, B., Kouro, S., Wang, H., Zhang, D., 2012. Cascaded H-bridge multilevel converter topology and three-phase balance control for large scale photovoltaic systems. Third IEEE international symposium on power electronics for distributed generation systems, 69, 0–7.

Sadabadi, M.S., Shafiee, Q., Karimi, A., 2017, Plug-and-play voltage stabilization in inverter-interfaced microgrids via a robust control strategy, IEEE Transactions on Control Systems Technology, 25, (3), 781 – 791.

Salam, A.A., Barakat, G., Hannanand, M.A., Shareef, H., 2010. An improved inverter control scheme for managing the distributed generation units in a microgrid. IREE, 5. (5), 891-899.

Sannino, A., Svensson, J., Larsson, T., 2003. Power-electronic solutions to power quality problems, Electric Power Systems Research, (66), 71–82.

Sarkar, T.K., Su, C.A., Salazar-Palma, R., Garcia-Castillo, M., Boix, L.R.R., 1998. A tutorial on wavelets from an electrical engineering perspective. I. Discrete wavelet techniques. IEEE Antennas and Propagation Magazine, 40, (5), 49-68.

Shafiyi, MA., Khederzadeh, M., Sadeghi, M., Khani, S., 2012. A grid-connected PV power supply based on flying capacitor multicell converter with modified MPPT based control for active power filtering. In: Second Iranian conference on renewable energy and distributed generation. 141–146.

Shamiur Rahman, Md., Hossain, M.J., Rafi, F.H. M., Lu, J., 2016, A multi-purpose interlinking converter control for multiple hybrid AC/DC microgrid operations, IEEE Innovative Smart Grid Technologies, 221 – 226.

Selvaraj, J., Rahim, NA., 2009, Multilevel inverter for grid-connected PV system employing digital PI controller. IEEE Trans Ind Electron Jan., 56, (1), 1, 49–58.

Sharma, P., V., Agarwal, 2014, Exact maximum power point tracking of grid-connected partially shaded PV source using current compensation concept, IEEE Transactions on Power Electronics, 29, (9), 4684 – 4692.

Shimizu, T., Hashimoto, O., Kimura, G., 2003. A novel high-performance utility-interactive photovoltaic inverter system. IEEE Trans. Power Electron., 18, (2), 704–711.

Siemens AG, 2011, 2011, Utility-scale photovoltaic power plants, 14. http://www.siemens.com/pv

Singh, B., Mukherjee, V., Tiwari, P., 2015, A survey on impact assessment of DG and FACTS controllers in power systems, Renewable and Sustainable Energy Reviews, 42, 846-882.

Whaite, S., Grainger, B., Kwasinski, A., 2015, Power quality in dc power distribution systems and microgrids, Energies, 8, (5), 4378-4399.

Somogyi, C.A., 2015. Common mode voltage mitigation strategies using PWM in neutral-point-clamped multilevel inverters, Marquette University, MSc Thesis, 191.

Steurer, M.M., Schoder, K., Faruque, O., Soto, D., Bosworth, M., Sloderbeck, M., Bogdan, F., Hauer, J., Winkelnkemper, M., Schwager, L., Blaszczyk, P., 2016, Multifunctional megawatt-scale medium voltage DC test bed based on modular multilevel converter technology, IEEE Transactions on Transportation Electrification, 2, (4), 597 – 606.

Subasi, A., Yilmaz, A.S., Tufan, K., 2011. Detection of generated and measured transient power quality events using Teager Energy Operator. Energy Conversion and Management, 52, (4), 1959–1967.

Teke, A., Barghi-Latran, M., 2014, Review of Multifunctional Inverter Topologies and Control Schemes Used in Distributed Generation Systems, Journal of Power Electronics, 14, (2), 324-340.

Teke, A., Bayindir, K.Ç., Tümay, M., 2009.Fast sag/swell detection method for fuzzy logic based dynamic voltage restorer. Inst. Eng. Technol. Gen., Transm. Distrib., 4, (1), 1–12.

Teke, A., Saribulut, L., Tumay, M., 2011. A novel reference signal generation method for power-quality improvement of unified power-quality conditioner. IEEE Transactions on Power Delivery, 26, (4), 2205-2214.

Tey, K.S., Mekhilef, S., 2014. Modified incremental conductance algorithm for photovoltaic system under partial shading conditions and load variation. IEEE Trans. Ind. Electron., 61, (10), 5384 – 5392.

Toma, S., Senjyu, T., Miyazato, Y., Yona, A., Funabashi, T., Saber, A.Y., Kim, C.H., 2008, Optimal coordinated voltage control in distribution system, Power and Energy Society General Meeting - Conversion and Delivery of Electrical Energy in the 21st Century, 1 – 7.

Torrent-Fontbona, F., Lopez, B., 2016, Decision support for grid-connected renewable energy generators planning, Energy, 151, (1) 577–590.

Tsengenes, G., Adamidis, G., 2011. A multi-function grid connected PV system with three level NPC inverter and voltage oriented control. Sol Energy, 85, (11), 2, 595–610.

Tsengenes, G., Nathenas, T., Adamidis G., 2012. A three-level space vector modulated grid connected inverter with control scheme based on instantaneous power theory. Simul Modell Pract Theory, 25, 1, 34–47.

U.S. Energy Information Administration. 2013. Levelized cost of new generation resources in the annual energy; Available: ⟨http://www.eia.gov/⟩.

Villanueva, E., Correa, P., Rodriguez, J., Pacas, M., 2009, Control of a single-phase cascaded H-Bridge multilevel inverter for grid-connected photovoltaic systems. IEEE Trans Ind Electron., 56, (11), 4, 399–406.

Villegas-Nunez, J., 2013. Multilevel topologies: can new inverters improve solar farm output?. Solar industry.

Walker, G.R., 2001. Evaluating MPPT converter topologies using a Matlab PV model. Australian Journal of Electrical & Electronics Engineering, 21, (1), 49-55.

Wang, X., Guerrero, J.M., Chen, Z., 2010, Control of grid interactive AC microgrids, IEEE International Symposium on Industrial Electronics, 2211 – 2216.

Wang, S., Chen, S., Ge, L., Wu, L., 2016, Distributed generation hosting capacity evaluation for distribution systems considering the robust optimal operation of OLTC and SVC, IEEE Transactions on Sustainable Energy, 7, (3), 1111 – 1123.

Wang, X., Zhuo, F., Li, J., Wang, L., Ni, S., 2013. Modeling and Control of Dual-Stage High-Power Multifunctional PV Systemin d -q-o Coordinate. IEEE Transactions on Industrial Electronics, 60, (4), 1556-1570.

Wu, F.F., Varaiya, P.P., Hui, R.S.Y., 2015, Smart grids with intelligent periphery: An architecture for the energy internet, Engineering, 1, (4), 436-446.

Xiangwu, Y., Bo, Z., Xiaobin, G., Lixia, Z., Heming, L., 2007. Double closed-loop control of three-phase five-level PWM current source inverter. In: 33rd IEEE annual conference of the industrial electronics society. 2110–2114.

Xiao, B., Filho, F., Tolbert, LM., 2011. Single-phase cascaded H-Bridge multilevel inverter with nonactive power compensation for grid-connected photovoltaic generators. In: IEEE energy conversion congress and exposition, phoenix, 2733–2737.

Zafar, R., Ravishankar, J., 2016, Coordinated control of step voltage regulator and D-STATCOM in the presence of distributed photovoltaic systems, IEEE International Conference on Power System Technology, 1 – 6.

Zafar, T., Morsi, W.G., 2013. Power quality and the un-decimated wavelet transform: An analytic approach for time-varying disturbances. Electric Power Systems Research, 96, 201–210.

Zhang, Z., Ooi, B., 1992. Multi-modular current-source SPWM converters for superconducting magnetic energy storage system. In: 23rd IEEE annual conference on power electronics specialists, 561–568.

Zeng, Z., Yang, H., Zhao, R., Cheng, C., 2013. Topologies and control strategies of multifunctional grid-connected inverters for power quality enhancement: a comprehensive review. Renewable Sustainable Energy Rev, 24, 223–70.

Zeng, G., Cao, M., Chen, Y., 2012. A multi-functional utility interface of BIPV systems based on cascade multilevel converter. Energy Procedia (Part A), 3, 56–65.

Zhou, L., Fu, Q., Li, X., Liu, C., 2009. A novel photovoltaic grid-connected power conditioner employing hybrid multilevel inverter. In: International conference on sustainable power generation and supply, 1–7.

Zhukov, S., 2012. Loss modelling of three-level inverters controlled with space vector modulation technique. LAPPEENRANTA UNIVERSITY OF TECHNOLOGY, MSc Thesis, 87.

CURRICULUM VITAE

Mohammad BARGHI LATRAN was born in Ardebil, Iran in 1984. He received his B.S. degree in Power Electric Engineering Department from the Islamic Azad University, Ardabil Branch in 2007 and M.Sc. degree in Electrical and Electronics Engineering Department from Hacettepe University in 2012.

He joined the power quality research group in 2012 to pursue a Ph.D. degree in Electrical and Electronics Engineering. He has worked in several research projects supported by Scientific and Technological Council of Turkey and Scientific Research Project Unit of Çukurova University. His research areas are power quality, active power quality conditioners, smart grid, interconnected AC/DC microgrids, renewable and sustainable energies and power electronic applications in renewable energy sources.